SECTION A

JOURNAL OF RESEARCH

of the NATIONAL BUREAU OF STANDARDS

JNBAAR 78A(3) 315/445, May-June 1974

U.S. DEPARTMENT OF COMMERCE / National Bureau of Standards

Physics and Chemistry

Journal of Research

of the

National Bureau of Standards

A. Physics and Chemistry

May–June • 1974

VOLUME • 78A

NUMBER • 3

Editor: C. W. Beckett

Associate Editor: D. D. Wagman

Publication dates:
Feb. 1, Apr. 1, June 1, Aug. 1, Oct. 1, Dec. 1, 1974

J. Res. Nat. Bur. Stand. (U.S.), A

JOURNAL OF RESEARCH

The National Bureau of Standards Journal of Research reports research and development in the fields of activity shown at right. Also included from time to time are survey articles on topics closely related to the Bureau's scientific and technical program.

The Journal is published in two separate sections as follows:

A. Physics and Chemistry

Contains papers of interest primarily to scientists working in these fields. Issued six times a year. Annual subscription: domestic, $17.00; foreign $21.25. Single copy, varies.

B. Mathematical Sciences

Presents studies and compilations designed mainly for the mathematician and the theoretical physicist. Issued quarterly. Annual subscription: domestic, $9.00; foreign, $11.25. Single copy, $2.25.

The National Bureau of Standards[1] was established by an act of Congress March 3, 1901. The Bureau's overall goal is to strengthen and advance the Nation's science and technology and facilitate their effective application for public benefit. To this end, the Bureau conducts research and provides: (1) a basis for the Nation's physical measurement system, (2) scientific and technological services for industry and government, (3) a technical basis for equity in trade, and (4) technical services to promote public safety. The Bureau consists of the Institute for Basic Standards, the Institute for Materials Research, the Institute for Applied Technology, the Institute for Computer Sciences and Technology, and the Office for Information Programs.

THE INSTITUTE FOR BASIC STANDARDS provides the central basis within the United States of a complete and consistent system of physical measurement; coordinates that system with measurement systems of other nations; and furnishes essential services leading to accurate and uniform physical measurements throughout the Nation's scientific community, industry, and commerce. The Institute consists of a Center for Radiation Research, an Office of Measurement Services and the following divisions:

Applied Mathematics — Electricity — Mechanics — Heat — Optical Physics — Nuclear Sciences[2] — Applied Radiation[2] — Quantum Electronics[3] — Electromagnetics[3] — Time and Frequency[3] — Laboratory Astrophysics[3] — Cryogenics[3].

THE INSTITUTE FOR MATERIALS RESEARCH conducts materials research leading to improved methods of measurement, standards, and data on the properties of well-characterized materials needed by industry, commerce, educational institutions, and Government; provides advisory and research services to other Government agencies; and develops, produces, and distributes standard reference materials. The Institute consists of the Office of Standard Reference Materials and the following divisions:

Analytical Chemistry — Polymers — Metallurgy — Inorganic Materials — Reactor Radiation — Physical Chemistry.

THE INSTITUTE FOR APPLIED TECHNOLOGY provides technical services to promote the use of available technology and to facilitate technological innovation in industry and Government; cooperates with public and private organizations leading to the development of technological standards (including mandatory safety standards), codes and methods of test; and provides technical advice and services to Government agencies upon request. The Institute consists of a Center for Building Technology and the following divisions and offices:

Engineering and Product Standards — Weights and Measures — Invention and Innovation — Product Evaluation Technology — Electronic Technology — Technical Analysis — Measurement Engineering — Structures, Materials, and Life Safety[4] — Building Environment[4] — Technical Evaluation and Application[4] — Fire Technology.

THE INSTITUTE FOR COMPUTER SCIENCES AND TECHNOLOGY conducts research and provides technical services designed to aid Government agencies in improving cost effectiveness in the conduct of their programs through the selection, acquisition, and effective utilization of automatic data processing equipment; and serves as the principal focus within the executive branch for the development of Federal standards for automatic data processing equipment, techniques, and computer languages. The Center consists of the following offices and divisions:

Information Processing Standards — Computer Information — Computer Services — Systems Development — Information Processing Technology.

THE OFFICE FOR INFORMATION PROGRAMS promotes optimum dissemination and accessibility of scientific information generated within NBS and other agencies of the Federal Government; promotes the development of the National Standard Reference Data System and a system of information analysis centers dealing with the broader aspects of the National Measurement System; provides appropriate services to ensure that the NBS staff has optimum accessibility to the scientific information of the world. The Office consists of the following organizational units:

Office of Standard Reference Data — Office of Technical Information and Publications — Library — Office of International Relations.

---

[1] Headquarters and Laboratories at Gaithersburg, Maryland, unless otherwise noted; mailing address Washington, D.C. 20234.
[2] Part of the Center for Radiation Research.
[3] Located at Boulder, Colorado 80302.
[4] Part of the Center for Building Technology.

U.S. DEPARTMENT OF COMMERCE
Frederick B. Dent, Secretary
NATIONAL BUREAU OF STANDARDS
Richard W. Roberts, Director

Order all publications from the Superintendent of Documents
U.S. Government Printing Office, Washington, D.C. 20402

The Secretary of Commerce has determined that the publication of this periodical is necessary in the transaction of the public business required by law of this Department. Use of funds for printing this periodical has been approved by the Director of the Office of Management and Budget through June 30, 1976.

JOURNAL OF RESEARCH of the National Bureau of Standards—A. Physics and Chemistry
Vol. 78A, No. 3, May–June 1974

Photoionization of CO_2-CO-O_2 Mixtures. Formation and Reactions of Ion Clusters*

L. W. Sieck and R. Gorden, Jr.

Institute for Materials Research, National Bureau of Standards, Washington, D.C. 20234

(January 18, 1974)

Various mixtures containing combinations of CO_2, O_2, or CO have been photoionized at 16.7 and 21.2 eV at pressures up to 1.5 torr in the NBS high pressure photoionization mass spectrometer. In CO_2-CO mixtures the interactions of CO_2^+ ions eventually lead to the formation of $(CO)_2^+$ and $[(CO)_2 \cdot CO_2]^+$ cluster ions, while photoionization of CO_2-CO-O_2 mixtures yields mainly oxygen-containing clusters at higher pressures. The investigation of O_2-CO mixtures also revealed reactions between O_4^+ and CO. The role of impurity reactions involving H_2O is considered in some detail, and the implications of all of these data to the vapor phase radiolysis of CO_2 is discussed.

Key words: CO; CO_2; ion-molecule reactions; O_2; photoionization; radiolysis; rate constants.

1. Introduction

The apparent stability of CO_2 towards ionizing radiation in the vapor phase is a well-documented phenomenon [1],[1] and the extensive literature on this subject strongly suggests the dominant role of ions in whatever mechanism is responsible for the reoxidation of CO to CO_2. The various arguments involved in reaching this conclusion have been outlined in detail in the review by Anderson and Dominey [1]. A recent article by Parkes [2] has considered the possible role of negative ions, but the magnitude of the measured rate constants for the probable anionic reactions are far too low to account for the observed radiation effects. It is known [3], however, that CO_2^+ parent cations will react with O_2 to yield O_2^+ ions, which, in turn, associate with CO_2 at higher pressures to yield $(O_2 \cdot CO_2)^+$;

$$CO_2^+ + O_2 \rightarrow O_2^+ + CO_2 \qquad (1)$$

$$O_2^+ + CO_2 \xrightarrow{CO_2} (O_2 \cdot CO_2)^+ + CO_2. \qquad (2)$$

On the basis of these observations, Parkes [2] has suggested an alternative mechanism for the radiolysis which involves attack of $(O_2 \cdot CO_2)^+$ on CO:

$$(O_2 \cdot CO_2)^+ + CO \rightarrow CO_3^+ + CO_2 \qquad (3)$$

followed by

$$CO_3^+ + CO \rightarrow CO_2^+ + CO_2. \qquad (4)$$

Since CO_2^+ is regenerated, this overall sequence would represent a chain mechanism for destruction of the accumulated radiolysis products. Essentially the same formalism, again involving CO_3^+ as an intermediate, was originally proposed by Clay et al. [4] to explain the chain oxidation of CO also observed in the radiolysis of O_2-CO mixtures. However, reactions 3 and 4 have not been detected experimentally as of this writing, and the exact mechanism for the radiation effects still remains unresolved.

In a recent article from this laboratory [5] we described the results of experiments involving the NBS High Pressure Mass Spectrometer in which N_2O was photoionized at elevated pressures in the presence of its radiolytic decomposition products N_2, NO, and O_2, and a number of novel ionic reactions were discovered which had remained undetected in other mass spectrometric studies. As a result of these experiments the radiolysis of N_2O was reevaluated and several of the observed chemical effects were rationalized in terms of these new cationic reactions.

Our goal in the present study was to investigate the positive ion chemistry occurring in mixtures of CO_2 with CO and O_2, in the hope of detecting reactions which might also account for the observed radiation stability of this molecule. These efforts were also extended to the O_2-CO system.

2. Experimental Procedures

All of the experiments reported here were carried out with the NBS High Pressure Photoionization Mass Spectrometer using the self-enclosed Ne (16.66–16.84 eV) and He (21.2 eV) resonance lamps as ionization

* This work supported in part by the U.S. Atomic Energy Commission.
[1] Figures in brackets indicate the literature references at the end of this paper.

sources. The adaptation of these lamps to the reaction chamber has been described in a recent article from this laboratory [5], and the methodology involved in deriving rate coefficients and other kinetic parameters has also been discussed elsewhere [6]. All of the experiments were carried out at room temperature under such conditions that the reactant ions have a kinetic energy distribution corresponding to kT at 300 K (thermal ions).

3. Results and Discussion

3.1. Pure CO_2

The behavior observed when CO_2 (I.P. = 13.79 eV)[7] was photoionized at 21.2 eV over the pressure range 10^{-3} to approximately 1 torr is given in figure 1. At

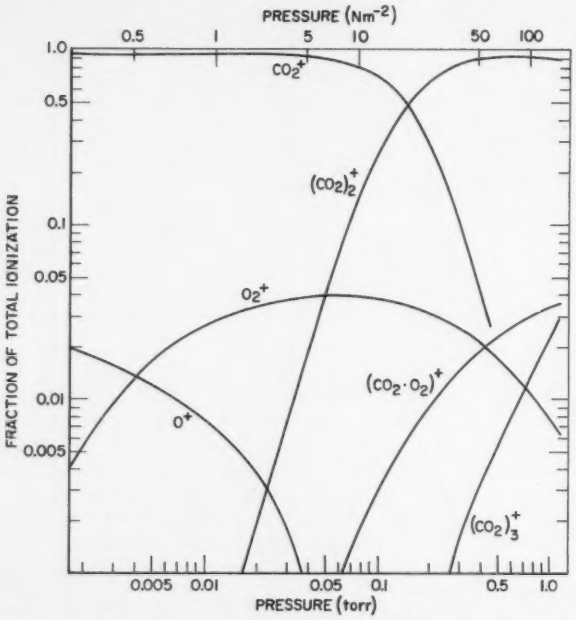

FIGURE 1. *Composite mass spectrum obtained from the 21.2 eV photoionization of* CO_2 *as a function of pressure.*

pressures below 0.01 torr, where only bimolecular processes are observed, the only significant reaction found was

$$O^+ + CO_2 \rightarrow O_2^+ + CO \qquad \Delta H = -118.3 \text{ kJ/mol} \qquad (5)$$

which is quantitative for removal of the minor O^+ fragment ion from the system. Although we did not attempt to derive an accurate rate coefficient for this reaction, our decay curve for O^+ is consistent with rate constants in the range 0.8 to 1.2×10^{-9} cm³/molecule-s reported for this process from other laboratories [3, 8]. The O_2^+ produced from the reaction of O^+ with CO_2 reacts with CO_2 at pressures greater than a few tenths of a torr to yield the $(O_2 \cdot CO_2)^+$ association ion

$$O_2^+ + CO_2 \xrightarrow{CO_2} (O_2 \cdot CO_2)^+ . \qquad (2)$$

In addition, the $(O_2 \cdot CO_2)^+$ ion formed in this manner also associates with a second molecule of CO_2 at higher pressures, although the fractional yield in pure CO_2 is too small to show over the pressure range covered by figure 1.

$$(O_2 \cdot CO_2)^+ + CO_2 \xrightarrow{M} [O_2 \cdot (CO_2)_2]^+ . \qquad (6)$$

At pressures greater than approximately 0.01 torr the $(CO_2)_2^+$ association ion was detected;

$$CO_2^+ + CO_2 \xrightarrow{CO_2} (CO_2)_2^+ . \qquad (7)$$

Under our experimental conditions (300 K, 21.2 eV photoionization) we derive a termolecular rate coefficient for this process of $3.3 \pm 0.3 \times 10^{-28}$ cm⁶/molecule²-s using the growth curve for $(CO_2)_2^+$ at pressures below 0.03 torr, which compares favorably with the value of 3.0×10^{-28} cm⁶/molecule²-s reported by Paulson et al. [9] in electron impact ionization experiments. We cannot confirm or deny the occurrence of overall processes such as

$$CO_2^+ + nCO_2 \rightarrow (CO_2)_2^+ + (n-1)CO_2 \qquad (8)$$

(where $n > 2$) at higher pressures, although higher order processes of this type were observed by Schildcrout and Franklin [8] in electron impact ionization experiments at pressures in the range from 0.05 to approximately 1 torr. In any event, regardless of the exact mechanism at higher pressures, the formation of $(CO_2)_2^+$ is essentially quantitative above 0.6 torr. We also observed, for the first time, the formation of $(CO_2)_3^+$, which reaches a level of 2.5% of the total ionization in CO_2 at 1 torr total pressure (see fig. 1).

3.2. Impurity Reactions in CO_2

In spite of the most judicious handling of the CO_2 samples used in this study, several ions appeared in the composite mass spectrum at pressures approaching 1 torr which could be assigned to interactions of $(CO_2)_2^+$ and $(O_2 \cdot CO_2)^+$ with residual water present in the mass spectrometer. Particularly "wet" samples typically gave high pressure mass spectra which included m/e 36, $(H_3O^+ \cdot OH)$, m/e 50, $(O_2 \cdot H_2O)^+$, m/e 62, $(H_2O \cdot CO_2)^+$, and m/e 106, $[(CO_2)_2 \cdot H_2O]^+$. The formation of these ions could be ascribed to the following reactions:

$$(CO_2)_2^+ + H_2O \rightarrow (CO_2 \cdot H_2O)^+ + CO_2 \qquad (9)$$

$$(CO_2)_2^+ + H_2O \xrightarrow{CO_2(?)} [(CO_2)_2 \cdot H_2O]^+ \qquad (10)$$

$$(O_2 \cdot CO_2)^+ + H_2O \rightarrow (O_2 \cdot H_2O)^+ + CO_2 \qquad (11)$$

$$(O_2 \cdot H_2O)^+ + H_2O \rightarrow H_3O^+ \cdot OH + O_2 \qquad (12)$$

All of these reactions represent "switching" mechanisms in which a more weakly bound entity is replaced by a more strongly bound neutral (H_2O). The product ion appearing at m/e 36 is assigned the structure $H_3O^+ \cdot OH$ since it has been shown [10] that OH is displaced from the collision complex when this ion interacts with another molecule of water.

$$H_3O^+ \cdot OH + H_2O \rightarrow H^+(H_2O)_c + OH. \qquad (13)$$

Process 12 has also been observed by Good et al. [10] in ionized moist oxygen and air.

The water vapor content in our various samples cannot, of course, be determined accurately since the level corresponds to residual adsorbed material within the mass spectrometer system. However, because the water-containing clusters are more stable than those containing CO_2, the CO_2-containing clusters will eventually find a water molecule if given sufficient reaction time. The analogous behavior has also been found in this laboratory [5] in photoionized N_2O at higher pressures. Our "driest" experiments in pure CO_2 usually yielded a composite mass spectrum containing 3 to 4 percent $[(CO_2)_2 \cdot H_2O]^+$, and no other water-containing ions, at a CO_2 pressure of 1 torr. It is from these experiments that the curves given in figure 1 are constructed.

3.3. Pure CO

Pure CO, (I.P. = 14.01 eV) was studied at both 16.7 and 21.2 eV. The only reaction channel observed was the termolecular association reaction

$$CO^+ + CO \xrightarrow{CO} (CO)_2^+ \qquad (14)$$

for which a rate coefficient of $1.48 \pm 0.08 \times 10^{-28}$ cm^6/molecule^2-s was derived. This value agrees very well with the value of 1.44×10^{-28} cm^6/molecule^2-s reported by Chong and Franklin [11] as a result of electron impact ionization experiments.

3.4. CO_2-CO Mixtures

Various CO_2-CO mixtures, which varied in composition from 0.3 to 50 mol percent CO, were investigated at both 16.7 and 21.2 eV. As the pressure was increased in such mixtures the CO^+ ion, produced by the direct photoionization of the CO component, was observed to charge exchange efficiently with CO_2 to yield CO_2^+;

$$CO^+ + CO_2 \rightarrow CO_2^+ + CO$$

$$\Delta H = -28.0 \text{ kJ/mol}. \qquad (15)$$

Our rate coefficient for this near-resonant process, $1.42 \pm 0.20 \times 10^{-9}$ cm^3/molecule-s, falls between that reported by Fehsenfeld et al. [12] (1.1×10^{-9}) and Schildcrout and Franklin [8] (2.0×10^{-9}), and is independent of photon energy within the experimental error.

As the total pressure was increased in CO_2-CO mixtures a rather complex and unexpected reaction scheme was observed involving consecutive reactions of association ions. This behavior is best understood by considering the data obtained from a CO_2 sample containing 0.33 percent added CO (fig. 2).

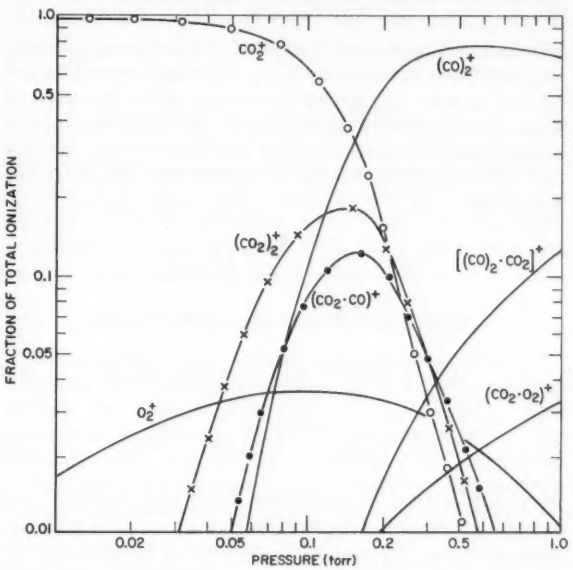

FIGURE 2. *Composite mass spectrum obtained from the 21.2 eV photoionization of* CO_2 *containing 0.33 percent* CO *as a function of pressure.*

Because this sample contains essentially trace quantities of added CO, the initial reactions involve only the bulk component, CO_2, as evidenced by the formation of the $(CO_2)_2^+$ dimer ion;

$$CO_2^+ + CO_2 \xrightarrow{CO_2} (CO_2)_2^+. \qquad (7)$$

However, in contrast to pure CO_2, the yield of $(CO_2)_2^+$ reaches a level of only 15 percent of the total ionization at approximately 0.15 torr, and then decreases rapidly to zero at pressures greater than 0.6 torr. Over this same pressure range two new major ions appear in the mass spectrum. These are, in order of appearance, m/e 72, $(CO_2 \cdot CO)^+$, which reaches a maximum at 0.16 torr and then decreases rapidly, indicating further reaction, and finally m/e 56, $(CO)_2^+$, which is the major ionic species present above 0.15 torr. At pressures above 0.1 torr the $(CO)_2^+$ ion is also found to associate with CO_2, yielding $[(CO)_2 \cdot CO_2]^+$, m/e 100. The O_2^+ ion produced by the reaction of the primary fragment, O^+, with CO_2 (process 5) reacts only with CO_2 to yield the $(O_2 \cdot CO_2)^+$ association ion. Exactly the same overall behavior was observed in other experiments in which the mole fraction of added CO was varied over

the range 0.003 to 0.50. At higher total pressures the the reaction scheme initiated by CO_2^+ leads quantitatively to the formation of $[(CO)_2 \cdot CO_2]^+$. No reaction was detected between O_2^+ and CO in any mixture. An additional set of experiments was carried out which involved the substitution of CO^{18} for CO^{16} in various CO_2 mixtures. In this case the association ions appeared exclusively at m/e 74 $(CO^{18} \cdot CO_2)^+$, m/e 60, $(CO^{18})_2^+$, and m/e 104 $[(CO^{18})_2 \cdot CO_2]^+$, verifying the efficient incorporation of neutral CO in the ion clustering reactions initiated by CO_2^+. Through consideration of the growth and decay curves for all of the various ionic intermediates observed in all of these experiments, the following reaction mechanism was derived for the cationic chemistry occurring in CO_2-CO mixtures:

$$CO^+ + CO_2 \xrightarrow{CO_2} (CO_2)_2^+ \tag{7}$$

$$(CO_2)_2^+ + CO \rightarrow (CO_2 \cdot CO)^+ + CO_2 \tag{16}$$

$$(CO_2 \cdot CO)^+ + CO \rightarrow (CO)_2^+ + CO_2 \tag{17}$$

$$(CO)_2^+ + CO_2 \xrightarrow{CO_2} [(CO)_2 \cdot CO_2]^+. \tag{18}$$

It is interesting to note that $(CO \cdot CO_2)^+$ and $(CO)_2^+$ were also reported by Schildcrout et al. [13], as being formed in an irreproducible manner in a mass spectrometric study of ion-neutral reactions occurring in CO_2 during decomposition via a radio frequency discharge. The fact that these ions were seen is understandable when one considers that CO is a major CO_2 decomposition product in such experiments, and would therefore participate in the reaction sequence indicated by processes 7, 16, and 17. The abundance of the CO containing clusters would depend very critically on the extent of CO_2 decomposition, which would account for the reported irreproducibility of the $(CO \cdot CO_2)^+$ and $(CO)_2^+$ ion signals.

The net result of reactions 16, 17, and 18 is equivalent to the following overall conversion:

$$(CO_2)_2^+ + 2CO \rightarrow 2CO_2 + (CO)_2^+. \tag{19}$$

Taking ΔH_f for $(CO_2)_2^+$ as $\cong 539$ kJ/mol [11], CO as -109 kJ/mol, CO_2 as -393 kJ/mol, and $(CO)_2^+$ as ~ 1020 kJ/mol [14] the overall sequence represented by eq (19) is exothermic by approximately 22 kcal/mol (92 kJ/mol). Although we did not attempt to evaluate specific rate coefficients for the various switching reactions in which CO is substituted for CO_2 in the ion clusters, it can be estimated that these processes occur at essentially every collision of $(CO_2)_2^+$ and $(CO \cdot CO_2)^+$ with CO. Furthermore, the ionization potential of $(CO)_2$, 12.8 ± 0.3 eV, reported by Munson et al. [14], is far below that of CO_2 (I.P. = 13.79 eV), which explains why $(CO)_2^+$, once formed, does not charge exchange with CO_2 but rather forms the $[(CO)_2 \cdot CO_2]^+$ association ion.

3.5. Impurity Reactions in CO_2-CO Mixtures

A number of ionic products were observed in CO_2-CO mixtures which could be ascribed to the interactions of CO_2-CO cluster ions with water present as an impurity. Data obtained for a particularly wet sample containing nominally 70 percent CO_2 and 30 percent CO are given in figure 3. The initial reaction in such a mixture necessarily involves the bulk components, CO_2 and CO, as evidenced by the rapid appearance of $(CO)_2^+$ ions due to processes 7, 16, and 17 at pressures below 0.2 torr. As the total pressure is increased above this range, however, three new major ions appear in the mass spectrum which can be ascribed to reactions involving H_2O impurities. Of these, m/e 46, $(CO \cdot H_2O)^+$, and m/e 90, $(CO \cdot CO_2 \cdot H_2O)^+$, can be accounted for by the following reactions:

$$(CO)_2^+ + H_2O \rightarrow (CO \cdot H_2O)^+ + CO \tag{20}$$

$$(CO \cdot CO_2)^+ + H_2O \xrightarrow{M} (CO \cdot CO_2 \cdot H_2O)^+ \tag{21}$$

or

$$(CO \cdot H_2O)^+ + CO_2 \xrightarrow{M} (CO \cdot CO_2 \cdot H_2O)^+. \tag{22}$$

Process 20, the displacement of CO by H_2O, has also been reported to occur in wet CO by Chong and Franklin [11]. The major impurity peak noted in this particular experiment (fig. 3) occurs at m/e 60. Early in this study we determined that the ionic product at m/e 60 was found in large relative yields in CO and CO_2-CO samples which had been extensively dried prior to introduction into the mass spectrometer, and we concluded at that time that this ion was, in fact, CO_3^+ produced via reaction with an O_2 impurity:

$$CO^+ + O_2 \xrightarrow{CO_2} CO_3^+ \tag{23}$$

or

$$(O_2 \cdot CO_2)^+ + CO \rightarrow CO_3^+ + CO_2. \tag{3}$$

Subsequently, however, we found that the fractional yield of m/e 60 in a particular experiment was reduced considerably when the CO component was taken from a reservoir of CO which had been maintained at 77 K for several hours. Since trace quantities of O_2 would not be removed by this treatment, another source of m/e 60 in the mass spectrum had to be considered. Analytical (70 eV) mass spectrometric analysis of the condensible residue from the CO starting material

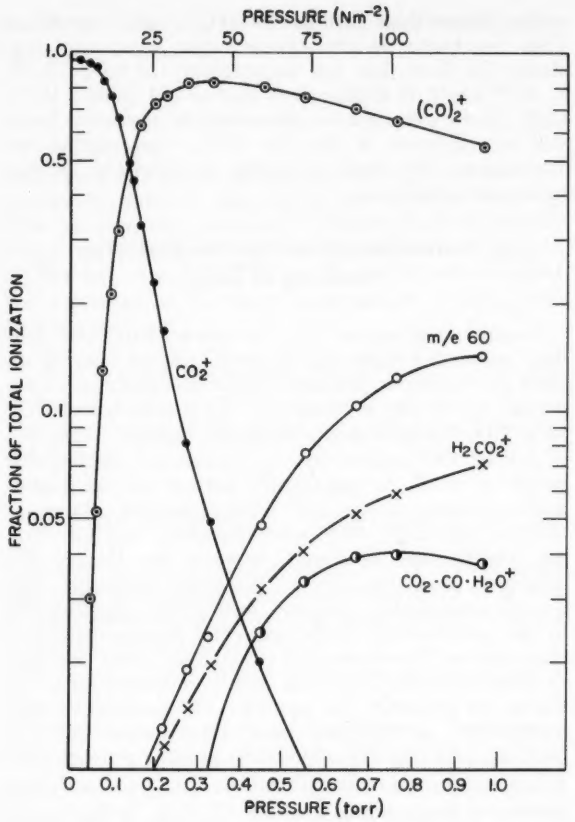

FIGURE 3. *Composite mass spectrum obtained from the 21.2 eV photoionization of a* CO_2-CO *mixture containing 70 percent* CO_2 *and 30 percent* CO *as a function of pressure.*

revealed the presence of m/e 60 in the condensate, which we assigned to ionization of a COS impurity (m/e $COS^+ = 60$). The substantial yields of m/e 60 noted in the earlier experiments could then be explained by any of the following reactions:

$$CO_2^+ [\text{or } (CO_2)_2^+] + COS \rightarrow COS^+ + CO_2 \text{ [or } 2CO_2] \quad (24)$$

$$(CO \cdot CO_2)^+ + COS \rightarrow COS^+ + CO + O_2 \quad (25)$$

and

$$(CO)_2^+ + COS \rightarrow COS^+ + 2CO \quad (26)$$

all of which are exothermic since the Ionization Potential of COS (11.2 eV) is lower than the recombination energies of the CO and CO_2 containing cluster ions. Multiple fractionation of the CO starting material at 77 K ultimately led to the disappearance of m/e 60 from the high pressure mass spectra of CO_2-CO mixtures and pure CO samples.

3.6. CO_2-O_2 Mixtures

Several mixtures of O_2 in CO_2 were also investigated at 21.2 eV. The following reaction scheme was observed:

$$CO_2^+ + O_2 \rightarrow O_2^+ + CO_2 \quad (1)$$

$$O_2^+ + CO_2 \xrightarrow{CO_2} (O_2 \cdot CO_2)^+ \quad (2)$$

and

$$(O_2 \cdot CO_2)^+ + CO_2 \xrightarrow{M} [O_2 \cdot (CO_2)_2]^+. \quad (6)$$

Although the occurrence of process 6 is reported here for the first time, rate constants for the charge exchange reaction involving CO_2^+ and the clustering process involving O_2^+ and CO_2 have been reported earlier from other laboratories [3].

3.7. Addition of CO-O_2 Mixtures to CO_2

Experiments were carried out which involved the addition of varying quantities of a CO-O_2 mixture having the composition 2CO: 1 O_2, to CO_2. This composition (2CO:1 O_2) was chosen due to the stoichiometry of the decomposition $2CO_2 \rightarrow 2CO + O_2$, which would presumably represent the product distribution obtained from the decomposition of CO_2 under ideal conditions. The growth and decay curves for the various ionic species formed following the 21.2 eV photoionization of CO_2 containing 0.67 percent CO and 0.33 percent O_2 are given in figure 4. As is evident from the data up to 0.15–0.2 torr, two separate reaction schemes are occurring initiated by CO_2^+. That is, the sequences

$$CO_2^+ \xrightarrow{CO_2} (CO_2)_2^+ \xrightarrow{CO} (CO \cdot CO_2)^+ \xrightarrow{CO} (CO)_2^+,$$

and

$$(CO_2)_2^+ \xrightarrow{O_2} O_2^+ \xrightarrow{2CO_2} (O_2 \cdot CO_2)^+,$$

which have been discussed previously, appear to proceed independently at lower total pressures. However, at total pressures above 0.3–0.4 torr the major cluster ions are those containing O_2; i.e., $(O_2 \cdot CO_2)^+$ and $[O_2 \cdot (CO_2)_2]^+$, and at pressures above approximately 1 torr all of the CO containing clusters have disappeared. This is due to the fact that the $(CO)_2^+$ dimer ion, once formed, reacts with O_2 via charge exchange to yield O_2^+;

$$(CO)_2^+ + O_2 \rightarrow O_2^+ + 2CO$$
$$\Delta H \cong -71 \text{ kJ/mol} \quad (27)$$

Although the occurrence of this process may not be immediately evident from the data given in figure 4, other experiments in which the mole fractions of CO

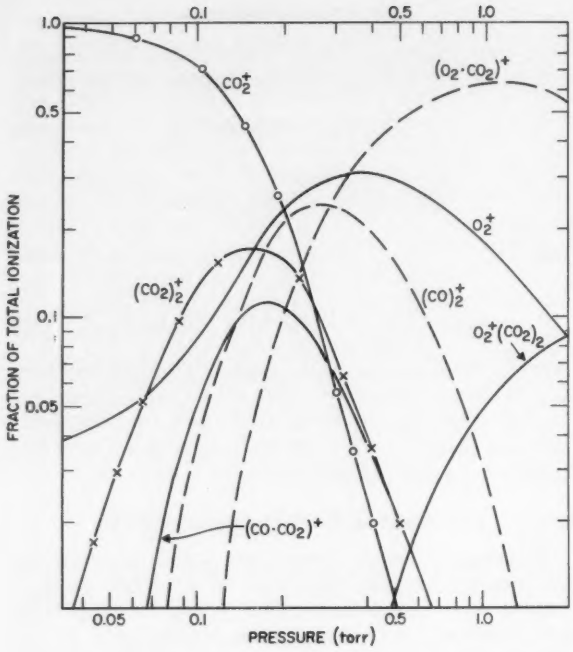

FIGURE 4. *Composite mass spectrum obtained from the 21.2 eV photoionization of a CO_2-CO-O_2 mixture having the composition 99 percent CO_2, 0.67 percent CO, and 0.33 percent O_2 as a function of pressure.*

and O_2 were substantially higher verify that this is the case. The same result was obtained in pure CO samples containing small amounts of added O_2. In this case the only reactions occurring were:

$$CO^+ + CO \xrightarrow{CO} (CO)_2^+ \qquad (14)$$

followed by:

$$(CO)_2^+ + O_2 \rightarrow O_2^+ + 2CO \qquad \Delta H \cong -71 \text{ kJ/mol} \qquad (27)$$

No other reactions were observed up to 1 torr total pressure. Additional experiments (other than that summarized in fig. 4) were carried out in which the mole fraction of the stoichiometric CO-O_2 mixture in CO_2 was varied over the range 0.001 to 0.50. In each of these experiments the major ionic species observed at a total pressure of 1 torr were always either O_2^+, $(O_2 \cdot CO_2)^+$, or $[O_2 \cdot (CO_2)_2]^+$. No evidence was found for production of CO_3^+ in any of the CO_2-CO-O_2 mixtures studied, indicating that the rate coefficient for the reaction

$$(O_2 \cdot CO_2)^+ + CO \rightarrow CO_3^+ + CO_2 \qquad (3)$$

is less than 10^{-12} cm^3/molecule-s, and that the binding energy in the $(O_2 \cdot CO_2)^+$ complex is therefore necessarily higher than that in the $(O_2 \cdot CO)^+$ complex. This conclusion is not unreasonable when one considers the fact that the polarizibility of CO_2, (2.59×10^{-24} cm^3), is higher than that of CO (1.93×10^{-24} cm^3), and a greater ion-induced dipole attractive force will be operative in the $(O_2 \cdot CO_2)^+$ association ion assumming the positive charge is localized on the molecular oxygen site.

4. Some Comments on the Radiation Stability of CO_2

Several conclusions can be drawn from the new data presented here which have a direct bearing on the CO_2 radiolysis problem. In the first place, we were unable to find any evidence for the production of CO_3^+ in a CO_2 environment containing various quantities of added CO and/or O_2. As mentioned above, this negative result is apparently related to the higher binding energy in the $(O_2 \cdot CO_2)^+$ complex relative to that in $(O_2 \cdot CO)^+$. We must therefore conclude that the mechanism proposed recently by Parkes [2], although attractive due to its chain character and overall energetics, cannot contribute significantly to the mechanism of the radiolytic decomposition in this system. The alternative explanation must be found in other reactions involving highly clustered ions. We know, for example, the neutral CO is efficiently and irreversibly incorporated into ion clusters initiated by CO_2^+, and that the major ionic species present after a few encounters with CO will be $(CO)_2^+$ and solvated species corresponding to $(CO)_2^+ \cdot (CO_2)_n$. In this sense accumulated CO produced in the radiolysis would act as a sink for the positive ions if the steady-state concentration of O_2 were substantially lower due to its removal at the walls of the vessel (as is observed in the photolysis) [1], O_3 formation due to interception of O atoms, etc. Although the neutralization products of such CO-containing clusters, as well as any containing O_2, cannot be specified, it is apparent that both of the decomposition products of the CO_2 radiolysis, CO and O_2, will act as efficient interceptors for CO_2^+ or $(CO_2)_n^+$ species, and it appears likely that the decrease in G(CO) observed at higher conversions in low dose rate experiments is due to modification of the neutralization processes when CO and/or O_2 are incorporated into the positive ion clusters.

5. The O_2-CO System

As stated in the Introduction, one of the goals of the present study was to determine whether we could detect any cationic reactions which might account for the radiation-induced chain oxidation of CO in O_2-CO mixtures. Experimentally, our approach was to admit a relatively high constant pressure of O_2 to the reaction chamber (1.5 torr), add increasing quantities of CO, and search for ionic reaction products. As the total pressure is increased in pure O_2 in our apparatus

the O_4^+ product ion, resulting from the thermolecular association reaction:

$$O_2^+ + O_2 \xrightarrow{O_2} O_4^+ \qquad (28)$$

dominates the mass spectrum. Although we did not attempt to derive a rate coefficient for this relatively slow process, our data are consistent with the recent value of $2.5 \pm 0.5 \times 10^{-30}$ cm^6/molecule^2-s reported by Howard, et al. [15]. The reaction of O_4^+ with residual water present in the mass spectrometer, yielding m/e 50 was detected.

$$O_4^+ + H_2O \rightarrow (O_2 \cdot H_2O)^+ + O_2. \qquad (29)$$

The production of $[O_2 \cdot (H_2O)_2]^+$, resulting from the reaction:

$$(O_2 \cdot H_2O)^+ + H_2O \xrightarrow{O_2} [O_2 \cdot (H_2O)_2]^+ \qquad (30)$$

was also noted. A representation of a typical mass spectrum of O_2 (major ions only), photoionized at 21.2 eV at a pressure of 1.5 torr, is given in part A of the histogram presented as figure 5.

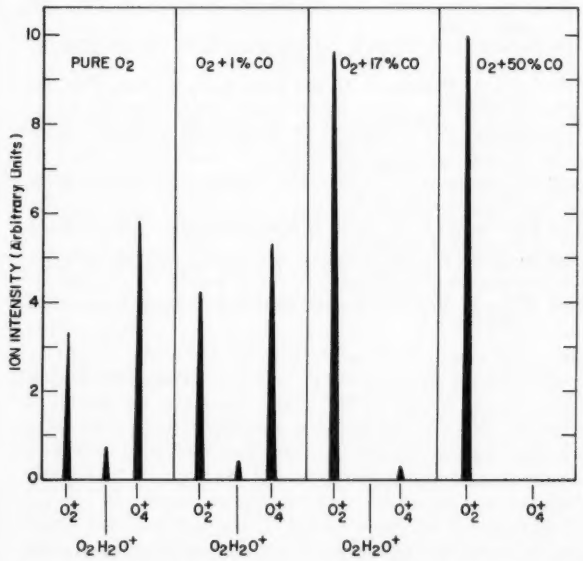

FIGURE 5. *Representation of mass spectra obtained from the 21.2 eV photoionization of* O_2 *and* O_2-CO *mixtures at a* O_2 *pressure of 1.5 torr.*

The results of the added CO experiments are also given in figure 5. It is apparent from this histogram that the net overall effect of adding increasing quantities of CO to O_2 is to remove the O_4^+ ions from the mass spectrum. The reaction product of O_4^+ with the water impurity, $(O_2 \cdot H_2O)^+$, also shows a concurrent decrease. In addition to the ion intensities given in figure 5, the mass spectrum of the mixture containing 1 percent added CO contained 0.8 percent of m/e 60, and that of the 17 percent mixture contained 1.2 percent of m/e 60 and 0.6 percent of m/e 44 (CO_2^+). The mixture containing 50 percent added CO yielded a mass spectrum which contained only O_2^+. No other ions were detected at a level which exceeded 10^{-3} percent of the total ionization. Those CO^+ ions produced by the direct photoionization of the CO component in these experiments, as well as any $(CO)_2^+$ dimer ions resulting from CO^+-CO interactions, are not detected under high pressure conditions due to the rapidity with which CO^+ and $(CO)_2^+$ charge exchange with the bulk component, O_2 (process 27). Whether or not the species appearing at m/e 60 in the more dilute mixtures was actually CO_3^+ or residual COS in the CO sample could not be established absolutely, although the CO starting material was extensively purified and the observation of 0.8 percent of m/e 60 (out of 10 total in the mass spectrum) would be in excess of that expected from ionization of a COS impurity by charge exchange from O_2^+ or O_4^+. The striking feature of the histogram, of course, is the gradual disappearance of O_4^+ as more CO is added, and the virtual absence of any ions other than O_2^+. Obviously O_4^+ is either destroyed by reaction with CO, or the production of O_4^+ is prevented by the interaction of O_2^+ with CO. The only likely reaction product in either case would be CO_3^+:

$$O_2^+ + CO \xrightarrow{O_2} CO_3^+ \qquad (31)$$

or

$$O_4^+ + CO \rightarrow CO_3^+ + O_2. \qquad (32)$$

The fact that we do not observe CO_3^+ as a product (with the possible exception of the trace yields of m/e 60 discussed above) could be due to either of two reasons. (i) The total ion transit time in our apparatus is on the order of 100 μs, depending to some extent, upon the mass of the charged species. If the lifetime of CO_3^+ produced by either process 31 or 32 is considerably less than 100 μs, we would detect only the O_2^+ ions resulting from the dissociation

$$CO_3^+ \rightarrow CO + O_2^+ \qquad (33)$$

which would occur after the CO_3^+ ions leave the sampling pinhole of the reaction chamber and enter the lens region of the mass analyzer. (ii) Alternatively, due to the nature of the experiment itself, it is possible that CO_3^+ once produced, reacts rapidly with CO to yield CO_2^+, which would in turn charge exchange immediately with O_2 to yield O_2^+

$$CO_2^+ + O_2 \rightarrow O_2^+ + CO_2. \qquad (1)$$

This is essentially the same mechanism postulated originally by Clay, et al. [4] and more recently by Willis, et al. [16] to explain the chain oxidation of CO

observed in the radiolysis. The requirements of our experiments are such that we were forced to add fairly substantial quantities of CO to the O_2 in order to observe any significant reaction of O_2^+ or O_4^+ with the CO. Unfortunately, under these conditions, any CO_3^+ produced would have ample time to react with the CO additive prior to removal from the reaction chamber through the ion exist pinhole which leads to the mass filter. This rationale requires that the collision efficiency for the reaction of CO_3^+ with CO to yield $CO_2^+ + CO_2$ (process 4) be very close to unity since we would have observed substantial yields of CO_3^+ (providing again that its dissociative lifetime is >50–100 μs) if the reaction efficiency were on the order of only 1 in 10 collisions. In summary, our experiments involving O_2-CO mixtures are inconclusive in that we were unable to observe significant yields of those ionic intermediates (CO_3^+ and CO_2^+) which have been suggested as being the chain carriers in the radiation-induced oxidation of CO. The chain reaction occurring in irradiated CO-O_2 mixtures is inhibited by low concentrations of added CO_2 [1]. Since we know that CO_3^+ is *not* produced in CO_2-CO-O_2 mixtures due to the fact that the binding energy in the $(O_2 \cdot CO_2)^+$ complex is greater than in either CO_3^+ or O_4^+, it is apparent that the termination step operative in the O_2-CO radiolysis experiments at higher conversions (excluding ion neutralization) is the formation of $(O_2 \cdot CO_2)^+$ or its more highly solvated analoges.

6. Conclusion

We may conclude that the ionic mechanisms occurring in CO_2 and O_2-CO mixtures are still poorly understood. This is particularly true with respect to the neutralization mechanisms, which most certainly involve highly clustered negative ions. In view of the large number of catonic clustering reactions we have observed it is apparent that further information is required concerning binding energies within these clusters and the specific rate constants involved in their production and destruction before any quantitative picture can be formulated for the radiolysis.

As always, we are indebted to Pierre Ausloos for his advice and encouragement during the course of this study.

7. References

[1] Anderson, A. R., and Dominey, D. A., Radiat. Res. Rev. **1,** 269 (1968).
[2] Parkes, D. A., Faraday, J. C. S., I. **69,** 198 (1973).
[3] Ferguson, E. E., Flowing Afterglow Studies in Ion-Molecule Reactions. Vol. **2,** J. L. Franklin, Ed. (Plenum Press, New York, 1972).
[4] Clay, P. G., Johnson, G. R. A., and Warmun, J. M., Disc. Faraday Soc. **36,** 46 (1963).
[5] Sieck, L. W., Gorden, R., Jr., Ausloos, P., Lias, S. G., and Field, F., Radiat. Res. (1973) in press.
[6] (a) Sieck, L. W., Searles, S. K., and Ausloos, P., J.A.C.S. **91,** 7627 (1969); (b) Sieck, L. W., and Searles, S. K., J. Chem. Phys. **53,** 7 (1970).
[7] Franklin, J. L., Dillard, J. G., Rosenstock, H. M., Herron, J. T., Draxl, K., and Field, F. H., Ionization potentials, appearance potentials, and heats of formation of gaseous positive ions, Nat. Stand. Ref. Data Ser., Nat. Bur. Stand. (U.S.), NSRDS-26 (1969).
[8] Schildcrout, S. M., and Franklin, J. L., J. Chem. Phys. **51,** 4055 (1969).
[9] Paulson, J. F., Dale, F., and Mosher, R. F., Nature **204,** 377 (1964).
[10] Good, A., Durden, D. A., and Kebarle, P., J. Chem. Phys. **52,** 222 (1970).
[11] Chong, S., and Franklin, J. L., J. Chem. Phys. **54,** 1487 (1971).
[12] Fehsenfeld, F. C., Schmeltekopf, A. L., and Ferguson, E. E., J. Chem. Phys. **45,** 23 (1966).
[13] Schildcrout, S. M., Collins, J. G., and Franklin, J. L., J. Chem. Phys. **52,** 5767 (1970).
[14] Munson, M. S. B., Field, F. H., and Franklin, J. L., J. Chem. Phys. **37,** 1790 (1962).
[15] Howard, C. J., Bierbaum, V. M., and Kaufman, F., J. Chem. Phys. **57,** 3491 (1972).
[16] Willis, C., Boyd, A. W., and Binder, P. E., Can. J. Chem. **50,** 3508 (1972).

(Paper 78A3–813)

JOURNAL OF RESEARCH of the National Bureau of Standards — A. Physics and Chemistry
Vol. 78A, No. 3, May–June 1974

Analysis of Low Temperature Viscosity Data for Three NBS Standard Glasses

A. Napolitano, J. H. Simmons, D. H. Blackburn, and R. E. Chidester

Institute for Materials Research, National Bureau of Standards, Washington, D.C. 20234

(February 5, 1974)

The low temperature viscosities of three glasses established as viscosity standards at the National Bureau of Standards are reported. The data overlap results which appear on the published certificates between 10^9 and 10^{12} poise and present extensive measurements up to 10^{16} poise. The measurements were made using both the fiber-elongation and beam-bending methods. No evidence of an Arrhenius behavior was found for any of the three glasses, even though the measurements covered a narrow range of temperatures. An analysis of the inherent measurement uncertainty associated with each method indicates that the fiber-elongation measurements are more precise than the beam-bending measurements. Analysis of the data and its uncertainty by the Fulcher Equation supports the conclusions of the error analysis.

Key words: Beam-bending; fiber-elongation; Fulcher equation; glass viscosity; standard reference material; viscosity; viscosity standard.

1. Introduction

In the past few years three types of glasses [1–4][1] have been established as viscosity standards in a standard reference material program at the National Bureau of Standards. The characterization of these glasses has involved extensive measurements of viscosities for each of these glasses at high and low temperatures. The low temperature viscosity data obtained on these glasses has not been completely analyzed and is considered in more detail along with newer data.

These glasses:[2] No. 710, a soda-lime-silica; No. 711, a lead silica; and No. 717, a borosilicate have been certified for viscosity form 10^2 to 10^{12}P (poise). The viscosity determinations were made by the rotating cylinder method [1–4] at high temperatures, and by the fiber elongation [1] and beam-bending methods [5] at the lower temperatures. Recently, a parallel-plate method [6] was used to measure viscosities in the intermediate temperature range by one of the laboratories involved in the round-robin measurements on these glasses.

Even though viscosity values for each of the three glasses have been certified only up to 10^{12} poise, many determinations were made above this value. We present here viscosity data taken at this laboratory on the three standard reference glasses by the fiber elongation and beam-bending methods. The apparatus for the former has been well described previously [1]. The apparatus for the latter is a greatly modified version of that described by Hagy [5].

In the range of viscosities from 10^{11} to 10^{16} P, roughly the transformation region of a glass, the measured viscosity at each temperature is time dependent; i.e., the lower the temperature the longer it takes to reach the equilibrium viscosity value. Therefore, to reach equilibrium values within reasonable times, measurements are usually limited to an upper value of 10^{15} P. In a few cases in the work presented here, stabilization times at 10^{15} P and above lasted between 200 to 300 h. Viscosities obtained at these long times were very close to the expected equilibrium values at each of the temperatures measured.

2. Apparatus and Method of Measurement

2.1. Fiber Elongation Method

The apparatus used to measure viscosity by the fiber elongation method has been described in a previous paper [1]. Briefly, a fiber 10-cm long and of uniform diameter is placed under tension at a constant temperature. Its rate of elongation is recorded. The viscosity is calculated from the following equation:

$$\eta = \frac{Fl}{3A\dfrac{dl}{dt}} \tag{1}$$

[1] Figures in brackets indicate the literature references at the end of this paper.

[2] The nominal composition by weight percent for the soda-lime-silica glass is: SiO_2—70.5 percent, Na_2O—8.7, K_2O—7.7, CaO—11.6, Sb_2O_3—1.1, SO_3—0.2, and R_2O_3—0.2 (Fe_2O_3—0.02 percent). The nominal composition by weight percent for the lead silica is: SiO_2—46.0 percent, PbO—45.3, K_2O—5.6, Na_2O—2.5, and R_2O_3—0.6. The nominal composition by weight percent for the borosilicate glass is: SiO_2—70 percent, B_2O_3—17.0, K_2O—8.0, Na_2O—1.0, Al_2O_3—3.0, and Li_2O—1.0. These glasses are not intended as standards for chemical analysis. The compositions are given only for information purposes.

where

η = viscosity (poises; $1P = 10^{-1}$ Pa·s)
F = extending force (dyn) (1 dyn = 10^{-5} N)
l = fiber length (cm)
A = fiber cross-section area (cm^2); instantaneous value
$\frac{dl}{dt}$ = elongation rate (cm/s).

2.2. Beam-Bending Method

The measurement of viscosity by the beam-bending technique has been developed and described by Hagy [5] and has now been accepted as a method for determining low temperature viscosity by many laboratories. It is particularly useful for glasses that cannot be flame-drawn into fibers.

Unusual glass compositions may devitrify or phase-separate in the flame-working process so that fibers cannot be made. At the same time with some glasses, surface volatilization may occur and the fibers may be of different chemical composition. All of these problems are eliminated by grinding bulk samples of the glass into regular rods (square, round or rectangular cross-section) [5]. The beam-bending method has also been adopted as a standard to determine the annealing point and strain point of glass by the ASTM [7].

A schematic drawing of the assembly of the apparatus for the beam-bending technique is shown in figure 1.

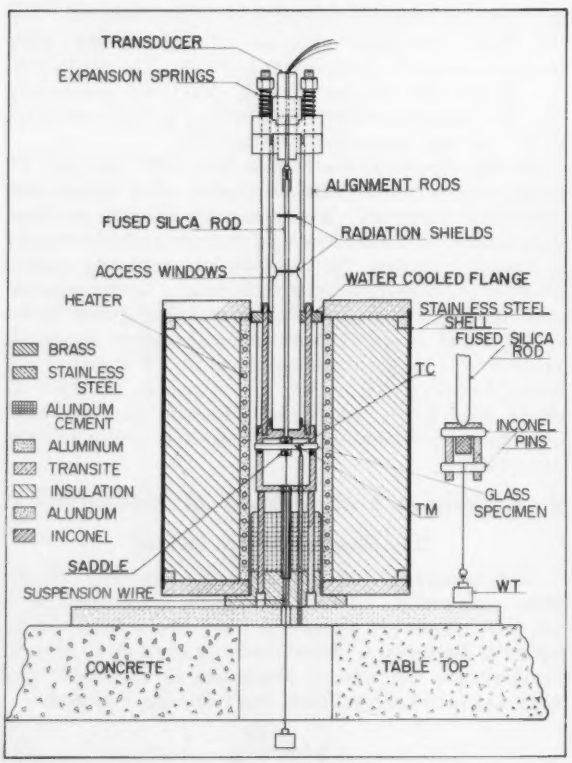

FIGURE 1. *Beam-bending apparatus showing furnace and table.*

This modified version of the beam-bending apparatus [5] was built at the National Bureau of Standards and is especially suitable for equilibrium viscosity measurements. The assembly consists of two sections. The first or bottom section is the sample holder and the second or top section is the transducer and sensor holder. The furnace and its apparatus have good temperature stability so that thermal equilibrium conditions are established in the glass sample before measurements are begun. The equilibrium conditions are especially helpful for long time measurements. The rate of bending can be continually monitored while the load is applied intermittently or continuously. All metal parts within the furnace are made of inconel.

The bottom half, figure 2, is the sample holder, which has two holes in the bottom. One of these, in the center, is for the suspension wire for the weight and is attached to the saddle. The other hole is for the thermocouples, one (Chromel-Alumel) for control and the other (Pt–Pt 10 percent Rh) to measure the test temperature. The sample holder is notched across one diameter, figure 2, to accommodate two inconel pins 0.3 cm in diameter that act as supports for the glass beam. The distance between supports is 5.715 cm and the glass beam about 6.5 cm long. The beams are square, rectangular, or circular in cross-section. Most of the beams used had square cross-sections with 0.318 cm and 0.635 cm sides. Samples with a rectangular cross-section (0.635 × 0.953 cm) were also used at high temperatures near the low-viscosity limit of the apparatus.

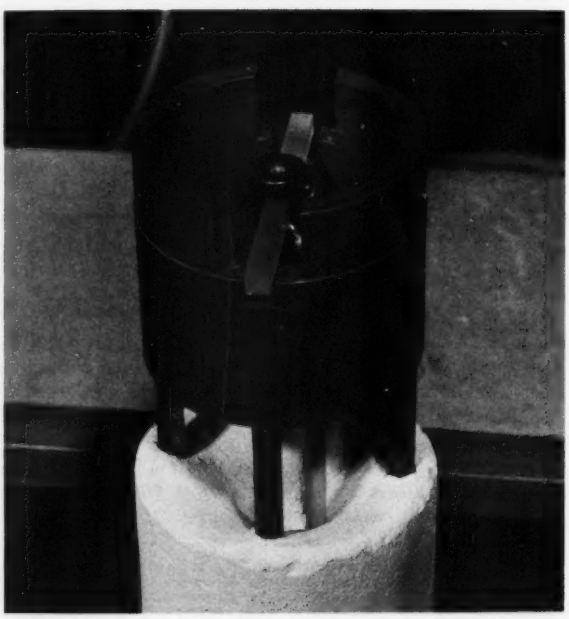

FIGURE 2. *The inconel sample holder showing glass bar and saddle.*
Note thermocouple next to glass bar.

An inconel saddle sitting on the glass specimen was used to apply the load and measure the deflection of the sample. The saddle has an inconel pin, 0.3 cm in diameter, which contacts the top surface of the sample and it reaches below the sample where a wire is attached. The wire extends below the furnace and provides a convenient means for applying the load. An indentation at the top of the saddle assembly provides a seat for a silica rod attached to the transducer element from the top section which measures the deflection of the sample. The separation of loading and deflection measuring devices in this instrument allows for a continuous measurement of the deflection rate during loadings and unloadings of the sample, thus yielding modulus and delayed elastic effect data.

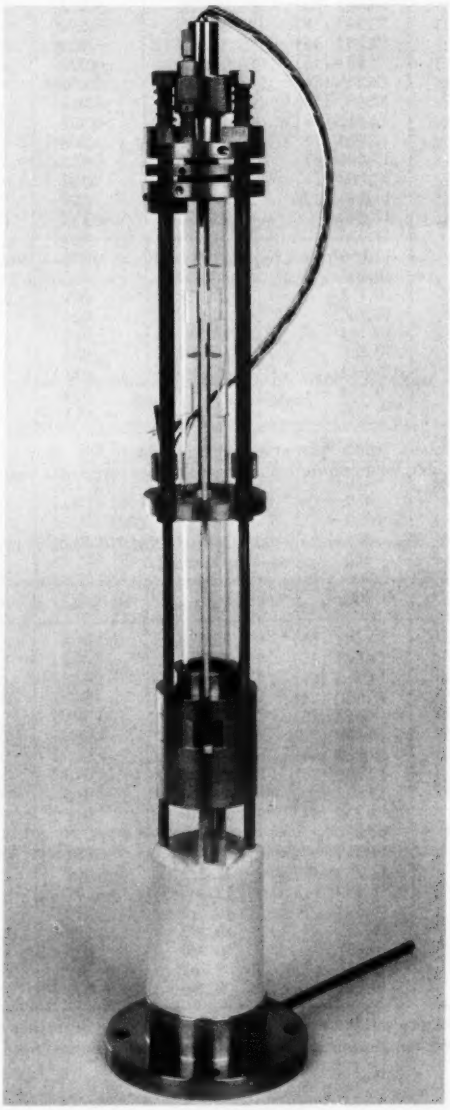

FIGURE 3. *Complete beam-bending apparatus without furnace.*

The top half of the instrument consists of two sections (e.g., the cover and measuring sections), figures 1 and 3. The lower part consists of an inconel cover which fits over the sample holder and sits close to the bar. Insulation above it reaches up to a water-cooled flange just above the furnace which prevents heating of the transducer element. Three brass rods serve to align the transducer support, but its vertical position is solely determined by the outer fused silica cyclinder. The transducer element is attached to a fused silica rod situated inside the cylinder and resting on the glass specimen by means of the saddle described above. This configuration reduces the thermal expansion correction to a negligible value during non-isothermal measurements. Springs at the top of the brass rods help seat the transducer holder firmly on the outer silica cyclinder.

The transducer is the linear deflection type with actual deflections of less than 0.6 cm measured in all of this work. The transducer element, as shown before, directly measures the bending of the center of the glass beam or specimen. The transducer output was 800 mv for each cm of travel and the rate of travel is calculated from a recorder trace. The temperature is controlled with a precision of $\pm$ 1/2 °C and is measured with a high sensitivity potentiometer (precision better than 0.1 °C).

The formula used for calculating viscosity by the beam-bending method is as follows:

$$\eta=\frac{gL^3}{2.4I_cV}\left(M+\frac{AL\rho}{1.6}\right) \tag{2}$$

where

η = viscosity (poises; $1P=10^{-1}$ Pa·s)
g = acceleration of gravity (cm/s^2)
L = support span (beam = $5.715+[.92\times10^{-4}\times(T-20)]$; T = temp °C
I_c = cross-sectional moment of inertia (cm^4) generaly 1/12 b^4 for square cross-sections of side b. (See reference [7].)
V = rate of deflection (cm/min) of the midpoint of the beam
M = mass of applied load (g)
ρ = density of glass specimen (g/cm^3)
A = cross-sectional area of specimen (cm^2).

3. Measurement Uncertainties

In order to estimate the inherent uncertainties in the two methods for measuring viscosity, it is necessary to consider the equations relating the physical measurements to viscosity (eqs. (1) and (2)) and evaluate the accuracies of these measurements. In the fiber elongation measurement, we find the following relationship:

$$\frac{\Delta\eta}{\eta}=\frac{\Delta F}{F}+\frac{\Delta l}{l}-\frac{2\Delta r}{r}-\frac{\Delta\left(\frac{dl}{dt}\right)}{\left(\frac{dl}{dt}\right)} \tag{3}$$

where r represents the radius of the fiber. The beam-bending method yields:

$$\frac{\Delta\eta}{\eta}=\frac{\Delta F}{F}+\frac{3\Delta l}{l}-\frac{4\Delta b}{b}-\frac{\Delta v}{v} \qquad (4)$$

where the force $F = Mg$ and we ignore the small contribution from the second term in the bracket of eq (2).

Since the measurement uncertainties can be both positive and negative, all the terms are additive. The following estimates are used for each measurement:

$$\Delta F/F = 0.003$$
$$\Delta l/l = .02$$
$$\Delta b/b = .02$$
$$\Delta r/r = .02$$
$$\frac{\Delta(dl/dt)}{(dl/dt)}=\Delta v/v = \begin{cases} .05 \text{ per time interval} \\ .01 \text{ when averaged over several intervals.} \end{cases}$$

This yields an uncertainty of ±4.5 percent in the fiber elongation measurement, and ±10 percent in the beam-bending measurement. Therefore, because of limitations in the size and deflection rate measurements, the beam-bending method yields an appreciably larger uncertainty than the fiber elongation method. However, glasses which can easily lose alkali oxides or other components during the drawing process are best measured by the beam-bending method for which ground cast pieces provide suitable samples.

4. Results and Analysis

The viscosity results obtained by both the fiber elongation and beam-bending methods were fitted to the Fulcher equation. The merits of this equation have been discussed in previous papers [1–4].

Since the data only cover a small range of viscosities the Fulcher equation, due to its simplicity, provides the easiest interpolation formula. We will use it here to compare both methods of measurement. The Fulcher equation follows:

$$\log_{10}\eta = A + \frac{B}{T - T_0} \qquad (5)$$

where

η = viscosity (poises)
T = temperature °C
A, B, T_0 = constants.

The log viscosity results of each method are given in tables 1–6 and are compared with the combined data for each glass in figures 4–6. The constants for each solution are given in table 7. The standard deviations listed in table 7 support the error analysis of the data which indicates that the fiber elongation method gives results with less scatter than the beam-bending method. In general, the values are larger than the measurement uncertainties calculated in section 3, and this is due to a detectable systematic deviation of the data from the Fulcher equation and to some probable random operator variations in preparing the test.

TABLE 1. *Low-temperature viscosities of SRM 710 Glass by the fiber elongation method*

Temp. °C	Log η_{obs}	Log η_{calc}	Deviation	10^4/K
519.2	15.048 (265)*	14.976	−0.072	12.62
529.4	14.190 (50)	14.352	.162	12.46
538.4	13.804 (100)	13.839	.035	12.32
548.9	13.385 (65)	13.282	−.103	12.17
556.6	12.968 (18)	12.899	−.070	12.05
558.3	12.854 (16)	12.817	−.038	12.03
560.2	12.751 (16)	12.726	−.025	12.00
564.7	12.486 (16)	12.516	.030	11.94
565.7	12.480 (16)	12.470	−.010	11.92
569.4	12.311 (8)	12.304	−.007	11.87
571.6	12.203 (2)	12.206	.003	11.84
574.6	12.064 (1)	12.076	.012	11.80
575.8	12.000 (1)	12.024	.024	11.78
580.4	11.804 (0.5)	11.831	.026	11.72
585.2	11.645	11.634	−.011	11.65
590.0	11.425	11.444	.019	11.59
600.1	11.066	11.060	−.006	11.45
603.2	10.904	10.947	.043	11.41
609.8	10.712	10.713	.001	11.33
618.7	10.436	10.411	−.025	11.21
626.5	10.144	10.159	.015	11.12
628.4	10.067	10.099	.032	11.09
633.9	9.918	9.929	.011	11.03
639.6	9.734	9.758	.024	10.96
648.0	9.586	9.515	−.071	10.86

*Numbers within parenthesis denote hours the fiber was held at indicated temperature before viscosity measurements were made.

TABLE 2. *Low-temperature viscosities of SRM 710 Glass by the beam-bending method*

Temp. °C	Log η_{obs}	Log η_{calc}	Deviation	10^4/K
510.8	15.341 (85)*	15.380	0.039	12.76
518.5	14.989 (15)	14.895	−.094	12.63
525.3	14.453 (63)	14.490	.037	12.53
536.1	13.830 (21)	13.885	.055	12.36
540.4	13.633 (15)	13.656	.023	12.29
548.0	13.298 (2.5)	12.268	−.030	12.18
554.9	12.954 (5)	12.933	−.021	12.08
562.8	12.576 (2)	12.566	−.010	11.96
563.0	12.573 (2)	12.557	−.016	11.96
569.5	12.252 (1)	12.270	.018	11.87
579.8	11.850	11.837	−.013	11.73
589.5	11.511	11.454	−.057	11.59
595.6	11.225	11.223	−.002	11.51
600.0	11.139	11.062	−.077	11.45
610.0	10.591	10.710	.119	11.33
619.9	10.261	10.380	.119	11.20
629.4	10.057	10.080	.023	11.08
640.0	9.871	9.762	−.109	10.95
660.0	9.211	9.206	−.005	10.72

* Numbers within parenthesis denote hours the beam was held at indicated temperature before viscosity measurements were made.

TABLE 3. *Low temperature viscosities of SRM 711 Glass by the fiber elongation method*

Temp. °C	Log η_{obs}	Log η_{calc}	Deviation	10^4/K
396.3	15.321 (335)*	15.341	0.020	14.94
411.1	14.451 (90)	14.464	.013	14.62
414.5	14.299 (260)	14.275	−.024	14.55
420.7	13.927 (65)	13.940	.013	14.42
422.3	13.869 (210)	13.855	−.014	14.38
431.5	13.429 (20)	13.387	−.042	14.19
441.3	12.902 (4)	12.916	.014	14.00
441.9	12.911 (4)	12.889	−.022	13.99
451.4	12.441 (2)	12.460	.019	13.80
456.0	12.280 (1)	12.261	−.019	13.72
460.7	12.042 (1)	12.062	.020	13.63
466.2	11.856	11.837	−.019	13.53
470.1	11.631	11.681	.050	13.46
475.3	11.509	11.479	−.030	13.36
482.2	11.202	11.219	.017	13.24
488.2	10.987	11.001	.014	13.14
491.3	10.864	10.891	.027	13.08
492.8	10.840	10.839	−.001	13.06
495.4	10.720	10.748	.028	13.01
501.5	10.565	10.541	−.024	12.91
506.5	10.399	10.376	−.023	12.83
511.9	10.204	10.203	−.001	12.74
516.9	10.065	10.046	−.019	12.66
521.9	9.897	9.893	−.004	12.58
526.7	9.727	9.750	.023	12.50
535.7	9.506	9.490	−.016	12.37

*Numbers within parenthesis denote hours the fiber was held at indicated temperature before viscosity measurements were made.

TABLE 4. *Low temperature viscosities of SRM 711 Glass by the beam-bending method*

Temp. °C	Log η_{obs}	Log η_{calc}	Deviation	10^4/K
398.0	15.118 (110)*	15.161	0.043	14.90
408.3	14.612 (20)	14.582	−.030	14.68
420.8	13.951 (20)	13.923	−.028	14.41
430.2	13.462 (6)	13.456	−.006	14.22
434.3	13.244 (1)	13.260	.016	14.14
441.6	12.912 (1)	12.921	.009	13.99
448.8	12.607 (1)	12.598	−.009	13.85
452.9	12.510 (1)	12.420	−.090	13.78
458.1	12.144 (1)	12.199	.055	13.69
475.3	11.570	11.508	−.062	13.36
479.6	11.235	11.343	.108	13.29
494.9	10.781	10.785	.004	13.02
502.0	10.481	10.539	.058	12.90
502.0	10.588	10.539	−.049	12.90
503.0	10.425	10.505	.080	12.89
510.4	10.309	10.258	−.051	12.76
520.9	9.970	9.921	−.049	12.60

*Numbers within parenthesis denote hours the beam was held at indicated temperature before viscosity measurements were made.

TABLE 5. *Low temperature viscosities of SRM 717 Glass by the fiber elongation method*

Temp. °C	Log η_{obs}	Log η_{calc}	Deviation	10^4/K
470.9	15.236 (71)*	15.263	0.027	13.44
485.5	14.603 (47)	14.587	−.016	13.18
501.1	13.917 (70)	13.905	−.012	12.92
515.0	13.375 (19)	13.330	−.045	12.69
528.7	12.788 (2)	12.791	.003	12.47
539.5	12.360 (1)	12.384	.024	12.31
549.0	12.025	12.038	.013	12.17
555.2	11.756	11.818	.062	12.07
556.0	11.796	11.790	−.006	12.06
560.0	11.636	11.651	.015	12.00
564.0	11.523	11.514	−.009	11.95
564.4	11.517	11.500	−.017	11.94
568.6	11.404	11.359	−.045	11.88
574.4	11.168	11.166	−.002	11.80
577.6	11.075	11.061	−.014	11.76
580.8	10.982	10.958	−.024	11.71
580.9	10.970	10.954	−.016	11.71
585.5	10.795	10.807	.012	11.65
590.4	10.660	10.653	−.007	11.58
596.0	10.440	10.479	.039	11.51
600.2	10.309	10.351	.042	11.45
600.4	10.318	10.345	.027	11.45
605.0	10.209	10.207	−.002	11.39
610.8	10.028	10.035	.007	11.31
614.9	9.932	9.916	−.016	11.26
620.7	9.792	9.749	−.043	11.19

*Numbers within parenthesis denote hours the fiber was held at indicated temperature before viscosity measurements were made.

TABLE 6. *Low temperature viscosities of SRM 717 Glass by the beam-bending method*

Temp. °C	Log η_{obs}	Log η_{calc}	Deviation	10^4/K
460.0	15.752 (138)*	15.799	.047	13.64
482.6	14.733 (38)	14.713	−.020	13.23
490.8	14.368 (15)	14.345	−.023	13.09
501.7	13.993 (15)	13.873	−.120	12.91
508.0	13.606 (3)	13.610	.004	12.80
517.7	13.162 (1)	13.218	.056	12.65
526.6	12.849 (0.5)	12.871	.022	12.51
542.0	12.308 (0.5)	12.297	−.011	12.27
544.3	12.221 (1.5)	12.214	−.007	12.24
550.7	11.941	11.987	.046	12.14
555.2	11.769	11.831	.062	12.07
563.1	11.528	11.563	.035	11.96
573.4	11.288	11.224	−.064	11.81
575.0	11.179	11.172	−.007	11.79
585.1	10.822	10.854	.032	11.65
591.0	10.682	10.673	−.009	11.57
594.3	10.605	10.573	−.032	11.53
613.3	10.105	10.020	−.085	11.28
615.3	9.943	9.964	.021	11.26
616.5	9.896	9.931	.035	11.24
618.1	9.868	9.886	.018	11.22

*Numbers within parenthesis denote hours the beam was held at indicated temperature before viscosity measurements were made.

TABLE 7. *Fulcher equation constants from the data obtained by each method*

	A	*B*	T_0	St'd. Dev. of Log η
SRM 710–F	−1.388	4208	262.0	0.051
SRM 710–B	−1.716	4513	246.8	.062
SRM 710–FB	−2.008	4669	242.9	.060
SRM 711–F	−2.588	5160	108.5	.023
SRM 711–B	−4.688	6801	55.3	.055
SRM 711–FB	−3.360	5740	88.8	.041
SRM 717–F	−9.049	12417	−39.8	.027
SRM 717–B	−7.112	10414	5.5	.047
SRM 717–FB	−7.936	11224	−12.9	.040

F–fiber elongation method.
B–beam-bending method.
FB–both methods combined.

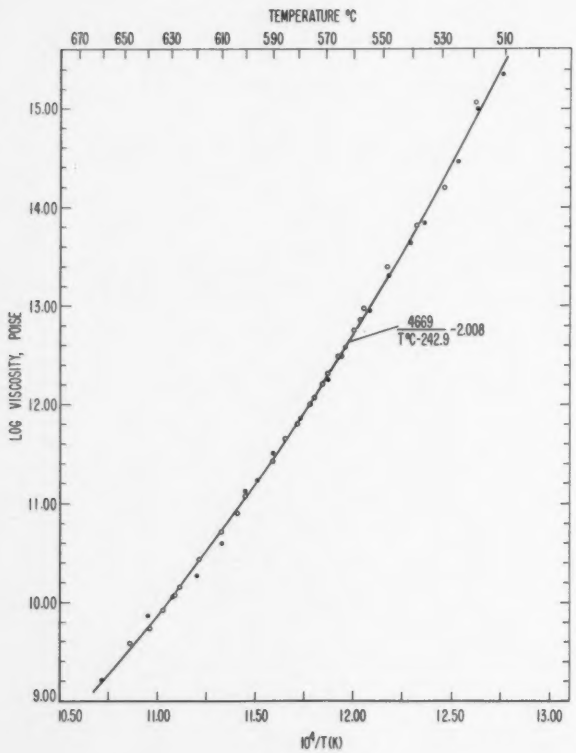

FIGURE 4. *The log viscosities obtained by each method for SRM 710 compared to the equation representing the combined data from both methods.*
○–fiber elongation method, and ●–beam-bending method.

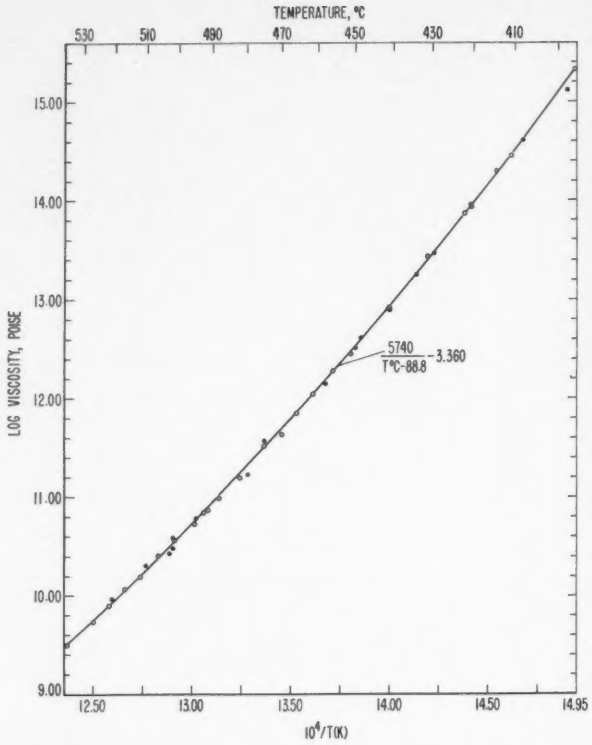

FIGURE 5. *The log viscosities obtained by each method for SRM 711 compared to the equation representing the combined data from both methods.*
○–fiber elongation method, and ●–beam-bending method.

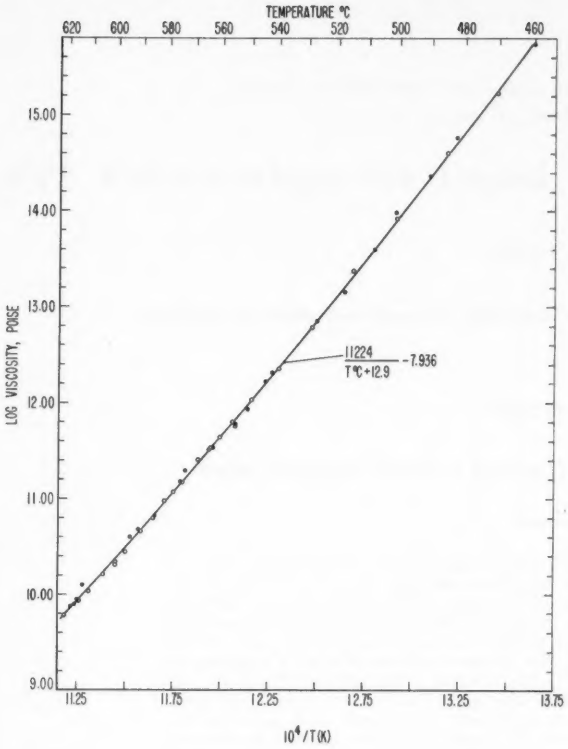

FIGURE 6. *The log viscosities obtained by each method for SRM 717 compared to the equation representing the combined data from both methods.*

○ – fiber elongation method, and ● – beam-bending method.

5. Summary

The viscosity of three standard glasses were measured at the lower temperatures (corresponding to the range 10^9 to 10^{15} P) by the fiber elongation and beam-bending methods.

The beam-bending apparatus was built with major modifications to previously existing equipment and used for studies in the measurement of viscosity at low temperatures.

The results of each method were compared to each other and to the combined data of both methods. It was shown that the scatter in viscosity data was less with the fiber elongation method than with the beam-bending method.

Using the Fulcher equation to analyze the data, no Arrhenius behavior was found for each of the three glasses over a temperature range of 150 °C (see figs. 4–6). This corresponds to viscosities ranging from $10^{9.5}$ to about 10^{16} P.

6. References

[1] Napolitano, A., and Hawkins, E. G., Viscosity of a standard soda-lime-silica glass, J. Res. Nat. Bur. Stand. (U.S.), **68A** (Phys. and Chem.), No. 5, 439 (September–October 1964).

[2] Napolitano, A., and Hawkins, E. G., Viscosity of a standard lead-silica glass, Nat. Bur. Stand. (U.S.), Misc. Publ. 260–11 (1966).

[3] Napolitano, A., and Hawkins, E. G., Viscosity of a standard borosilicate glass, Nat. Bur. Stand. (U.S.), Spec. Publ. 260–23 (1970).

[4] Napolitano, A., Macedo, P. B., and Hawkins, E. G., A wide-range (up to 10^{10}P) rotating cylinder viscometer, J. Res. Nat. Bur. Stand. (U.S.), **69A** (Phys. and Chem.). No. 5, 449 (September–October 1965).

[5] Hagy, H. E., Experimental evaluation of beam-bending method of determining glass viscosities in the range 10^8 to 10^{15} poises, J. Am. Ceram. Soc. **46,** No. 2, 93 (1963).

[6] Fontana, E. H., A versatile parallel plate viscometer for glass viscosity measurements to 1000°C, Am. Ceram. Soc. Bull. **49,** No. 6, 594 (1970).

[7] ASTM Standards, ASTM Designation C598–70T, Standard method of test for annealing point and strain point of glass by beam bending, Part 13 (1973).

(Paper 78A3–814)

JOURNAL OF RESEARCH of the National Bureau of Standards—A. Physics and Chemistry
Vol. 78A, No. 3, May–June 1974

PVT Relationships for Liquid and Glassy Poly(vinyl acetate)

John E. McKinney

Institute for Materials Research, National Bureau of Standards, Washington, D.C. 20234

and

Martin Goldstein

Belfer Graduate School of Science, Yeshiva University, New York, N.Y. 10033

(January 23, 1974)

PVT measurements were made on liquid and glassy poly(vinyl acetate) over ranges of −30 to 100 °C and 0 to 800 bar (gage pressure). The data were obtained by three different thermodynamic histories: (a) variable formation pressure. (b) constant formation pressure at one atmosphere, and (c) constant formation pressure at 800 bar. In all of these the glass was formed by isobaric cooling at 5 °C/h. The salient characteristics resulting from the different histories are the following. History (a) produces a glass of structure varying with formation pressure and, hence, does not necessarily give the proper thermodynamic properties of a "single physical substance." However, the liquid-glass intersection temperature, $T_g(P)$, is an important kinetic, or relaxational, property which approximates an isoviscous state. Accordingly, the values of dT_g/dP are in close agreement with those obtained from dynamic mechanical and dielectric time-temperature-pressure superposition. Constant formation histories (b) and (c) give proper thermodynamic properties of the glasses, but very little information with respect to kinetics. Increasing the pressure at which the glass is formed increases the density of the glass (at the given cooling rate) considerably in contrast to the entropy (from other work), which appears to be essentially independent of formation pressure.

A considerable part of the paper is definitional. The results are related to other *PVT*, dynamic mechanical, dielectric, and thermodynamic measurements. Interpretations are given in terms of both phenomenological and molecular models.

Key words: Density; dilatometer; entropy; glass transition; glass; liquid; polymer; poly(vinyl acetate); *PVT*; relaxation.

Contents

	Page
1. Introduction	331
2. Experimental apparatus and procedure	332
2.1. *PVT* apparatus	332
2.2 Dilatometer	333
a. Design	333
b. Operating equations	333
2.3. Sample	334
2.4. Thermodynamic histories and relaxational behavior	335
a. Variable formation of the glass	336
b. Constant formation of the glass at atmospheric pressure	336
c. Constant formation of the glass at 800 bar	336
3. Presentation of data	337
3.1. Liquid region	337
3.2. Transition region (glass formation)	337
3.3. Glasses	339
a. Variable formation glass	339
b. Glass formed at atmospheric pressure	340
c. Glass formed at 800 bar	341
4. Evaluation of data	341
4.1. Equations of state and the ordering parameter Z	341
4.2. Evaluation of T_g and T_g^{**} and corresponding properties	343
4.3. T_g and the isoviscous state	345
4.4. "Permanent" densification of the glass and T_g^* depression	345
4.5. Evaluation of the first Ehrenfest relation and its role in time-temperature-pressure superposition	348
4.6. Experimental uncertainties including estimates on T_g and T_g^*	350
5. Concluding remarks	352
6. References	353

1. Introduction

This work is concerned with the measurement and phenomenological evaluation of the *PVT* properties

533-558 OL - 74 - 2

of poly(vinyl acetate) with particular attention given to the influence of thermodynamic history. Although the properties of only one polymer were evaluated here, the general behavior and concepts are considered to be, at least in a qualitative sense, applicable to amorphous polymers and glass-forming liquids in general.

It is well known that the thermodynamic history used to form a glass has an important effect on its properties. Gee [1][1] and Ferry, in his recent treatise [2], devote considerable discussion to this point. For example, the influence of the rate of cooling on the densification of the glass and the corresponding shift of the glass transition temperature T_g on poly(vinyl acetate) have been studied over a large range of rates by Kovacs [3]. A similar effect may be obtained by forming a glass at elevated pressures as shown by Bianchi et al. [4], and later in this paper.

In this work the densification effect, among others, has been demonstrated extensively. The influence of thermodynamic history was studied by using suitable temperature-pressure-time variations which were grouped into three distinct classes. In these the glass was always formed using the same isobaric cooling rate at atmospheric and elevated pressures, always commencing at equilibrium in the liquid region, where properties are independent of history. The properties of the corresponding glasses were obtained subsequently by relatively fast temperature-pressure changes during which properties were assumed to be independent of time due to the slowness of the viscoelastic relaxations.

The parallel method of forming the glass by isothermal compressions at nearly constant rate used in references [5–8] was not employed here; however, some correlation between results from the two types of formations is included in the discussions.

The pressure range was limited to 800 bar (gage pressure)[2]. Although this range may appear to be small in comparison to that obtained in some other high pressure experiments, the compressibilities of polymers are relatively large, and accordingly, large changes in the transition properties are observed with pressure. On the other hand, as will be seen, a fourfold increase in the pressure range would be useful to study some of the limiting transitional phenomena predicted by some interpretations of these and other data.

In experimental observations on liquid-glass systems, one is faced with finding a suitable or appropriate definition of the glass transition temperature. A definition of $T_g(P)$ which is unique for each substance in that it is independent of the experimental mode by which it was determined is of course not possible. Different definitions of T_g are usually not equivalent. It has been proposed that with *PVT* measurements, a pressure dependent transition temperature should be defined from the intersection of the liquid and glass surfaces in *PVT* space [3, 4, 8]. Since, in this work, the glasses were formed by different histories, the intersection temperatures at each pressure will often take on different values, and also may have markedly different pressure dependences. In order to make appropriate distinctions, it is convenient to adopt the convention proposed by Goldstein [9], which is applicable to the histories used here. With this convention $T_g(P)$ is defined as the temperature of the liquid-glass intersection, where the glass was formed by isobaric cooling repeated at different pressures at the same constant rate. The values of $T_g(P)$ may be viewed as a set of characteristic temperatures at which a mean volume relaxation time is essentially constant as pressure is varied. Although $T_g(P)$ depends upon the rate of cooling, dT_g/dP has been found to be essentially independent of rate. The other quantity from Goldstein's convention, $T_g^*(P)$, is the temperature of the liquid-glass intersection where the glass is formed by isobaric cooling at constant rate only at one pressure, with the values at other pressures in the glassy region being obtained by extrapolation of the volume isobars. It is thus equivalent to the definition mentioned earlier (3, 4, 8). Although the values of T_g and T_g^* are identical at the formation pressure, it will be seen that dT_g/dP and dT_g^*/dP differ considerably.

The meaning of these quantities in terms of the experimental data will become clearer in later discussion. At this time it is important to remember that $T_g(P)$, as defined here, measures a relaxational or kinetic property, whereas $T_g^*(P)$ measures a thermodynamic property defined from the equations of state for the liquid and glass (in pseudoequilibrium) formed by a particular history. To the extent that the glass transition is as defined in a relaxational context, T_g may be regarded as the more significant parameter.

2. Experimental Apparatus and Procedure

2.1. *PVT* Apparatus

All of the measurements, except for the reference density determinations, were obtained by pressurized volume dilatometry. The dilatometer was placed in a pressure chamber with glass windows to permit visual observations of the height of the mercury column in the dilatometer. The chamber, in turn, was placed in a liquid thermostat, also with glass windows. The height of the mercury column was read with a cathetometer at various values of the independent variables, temperature and pressure.

A low-viscosity silicone oil capable of withstanding temperatures of 250 °C was used as a thermostating liquid over the high temperature range. At lower temperatures, where the silicone oil became too viscous, and temperature gradients became evident from striations, ethyl alcohol was used. The bath temperature was controlled by a proportional controller with a thermister element. For the isobaric cooling runs the multiturn potentiometer control was varied at constant angular velocity using a variable speed gear box driven by a synchronous motor. Since the resistance-temperature relationship is essentially linear, the bath temperature was, accordingly, varied at

[1] Figures in brackets indicate literature reference at end of this paper.
[2] The corresponding quantity in SI units is 80 megapascal (MPa).

constant rate. At temperatures below 40 °C accurate control was made possible by using a refrigerator with an adjustable back-pressure valve located between the suction side of the compressor and evaporator coil. The valve was manually set in accordance with the heat load to be removed. Final control was established by adding the appropriate amount of heat automatically with the proportional controller. The chamber temperature was read and recorded using a chromel-alumel thermocouple located within the chamber through a pressure seal. Although it would have been marginally desirable to control the chamber with a sensing element within the chamber, this is very difficult, because of the massiveness of the chamber and the difficulties encountered in using suitable sensing elements at elevated pressures. As a result a transient was introduced in the chamber temperature when a constant rate of cooling was initiated or terminated in the bath. A steady state of 0.4 °C difference between bath and chamber temperatures at a rate of cooling of 5 °C/h was reached in about 20 min. This transient response was of no consequence in these measurements because the runs were initiated well in the liquid regions and terminated in the glass. In both of these regions the effect of thermodynamic history is insignificant over the time scales which were used. By separate experiment at atmospheric pressure at the same cooling rate, the chamber temperature (at the thermocouple) and sample temperature were found to be the same within the experimental uncertainty.

The pressure chamber with glass windows is similar to that used by Martin and Mandelkern [10]. *Di*(ethyl hexyl) sebacate was used as the pressure transmitting fluid. The pressure was generated by a hand screw pump and measured with a 16-in bourdon tube gage. The bourdon gage is calibrated periodically against a dead weight piston gage. In the isobaric cooling runs the pressure was held constant by manual adjustment to compensate for the pressure drop resulting from the volume contractions of the constituents in the pressure chamber. In past experience the windows were found to be in danger of fracture at pressures in excess of 1 kbar. Accordingly, for a reasonable margin of safety, the maximum pressure was restricted to 800 bar.

2.2. Dilatometer

(a) Design

The dilatometer is a composite version which is described in detail in reference [11]. Only a brief description is given here for which a schematic diagram is shown in figure 1. Mercury was used as a confining fluid. The sample of polymer (O) was inserted into thimble (M), which at high temperatures prevented the molten sample from entering bore (B). The slots (N) in the thimble facilitated evacuation after assembly of the dilatometer. Sample bore (P), which is optional, reduced the thermal relaxation time of the sample. (This is true only if a strong conductor like mercury is used, as in this case, for the confining liquid.) The sample and thimble were inserted in cavity (F) which

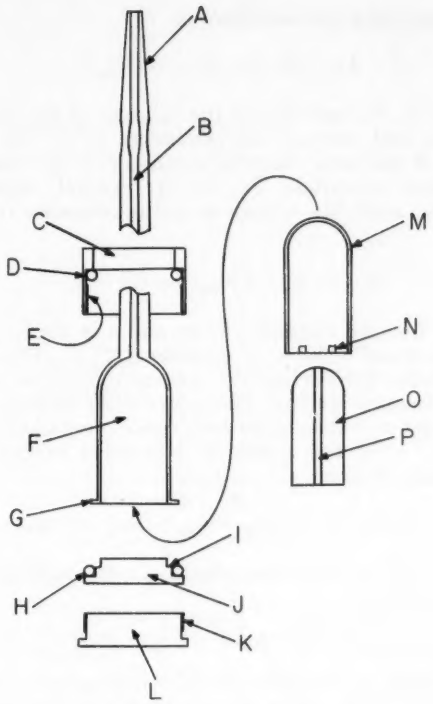

FIGURE 1. *Schematic diagram of the dilatometer: (A) tapered seal, (B) capillary bore, (C–L) brass clamp, (D) rubber "O" ring, (E) female thread, (F) cavity, (G) flange, (H) rubber "O" ring, (I) mating surface, (J) stainless steel base, (K) male thread, (M) thimble, (N) slots, (O) sample, (P) sample bore.*

was closed with stainless steel base (J). The base was secured by screwing a brass clamp (C–L), having very fine threads, until a seal was made completely by contact between flange (G) and surface (I). The dilatometer was then evacuated and filled with mercury. The chief advantage of a composite dilatometer with respect to polymers is that no heat sealing of the glass, from which there would be the danger of damaging the sample, is necessary. This composite dilatometer was found to be as stable over many cycles of varying temperature and pressure as the unit construction type.

(b) Operating Equations

The operating equations for the dilatometer relate the experimental observables, which are temperature, pressure, and displacement of the mercury column, to the corresponding density, or specific volume, of the sample. In the derivations of these equations it is assumed that the volumes of the dilatometer constituents are additive, and all deformations, including those of the dilatomer itself are homogeneous. The assumption of volume additivity implies that the associated compliances, $\Delta V_i/P$, are additive under hydrostatic conditions.

The total available volume V of the dilatometer up to the meniscus of the mercury column taken at some

arbitrary reference condition is

$$V_0 = (V_T)_0 + (V_S)_0 + (V_{Hg})_0 \quad (1)$$

where V_T, V_S, and V_{Hg} are the volumes of the thimble, sample and mercury at conditions T, P. The subscript 0 indicates that these quantities are taken at reference conditions T_0, P_0. At general conditions T, P the available volume up to the reference reading h_0 is

$$V = V_T + V_S + V_{Hg} - \pi r^2 (h - h_0) \quad (2)$$

where r is the capillary radius and h is the height of the mercury column at conditions T, P. The right-hand term is therefore the volume of mercury above the reference reading. The temperature and pressure dependences of the dilatometer glass contained in the terms $V - V_T$ and r may be expressed explicitly by rewriting eq (2) as

$$V_S = x^3 (V - V_T)_{25} - V_{Hg} + \pi x r_{25}^2 (h - h_0) \quad (3)$$

where x is an effective extension ratio approximated linearly by

$$x^3 = 1 + \alpha_D (T - 25) - \beta_D P.$$

The values $\alpha_D = 0.99 \times 10^{-5} °C^{-1}$ [12] and $\beta_D = 2.92 \times 10^{-5}$ bar^{-1} [13], taken as constants, are the thermal expansivity (cubic) and compressibility of borosilicate glass taken at 25 °C.

The linear dependence of the right-hand term of eq (3) on x results from the fact that the radius and the distance between any two graduations on the capillary both vary linearly with x. Accordingly, the multiplying factor is $x^2/x = x$. If the readings were read solely with a cathetometer (at ambient conditions) the right-hand term would depend upon x^2. In our work the cathetometer was used only to interpolate between adjacent graduations.

From eq (3) the volume available for the sample and mercury at reference conditions is

$$(V_S)_0 + (V_{Hg})_0 = x_0^3 (V - V_T)_{25}.$$

This result is used to eliminate $(V - V_T)_{25}$ in eq (3). With some rearrangement and division by W_s, the sample mass, the final, desired result for the sample specific volume is obtained:

$$v_s = \frac{1}{W_S} \left\{ V_{S0} - [V_{Hg} - (V_{Hg})_0] - \left(1 - \frac{x^3}{x_0^3}\right) [(V_{Hg})_0 + (V_S)_0] + \pi x r_{25}^2 (h - h_0) \right\}. \quad (4)$$

In the above equations the contributions to the sample volume given by the terms in the braces may be identified as the reference sample volume, the change in the total volume of mercury, the change in the available volume of the dilatometer up to h_0, and the volume of mercury above h_0.

Since the thimble is made from the same material (borosilicate glass) as the dilatometer, V_T does not enter into equation (4).

The values for the specific volume of mercury were taken from the data of Carnazzi [14].

2.3. Sample

All measurements were made on a single sample of high molecular weight poly(vinyl acetate), grade AYAT, supplied by the Plastics Division of the Union Carbide Company.[3] The intrinsic viscosity $[\eta]$ is given as 0.69 dl/g at 20 °C in cyclohexanone. The corresponding molecular weight may be estimated from the Mark-Houwink Equation [15],

$$[\eta] = K M_v^{\alpha}$$

where M_v is the viscosity average molecular weight. The values $K = 15.8 \times 10^{-5}$ dl/g and $\alpha = 0.69$ are taken from reference [16] which apply to acetone solutions at 20 °C. Since acetone and cyclohexanone have the same solubility parameter, $\delta = 9.9$ [17], it is expected that the above values of K and α are applicable to cyclohexanone solutions to within the accuracy desired here. Using these values in the above equation, the value $M_v = 189{,}000$ was obtained for this sample. The viscosity-average lies between the number- and weight-average molecular weights, but is usually closer to the weight-average.

The above value of M_v is expected to be sufficiently high for T_g to be essentially independent of molecular weight. The validity of this assumption is indicated from the relation [18]

$$T_g = T_{g\infty} - \frac{K'}{M}$$

where M is the molecular weight of a monodisperse polymer. From references [19] and [20][4] experimental values of K', ranging over a factor of two, may be approximated by 1.0×10^5 for the several polymers investigated. Although poly(vinyl acetate) was not included in the above investigations, it seems reasonable to assume that this value of K is also roughly applicable to this polymer. Using the values $K' = 1.0 \times 10^5$ and $M = 190{,}000$ in the above equation, the difference between T_g and $T_{g\infty}$ is only 0.5 °C, which is generally within the range of experimental uncertainty.

Since the presence of even small traces of residual solvent lowers the value of T_g considerably [21], the following procedure was used to remove the solvent.

The PVAc pellets which averaged about 5 mm in diameter were placed in a cylindrical glass tube with a tapered seal and diameter slightly larger than the thinble shown in figure 1. The tube containing the sample was evacuated to less than one torr (133 Pa)

[3] Commercial material used in this experiment does not imply recommendation or endorsement by the National Bureau of Standards, nor does it imply that the material identified is necessarily the best available for the purpose.

[4] The value of $K' = 1.2 \times 10^5$ for poly(tetramethyl-*p*-silphenylene)-siloxane is not given explicitly in this reference, but was obtained from calculations on data obtained therein.

and brought up to 120 °C using a silicone oil bath. These conditions were maintained for about three weeks, which was more than sufficient time for the sample weight to stabilize. The loss of weight over the entire process was about 1 percent, which is attributed to residual solvent. During this period the pellets flowed together and the sample assumed the shape of the container. Over several days the sample was cooled to room temperature. The tube was broken, and one end of the sample was faced on a lathe to a length slightly shorter than the thimble. A two millimeter hole was drilled through the sample, as shown in figure 1, in order to shorten the time to reach thermal equilibrium. The final dimensions of the sample shown on figure 1 are 35 × 15 mm diam with a 2 mm diam bore.

A reference value of the specific volume for the polymer was obtained using the usual hydrostatic weighing procedure [22]. A value of 0.8487 cm^3/g at 40 °C was obtained after making the air buoyancy corrections [23]. 40 °C is a high enough temperature for the sample to reach viscoelastic equilibrium in a short time and low enough not to unduly complicate the hydrostatic weighing procedure.

2.4. Thermodynamic Histories and Relaxational Behavior

As stated earlier the thermodynamic history of a polymer, or glassforming liquid, has considerable influence on the experimental properties in the transition and glass regions. In this work comparisons were made between data obtained from the histories used to form the glass. All of these involved commencing a "run" at true equilibrium in the liquid region, where the properties are independent of history, and forming the glass isobarically at different pressures at a constant rate of cooling at 5 °C/hr. This rate is small enough to essentially maintain thermal equilibrium within the sample. The constant rate was terminated at some temperature well within the glassy region characterized by viscoelastic relaxation times sufficiently long in comparison to experimental times that no further changes in density with time at constant temperature were observed. Subsequent measurements in the glass were taken by an accelerated procedure.

A typical volume-temperature curve obtained by isobaric cooling at constant rate, used to form the glass, is shown schematically on figure 2a. The glass temperature, T_g, is manifested here by the rapidly changing slope as shown. In the liquid region at temperatures well above T_g, for example T_a, the time-dependent response in volume resulting from a sudden change in temperature or pressure is shown on figure 2b, where two relaxation[5] processes may be realized. The first is a viscoelastic, or structural relaxation, which may be completed so rapidly at very high temperatures that it will not be observed by this technique. The second is a thermal relaxation, which results from a time dependent macroscopic distribution of

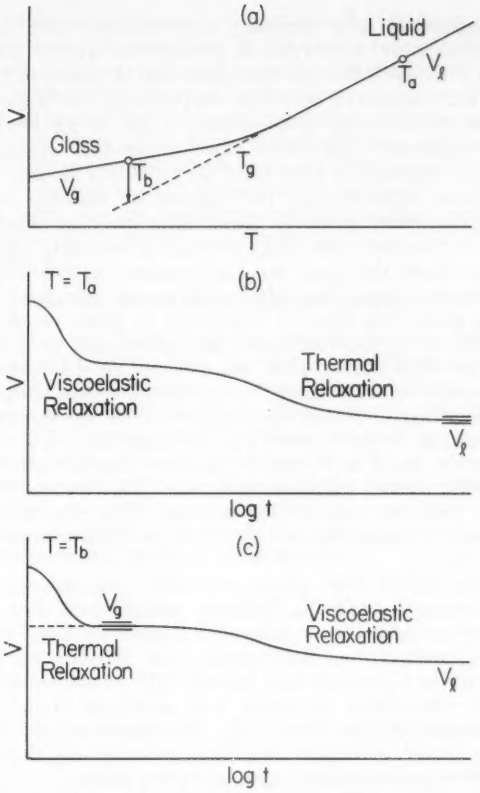

FIGURE 2. *Relaxational Response in Liquid and Glass.*

temperatures and corresponding densities over the sample and apparatus components equilibrating through heat transfer. The information obtained from thermal relaxations is of no interest here. In our work the thermal relaxations equilibrated in about 20 min essentially independent of temperature and pressure. At the conclusion of both relaxations the true equilibrium value, V_l, was obtained. A set of values in the liquid region was obtained by rapidly changing the temperature or pressure to the desired values and allowing true equilibrium to be attained at each point. This procedure reaching either true or apparent equilibrium at each point is referred to here as the temperature-pressure jump method.

As a result of the large increase in viscoelastic relaxation times with decreasing temperature and the constancy of the thermal relaxation times, the order of the two relaxation processes is reversed at temperatures well below T_g. Figure 2c shows the time-dependent response resulting from thermodynamic response in the glass, say at T_b, on figure 2a. The thermal relaxation is completed in about the usual 20 min followed by the viscoelastic one which may be extended over many years depending upon the temperature and pressure. Since the observed volume is essentially stationary during and well after the thermal relaxation, the value of volume obtained at the completion of the thermal relaxation appears to have reached

[5] More strictly, "retardation" is used to express time-dependent strain at constant stress in contrast to "relaxation" for time-dependent stress at constant strain. In this work "relaxation" is used in a more general sense to cover both.

equilibrium over ordinary experimental time scales. Accordingly, this value is referred to as the pseudo-equilibrium value for the glass and is taken to be the initial value V_g for the viscoelastic relaxation as indicated by the dashed line. A set of values of V_g at different conditions are, therefore, considered as isochronal at zero time with respect to the viscoelastic relaxations. The apparent stability in V_g implies that a set of these data are representative of a thermodynamically reversible system, i.e., one for which the data are independent of the thermodynamic path by which they are obtained after the glass was formed. Note that in order to obtain a value of V_g, the relaxation processes must be distinct. When this was true, it was not practical to obtain V_l because of the large experimental times required. Accordingly, it was not practical with our equipment to obtain both V_l and V_g at the same conditions. The parallel lines at V_l and V_g indicate regions where the proper values of these quantities are obtained within the precision of the experiment. This region for V_g is finite, while the one for V_l is, of course, extended to $t \rightarrow \infty$.

No effort was made to obtain relaxational data between V_l and V_g. Volume relaxational data have been obtained over extensive ranges of temperature and pressure on polystyrene over periods up to 25 hours by Goldbach and Rehage [24]. In our work when any viscoelastic response was observed in the glass at temperatures close to T_g, the glass was reheated to the liquid condition and then reformed by the same history before subsequent data were taken.

In view of these remarks the three histories used to form the glass are described below.

a. Variable Formation of the Glass

A schematic diagram of the variable formation history (a) is given in figure 3a. The measurements were commenced at an elevated temperature sufficiently high to be in the equilibrium region at some arbitrary pressure P_i. The sample was then cooled isobarically at 5 °C/hr through the apparent $T_g(P)$ to a terminal temperature well below this where the structure is "frozen in." Subsequent pseudoequilibrium measurements in the glass were taken isobarically at P_i using the temperature jump method with regular checks on the reproducibility to insure that viscoelastic relaxations have not occurred. The same procedure was repeated at different pressures until the desired data were obtained. All pressure changes were made in the liquid state.

b. Constant Formation of the Glass at Atmospheric Pressure

History (b) (constant formation at atmospheric pressure) is illustrated schematically in figure 3b. The glass was formed in the same manner as the previous case except that isobaric cooling was at atmospheric pressure only. After the terminal temperature within the glass was reached, pseudoequilibrium measurements were taken using the temperature-pressure jump method with regular checks to insure the absence of significant viscoelastic relaxations. All pressure changes were made in the glass.

c. Constant Formation of the Glass at 800 Bar

The schematic diagram for history (c) (constant formation at 800 bar) is shown in figure 3c. With this history the glass was formed in the same manner as

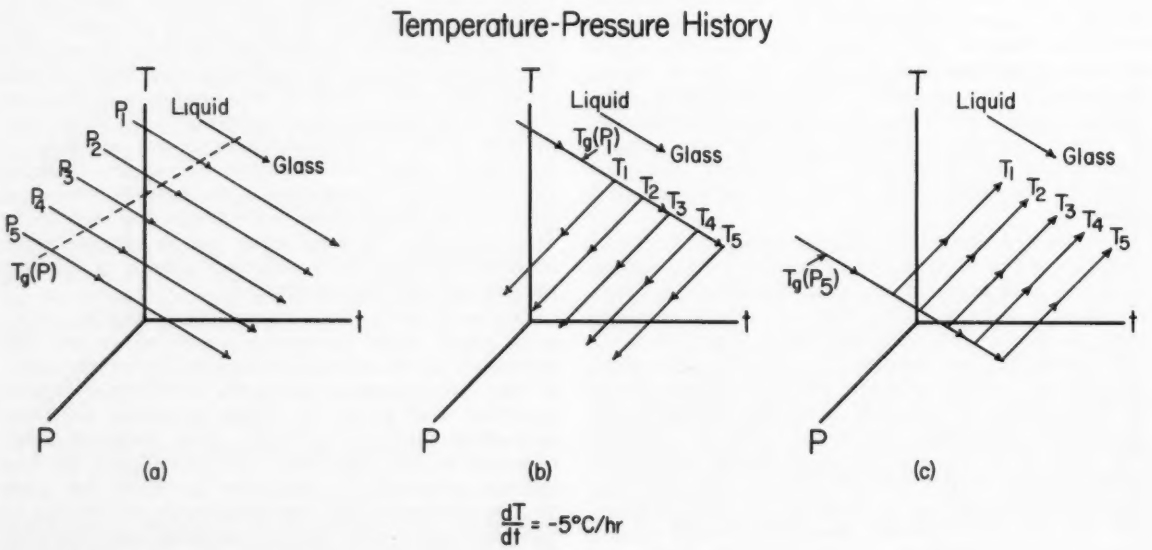

FIGURE 3. *Thermodynamic histories used to form the glass: (a) variable formation, (b) glass formed at atmospheric pressure, and (c) glass formed at 800 bar.*

the previous one (b) except that the isobaric cooling was at 800 bar. Pseudoequilibrium measurements within the glass were again obtained by the temperature-pressure jump method. Although the "jumps" in the glass in both histories b and c are shown schematically as isothermal, actual paths followed were not necessarily isothermal, the exact thermodynamic path in the glassy region being irrelevant over these experimental time scales.

Note that a principal distinction between the variable formation history (a) and the constant formation histories (b and c) is that with the former, all pressure changes are made in the liquid, and with the latter, all pressure changes are made in the glass.

3. Presentation of Data

3.1. Liquid Region

The liquid *PVT* data are given in table 1. All of these values are displayed by open circles on the right-hand sides of each of figures 4, 5, and 6. (These points are the least obscured from other data sets in fig. 6.) The liquid measurements were taken by the temperature-pressure jump method. At the higher temperatures one-half hour was allowed to attain equilibrium after each jump. Since thermal relaxations equilibrated in about 20 min independent of conditions, the one half hour used here was more than sufficient. In other cases, at lower temperatures, where viscoelastic relaxations were apparent at longer times, as much as four hours were allowed to attain equilibrium. Data which did not equilibrate within this period were excluded from the set.

3.2. Transition Region (glass formation)

The data resulting from the isobaric cooling paths at 5 °C/hr, used to form the glass, are tabulated in table 2 and illustrated in figure 4 with solid circles. In all cases the measurements commenced at equilibrium in the liquid region and terminated well in the glass where viscoelastic relaxation times were large in comparison to experimental times. In the liquid region there was, of course, no distinction observed between a datum obtained by the isobaric cooling method and the temperature-pressure jump method.

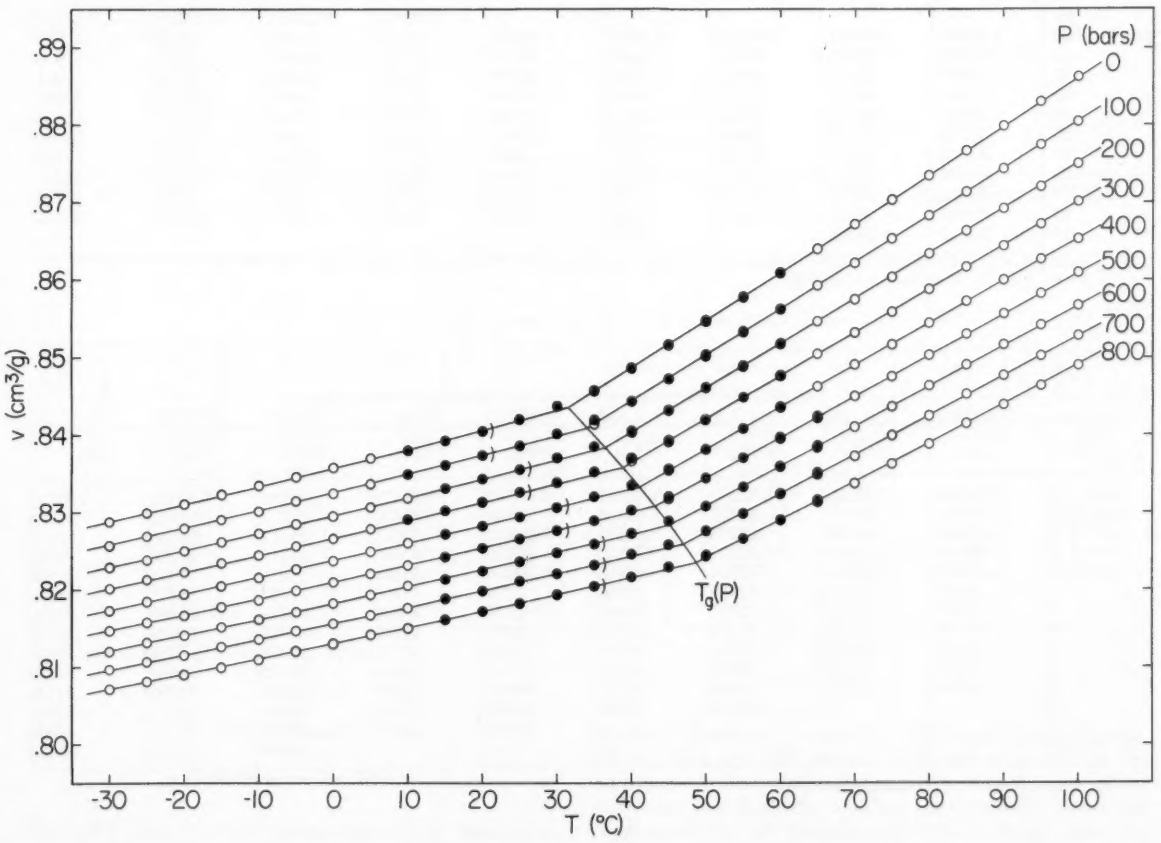

FIGURE 4. *Specific volume versus temperature at different pressures using the variable formation history (a) to form the glass.*

TABLE 1. *Specific volume data for the liquid region*

T \ P	0	100	200	300	400	500	600	700	800
35	0.84572	0.84148							
40	.84870	.84444	0.84041	0.83670					
45	.85174	.84733	.84321	.83921	0.83549	0.83184			
50	.85486	.85041	.84608	.84206	.83817	.83447	0.83087	0.82757	
55	.85791	.85349	.84894	.84491	.84092	.83709	.83340	.82988	0.82666
60	.86104	.85628	.85179	.84769	.84367	.83980	.83607	.83256	.82904
65	.86407	.85933	.85472	.85052	.84648	.84250	.83874	.83523	.83174
70	.86723	.86218	.85755	.85324	.84913	.84507	.84108	.83734	.83378
75	.87038	.86536	.86038	.85594	.85171	.84762	.84367	.84000	.83626
80	.87343	.86829	.86342	.85881	.85453	.85036	.84641	.84257	.83889
85	.87669	.87140	.86636	.86169	.85728	.85308	.84911	.84532	.84155
90	.87986	.87438	.86923	.86444	.86000	.85574	.85172	.84776	.84396
95	.88301	.87741	.87207	.86722	.86269	.85823	.85424	.85025	.84641
100	.88622	.88043	.87500	.87012	.86534	.86095	.85678	.85284	.84904

Units: T in °C, P in bars, v in cm³/g.

TABLE 2. *Specific volume data for the transition region*

T \ P	0	100	200	300	400	500	600	700	800
65						0.84235	0.83853	0.83500	0.83150
60	0.86094	0.85634	0.85193	0.84769	0.84362	.83973	.83602	.83248	.82912
55	.85782	.85329	.84903	.84489	.84094	.83710	.83343	.82999	.82670
50	.85468	.85023	.84615	.84208	.83819	.83446	.83094	.82772	.82461
45	.85165	.84733	.84331	.83938	.83564	.83213	.82898	.82594	.82307
40	.84861	.84443	.84061	.83710	.83360	.83039	.82732	.83467	.82176
35	.84578	.84199	.83864	.83534	.83205	.82904	.82600	.82330	.82055
30	.84374	.84023	.83706	.83392	.83069	.82776	.82482	.82216	.81948
25	.84209	.83874	.83559	.83266	.82950	.82663	.82363	.82111	.81830
20	.84061	.83747	.83436	.83145	.82831	.82542	.82250	.81995	.81728
15	.83937	.83622	.83319	.83033	.82720	.82434	.82142	.81892	.81622
10	.83812	.83503		.82915					

Units: T in °C, P in bars, v in cm³/g.

TABLE 3. *Specific volume values for the variable formation glass*

T \ P	0	100	200	300	400	500	600	700	800
−30	0.82884	0.82573	0.82292	0.82019	0.81735	0.81472	0.81206	0.80971	0.80723
−25	.83002	.82693	.82381	.82130	.81848	.81580	.81321	.81072	.80823
−20	.83110	.82797	.82503	.82236	.81944	.81672	.81412	.81166	.80910
−15	.83238	.82910	.82619	.82345	.82048	.81780	.81517	.81260	.81003
−10	.83350	.83019	.82734	.82453	.82156	.81876	.81621	.81364	.81108
−5	.83467	.83146	.82849	.82568	.82270	.81993	.81725	.81472	.81210
0	.83581	.83250	.82957	.82666	.82377	.82098	.81831	.81569	.81310
5	.83706	.83375	.83074	.82791	.82497	.82211	.81941	.81680	.81424
10	.83812	.83503	.83191	.82915	.82608	.82321	.82058	.81786	.81509
15	.83937	.83622	.83319	.83033	.82720	.82434	.82142	.81892	.81622
20	.84061	.83747	.83436	.83145	.82831	.82542	.82250	.81995	.81728
25			.83559	.83266	.82950	.82663	.82363	.82111	.81830
30					.83069	.82776	.82482	.82216	.81948
35							.82600	.82330	.82055

Units: T in °C, P in bars, v in cm³/g.

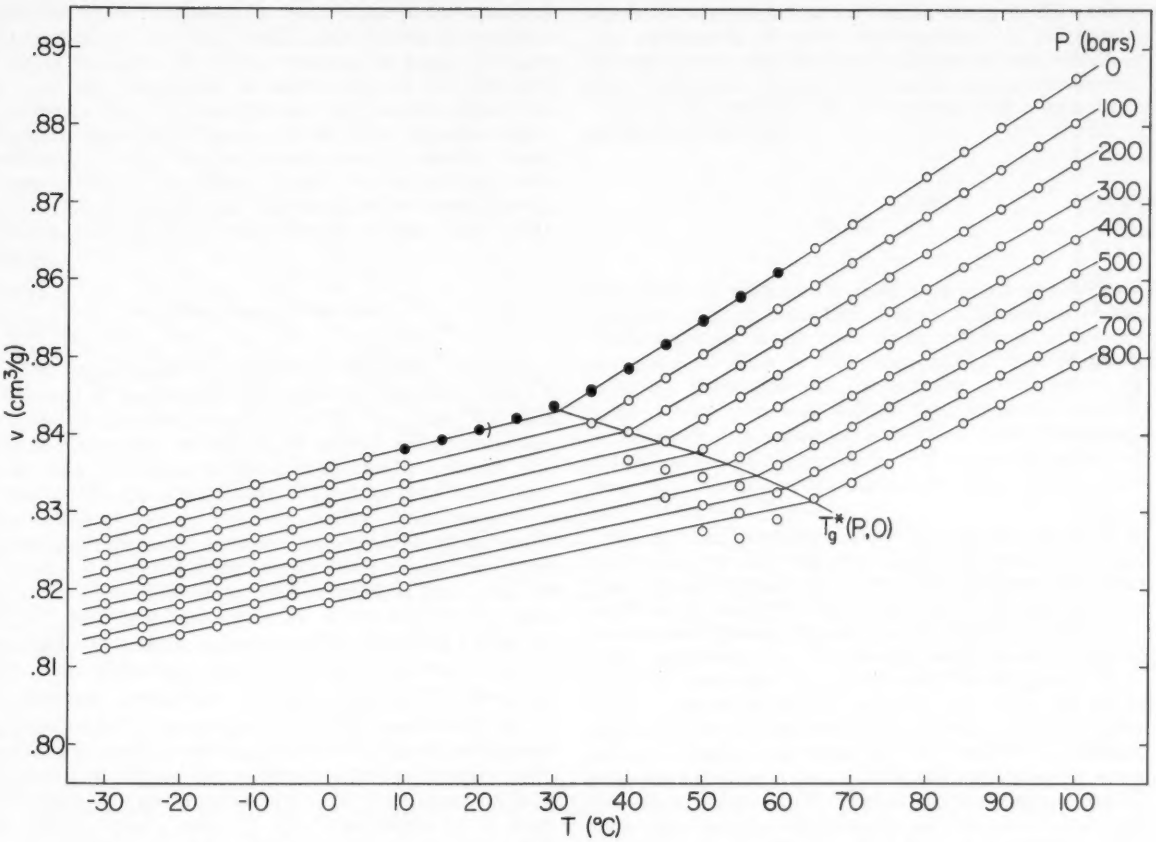

FIGURE 5. *Specific volume versus temperature at different pressures using the atmospheric pressure history (b) to form the glass.*

TABLE 4. *Specific volume values for the one atmosphere glass*

T \ P	0	100	200	300	400	500	600	700	800
−30	0.82884	0.82654	0.82438	0.82225	0.82017	0.81816	0.81613	0.81419	0.81237
−25	.83002	.82768	.82547	.82334	.82121	.81914	.81715	.81516	.81327
−20	.83110	.82874	.82648	.82430	.82218	.82010	.81808	.81606	.81415
−15	.83238	.82997	.82767	.82549	.82331	.82117	.81919	.81717	.81522
−10	.83350	.83117	.82886	.82663	.82443	.82224	.82022	.81817	.81620
−5	.83467	.83233	.83003	.82774	.82557	.82340	.82131	.81933	.81729
0	.83581	.83351	.83115	.82889	.82666	.82447	.82237	.82033	.81825
5	.83706	.83478	.83241	.83012	.82794	.82569	.82355	.82140	.81941
10	.83812	.83593	.83359	.83130	.82903	.82679	.82465	.82248	.82040
15	.83937								
20	.84061								

Units: T in °C, P in bars, v in cm³/g.

3.3. Glasses

a. Variable Formation Glass

The *PVT* data for the glass formed by history a, using all of the formation paths included in table 2, are given in table 3. All of the measurements in the glass were taken isobarically by the temperature jump method allowing at least one half hour to equilibrate. These data are illustrated in figure 4 by all of the points to the left of the parenthesis. Since some of the solid circles (isobaric cooling at constant rate) are representative of pseudoequilibrium, these were included in this set. The isobaric cooling data at these conditions were in agreement with those taken by the temperature jump method.

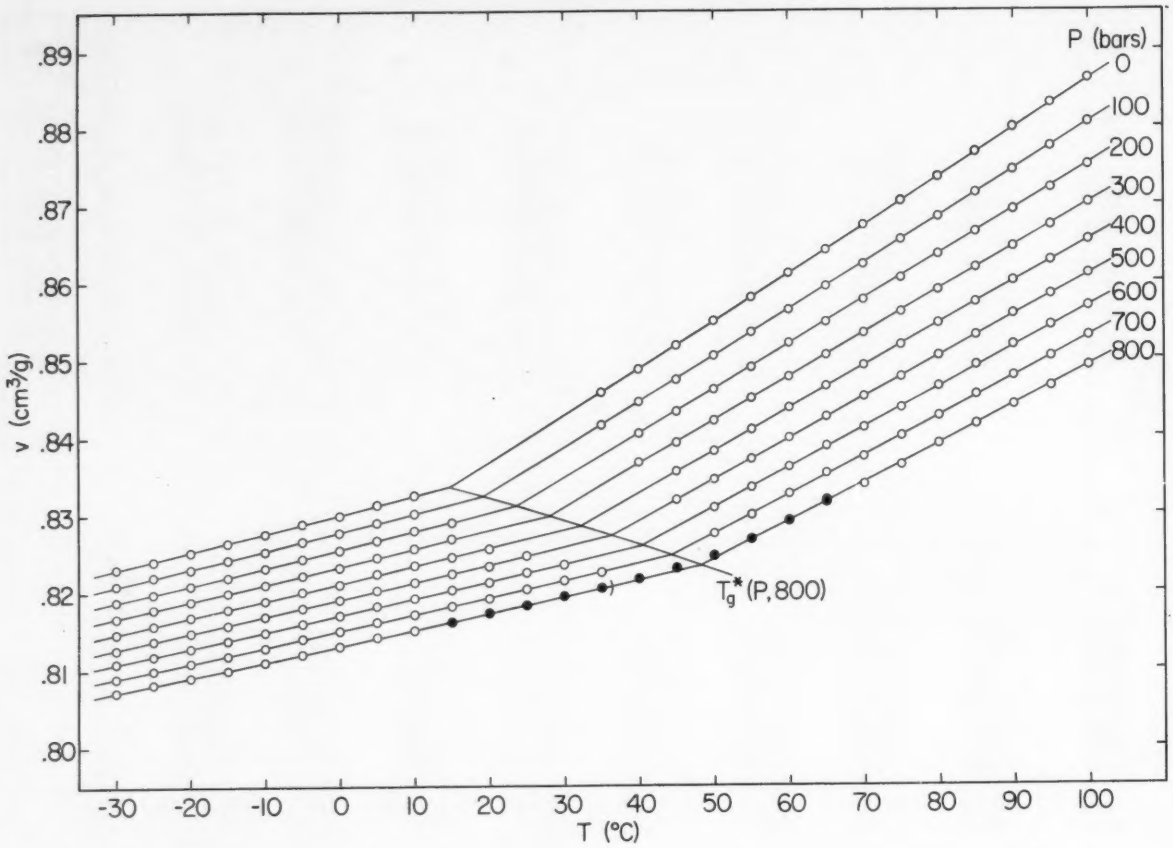

FIGURE 6. *Specific volume versus temperature at different pressures using the 800 bar history (c) to form the glass.*

TABLE 5. *Specific volume values for the 800 bar glass*

T \ P	0	100	200	300	400	500	600	700	800
−30	0.82311	0.82100	0.81886	0.81676	0.81476	0.81274	0.81087	0.80901	0.80723
−25	.82414	.82207	.81991	.81792	.81585	.81388	.81190	.81004	.80823
−20	.82526	.82308	.82097	.81891	.81688	.81484	.81291	.81101	.80910
−15	.82642	.82427	.82203	.81999	.81791	.81585	.81387	.81192	.81003
−10	.82758	.82533	.82321	.82107	.81898	.81693	.81493	.81294	.81108
−5	.82889	.82663	.82440	.82227	.82018	.81804	.81605	.81410	.81210
0	.82993	.82769	.82547	.82335	.82126	.81911	.81704	.81507	.81310
5	.83133	.82900	.82671	.82457	.82244	.82033	.81827	.81620	.81424
10	.83249	.83016	.82794	.82567	.82350	.82132	.81926	.81716	.81509
15			.82901	.82683	.82456	.82241	.82034	.81821	.81622
20					.82557	.82335	.82127	.81919	.81728
25						.82466	.82254	.82039	.81830
30							.82354	.82148	.81948
35								.82257	.82055

Units: T in °C, P in bars, v in cm³/g.

b. Glass Formed at Atmospheric Pressure

The *PVT* data for the glass formed by history b (isobaric cooling at atmospheric pressure) are given in table 4. The formation data are given in column 1 of table 2. The glass data is shown in figure 5 by the open circles to the left of T_g^* and the three solid circles to the left of the parenthesis. The data shown by open

circles were obtained by the temperature-pressure jump method, and those with solid circles by constant rate of cooling at 5 °C/hr. Although in figure 3b these jumps are illustrated as isothermal at the elevated pressures, the thermodynamic path in the glass was found to have no influence on the data. In some observations at the higher temperatures where some irreversibility resulting from viscoelasticity was observed, the glass was reformed by the same history before subsequent measurements in the glass were taken.

c. Glass Formed at 800 Bar

The procedure for history c (isobaric cooling at 800 bar) is essentially the same as that for history b except the glass was formed at 800 bar. The *PVT* data for the glass are contained in table 5 with the formation data contained in the last column of table 2. The data for the glass are illustrated in figure 6 by the open and solid circles to the left of the parenthesis. The principal difference between the results from histories b and c is that the higher formation pressure produces a more densified glass with corresponding shift in $T_g^*(P)$ to lower temperatures. With history c it was possible to obtain pseudoequilibrium data closer to T_g^*. This difference may be attributed largely to experimental procedure. In approaching T_g^* from the glassy region it is desirable to take successive observations in such a way that relaxation times are always decreasing. Since the relaxation times increase with pressure at constant temperature, such a procedure to obtain values near T_g^* was impossible, or at least very difficult, with history b.

4. Evaluation of Data

4.1. Equations of State and the Ordering Parameter Z

PVT relations including thermodynamic equations of state are often used to facilitate the analysis of *PVT* data. A general expression applicable to both liquid and glass connected by a transition region would be very difficult to obtain. Not only would such an expression have to contain a large number of adjustable parameters to fit the complicated curvature, but it would have to contain the influence of thermodynamic history. A satisfactory alternative often used is to fit separate relations: one to the liquid and one to each of the glasses formed by a different history. The transition properties according to the more general definition of Kovacs [3], Bianchi [4] and Quach and Simha [8] may thus be evaluated at the intersection of the liquid and glass surfaces in *PVT* space.

The Tait equation [25, 26] which has two adjustable isothermal parameters has been used to fit data in both the liquid and glassy regions. (See for example references [8, 27].) Although the Tait equation gives a good fit with a small number of parameters, its algebraic manipulation in finding some of the transition properties is very cumbersome. A polynomial approach was used here to facilitate the estimation of these properties, and in some cases, their uncertainties.

Using the OMNITAB Fit routine [28] a quadratic equation of the form

$$v=\sum_{i=0}^{2}\sum_{j=0}^{2}a_{ij}T^iP^j \tag{5}$$

was fitted to each of the data sets given in section 3 exclusive of the transition region. The values of the coefficients a_{ij} along with their standard deviations are given in table 6. The Sequential F test [29] was used to determine the significant coefficients. In cases where the test failed, the respective coefficients were set equal to zero. The solid lines with positive slope on figures 4, 5, and 6 give the values of the specific volumes calculated from the appropriate forms of eq (5).

As applied to these data the above equation is representative of thermal equilibrium in all cases. The liquid equation is a true equilibrium one independent of thermodynamic history. The equation for the various glasses are pseudoequilibrium representations applicable to "frozen in" structures resulting from the particular thermodynamic histories.

As a thermodynamic equation of state, eq (5) is applicable to the liquid region and constant formation glasses. This is not true for the variable formation glass (a) because it has a different structure for each formation pressure P'. Therefore, in this case, eq (5) gives the proper thermodynamic response only for isobaric changes with $P=P'$. Accordingly, the thermal expansions derived from eq (5) for the variable formation history are proper thermodynamic quantities, whereas the compressibilities are not because they do not apply to a "single physical substance".[6] In order to make the distinction between the compressibilities, we will use Goldstein's convention [9] for which β_g is the proper thermodynamic isothermal compressibility of the glass and β_g^* is an apparent isothermal compressibility of the "glass" obtained from the variable formation history.

This argument applied to isothermal compression measurements where the measurements are commenced in the liquid and the glass is formed by increasing the pressure at constant temperature is analogous, but reversed. In this case the structure of the glass varies with the formation temperature T'. Accordingly, in this case, the derived compressibilities are proper thermodynamic quantities and the thermoexpansivities are not.

The pressure dependences of the isobaric thermal expansivities and isothermal compressibilities for the

[6] Glasses formed by different thermodynamic histories may have different thermodynamic properties at the same temperature and pressure. They thus may be regarded as different substances even though they have identical chemical composition. Accordingly, the properties of a glass derived from data at different temperatures and pressures, but obtained from using only one history are said to pertain to a "single physical substance."

TABLE 6. *Coefficients and their standard deviations*

for a_{ij} *in* $v = \sum_{i=0}^{2} \sum_{j=0}^{2} a_{ij} T^i P^j$

Liquid

i \ j	0	1	2
0	0.82496 ± .00030	−(0.396 ± .022) × 10^{-4}	(0.124 ± .032) × 10^{-7}
1	(.5820 ± .0092) × 10^{-3}	− (.32 ± .65) × 10^{-7}	− (.177 ± .091) × 10^{-9}
2	(.294 ± .067) × 10^{-6}	− (.146 ± .046) × 10^{-8}	(.193 ± .062) × 10^{-11}

Glasses

(a) Variable Formation Glass

i \ j	0	1	2
0	0.835773 ± .000020	− (0.3147 ± .0011) × 10^{-4}	(0.394 ± .013) × 10^{-8}
1	(.24019 ± .00086) × 10^{-3}	− (.460 ± .017) × 10^{-7}	0
2	(.246 ± .023) × 10^{-6}	0	0

(b) Glass Formed at Atmosphereic Pressure

i \ j	0	1	2
0	0.835861 ± .000020	− (0.2375 ± .0013) × 10^{-4}	(0.225 ± .016) × 10^{-8}
1	(.2356 ± .0012) × 10^{-3}	− (.217 ± .080) × 10^{-7}	− (.25 ± .10) × 10^{-10}
2	0	0	0

(c) Glass Formed at 800 Bar

i \ j	0	1	2
0	0.830031 ± .000019	− (0.22950 ± .00098) × 10^{-4}	(0.225 ± .011) × 10^{-8}
1	(.2393 ± .0010) × 10^{-3}	− (.452 ± .018) × 10^{-7}	0
2	(.207 ± .023) × 10^{-6}	0	0

liquid and glasses formed by the three histories a, b, and c are given in tables 7 and 8. These expressions are evaluated from the appropriate operations on eq (5) to obtain

$$\alpha = (1/V)(\partial V/\partial T)_P \text{ and } \beta \text{ or } \beta^* = -(1/V)(\partial V/\partial P)_T$$

using the values of coefficients contained in table 6. The liquid and glasses were evaluated at 70 and 0 °C. The purpose for the inclusion of these tables, aside from reference purposes, is to illustrate the point of the argument given in the last two paragraphs. The values of α_g at any particular pressure are nearly independent of the histories used here, whereas the values of β_g^* for the variable formation history (a) are about 30 percent larger than the corresponding values for β_g from the constant formation histories (b and c). If the analogous procedure were conducted with isothermal compression, the corresponding variation would be in the thermal expansivities.

It has been proposed that the thermodynamic properties of liquids near T_g may be specified by an ordering parameter set $\{Z\}$, the values being functions of T and P at equilibrium, but becoming constant in the glass at the values they have at T_g. Experimental data may be used to answer two questions about such a set of ordering parameters: first, is one sufficient, or is more than one necessary, and second, when glasses are formed at constant cooling rate (and hence at constant relaxation time) under various pressures, are the values of the Z_i's frozen in independent of, or vary with, the formation pressure. The first is answered by testing the inequality $\Delta\beta/\Delta\alpha \geq TV\Delta\alpha/\Delta C_p$, where C_p is the heat capacity at constant pressure. If they are equal, one is sufficient [30]. In the absence of C_p data on this sample of polymer, the question cannot be answered; the evidence on a number of glass-formers available in the literature indicates that $\Delta\beta/\Delta\alpha$ is about twice $TV\Delta\alpha/\Delta C_p$, and hence a single ordering parameter is not sufficient. Incidentally the sense of the inequality

$$\Delta\beta/\Delta\alpha \geq TV\Delta\alpha/\Delta C_p$$

is based on considerations of thermodynamic stability, and must always be satisfied if the hypotheses used in obtaining the configurational properties (those prefixed by Δ) are justified. (See ref [9] for a detailed discussion.)

The fact that configurational volume is a function of P' for constant cooling rate (or in other words, two different samples of glass prepared by cooling the liquid under two different pressures at the same constant

TABLE 7. *Thermal expansivities typical of the liquid and glasses* a, b, *and* c

$\alpha \times 10^4$ (°C^{-1})				
P bar	Liquid, 70 °C	Glass, 0 °C		
		a	*b*	*c*
0	7.186	2.874	2.819	2.884
100	6.963	2.829	2.798	2.837
200	6.758	2.784	2.771	2.790
300	6.571	2.739	2.737	2.742
400	6.403	2.692	2.697	2.694
500	6.253	2.645	2.650	2.646
600	6.123	2.598	2.598	2.598
700	6.013	2.550	2.538	2.548
800	5.922	2.501	2.472	2.499

TABLE 8. *Compressibilities typical of the liquid and glasses* a, b, *and* c

$\beta \times 10^5$ (bar^{-1})				
P bar	Liquid, 70 °C	Glass, 0 °C		
		a	*b*	*c*
0	5.653	3.765	2.841	2.765
100	5.463	3.685	2.795	2.718
200	5.270	3.603	2.749	2.671
300	5.074	3.521	2.702	2.623
400	4.875	3.437	2.655	2.575
500	4.673	3.353	2.607	2.527
600	4.467	3.268	2.559	2.478
700	4.259	3.181	2.510	2.429
800	4.048	3.094	2.462	2.380

cooling rate, and then compared at the same T and P below T_g, have different volumes), implies that configurational volume does not determine relaxation time, and hence does not determine T_g. This is equivalent to saying that whatever ordering parameter is associated with free volume does not take a constant value independent of formation pressure (for fixed cooling rates).

In view of these remarks specification of any property of a glass requires knowledge both of the present observables (T and P) and the thermodynamic history by which the glass was formed. For example, when isobaric cooling at constant rate $k=-dT/dt$ is used to form the glass, any property may be expressed in terms of the arguments T, P, P', and k, where T and P are the present values and P' and k specify the history. A generalized equation of state for a glass formed in this manner would be $v=v(T, P, P', k)$. For isothermal compression at constant rate the corresponding arguments would be T, P, T', and $c=dP/dt$, where T' is the formation temperature.

4.2. Evaluation of T_g and T_g^* With Corresponding Properties

As stated in the Introduction T_g and T_g^* are defined as the temperature at the intersection of the liquid and appropriate glass surfaces in PVT space, where T_g is obtained from the variable formation glass (a), and T_g^* is obtained from either of the constant formation glasses (b or c). T_g^* will of course take on different values for the two glasses. In general for these histories, the above definitions imply that at the intersection temperature $T(\Delta V=0)$, where $\Delta V=V_l-V_g$,

$$T(\Delta V=0)=T_g^*(P, P'),$$

and

$$T(\Delta V=0)=T_g(P), \text{ when } P=P'.$$

Accordingly, $T_g=T_g^*$ only when $P=P'$, as is always true with the variable formation history (a). Since T_g is a function of only one independent variable (since the cooling rate was the same in all cases) T_g appears to be unique while T_g^* is not.

The temperature of intersection for each history may be obtained by equating the right-hand sides of the two forms of eq (5) with appropriate coefficients for liquid and glass taken from table 6. The solution for T_g or T_g^* is quadratic in P, but only one branch is appropriate in the physical sense over the experimental pressure range. These transitions are illustrated by the solid lines with negative slopes in figures 4, 5, and 6. Other pressure dependent properties may thus be obtained at the intersection from the appropriate manipulation of these equations with $T=T_g$ (or T_g^*) without resorting to numerical or graphical methods, as is often done using the Tait Equation.

Quach and Simha [8] have used an interesting approach to define and determine glass transition temperatures from their data on polystyrene. They used two methods to evaluate these characteristic temperatures from the same set of data, which were obtained using the following procedure. Commencing in the liquid region, the sample was cooled isobarically at atmospheric pressure at a rate of 10 °C/h to some terminal temperature T_i. At T_i the procedure was changed to isothermal compression at approximately 400 bar/h. This procedure was repeated at successively lower values of T_i. Accordingly, for values of $T_i<T_g(O)$, the glass was formed by isothermal compression and $T_g(P)$ was defined from the pressure at which the derivative of the compressibility went through a maximum along isotherm T_i. They call the glass obtained from the data at pressures above that for the compressibility slope maximum, the "high pressure glass." In the other case ($T_i<T_g(P)$), where the glass is formed at atmospheric pressure, $T_g(P)$ (their definition) was defined from the intersection of liquid and glass surfaces. They call this glass the "low pressure glass."

In making the comparison between the terminology used in their and our work, Quach and Simha's "high pressure glass" is nearly analogous to our "variable formation glass." It turns out that T_g determined from the maximum in compressibility slope nearly corresponds to that from the liquid glass surface intersection obtained from the same data. Accordingly, their "high pressure glass" is formed by isothermal compres-

sion at different temperatures whereas our "variable formation glass" is obtained by isobaric cooling at different pressures. Both of these histories produce glasses with varying structure. Their "low pressure glass" corresponds directly to our "constant formation at atmospheric pressure," with their "low pressure" T_g corresponding to our T_g^*.

The values of T_g and T_g^* and other properties at these conditions as functions of pressure for these histories are given in table 9. These properties include the specific volume v, liquid and glass thermal expansivities α_l and α_g and compressibilities β_l and β_g or β_g^*. In keeping with the convention used by Goldstein [9] the * used in connection with the compressibility indicates that it is not a proper thermodynamic property. In this work β_g^* designates the apparent compressibility for the "variable formation glass (a)" which is not a single physical substance. As stated earlier a corresponding distinction is not necessary for the thermal expansivity when the glass is formed by isobaric cooling at constant rate. Also included in table 9 are $\Delta\alpha=\alpha_l-\alpha_g$, $\Delta\beta$ (or $\Delta\beta^*$) $=\beta_l-\beta_g$ (or β_g^*), and dT_g/dP (or $dT_g^*/dP=\Delta\beta/\Delta\alpha$ [9]).

Since a constant rate of cooling was used, T_g or T_g^* may be specified uniquely as functions of the present pressure P and formation pressure P'. The transition map shown in figure 7 gives T_g and T_g^* as a function of P with parameter P'. As pointed out in section 4.2 the variable formation history a, is the only one for which it is always true that $P=P'$. The values of dT_g/dP and dT_g^*/dP differ by nearly a factor of two. The fact that these curves do not intersect at precisely 0 and 800 bar is an artifact resulting from the statistical treatment of the data. The three curves were evaluated from three different sets of data for which glasses a and b have common specific volume values at atmospheric pressure, and a and c, at 800 bar. The corresponding intersections on figure 7 occur at these

TABLE 9. *Transition parameters*

(a) Variable Formation Glass

P	T_g	v	$\alpha_l \times 10^4$	$\alpha_g \times 10^4$	$\Delta\alpha \times 10^4$	$\beta_l \times 10^5$	$\beta_g^* \times 10^5$	$\Delta\beta^* \times 10^5$	dT_g/dP	$T_g\Delta\alpha$
bar	°C	cm³/g	°C⁻¹	°C⁻¹	°C⁻¹	bar⁻¹	bar⁻¹	bar⁻¹	°C/bar	
0	31.50	0.84358	7.118	3.031	4.088	4.990	3.902	1.088	0.0266	0.1245
100	34.08	.84098	6.997	3.000	3.996	4.838	3.834	1.003	.0251	.1228
200	36.53	.83840	6.850	2.969	3.881	4.690	3.766	.924	.0238	.1202
300	38.85	.83585	6.685	2.937	3.748	4.543	3.696	.848	.0226	.1169
400	41.05	.83334	6.509	2.904	3.606	4.397	3.624	.773	.0214	.1133
500	43.13	.83085	6.328	2.869	3.459	4.249	3.552	.697	.0202	.1094
600	45.08	.82839	6.148	2.834	3.314	4.098	3.478	.620	.0187	.1055
700	46.86	.82596	5.973	2.797	3.176	3.942	3.403	.539	.0170	.1016
800	48.46	.82355	5.807	2.759	3.048	3.780	3.326	.454	.0149	.0980

(b) One Atmosphere Glass

P	T_g^*	v	$\alpha_l \times 10^4$	$\alpha_g \times 10^4$	$\Delta\alpha \times 10^4$	$\beta_l \times 10^5$	$\beta_g \times 10^5$	$\Delta\beta \times 10^5$	dT_g^*/dP [a]	$T_g^*\Delta\alpha$
bar	°C	cm³/g	°C⁻¹	°C⁻¹	°C⁻¹	bar⁻¹	bar⁻¹	bar⁻¹	°C/bar	
0	30.68	.84309	7.117	2.795	4.322	4.981	2.896	2.085	0.0482	0.1313
100	35.42	.84177	6.996	2.771	4.225	4.856	2.880	1.976	.0468	.1304
200	40.05	.84042	6.840	2.740	4.100	4.743	2.869	1.874	.0457	.1284
300	44.57	.83905	6.664	2.704	3.960	4.637	2.864	1.773	.0448	.1258
400	49.00	.83765	6.480	2.662	3.818	4.532	2.864	1.668	.0437	.1230
500	53.29	.83620	6.300	2.614	3.686	4.420	2.868	1.552	.0421	.1203
600	57.39	.83468	6.136	2.559	3.576	4.298	2.877	1.421	.0397	.1182
700	61.20	.83308	5.998	2.499	3.499	4.158	2.889	1.270	.0363	.1170
800	64.61	.83137	5.894	2.433	3.461	3.999	2.903	1.096	.0317	.1169

(c) 800 Bar Glass

P	T_g^*	v	$\alpha_l \times 10^4$	$\alpha_g \times 10^4$	$\Delta\alpha \times 10^4$	$\beta_l \times 10^5$	$\beta_g \times 10^5$	$\Delta\beta \times 10^5$	dT_g^*/dP [a]	$T_g^*\Delta\alpha$
bar	°C	cm³/g	°C⁻¹	°C⁻¹	°C⁻¹	bar⁻¹	bar⁻¹	bar⁻¹	°C/bar	
0	14.75	.83361	7.085	2.944	4.141	4.849	2.833	2.016	.0487	.1192
100	19.44	.83240	7.010	2.918	4.092	4.668	2.809	1.860	.0454	.1197
200	23.87	.83115	6.885	2.890	3.996	4.511	2.783	1.728	.0433	.1187
300	28.12	.82986	6.726	2.861	3.865	4.371	2.756	1.615	.0418	.1164
400	32.25	.82856	6.542	2.832	3.711	4.244	2.728	1.516	.0409	.1133
500	36.30	.82726	6.348	2.802	3.546	4.126	2.700	1.425	.0402	.1097
600	40.29	.82596	6.153	2.771	3.382	4.010	2.672	1.338	.0396	.1060
700	44.21	.82466	5.968	2.741	3.228	3.894	2.643	1.251	.0388	.1024
800	48.02	.82335	5.804	2.709	3.095	3.773	2.614	1.159	.0374	.0994

[a] $\frac{dT_g^*}{dP}=\frac{\Delta\beta}{\Delta\alpha}$.

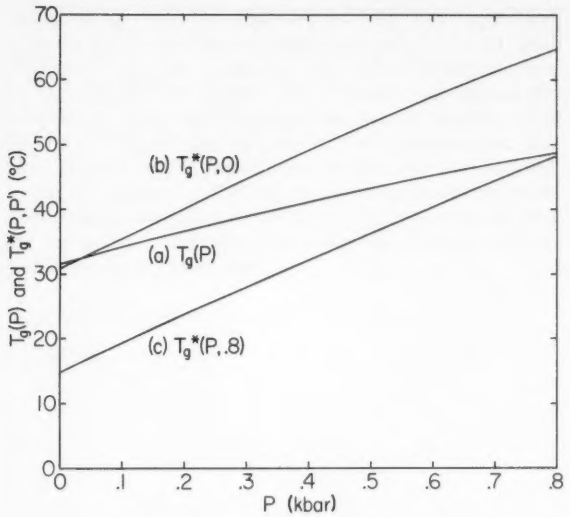

FIGURE 7. *Transition map showing* T_g *and* T_g^* *versus pressure for histories (a) variable formation* ($P'=P$), *(b) glass formed at atmospheric pressure* ($P'=0$), *and (c) glass formed at 800 bar* ($P'=800$).

values, within the 95 percent confidence limits on T_g and T_g^* (see sec. 4.6).

From a comparison of the specific volumes at T_g or T_g^* in table 9, it is seen that the constant formation histories produce a more nearly constant volume "transition" than the variable formation one. The fact is clearly evident through comparison of figures 5 and 6 with 4.

Simha and Boyer [31] have proposed a free volume model which rationalizes the observation that the quantity $T_g\Delta\alpha$ is nearly constant for different polymers. Accordingly, it appears to be appropriate to consider the constancy of $T_g\Delta\alpha$ and, possibly, $T_g^*\Delta\alpha$ over pressure for any given polymer. The values given in table 9 tend to decrease with pressure. The variation for $T_g^*\Delta\alpha$ is 11 percent (history b) compared with 21 percent for $T_g\Delta\alpha$ (history a). Similar behavior with increasing pressure was observed for polystyrene [32].

The Simha-Boyer Relation can be tested more sensitively also be examining its prediction of dT_g/dP. This has been done by Goldstein [9] using the data of this paper: the result is an over-estimate of dT_g/dP by a factor of nearly 3.

4.3. T_g and the Isoviscous State

It has been asserted that the dilatometric T_g as observed in this study corresponds, for any given liquid, to that temperature at which a characteristic value of viscosity is attained. According to Turnbull [33], a common value for the steady flow shear viscosity for simple liquids where it has been measured at T_g, is 10^{15} P. At elevated pressures the value of T_g will increase as required to maintain the isoviscous state.

With our variable formation history (a) from which we define $T_g(P)$, the intersection of the liquid and glass PVT surfaces will occur at a temperature at which a mean volume relaxation time corresponds to the effective experimental time. This will of course depend upon the rate of isobaric cooling. Since all of the volume isobars were obtained at the same rate of cooling, T_g may be viewed upon as the temperature for constant average volume relaxation time. Accordingly, since there is very little distinction between the values of average shear and volume relaxation times at the same conditions [45], and since the relative temperature and pressure dependences of the compressibilities are small in comparison to those for shear viscosity $T_g(P)$ (from the variable formation history) should be a resonable approximation to an isoviscous state.

Although the above assumption is plausible, it is not to be understood as an exact relationship. On the other hand, there is an independent experimental confirmation [2, 6, 34] in view of the fact that our values of dT_g/dP are in close agreement with those obtained from the shift in characteristic temperatures with pressure at constant frequency obtained through time-temperature-pressure superposition of both dielectric and dynamic mechanical data. $(\partial T/\partial P)_\omega$ has been shown to approximate the isorelaxation time or isoviscous state from both phenomenological and molecular models.

4.4. "Permanent" Densification of the Glass and T_g^* Depression

As seen from comparing the glass data of the two constant formation histories b and c, a "permanent" densification of the glass results from increasing the formation pressure. Although these glasses are not in true equilibrium, they are taken to be in pseudo-equilibrium, or as having a fixed (nonrelaxing) structure, over an observable time scale. At very long times, however, significant relaxations may occur at temperatures in the proximity of T_g. Densification has been observed on poly(methyl methacrylate) by Kimmel and Uhlmann [35] at pressures up to 50 kbar. However, at no time was the formation pressure applied entirely in the liquid region. In their work pressures were so high that permanent densification could be obtained by applying pressure in the glass. In our work no irreversible response was observed in the glass at temperatures well below T_g.

The densification effect is illustrated in figure 8 where the 0 and 800 bar curves are taken from each of figures 4 and 5 (constant formation histories b and c). The effect of increasing the formation pressure P' is to produce a permanent decrease in the specific volume of the glass with a corresponding decrease in $T_g^*(P,P')$ for a given value of P.

In this application for constant rate of cooling the densification rate (with respect to formation pressure), may be defined as

$$\beta'(T,P,P') = -\frac{1}{V}\left(\frac{\partial V}{\partial P'}\right)_{T,P},$$

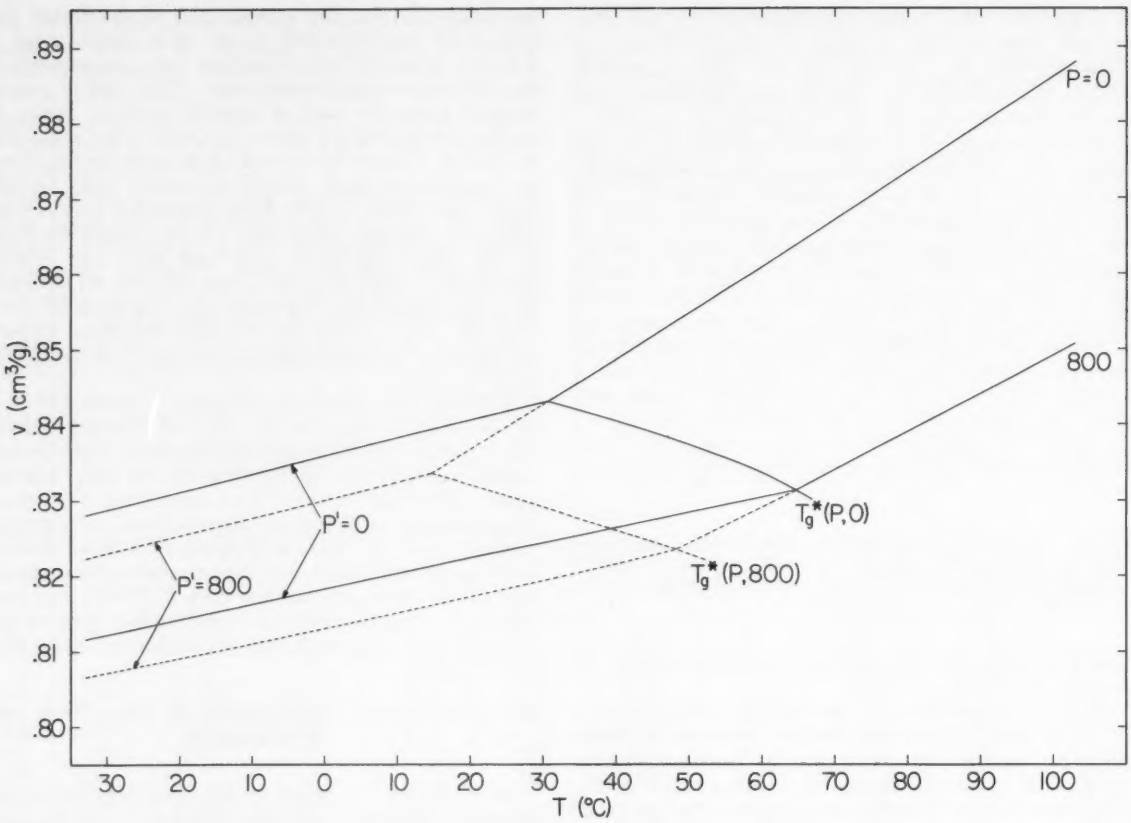

FIGURE 8. *Illustration of densification and* T_g^* *depression from elevated formation pressures. Specific volume versus temperature at atmospheric pressure and 800 bar for constant formation histories* (*b*) $P'=0$ *and* (*c*) $P'=800$ *bar.*

which is analogous in form to the isothermal compressibility

$$\beta(T, P, P') = -\frac{1}{V}\left(\frac{\partial V}{\partial P}\right)_{T,P'} .$$

Since we have a complete description of the glass at only two values of P' (0 and 800 bar), the average of β' over P' is

$$\beta' = \frac{2[v(T, P, 0) - v(T, P, 800)]}{800[v(T, P, 0) + v(T, P, 800)]} .$$

Using the values $v(0, 0, 0) = 0.83586$ and $v(0, 0, 800) = 0.83003$ cm³/g from eq (5) with appropriate coefficients from table 6 gives $\beta' = 0.88 \times 10^{-5}$ bar^{-1}. This value may be compared to the corresponding isothermal compressibility $\beta = 2.81 \times 10^{-5}$ which is the average for histories b and c at $P=0$.

With the pressure induced densification there is a corresponding pressure induced T_g^* depression, $(\partial T_g^*(P, P')/\partial P')_P$ for which the average value over P' at $P=0$ is $[T_g^*(0, 800) - T_g^*(0, 0)]/800$. Taking the values of T_g^* at $P=0$ for histories b and c gives an average value of

$$\left(\frac{\partial T_g^*(0, P')}{\partial P'}\right)_P = \frac{14.75 - 30.68}{800} = -0.020 \text{ °C/bar} .$$

Note that $T_g^*(P, P')$ is increased by increasing the present pressure, but decreased by increasing the formation pressure.

As evident from figure 8 increasing the formation pressure P' produces a permanent densification and corresponding depression of the intersection temperature in a manner similar to that which would be obtained by appropriately increasing the rate of cooling k. These effects are compared schematically in figure 9, which illustrates volume-temperature curves at atmospheric pressure for the two cases: (a) that obtained from isobaric cooling at 5 °C/h at the two formation pressures, atmospheric and 800 bars, and (b) that obtained from isobaric cooling at atmospheric pressure at the two cooling rates, 5 °C/h and k_1 necessary to obtain the same value for the intersection temperature as with the 800 bar formation pressure in (a), i.e., $T_g(0, k_1) = T_g^*(0, 800, 5)$. Note that, in accordance with our convention including different constant

cooling rates, the functions T_g and T_g^* are expressed here in terms of their arguments as $T_g(P, k)$ and $T_g^*(P, P', k)$. For simplicity the volume-temperature curves on the two figures are taken to be identical; however, it is recognized that there may be some difference between the slopes of these curves for the glass formed at 800 bar (glass B) and the one formed at rate k_1 (glass C). (There is no distinction between glass A in (a) and glass A in (b).) In figure 9b the dashed line for glass C indicates behavior which could not be evaluated from these data.

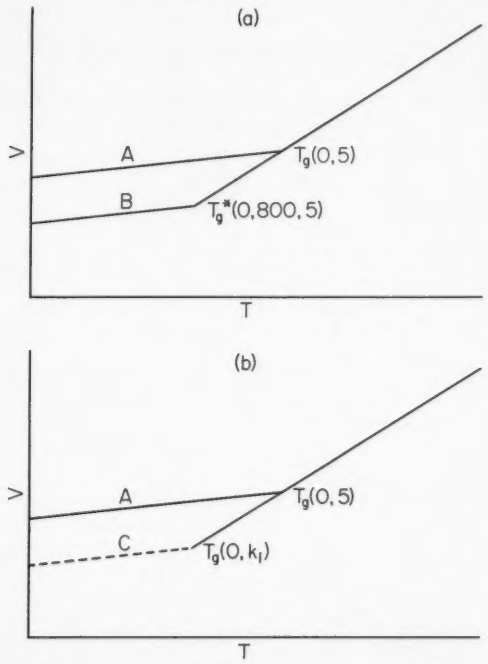

FIGURE 9. *Schematic volume-temperature diagram illustrating identical volumes of glasses at* $T_g(P, k)$ *and* $T_g^*(P, P', k)$ *obtained from (a) isobaric cooling at 5 °C/h at formation pressures, 0 (Glass A) and 800 bar (Glass B), and (b) from isobaric cooling at atmospheric pressure at rates 5 °C/h (Glass A) and* k_1 *(Glass C) necessary for* $T_g^*(0, 0, 5) = T_g(0, k_1)$.

The dashed line indicates behavior which could not be evaluated from these data.

We wish to estimate the value of k_1 necessary to make $T_g(0, k_1) = T_g^*(0, 800, 5)$ for glasses B and C, respectively. Although the validity of the WLF Equation [36]

$$\log a_T = -\frac{T - T_g}{2.303 f_g (f_g/\alpha_f + T - T_g)} \tag{6}$$

is questionable at temperatures below T_g, it may be used to obtain a crude estimate of k_1. In eq (6) T_g is the nominal pseudoequilibrium value at atmospheric pressure which may be taken to be equal to our $T_g(0, 5)$, a_T is the ratio of relaxation times at an arbitrary temperature T to those at T_g, f_g is the free volume fraction f at T_g, and α_f is the temperature coefficient of f. Taking $f_g = 0.028$ and $\alpha_f = 4.4 \times 10^{-4}$ °C^{-1} from reference [37] and $T - T_g = -16$ °C, which is the value obtained from these data by taking $T_g(0, k_1) - T_g(0, 5) = T_g^*(0, 800, 5) - T_g^*(0, 0, 5)$, gives the value of $\log a_T = 5.2$.

Assuming that the ratio of cooling rates is equal to $1/a_T$ gives a rate of 3×10^{-5} °C/h compared to our 5 °C/h rate. According to this model a formation pressure of 800 bar over a period of 10 h (60 to 10 °C at 5 °C/h) produces the same effect on the glass as a constant rate of cooling over 200 years at atmospheric pressure.

Although equal volumes in the glass at the same conditions can be obtained from vastly different histories, as indicated from the example above, this fact does not imply that the thermodynamic states, and hence all properties at the same volumes at the same conditions will be identical for different histories. From the Lorentz-Lorenz Equation, it is expected that increasing the density will result in a corresponding increase in the refractive index. Accordingly, it appears possible to produce glasses with higher refractive indices by increasing the formation pressure in lieu of commensurately decreasing the rate of cooling. On the other hand relaxation times for glasses of a given configurational volume obtained by slow rates of cooling would be expected to be much longer than those formed by increasing the formation pressure but keeping cooling rate constant. Since the Second Ehrenfest Relation,

$$\frac{dT_g}{dP} = \frac{TV\Delta\alpha}{\Delta C_p}, \tag{7}$$

appears to hold for most glasses examined, its obedience implies a single entropy surface for glasses obtained from different formation pressures [9]. Obedience to eq (7) does not imply, however, that there will be a single entropy surface for glasses formed at different rates of cooling. The fact that longer relaxation times are produced by cooling at a slower rate than commensurately increasing P' is related to the apparent dominance of entropy over volume in determining relaxation times. A liquid cooled under a high pressure has a lower configurational volume than one cooled at lower pressures, even though the volume relaxation time is the same for both at their respective T_g's. To prepare a liquid by cooling at low pressure with the same volume as that achieved by high pressure cooling, one must cool very slowly, meaning that the T_g corresponds to a much longer relaxation time than the high pressure experiment. Accordingly, it appears that a more stable glass may be produced by decreasing the rate of cooling in lieu of commensurately increasing the formation pressure to obtain the same volume.

Related to the above argument is the possibility of approaching the hypothetical ground state by increasing the formation pressure. According to a theory of Gibbs and DiMarzio [38] there exists a ground state reached at temperature $T_2 > 0$ at which the configura-

533-558 OL - 74 - 3

tional entropy vanishes. The theory predicts that there will be a corresponding equilibrium second order transition at T_2 which, in principle, could be reached by an infinitely slow rate of cooling. From observation of figures 9a and 9b, for which the volume-temperature response is identical, one might expect to approach T_2, and hence the ground state, by sufficiently increasing the formation pressure in lieu of decreasing the rates of cooling to values which would be impractical to attain experimentally. This possibility appears to be precluded by the apparent existence of a single entropy surface as mentioned in the last paragraph. Thus increasing the formation pressure would not enable us to come closer to the ground state, unless the relation (7) does not hold at higher pressures, or in other words, unless constant entropy does not imply constant relaxation time.

4.5. Evaluation of the First Ehrenfest Relation and Its Role in Time-Temperature-Pressure Superposition

The *PVT* data obtained here can be used to test the validity of the First Ehrenfest Relation

$$\frac{dT_2}{dP}=\frac{\Delta\beta}{\Delta\alpha} \tag{8}$$

where T_2, here, is a second order transition temperature at which the free energy surfaces of two distinct thermodynamic phases are tangent along the transition line in *PVT* space. $\Delta\beta$ and $\Delta\alpha$ are the differences between the compressibilities and thermal expansions for the two states. The problem here is to determine the corresponding properties applicable to the glass transition and to test if eq (8) is true or not.

The evaluation of the properties that appear in eq (8) may be better realized through consideration of figure 10, which gives a schematic representation of all the *PVT* surfaces obtained comprising the liquid, variable formation (a), glass formed at atmospheric pressure (b), and glass formed at 800 bar (c). For simplicity all surfaces are represented by planes. The intersection designated by T_2 indicates the possibility of the existence of an equilibrium, second order transition as predicted from the theory of Gibbs and DiMarzio mentioned earlier. As indicated by figure 10, the surfaces are continuous through liquid-glass intersections as shown. The extension of the liquid surface to lower temperatures (or higher pressures) may be realized by conducting the experiments at sufficiently long time scales, as is illustrated in figure 5. In turn, extensions of the glass surfaces, may be realized through sufficiently rapid increases in temperature (or decreases in pressure) commencing in the glassy state. The glass surface extensions are very unstable, however, because of the very short viscoelastic relaxation times at these conditions, nevertheless they can be experimentally realized through, for example, ultrasonic techniques.

It has been shown by Passaglia and Martin [39], see also Goldstein [9], that if the quantities $\Delta\beta/\Delta\alpha$ or dT_g/dP are obtained by defining their values from 2 surfaces intersecting in 3 dimensional space, the equation will be true tautologically. To test it in a nontrivial sense is equivalent to asking if the surfaces in *PVT* space corresponding to glasses formed under different pressures coincide to form a single surface or not. If they had coincided the following relationships would apply

$$\Delta\beta=\Delta\beta^*$$

$$dT_g/dP=dT_g^*/dP$$

and

$$dT_g/dP=\Delta\beta/\Delta\alpha=\Delta\beta^*/\Delta\alpha.$$

Since however, our results show that the glass surfaces in *PVT* space do not coincide, it follows that

$$\frac{dT_g}{dP}\neq\frac{\Delta\beta}{\Delta\alpha}, \tag{9}$$

although

$$\frac{dT_g^*}{dP}=\frac{\Delta\beta}{\Delta\alpha} \quad \text{and} \quad \frac{dT_g}{dP}=\frac{\Delta\beta^*}{\Delta\alpha}. \tag{10}$$

It is possible to evaluate both terms of ineq (9) at the two points A and B (fig. 10) directly from these data. These are the triple intersection points for the (liquid-glass a-glass b) and (liquid-glass a-glass c) surfaces. (The points A and B correspond to the intersections shown on fig. 7 at 0 and 800 bar.) At point A, dT_g/dP is evaluated from the liquid-glass a intersection line, whereas $\Delta\beta/\Delta\alpha$ is evaluated from the liquid-glass b intersection line. Taking the value at $P=0$ from table 9a, we find $dT_g/dP=0.027$ °C/bar; and from the value of dT_g^*/dP at $P=0$ from table 9b and applying eq (10), we find $\Delta\beta/\Delta\alpha=0.048$. Similarly at point B (800 bar) the appropriate values are taken from tables 9a and 9c which give $dT_g/dP=0.015$ and $\Delta\beta/\Delta\alpha=0.037$. Accordingly, these data confirm that ineq (9) may be replaced by a stronger one which is obeyed here at both $P=P'=0$ and 800 bar:

$$\frac{dT_g}{dP}<\frac{\Delta\beta}{\Delta\alpha}. \tag{11}$$

Our average (over pressure) value, $dT_g/dP=0.021$, obtained from our variable formation history at $P=0$, is in close agreement with the value $(\partial T/\partial P)_\omega=0.020$ from dynamic compressibility measurements [34] and $(\partial T/\partial P)_\omega=0.022$ from dielectric measurements [6], on poly(vinyl acetate).

The fact that both sides of ineq (11) decrease markedly with increasing pressure suggests that dT_g/dP may vanish at a finite pressure. This possibility is also apparent in reference [32] on polystyrene data over a wider pressure range. According to the data, values of $\Delta\beta$ at T_g are nearly linear with T_g from which an extrapolation gives $\Delta\beta=0$ at a finite T_g corresponding to finite pressure. Also from dynamic compressibility

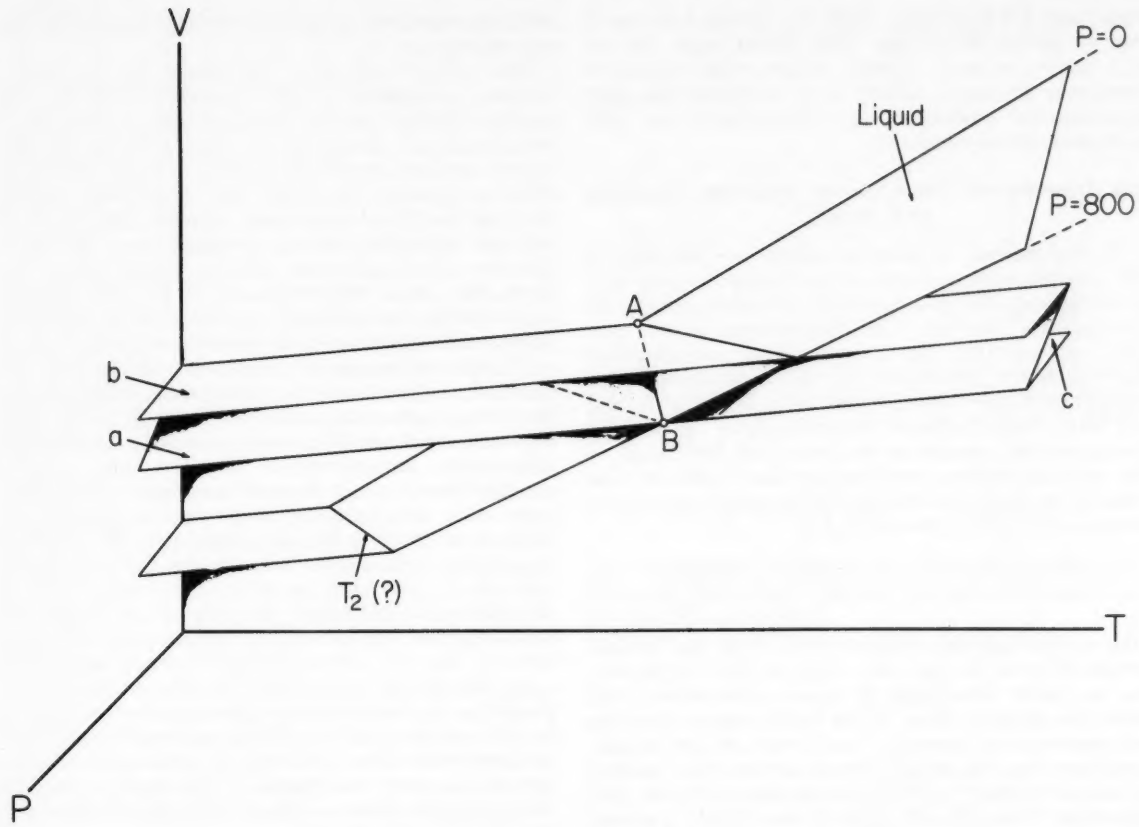

FIGURE 10. *Schematic diagram illustrating liquid and glass surfaces a (variable formation), b (glass formed at atmospheric pressure), and c (glass formed at 800 bar) in* PVT *space.*

data on poly(vinyl acetate) [34], linear extrapolations of ΔB, the difference between high- and low-frequency limiting adiabatic compressibilities, which correspond to $\Delta\beta$, predict that this quantity vanishes at a finite pressure. Upon considering the data in this paper, from which we evaluate $\Delta\beta$ and $\Delta\alpha$ at T_g at the two points as given above, we find that $\Delta\beta$ at 800 bar is down 44 percent from its value at atmospheric pressure, whereas the corresponding value of $\Delta\alpha$ is down only 28 percent. This might suggest that $\Delta\beta$ could vanish while $\Delta\alpha$ remains finite. However a relation of thermodynamic stability among $\Delta\beta$, $\Delta\alpha$ and ΔC_p places restrictions on this possibility:

$$\Delta\beta \geq \frac{TV\Delta\alpha^2}{\Delta C_p}$$

so that unless ΔC_p approaches infinity while $\Delta\alpha$ remains finite, $\Delta\beta$ cannot approach zero. Since there is no reason to expect this behavior of ΔC_p, the behavior of $\Delta\beta/\Delta\alpha$ cannot be what is inferred from the 0–800 bar data, and experiments must be performed at higher pressures to find out what will happen.

The evaluation of ineq (11) as given earlier in this section reveals a contradiction with respect to the free volume theory [2] as applied to time-temperature-pressure superposition, for which the characteristic temperatures are those approximating the isoviscous state. The free volume theory stipulates that the viscosity η is a single valued function of the free volume fraction which may be written explicitly in terms of the present temperature and pressure by

$$f = f_g + \alpha_f(T - T_{g0}) - \beta_f P \tag{12}$$

where T_{g0} is the value of T_g at atmospheric pressure. If the coefficients α_f and β_f are assumed to be given respectively by $\Delta\alpha$ and $\Delta\beta$, substitution in eq (12), followed by differentiation with respect to P at constant η (which is equivalent to constant f, since η is a single valued function of f) gives

$$\left(\frac{\partial T}{\partial P}\right)_\eta = \frac{\Delta\beta}{\Delta\alpha}. \tag{13}$$

Since T_g may be taken to be the characteristic temperature for the isoviscous state, the above result is in apparent contradiction with in eq (11) for which the

right- and left-hand sides differ by nearly a factor of two as shown from these data. Accordingly, the eq (13) implies a single volume surface with respect to formation pressure, which is in contradiction with experimental evidence. This discrepancy has also been noted by Goldstein [9].

4.6. Experimental Uncertainties Including Estimates on T_g and T_g^*

In the absence of spurious effects the precision of the specific volume should depend upon the precision in measuring the experimental variables, which are temperature, pressure, and displacement of the mercury column. From the manufacturer's specifications the maximum deviations of the measurements of temperature and pressure are given as ±0.25 °C and ±2 bar. From replicate determinations on a fixed menincus the maximum deviations on the height of the mercury column were found to be ± 0.002 cm. The relative precision (as determined by maximum relative deviation) may be approximated by

$$\left|\frac{\delta v}{v}\right| = \left|\frac{a_{10}\,\delta T}{a_{00}}\right| + \left|\frac{a_{01}\,\delta P}{a_{00}}\right| + \left|\frac{\pi r^2 \delta h}{W_s}\right| \qquad (14)$$

where the capillary radius $r = 0.1$ cm. the sample weight $W_s = 6.27$g and the values of the coefficients a_{ij} are taken from table 6. These uncertainties will have the greatest effect in the liquid region since the temperature and pressure coefficients are the largest. Applying eq (14) to the liquid region, the relative precision is $\delta v/v = \pm 0.028$ percent, for which the contributions from δT, δP, and δh are ±0.017 percent, ±0.010 percent, and ±0.001 percent, of which the last is nearly insignificant. For the glasses the values of $\delta v/v$ decrease to (a) variable formation, ±0.016 percent; (b) glass formed at atmospheric pressure, ±0.014 percent; and (c) glass formed at 800 bar, ±0.014 percent.

An alternative approach to evaluating the relative precision is to make use of the residual variation of the quadratic regression. (See Sec. 4.1.) The relative precision (as determined by relative standard deviation) of the specific volume may be approximated by $s/|a_{00}|$ where s is the estimated standard deviation of the residuals of the quadratic regression. It is noted that both of these methods are dependent upon the validity of the quadratic model. Also, it must be remembered that the maximum deviation and standard deviation usually differ by a factor between 2.0 and 2.5. The value of $s/|a_{00}|$ for the liquid is 0.013 percent, and the values for the glasses are (a) 0.009 percent, (b) 0.009 percent, and (c) 0.008 percent. The ratios of the precisions determined from maximum deviations to those by standard deviations vary from 2.2 for the liquid to 1.5 for glass b. The fact that these ratios are slightly smaller than expected indicates that the maximum deviations assumed for the experimental observables are too small, or that some unknown spurious effect was present. The latter could be a manifestation of irreversible expansion of the dilatometer with pressure and temperature, which is possible, but not expected.

The relative precision (as measured by relative standard deviation) of the thermoexpansivities and compressibilities may be approximated by $\delta a_{10}/|a_{10}|$ and $\delta a_{01}/|a_{01}|$, respectively, where δa_{ij} is the estimated standard deviation of a_{ij}. For the liquid these relative standard deviations are 1.6 percent and 5.6 percent. For the glasses these values decrease to 0.42 percent and 0.44 percent averaged over the three histories. No explanation has been proposed to explain the large difference (4-fold for the thermoexpansivities and 12-fold for the compressibilities) between the corresponding values from liquid to glass.

The thermal expansion at atmospheric pressure was checked independently by hydrostatic weighing over the temperature range of 35–70 °C. At 40 °C the value obtained was down 3.6 percent from the corresponding dilatometer determination. However, the relative standard deviation in thermal expansion obtained by hydrostatic weighing was 7.8 percent compared with 1.6 percent given in the last paragraph. The principal reason for such a large value of the former was the difficulty in obtaining good temperature control at the higher temperatures. In view of the larger uncertainties with the hydrostatic weighing, the difference between the two determinations is hardly significant.

As pointed out in section 2.2, a correction was included in the formulation leading to eq (4) to account for the expansion of the dilatometer with temperature and pressure. This correction is small, and is often ignored by many investigators. Neglecting to include this correction gives a value for the thermal expansion at 40° and atmospheric pressure which is down 2.2 percent.

The accuracy of the specific volume measurements depends upon several sources of possible systematic error, or bias: the experimental observables given above, the reference specific volume determination (Sec. 2.3), mercury and glass expansion values (Sec. 2.2b), capillary bore and length measurements, weighings, and inhomogeneous dilatometer expansion.

Calibrations on temperature and pressure detecting apparatus showed that their systematic errors were small in comparison to their maximum deviations given above. Also measurements and calculations on the mercury and glass expansion values, capillary bore and length measurements, and weighings indicate that their contributions are negligible relative to those from the random deviations in temperature and pressure. Little is known about irregularities in the expansion characteristics of dilatometers; however, the expansion with temperature and pressure is generally believed to be homogeneous, and any possible contribution from inhomogeneous expansion is assumed to be minimal, or insignificant.

The contribution from the specific volume reference determination, apparently, is nonnegligible. An error in the reference value would bias all of the values obtained from the dilatometer measurements. The reference value was obtained by the usual hydrostatic

weighing procedure. As a result of water absorption by the sample, replicate measurements are difficult and time-consuming. Based on only three determinations at 40 °C (0.8488, 0.8485, and 0.8489 cm^3/g) the average 0.8487 cm^3/g was used as the reference value. Although statistics from only three values may not give results as reliable as desired, they do appear to have some utility, and appear to be reasonable, in this case. The average value has an estimated standard deviation and relative standard deviation of 0.00012 and .014 percent, respectively. A 95 percent confidence interval for the relative systematic error is $\pm 4.3 \times 0.014\% = \pm 0.060$ percent. Thus the overall relative accuracy is estimated to be $\pm (0.060\% + 2.0 \times 0.028\%) = \pm 0.116$ percent based on a relative precision of ± 0.028 percent for the liquid and an estimated bound of ± 0.060 percent on the systematic error. The factors 4.3 and 2.0 are the 97.5 percent points of the Students t distribution [40] with 101 and 2 degrees of freedom, respectively. The large factor 4.3 used in determining the systematic error bound results from only three available replicate determinations. In view of large sample to sample variations in polymers, in general, the bias factor 0.060 percent given above is not considered excessive. Similar calculations on the glass values will give slightly smaller values for their overall relative accuracy.

Since the relative uncertainties of the thermoexpansivities and compressibilities are large in comparison to those for the specific volume, they are not significantly influenced by errors in the reference determination. Accordingly, there should be no significant distinction between the imprecision and total uncertainty of these two quantities.

The uncertainty in T_g, (or T_g^*) which results from the uncertainties in the positions of the liquid and glass surfaces in PVT space, is one of the more useful, but one of the most difficult to evaluate. A statistical method giving the confidence limits on the intersection of the two quadratic surfaces used here would be extremely difficult to apply. In references [41, 42] methods are described which give the abscissca of the intersection of two linear regressions. These methods may be applied here to determine the confidence limits on T_g (or T_g^*) using paired linear regressions (liquid and glass) of the form $v = a + bT$ along each isobar. A FORTRAN Program for this calculation and examples are contained in reference [42].

The information required for these calculations consists of liquid-glass pairs of the following quantities: N, the number values; a, the intercept; b, the slope; $\bar{T}$, the average temperature; s, the standard deviation of the residuals of v; and

$$S^2 = \sum_{i=1}^{N} (T_i - \bar{T})^2.$$

Using the equal variance assumption, the confidence limits T^+ and T^- are the solutions of the quadratic equation

$$T^{\pm} = \frac{-B \pm \sqrt{B^2 - 4AC}}{2A}$$

where

$$A = (b_l - b_g)^2 - S_p^2 G^2 \left(\frac{1}{S_l^2} + \frac{1}{S_g^2} \right)$$

$$B = 2(a_l - a_g)(b_l - b_g) + 2S_p^2 G^2 \left(\frac{\bar{T}_l}{S_l^2} + \frac{\bar{T}_g}{S_g^2} \right)$$

$$C = (a_l - a_g)^2 - S_p^2 G^2 \left(\frac{1}{N_l} + \frac{1}{N_g} + \frac{\bar{T}_l^2}{S_l^2} + \frac{\bar{T}_g^2}{S_g^2} \right)$$

where G is the 97.5 percent point of the t distribution with N_p degrees of freedom (see [40], for example), where $N_p = N_l + N_g - 4$, and the pooled variance, S_p^2, is defined as

$$S_p^2 = \frac{1}{N_p} \left[s_l^2 (N_l - 2) + s_g^2 (N_g - 2) \right].$$

The subscripts l and g pertain to the liquid and glass as usual. (Note that $\bar{T}_g$ here is not to be confused with the glass temperature.)

It is interesting to observe that the midpoint,

$$\frac{T^+ + T^-}{2} = -\frac{B}{A},$$

is nearly the same as, but not identical to, the estimate of T_g (or T_g^*) obtained from

$$T_g = -\frac{a_l - a_g}{b_l - b_g},$$

which is obtained by equating the two linear regressions. These two quantities are identical, however, in the limit $S_p \to 0$.

The results of this analysis are displayed in figure 11 where the 95 percent confidence bands are shown encompassing the estimated values of T_g or T_g^* as functions of pressure for the three histories. The values of T_g and T_g^* are taken from table 9 (shown also on fig. 7). The confidence bands, centered about T_g and T_g^*, are taken from the quadratic regressions of the calculated values of $\Delta T = T^+ - T^-$ with respect to pressure. The smoothed confidence bands shown on figure 11 range from 0.88 to 3.64 °C over the three histories. It was mentioned in section 4.2 that although the values of T_g and T_g^* are evaluated from the same sets of data for histories a and b at atmospheric pressure, and a and c at 800 bar, the intersections of the estimated values for which $T_g = T_g^*$ do not occur precisely at these pressures for the reason given. As seen from figure 11, however, the 95 percent confidence bands do overlap at 0 and 800 bar.

An additional reason for the inclusion of this figure is to illustrate how the proximity of the specific volume data to the estimated values of T_g or T_g^* influences their uncertainty. This effect is most clearly seen by curve

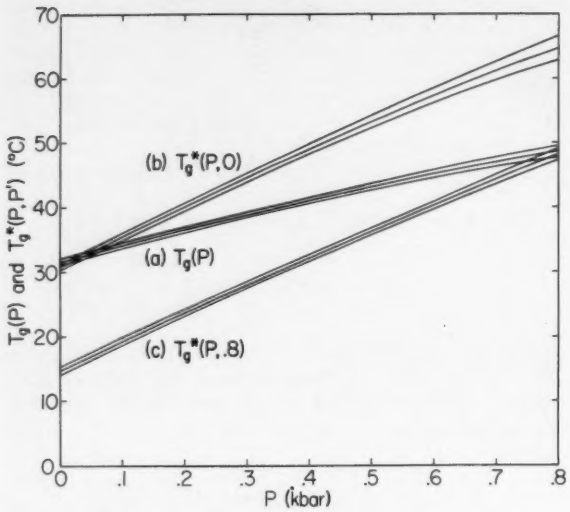

FIGURE 11. *Transition map showing estimated values of* T_g *and* T_g^* *and 95 percent confidence limits versus pressure for histories* (*a*) $P'=P$, (*b*) $P'=0$, *and* (*c*) $P'=0.8$ *kbar.*

b for which the specific volume data are displayed on figure 5. No problem arises from the proximity of the liquid data; however, with the glass there is a large region immediately below T_g^* for which there are no experimental data. At atmospheric pressure the difference between the estimated value of T_g^* and the closest experimental temperature in the glass is 10.68 °C. At 800 bar this difference increases to 54.61 °C. The confidence bands over this pressure range correspondingly go from 1.10 to 3.64 °C. This behavior illustrates the importance of obtaining data in the proximity of T_g (or T_g^*) in order to obtain an accurate estimate.

5. Concluding Remarks

The thermodynamic history by which a glass is formed has considerable influence on its structure and corresponding properties, as confirmed by the results of these experiments. The role of thermodynamic history was manifested by significant changes in the apparent glass temperature (T_g or T_g^*) the second order properties, and "permanent" densification.

In addition to the principal, or glass transition (sometimes referred to as α transition), observed in this work, secondary transitions, often called β transitions, have been reported from *PVT* measurements on certain polymers. The α transitions for amorphous polymers are taken to be manifestations of restrictions on the mobility of polymer chains, or long segments of the chains. The β transitions are attributed to restrictions on the mobility of short chain segments, or side group rotations. The *PVT* measurements of Quach and Simha [8] on polystyrene have revealed a β transition appearing within the glassy region with $dT_\beta/dP=65.3$ °C/kbar. This value falls between the values of dT_g/dP for their "low" and "high pressure" glasses. In our work there was some suspicion that the wide temperature range of observable relaxations using the constant formation history b ($P'=0$) could be attributed to a β process. The observed relaxations were responsible for the absence of reported data at temperature immediately below T_g^* in figure 5. As pointed out in section 3.3, there was much less difficulty in obtaining pseudoequilibrium data immediately below T_g^* using history c ($P'=800$ bar). From this information one might attribute the wide temperature range of observed relaxation with history b to a β process which would become "frozen in" at higher pressures. This could result from a large dT_β/dP as reported by Quach and Simha for which the α and β transitions would tend to merge at higher pressures.

On the other hand the evidence given by McCrum, Read, and Williams [43] precludes the possibility of a β transitions occurring within our experimental range. They give a log f (Hz) versus $1/T$ plot for the β relaxation taken from various dynamic data. Using the dashed curve of their figure 9.4 estimated to be of the form $\log f=13.3-2.1\times10^{-3}/T$, and using a conservative estimate of $\log f=-3$ gives a value of $T_\beta=-145$ °C, which is well below our experimental range (−30 to 100 °C). With a similar plot for polystyrene [44] estimated to be of the form, $\log f=25.2-8.0\times10^{-3}/T$, and using the same value of $\log f$ gives $T_\beta=11$ °C. The value obtained from extrapolating the *PVT* data of Quach and Simha to atmospheric pressure gives $T_\beta=3$ °C. Aside from other possible discrepancies, the difference between these values indicates that our choice of the value of $\log f$ was too conservative. Accordingly, this evidence would appear to preclude the possibility of a β transition being observed over our experimental range. As stated in section 3.3, the difficulty in obtaining pseudoequilibrium data close to T_g^* for history b apparently arises from the manner in which the data were observed.

With respect to the First Ehrenfest Relation (eq (8), Sec. 4.5), it should be remembered that this relation may be considered to be a tautology when applied to liquid-glass systems using the apparent values of the second order properties, obtained from the data, which are not necessarily the proper thermodynamic ones. If the proper thermodynamic properties are used the First Ehrenfest Relation fails for the isoviscous state, and must be replaced by its corresponding inequality

$$\frac{dT_g}{dP}<\frac{\Delta\beta}{\Delta\alpha}. \tag{11}$$

Obedience of ineq (11) is tantamount to higher densities with increasing formation pressures, as illustrated by these experiments. This result has been shown to be in contradiction with the free volume theory. The fact that the volume of a glass decreases with the formation pressure, and the entropy, apparently, does not (which is tantamount to the satisfaction of ineq (11) and eq (7)), supports an entropy rather than a volume basis for the transition or relaxation processes.

The results of these and related experiments have

technological importance. With highly densified glasses one would expect corresponding increases in cohesive energy density giving harder and stronger glasses along with larger refractive indices.

Note added in proof: From graphical C_p data [46] on poly(vinyl acetate) taken through T_g a value of $\Delta C_p = 0.097$ cal/g-K (0.405j/g-K) is obtained at $T = T_g$. Applying this value to eq (7) gives for the right-hand side 0.027 °C/bar, which is in agreement with our value of dT_g/dP at atmospheric pressure. (See table 9a.) This result confirms the validity of eq (7), which implies the existence of a single entropy surface with respect to formation pressure for this polymer.

The authors acknowledge and appreciate the assistance from H. V. Belcher and M. R. Brockman in obtaining these data, from J. J. Filliben in statistical analysis, and from R. S. Marvin in planning this work and for suggestions in preparing this manuscript.

6. References

[1] Gee, G., Contemp. Phys. **11**, 313 (1970).
[2] Ferry, J. D., Viscoelastic Properties of Polymers, Chapt. 11 (John Wiley and Sons, New York, 1970).
[3] Kovacs, A. J., J. Polymer Sci. **30**, 131 (1958).
[4] Bianchi, U., Turturro, A., and Basile, G., J. Phys. Chem. **71**, 3666 (1967).
[5] Matsuoka, S., and Maxwell, B., J. Polymer Sci. **32**, 131 (1958).
[6] O'Reilly, J. M., J. Polymer Sci. **57**, 429 (1962).
[7] Hellwege, K. H., Knappe, W., and Lehmann, P., Kolloid Z. und Z. für Polymere **183**, 110 (1963).
[8] Quach A., and Simha, R., J. Appl. Phys. **42**, 4592 (1971).
[9] Goldstein, M., J. Phys. Chem. **77**, 667 (1973).
[10] Martin, G. M., and Mandelkern, L., J. Appl. Phys. **34**, 2312 (1963).
[11] McKinney, J. E., and Penn, R. W., Rev. Sci. Instr. **43**, 1211 (1972).
[12] Forsythe, W. E., Smithsonian Physical Tables, p. 152, Smithsonian Institution, Washington, D.C. (1954).
[13] Bridgman, P. W., Am. J. Sci. **10**, 359 (1925).
[14] Carnazzi, P., Nuovo Cimento **5**, 180 (1903).
[15] See for example, Tanford, C., Physical Chemistry of Macromolecules (Wiley and Sons, New York, 1961), p. 407.
[16] Kurata, M., Iwana, M., and Kamada, K., in Polymer Handbook, Ed. Broadrup, J., and Immergut, E. H. (Interscience, New York, 1966, Section 4), p. 16.
[17] Burrel, H. and Immergut, E. H., in reference 46, Section 4, p. 347.
[18] Fox, T. G., Gratch, S., and Loshaek, S., in Rheology, F. R. Eirich, Ed., Vol. **I**, Chapt. 12 (Academic Press, New York, 1956).
[19] Fox, T. G., and Loshaek, S., J. Poly. Sci. **15**, 371 (1955).
[20] Magill, J. M., J. Appl. Phys. **35**, 3249 (1964).
[21] Ref. [2], p. 519.
[22] Bauer, N., in Physical Methods of Organic Chemistry, A. Weissberger, Ed., Vol. **I**, Chapt. 6 (Interscience, New York, 1949).
[23] Standard Density and Volumetric Tables, Circular of the Bureau of Standards, No. 19 (1924).
[24] Goldbach, G., and Rehage, G., J. Polymer Sci., Part C, **16**, 2289 (1967).
[25] Tait, P. G., Physics and Chemistry of the Voyage of the H. M. S. Challenger (University Press, Cambridge, 1900), Vol. **II**, Part IV, Scientific Papers LXI, Vol. **II**, p. 1 (1888).
[26] Wood, L. A., Polymer Letters **2**, 703 (1964).
[27] Gee, G., Polymer **7**, 177 (1966).
[28] Hilsenrath, J., Ziegler, G. G., Messina, C. G., Walsh, P. J., and Herbold, R. J., OMNITAB, a computer program for statistical and numerical analysis, Nat. Bur. Stand. (U.S.), Handb. 101, 93 pages (April 1968).
[29] Draper, N. R., and Smith, H., Applied Regression Analysis (John Wiley and Sons, New York, 1966), p. 71.
[30] Davies, R. O., and Jones, G. O., Adv. Phys. **2**, 370 (1953).
[31] Simha, R., and Boyer, R. F., J. Chem. Phys. **37**, 1003 (1962); Boyer, R. F., and Simha, R., Polymer Letters Edition **11**, 33 (1973).
[32] Boyer, R. F., in Styrene polymers, R. F. Boyer, Ed., Ency. Polymer Sci. and Tech. Vol. **13**, 1970, p. 297.
[33] Turnbull, D., Contemp. Phys. **10**, 473 (1969).
[34] McKinney, J. E. and Belcher, H. V., J. Res. Nat. Bur. Stand. (U.S.), **67A** (Phys. and Chem.), No. 1, 43–53 (Jan.–Feb. 1963).
[35] Kimmel, R. M., and Uhlman, D. R., J. Appl. Phys. **41**, 2917 (1970).
[36] Reference [2], p. 314.
[37] Reference [2], p. 316.
[38] Gibbs, J. H., and DiMarzio, E. A., J. Chem. Phys. **28**, 373 (1958).
[39] Passaglia, E., and Martin, G. M., J. Res. Nat. Bur. Stand. (U.S.), **68A** (Phys. and Chem.), No. 3, 273–276 (May–June 1964).
[40] Beyer, W. H., Ed., Handbook of Probability and Statistics, p. 82, Chemical Rubber Co., Cleveland, 1966.
[41] Kastenbaum, M. A., Biometrics **15**, 323 (1959).
[42] Filliben, J. J. and McKinney, J. E., J. Res. Nat. Bur. Stand. (U.S.), **76B** (Math. Sci.), Nos. 3 & 4, 179–192 (July–Dec. 1972).
[43] McCrum, N. G., Read, B. E., Williams, G., Anelastic and Dielectric Effects in Polymeric Solids, (Wiley and Sons, New York, 1967), p. 304.
[44] Ibid, p. 414.
[45] Marvin, R. S., and McKinney, J. E., in Physical Acoustics, W. P. Mason, Ed., (Academic Press, New York, N.Y., 1965, Vol. **2B**, Chapt. 9).
[46] Vol'kenshtein, M. V., in Structure of Glass, Vol. 2, Consultants Bureau, New York, 1961, p. 111 (Translation).

JOURNAL OF RESEARCH of the National Bureau of Standards—A. Physics and Chemistry
Vol. 78A, No. 3, May–June 1974

Correction and Extension of van der Poel's Method for Calculating the Shear Modulus of a Particulate Composite

Jack C. Smith

Institute for Materials Research, National Bureau of Standards, Washington, D.C. 20234

(January 28, 1974)

Van der Poel's method (Rheol. Acta **1**, 198 (1958)) for calculating the shear modulus of a particulate composite agrees well with experimental data, but its validity has been questioned, and it was applicable only to composites in which the matrix material is incompressible. These limitations are removed in this paper in which an error in the original derivation is corrected, and the method generalized to apply to any matrix material. Calculations using the corrected theory show that despite the error, a table of shear modulus values published with the original theory is sufficiently correct for most practical purposes. Applicability of the generalized method to the large class of composites having compressible matrices is discussed. Shear moduli calculated by the corrected and extended method are compared with corresponding values calculated by other methods currently used.

Key words: Bulk modulus; composite materials; elastic constants; filled polymers; mechanical properties; particulate composites; shear modulus; theory of elasticity.

1. Introduction

Consider an idealized composite material consisting of small spheres imbedded in a matrix. The spheres are of approximately the same size, are firmly attached to the matrix, and are uniformly distributed so that the composite material is macroscopically homogeneous and isotropic. An important question then arises—that of calculating the two mechanical moduli characterizing this material in terms of the moduli characterizing the filler spheres and the matrix.

Several solutions have been given to this problem. The best known ones are those of Hashin and Shtrikman [1],[1] Kerner [2], and Budiansky [3]. Hashin and Shtrikman's formulae, which provide upper and lower bounds for the shear and bulk moduli of the composite as a function of filler content, are: for the highest lower bound (HLB),

$$G = G_m + \frac{\varphi_f}{\dfrac{1}{G_f - G_m} + \dfrac{6(K_m + 2G_m)\varphi_m}{5G_m(3K_m + 4G_m)}} \tag{1}$$

$$K = K_m + \frac{\varphi_f}{\dfrac{1}{K_f - K_m} + \dfrac{3\varphi_m}{3K_m + 4G_m}} \tag{2}$$

for the lowest upper bound (LUB),

$$G = G_f + \frac{\varphi_m}{\dfrac{1}{G_m - G_f} + \dfrac{6(K_f + 2G_f)\varphi_f}{5G_f(3K_f + 4G_f)}} \tag{3}$$

$$K = K_f + \frac{\varphi_m}{\dfrac{1}{K_m - K_f} + \dfrac{3\varphi_f}{3K_f + 4G_f}}. \tag{4}$$

In these formulae G represents the shear modulus, K bulk modulus, and φ volume fraction, the subscripts f and m refer to the filler and matrix respectively.

Kerner's formulae, although derived by a different method, can be shown by algebraic manipulation to be the same as those for Hashin and Shtrikman's highest lower bound (1, 2).

Budiansky provides the pair of coupled implicit equations:

$$\frac{1}{G} = \frac{1}{G_m} + \left(1 - \frac{G_f}{G_m}\right)\frac{\varphi_f}{G + \beta(G_f - G)} \tag{5}$$

$$\frac{1}{K} = \frac{1}{K_m} + \left(1 - \frac{K_f}{K_m}\right)\frac{\varphi_f}{K + \alpha(K_f - K)} \tag{6}$$

where

$$\alpha = \frac{3K}{3K + 4G} \tag{7}$$

and

$$\beta = \frac{6(K + 2G)}{5(3K + 4G)} \tag{8}$$

[1] Figures in brackets indicate the literature references at the end of this paper.

Young's modulus E and Poisson's ratio ν can be calculated from the well known expressions:

$$E=\frac{9KG}{3K+G} \tag{9}$$

$$\nu=\frac{3K-2G}{6K+2G}. \tag{10}$$

In van der Poel's solution [4], for which excellent agreement with experimental data is claimed [4, 5], the formula for K can be shown to be the same as eq (2), but the calculation for G is too complicated to be expressed conveniently in closed form. Van der Poel has treated the special case in which the matrix of the composite has a Poisson's ratio $\nu=0.5$. The value of G is obtained by interpolation from a table of values he has provided. It would be useful to have a formula applicable when the matrix has any value for Poisson's ratio. This was the purpose of the present work. During its progress an error was discovered in van der Poel's solution. The corrected form is given along with details of the derivation.

2. Derivation

The derivation is based on a method developed by Fröhlich and Sack [6].

To simplify calculations consider a unit length chosen such that on the average there is one sphere of filler in each spherical volume $4\pi/3$ of unit radius. If a is the radius of the filler sphere, then by definition of the unit radius, a^3 is equal to the volume fraction φ_f of the filler.

Consider a large cube of homogeneous material with edges parallel to the axes of a cartesian coordinate system having its origin at the center. Consider also a second cube in which the region at the center has the following structure: A filler sphere of radius a is located at the origin. Surrounding this out to a radius unity is a sphere of matrix material which in turn is imbedded in the homogeneous material. The mechanical properties of this homogeneous material are assumed to be the same as the average macroscopic properties that are sought for the composite material considered here.

If the same boundary stresses are applied to each of the cubes, it is assumed that the displacements in the two cubes are the same at a distance $r=R\gg 1$ except for terms of a high order in $1/r$. In the second cube the influence of the structure within the radius $r=1$ on the displacement at $r=R$ is expected to be of the same order as the ratio of the two volumes, i.e., $\sim 1/R^3$. Thus it will be required that

$$\frac{\text{Displacement at } r=R \text{ in second cube}}{\text{Displacement at } r=R \text{ in first cube}} = 1+\sum_{n>3}\frac{\text{const}}{R^n}. \tag{11}$$

Let the cube of homogeneous material (first cube) be subjected to the deviatoric stress system

$$\sigma_x=\sigma_y=-T,\ \sigma_z=2T,\ \tau_{xy}=\tau_{yz}=\tau_{zx}=0 \tag{12}$$

where the σs represent tensile and the τs shear stresses. Assuming Hooke's law, it is easily seen that this stress system gives rise to the following displacements u_x, u_y, u_z within the material;

$$u_x=-\frac{T(1+\nu)x}{E}=-\frac{Tx}{2G},\ u_y=-\frac{Ty}{2G},\ u_z=\frac{Tz}{G}. \tag{13}$$

In spherical polar coordinates the components of stress and displacement are obtained by transformation as

$$\sigma_r=2TP_2(\operatorname{Cos}\theta),\ \tau_{r\theta}=TP_2'(\operatorname{Cos}\theta),\ \tau_{r\varphi}=0 \tag{14}$$

$$u_r=\frac{Tr}{G}P_2(\operatorname{Cos}\theta),\ u_\theta=\frac{Tr}{2G}P_2'(\operatorname{Cos}\theta),\ u_\varphi=0 \tag{15}$$

where $P_2(\operatorname{Cos}\theta)$ is the second Legendre polynomial and $P_2'(\operatorname{Cos}\theta)$ is its derivative with respect to θ.

$$\begin{aligned} P_2(\operatorname{Cos}\theta)&=\tfrac{1}{2}(3\operatorname{Cos}^2\theta-1),\\ P_2'(\operatorname{Cos}\theta)&=-3\operatorname{Cos}\theta\operatorname{Sin}\theta. \end{aligned} \tag{16}$$

In order to find the displacements in the cube containing the special spherical structure at the center (second cube), it is necessary to find appropriate solutions to Lamé's equations expressed in spherical polar coordinates. These equations are tabulated by Love [7]. Because of symmetry of the stress system about the z axis, the displacements u_r and u_θ are independent of the azimuthal angle φ, and the displacement $u_\varphi=0$. Lamé's equations thus simplify to

$$\begin{aligned} &(\lambda+2G)\operatorname{Sin}\theta\frac{\partial\Delta}{\partial\theta}+2G\frac{\partial}{\partial r}(r\omega_\varphi\operatorname{Sin}\theta)=0\\ &(\lambda+2G)r\operatorname{Sin}\theta\frac{\partial\Delta}{\partial r}-2G\frac{\partial}{\partial\theta}(\omega_\varphi\operatorname{Sin}\theta)=0 \end{aligned} \tag{17}$$

where according to Love [8] the dilatation Δ is given by

$$\Delta=\frac{1}{r^2\operatorname{Sin}\theta}\left\{\frac{\partial}{\partial r}(r^2u_r\operatorname{Sin}\theta)+\frac{\partial}{\partial\theta}(ru_\theta\operatorname{Sin}\theta)\right\} \tag{18}$$

and the rotation ω_φ by

$$\omega_\varphi=\frac{1}{2r}\left\{\frac{\partial}{\partial r}(ru_\theta)-\frac{\partial}{\partial\theta}u_r\right\} \tag{19}$$

Lamé's constant λ is given by

$$\lambda=\frac{2G\nu}{1-2\nu}. \tag{20}$$

The most general solution having the same P_2 symmetry as the displacement system (15) is obtained by setting $u_r = r^\beta P_2\ (\mathrm{Cos}\ \theta)$, $u_\theta = \alpha r^\beta P_2'\ (\mathrm{Cos}\ \theta)$ in eqs (17) to (19), and substituting for λ using eq (20) to obtain the set of linear homogeneous equations in α:

$$[(1-2\nu)(\beta+1)\beta-12(1-\nu)]\alpha+[\beta+4(1-\nu)]=0$$
$$[-3\beta+9-12\nu]\alpha+[(1-\nu)(\beta+1)\beta-5+8\nu]=0. \tag{21}$$

In order that these equations be compatible, it is necessary that

$$\frac{\beta+4(1-\nu)}{(1-2\nu)(\beta+1)\beta-12(1-\nu)} = \frac{(1-\nu)(\beta+1)\beta-5+8\nu}{-3\beta+9-12\nu} \tag{22}$$

or, after simplification

$$(\beta-1)(\beta+2)(\beta-3)(\beta+4)=0 \tag{22}$$

The value of α corresponding to each root of eq (22) is found by substituting into eq (21). The solutions for u_r and u_θ thus become.[2]

$$u_r=[Ar+Br^{-4}+Cr^3+Dr^{-2}]P_2(\mathrm{Cos}\ \theta) \tag{23}$$

$$u_\theta=\left[\frac{1}{2}Ar-\frac{1}{3}Br^{-4}+bCr^3+cDr^{-2}\right]P_2'(\mathrm{Cos}\ \theta) \tag{24}$$

where

$$b=\frac{7-4\nu}{12\nu},\ c=\frac{1-2\nu}{5-4\nu} \tag{25}$$

and A, B, C, D are constants.

The strains e_{rr} and $e_{r\theta}$ are found from the relations

$$e_{rr}=\frac{\partial}{\partial r}u_r,\ e_{r\theta}=\frac{\partial}{\partial r}u_\theta-\frac{u_\theta}{r}+\frac{1}{r}\frac{\partial}{\partial\theta}u_r \tag{26}$$

and the stresses necessary for the solution are then calculated using

$$\sigma_r=\frac{2G\nu}{1-2\nu}+2Ge_{rr},\ \tau_{r\theta}=Ge_{r\theta} \tag{27}$$

to obtain [2]

$$\sigma_r=2G[A-4Br^{-5}+k_1Cr^2+k_3Dr^{-3}]P_2(\mathrm{Cos}\ \theta) \tag{28}$$

$$\tau_{r\theta}=G\left[A+\frac{8}{3}Br^{-5}+k_2Cr^2+k_4Dr^{-3}\right]P_2'(\mathrm{Cos}\ \theta) \tag{29}$$

where

$$k_1=-\frac{1}{2},\ k_2=\frac{7+2\nu}{6\nu},\ k_3=-\frac{2(5-\nu)}{5-4\nu},$$
$$k_4=\frac{2(1+\nu)}{5-4\nu}. \tag{30}$$

Within the filler sphere $r \leq a$ the requirement that the displacement be zero at the origin necessitates that $B_f = D_f = 0$, where the subscript f refers to the filler medium. The solution applicable in the region $a \leq r \leq 1$ involves the constants A_m, B_m, C_m, D_m where the subscript m refers to the matrix medium. Within the region $1 \leq r \leq R$ requirement (11) necessitates that $A = T/G$, $C = D = 0$. A must be regarded as an unknown constant as it involves the shear modulus G, the quantity which is to be calculated.

At the boundaries $r=a$ and $r=1$ the radial and tangential components of the displacement and the stress must be continuous. This gives rise to the following set of linear homogeneous equations in the unknowns A_f, C_f, A_m, B_m, C_m, D_m, A, B.

$$MA_f-\frac{1}{2}Ma^2C_f-A_m+4a^{-5}B_m+\frac{1}{2}a^2C_m-k_{3m}a^{-3}D_m=0$$
$$MA_f+Mk_{2f}a^2C_f-A_m-\frac{8}{3}a^{-5}B_m-k_{2m}a^2C_m-k_{4m}a^{-3}D_m=0$$
$$aA_f+a^3C_f-aA_m-a^{-4}B_m-a^3C_m-a^{-2}D_m=0$$
$$\frac{1}{2}aA_f+b_fa^3C_f-\frac{1}{2}aA_m+\frac{1}{3}a^{-4}B_m-b_ma^3C_m-c_ma^{-2}D_m=0.$$
$$A_m-4B_m-\frac{1}{2}C_m+k_{3m}D_m+4NB-NA=0$$
$$A_m+\frac{8}{3}B_m+k_{2m}C_m+k_{4m}D_m-\frac{8}{3}NB-NA=0$$
$$A_m+B_m+C_m+D_m-B-A=0$$
$$\frac{1}{2}A_m-\frac{1}{3}B_m+b_mC_m+c_mD_m+\frac{1}{3}B-\frac{1}{2}A=0 \tag{31}$$

where

$$M=G_f/G_m,\ N=G/G_m. \tag{32}$$

In order that the solution be nontrivial the determinant of the coefficients must be set equal to zero. Solving the resulting equation will evaluate the shear modulus of the material G, which is the quantity desired.

[2] For an incompressible material ($\nu=0.5$) van der Poel's solution agrees with the solution obtained here, but when $\nu \neq 0.5$ the exponents in the terms having coefficients C and D in van der Poel's solution are erroneously given as functions of ν. This error has previously been noted by Hashin [9].

After simplifications the determinantal equation becomes [3]

$$\begin{vmatrix} 2M & -2M\nu_f & -2 & 8 & 2\nu_m & 4(5-\nu_m) & 0 & 0 \\ 0 & 2M(7+5\nu_f) & 0 & -40 & -2(7+5\nu_m) & -72 & 0 & 0 \\ 0 & -(7-10\nu_f) & 0 & -5 & 7-10\nu_m & -9 & 0 & 0 \\ 3 & 7-4\nu_f & -3 & 2 & -(7-4\nu_m) & -6(1-2\nu_m) & 0 & 0 \\ 0 & 0 & 0 & 0 & -14(1-\nu_m)a^{-2} & 48(1-\nu_m)a^3 & 8X & 0 \\ 0 & 0 & 0 & 0 & 0 & -30(1-\nu_m)a^3 & 0 & X \\ 0 & 0 & 1 & a^5 & 2\nu_m a^{-2} & (5-4\nu_m)a^3 & -1 & 0 \\ 0 & 0 & 5 & 0 & 7a^{-2} & 4(4-5\nu_m)a^3 & 0 & 1 \end{vmatrix} = 0 \quad (33)$$

where $X = N - 1 = \dfrac{G}{G_m} - 1.$ (34)

Equation (33) can be expanded into the form

$$AX^2 + BX + C = 0 \quad (35)$$

where

$$\begin{aligned} A = {} & 2(M-1)[M(7+5\nu_f) \\ & +4(7-10\nu_f)][4(7-10\nu_m)(4-5\nu_m)(1-a^3)(1-a^7) \\ & -63a^3(1-a^2)^2] \\ & +280(M-1)(7-10\nu_f)(1-\nu_m)(4-5\nu_m)(1-a^3)a^7 \\ & +60[M(7+5\nu_f) \\ & +4(7-10\nu_f)](1-\nu_m)(7-10\nu_m)(1-a^7) \\ & +2100(7-10\nu_f)(1-\nu_m)^2a^7 \end{aligned} \quad (36)$$

$$\begin{aligned} B = {} & 70(M-1)[M(7+5\nu_f) \\ & +4(7-10\nu_f)](1-\nu_m)[(4-5\nu_m)(1-a^3) \\ & -6a^3(1-a^2)] \\ & +525[M(7+5\nu_f)+4(7-10\nu_f)](1-\nu_m)^2 \\ & +60(M-1)[M(7+5\nu_f) \\ & +4(7-10\nu_f)](1-\nu_m)[10\nu_m a^3(1-a^7) \\ & -7a^5(1-a^5)] \\ & -2100(M-1)(7-10\nu_f)(1-\nu_m)^2a^{10} \end{aligned} \quad (37)$$

$$\begin{aligned} C = {} & -525(M-1)[M(7+5\nu_f) \\ & +4(7-10\nu_f)](1-\nu_m)^2a^3. \end{aligned} \quad (38)$$

One of the roots of eq (35) is negative and is extraneous. The positive root when substituted into eq (34) provides the value of the shear modulus G.

When the volume fraction $\varphi = a^3$ of the filler spheres is small, terms of higher order than a^3 can be neglected. The expressions for A, B, and C become much shorter, and a further simplification results because the term $[M(7+5\nu_f)+4(7-10\nu_f)]$ can be factored from each of these quantities. The solution of eq (35) for this case yields the following approximate formula for G:

$$\frac{G}{G_m} = 1 + \frac{15(1-\nu_m)(G_f - G_m)\varphi}{(8-10\nu_m)G_f + (7-5\nu_m)G_m}. \quad (39)$$

3. Discussion

It can be shown by algebraic manipulation that the formulas (39), (1), (5) and (3) for G can be displayed in the form

$$G = G_m + (G_f - G_m)\Phi = (1-\Phi)G_m + \Phi G_f \quad (40)$$

which, when $\Phi = \varphi$, is the well-known rule of mixtures. For the approximate van der Poel equation (39)

$$\Phi = \frac{(8-10\nu_m)G_m + (7-5\nu_m)G_m}{(8-10\nu_m)G_f + (7-5\nu_m)G_m}\varphi. \quad (41)$$

For Kerner, or Hashin and Shtrikman HLB, (1)

$$\Phi = \frac{(8-10\nu_m)G + (7-5\nu_m)G_m}{(8-10\nu_m)G_f + (7-5\nu_m)G_m}\varphi. \quad (42)$$

For Budiansky (5)

$$\Phi = \frac{(8-10\nu)G + (7-5\nu)G}{(8-10\nu)G_f + (7-5\nu)G}\varphi. \quad (43)$$

For Hashin and Shtrikman LUB (3)

$$\Phi = \frac{(8-10\nu_f)G + (7-5\nu_f)G_f}{(8-10\nu_f)G_f + (7-5\nu_f)G_f}\varphi. \quad (44)$$

[3] The determinant given by van der Poel agrees with the determinant, eq (33), when $\nu_m = 0.5$ except for elements in the second column. These elements in van der Poel's solution are more complicated functions of ν_f.

This display shows that these formulas are all of the same type, and can be interchanged into each other in a certain predictable way.

When the volume fraction of filler φ is very small so that $G \sim G_m$, and $\nu \sim \nu_m$, the values of Φ/φ computed by eqs (41) to (43) are essentially equal. Thus plots of $\Phi = (G-G_m)/(G_f-G_m)$ versus φ for these relations all have the same initial slope. Plots of G/G_m for these relations also have the same initial slope. Thus the initial increases of G/G_m with increasing φ, as calculated by the methods of Hashin and Shtrikman HLB, Kerner, van der Poel, and Budiansky, are the same.

The slope G/G_m computed from the approximate van der Poel formula (39) remains constant as φ increases, but the slope computed by the accurate method (35) is nonlinear because of the complicated dependence on various powers of a the filler sphere radius. The slopes computed using the formula of Kerner, or Hashin and Shtrikman HLB, (1) and Budiansky (5, 6) are also nonlinear, and increase with increasing φ.

When $\nu_m = 0.5$ and $G_f/G_m \gg 1$ as in the case of a gum rubber matrix loaded with rigid filler particles, the shear modulus for small values of φ should obey the equation

$$G = G_m(1+2.5\varphi). \tag{45}$$

This equation is analogous to an equation developed by Einstein [10] for the viscosity of a suspension of rigid spheres in a fluid medium, and has been used to predict reinforcement effects in rubber [11]. Under similar conditions the van der Poel formulae developed here (35), (39) and the formulae of Kerner, or Hashin and Shtrikman HLB, (1) and Budiansky (5, 6) reduce to eq (45). In fact the approximate formula (39) may be considered as a generalized form of eq (45) in which G_f and ν_m are specified in addition to G_m.

In order to calculate G using the formula of Kerner, or Hashin and Shtrikman HLB, (1), it is necessary to know only one of the moduli characterizing the filler material, i.e., G_f. This is in contrast to Budiansky's formulae (5, 6), where elimination of K leads to a relationship for G involving filler moduli G_f and K_f. Similarly for the corrected van der Poel computation (35), two filler moduli G_f and ν_f are required. The corrected van der Poel computation (35) and the formulae of Budiansky (5, 6) thus provide some indication of the relative effectiveness of the distortional (shear modulus) and dilatational (bulk modulus) properties of the filler in determining the shear modulus of the composite. To determine this relative effectiveness, computations were made by the two methods and the results are presented in tables 1 and 2.

In table 1 values of G/G_m calculated from Budiansky's formulae (5, 6) are given, corresponding to various values of filler Poisson's ratio ν_f and the ratio G_f/G_m, for a matrix Poisson's ratio $\nu_m = 0.5$. In the calculations the ratio of the shear or rigidity modulus of the filler to that of the matrix G_f/G_m ranges in value from 10 to 10^5, and from eq (10), the range of ν_f from 0.1 to 0.5 corresponds to a range of the bulk modulus K_f from $(11/12)G_f$ to ∞. The tabulated values show that the relative shear modulus G/G_m (Budiansky) can be strongly dependent upon the rigidity of the filler relative to the matrix G_f/G_m, but is only slightly sensitive to the value of the filler Poisson's ratio ν_f or the bulk modulus K_f.

TABLE 1. G/G_m *for various values of* ν_f *and* G_f/G_m, *calculated according to Budiansky's formulae (5, 6)*

ν_f	G/G_m corresponding to $G_f/G_m = 10$	100	1,000	10,000	100,000
		$\varphi = 0.25$, $\nu_m = 0.50$			
0.10	1.7759	2.4647	2.6428	2.6642	2.6664
.30	1.7861	2.4726	2.6440	2.6644	2.6664
.50	1.7958	2.4787	2.6449	2.6644	2.6664
		$\varphi = 0.50$, $\nu_m = 0.50$			
0.10	3.4855	17.871	146.56	1426.2	14221.
.30	3.5647	19.003	158.64	1548.6	15448.
.50	3.6565	20.143	170.74	1670.8	16671.

TABLE 2. G/G_m *for various values of* ν_f *and* G_f/G_m, *calculated according to the corrected van der Poel equation (35)*

ν_f	G/G_m corresponding to $G_f/G_m = 10$	100	1,000	10,000	100,000
		$\varphi = 0.25$, $\nu_m = 0.50$			
0.10	1.6842	2.0025	2.0490	2.0540	2.0545
.30	1.6843	2.0026	2.0491	2.0540	2.0545
.50	1.6845	2.0027	2.0491	2.0540	2.0545
		$\varphi = 0.50$, $\nu_m = 0.50$			
0.10	3.1083	6.4334	7.8687	8.0738	8.0952
.30	3.1235	6.4888	7.8810	8.0751	8.0953
.50	3.1393	6.5356	7.8909	8.0762	8.0954

Table 2 presents similar results calculated using the corrected van der Poel formula (35). Here again the values of the relative modulus G/G_m are seen to be insensitive to the value of the filler Poisson's ratio. Thus although the Budiansky and corrected van der Poel formulas make use of the value of filler Poisson's ratio in the calculations of G/G_m, the values obtained are insensitive to it, and in this respect these formulas offer little advantage over the formula of Kerner, or Hashin and Shtrikman HLB, in which the value of filler Poisson's ratio is not needed.

Table 3 presents values of G/G_m for various filler volume fractions φ and values of G_f/G_m, computed according to the corrected van der Poel equation (35). In these calculations Poisson's ratio of the filler spheres was $\nu_f = 0.25$, and of the matrix was $\nu_m = 0.5$. If these values are divided by G_f/G_m the resulting values are almost identical with the values of G/G_f given in a

TABLE 3. G/G_m *as a function of* φ *for various values of* G_f/G_m, *calculated according the corrected van der Poel equation (35)*

$\nu_m = 0.50, \nu_f = 0.25$

φ	G/G_m corresponding to $G_f/G_m = 2$	10	20	100	1,000	10,000	100,000
.00	1.0000	1.0000	1.0000	1.0000	1.0000	1.0000	1.0000
.05	1.0363	1.1025	1.1166	1.1296	1.1328	1.1331	1.1332
.10	1.0738	1.2177	1.2504	1.2814	1.2891	1.2899	1.2900
.15	1.1126	1.3499	1.4087	1.4665	1.4813	1.4828	1.4829
.20	1.1529	1.5038	1.6000	1.6998	1.7262	1.7289	1.7292
.25	1.1946	1.6843	1.8350	2.0026	2.0491	2.0540	2.0545
.30	1.2379	1.8962	2.1264	2.4066	2.4901	2.4991	2.5000
.35	1.2825	2.1438	2.4888	2.9606	3.1162	3.1333	3.1350
.40	1.3286	2.4301	2.9376	3.7398	4.0447	4.0798	4.0834
.45	1.3761	2.7559	3.4852	4.8580	5.4924	5.5713	5.5794
.50	1.4249	3.1196	4.1376	6.4759	7.8782	8.0748	8.0953
.55	1.4750	3.5174	4.8898	8.7861	12.031	12.578	12.636
.60	1.5264	3.9448	5.7280	11.948	19.569	21.236	21.423
.65	1.5791	4.3986	6.6336	15.978	33.437	38.824	39.482
.70	1.6332	4.8794	7.5946	20.684	58.323	76.204	78.710
.75	1.6889	5.3937	8.6140	25.740	99.923	159.63	170.20
.80	1.7463	5.9570	9.7226	30.888	160.66	356.81	408.82

similar table by van der Poel [4]. The elements in the second column of the determinantal equation evaluated by van der Poel involved different functions of ν_f than those given in eq (33) of this paper. Evidently van der Poel's results agree with those given in table 3 because of the insensitivity of the method of calculation to values of ν_f.

The way in which results of the corrected van der Poel calculation compare with results calculated by the other methods considered here is illustrated in figures 1 and 2. In the example chosen for figure 1, Poisson's ratio of the matrix is $\nu_m = 0.4$ and the ratio of filler to matrix rigidity is $G_f/G_m = 30$. For those cases in which it is used, the value of Poisson's ratio of the filler is $\nu_f = 0.25$. The plots of relative shear modulus G/G_m versus φ represent the expected shear properties of a series of particulate composites consisting of small glass spheres imbedded in a rigid epoxy matrix.

In the example depicted in figure 2, $\nu_m = 0.5$ and $G_f/G_m = 70{,}000$. When used, $\nu_f = 0.25$. The plots in this case represent the expected shear properties of a series of particulate composites consisting of small glass spheres imbedded in a lightly vulcanized matrix of natural rubber.

For the epoxy matrix composite, figure 1, the predictions of the van der Poel and Kerner, or Hashin and Shtrikman HLB, equations are about the same, but for the rubber matrix composite, figure 2, the predictions of these two formulas are much different. The Budiansky calculation predicts the highest values of G/G_m for both examples.

From assumptions made in the derivation, one should only expect reliable predictions from the van der Poel calculation when the volume fraction of the filler φ is small. However, agreement of the theory with experimental results appears to be good even for large values of the volume fraction of filler. According to van der Poel [4], calculations for the case

$$G_f/G_m = 100{,}000,\ \nu_f = 0.25,\ \nu_m = 0.5$$

are in good agreement for values of φ up to 0.60 with Eilers' [12] experimental values for the relative viscosity of suspensions of bitumin particles in water.

If the values in table 3 corresponding to these van der Poel calculations are compared with Eilers' data, the same degree of agreement is found. In table 3 there is only slight difference between the values for $G_f/G_m = 10^4$ and $G_f/G_m = 10^5$. Therefore the curve in figure 2 of G/G_m versus φ, calculated using $G_f/G_m = 70{,}000$ in the corrected van der Poel formula (35), lies very close to a similar curve that could be plotted from Eilers' data. The curves plotted using Budiansky's formulae and the Kerner, or Hashin and Shtrikman HLB, equation are quite different. It seems then that either eq (35) or van der Poel's original calculation provides the best agreement with Eilers' data.

Schwarzl [5] has studied the mechanical characteristics of composites consisting of NaCl crystals in a rubbery polyurethane matrix. He reports agreement for volume fractions of filler up to $\varphi = 0.50$ between his results and van der Poel's theory using the parameter values $G_f/G_m = 10^4$, $\nu_f = 0.25$, and $\nu_m = 0.50$. The curve in figure 2 calculated from the corrected van der Poel equation provides a good fit to Schwarzl's data, and the other two curves do not fit.

When measurements were made at low temperature so that the polyurethane matrix was in the glassy state, Schwarzl obtained data that could be fit by van der Poel's theory using the parameter values $G_f/G_m = 8.4$, $\nu_f = 0.25$, and $\nu_m = 0.5$. The value of $\nu_m = 0.5$ was used because van der Poel's table had been calculated for this value only. The value of ν_m that should have been used was probably close to $\nu_m = 0.4$. This suggests that values of G/G_m calculated by the van der Poel method are not sensitive to the value of the matrix Poisson's ratio ν_m, so calculations were made to check this.

In table 4 values of G/G_m calculated from the corrected van der Poel equation (35) are given, corresponding to various values of matrix Poisson's ratio ν_m

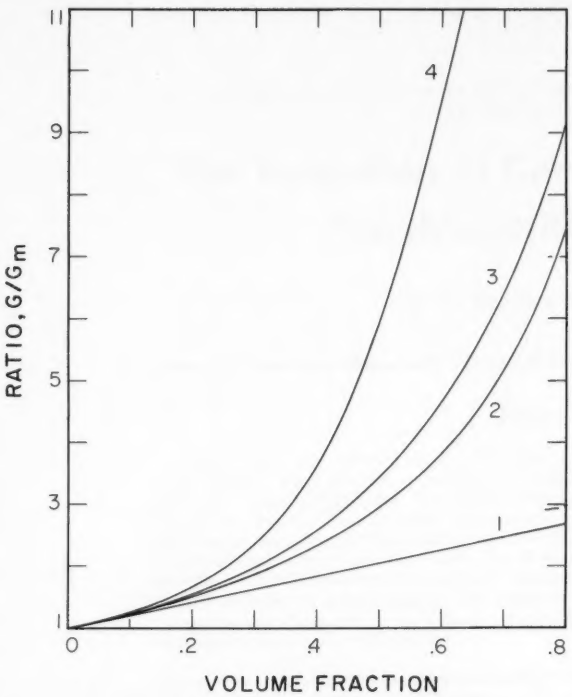

FIGURE 1. *Plot of relative shear modulus* G/G_m *versus volume fraction of filler for the case* $G_f/G_m = 30$, $\nu_f = 0.25$, $\nu_m = 0.40$.

Curve 1, Approximate van der Poel equation (39); 2, equation of Kerner, or Hashin and Shtrikman HLB, (1); 3, corrected van der Poel equation (35); 4, Budiansky's formulae (5, 6).

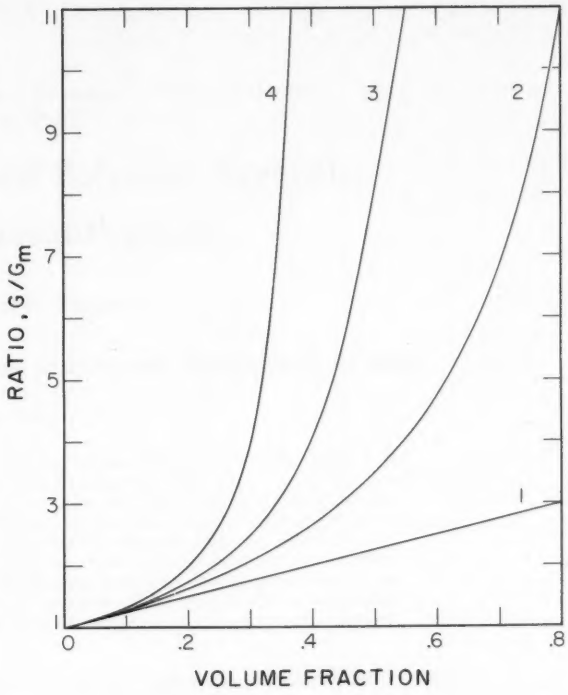

FIGURE 2. *Plot of relative shear modulus* G/G_m *versus volume fraction of filler for the case* $G_f/G_m = 70{,}000$, $\nu_f = 0.25$, $\nu_m = 0.50$.

Curve 1, Approximate van der Poel equation (39); 2, equation of Kerner, or Hashin and Shtrikman HLB, (1); 3, corrected van der Poel equation (35); 4, Budiansky's formulae (5, 6).

TABLE 4. G/G_m *for various values of* ν_m *and* G_f/G_m, *calculated according to the corrected van der Poel equation (35)*

ν_m	G/G_m corresponding to $G_f/G_m = 3$	10	30	100	1,000	10,000
		$\varphi = 0.25$, $\nu_f = 0.25$				
0.30	1.2955	1.5556	1.6747	1.7245	1.7451	1.7472
.40	1.3058	1.5992	1.7445	1.8077	1.8343	1.8371
.50	1.3224	1.6843	1.8982	2.0026	2.0491	2.0540
		$\varphi = 0.50$, $\nu_f = 0.25$				
0.30	1.6928	2.5562	3.0870	3.3470	3.4626	3.4747
.40	1.7156	2.7189	3.4400	3.8359	4.0231	4.0432
.50	1.7542	3.1197	4.7709	6.4759	7.8782	8.0748

and the ratio G_f/G_m, for a filler Poisson's ratio $\nu_f = 0.25$. These calculations show that when $G_f/G_m \sim 10$, changing ν_m from 0.5 to 0.4 changes the value of G/G_m obtained only by a small amount, which approximates the experimental error expected in a measurement. When $G_f/G_m \geq 30$, the change in the calculated value of G/G_m is significant, so that values of G/G_m taken from a table calculated assuming $\nu_m = 0.5$ would not provide a good fit to experimental data. Thus although Schwarzl was able to fit his low temperature data using van der Poel's table, the corrected and extended van der Poel equation (35) would be needed to fit data for a system in which $G_f/G_m \sim 30$, $\nu_m = 0.4$ such as glass spheres imbedded in a rigid epoxy matrix.

4. References

[1] Hashin, Z., and Shtrikman, S., J. Mech. Phys. Solids **11**, 127 (1963).
[2] Kerner, E. H., Proc. Phys. Soc. **B69**, 808 (1956).
[3] Budiansky, B., J. Mech. Phys. Solids **13**, 223 (1965).
[4] van der Poel, C., Rheol. Acta **1**, 198 (1958).
[5] Schwarzl, F. R., Mechanics and Chemistry of Solid Propellants, Proceedings of the Fourth Symposium on Naval Structural Mechanics, edited by A. C. Eringen, H. Liebowitz, S. L. Koh, and J. M. Crowley, (Pergamon Press, New York, N.Y., 1967), p. 503.
[6] Fröhlich, H. and Sack, R., Proc. Roy. Soc. **A185**, 415 (1946).
[7] Love, A. E. H., A Treatise on the Mathematical Theory of Elasticity, 4th ed. (Dover, 1941), p. 141.
[8] Love, A. E. H., loc cit, p. 56.
[9] Hashin, Z., Int. J. Solids Structures **6**, 539 (1970).
[10] Einstein, A., Ann. Physik **17**, 549 (1905); **19**, 289 (1906); **34**, 591 (1911).
[11] Nielsen, L. E., J. Comp. Matls. **1**, 100 (1967).
[12] Eilers, H., Kolloid Z. **97**, 313 (1941).

(Paper 78A3–816)

JOURNAL OF RESEARCH of the National Bureau of Standards—A. Physics and Chemistry
Vol. 78A, No. 3, May–June 1974

The Formation of Curved Polymer Crystals: Polychlorotrifluoroethylene

J. D. Barnes and F. Khoury

Institute for Materials Research, National Bureau of Standards, Washington, D.C. 20234

(January 29, 1974)

The habits and fine structure of crystals of polychlorotrifluoroethylene (PCTFE) grown from dilute solution were studied as functions of crystallization temperature. The solvent used was a low molecular weight PCTFE oil. The simplest crystals found were monolayered chain folded lamellae formed at 110 °C. These lamellae are planar and possess an unusual texture characterized by the presence of fine channel-like voids in the interior of the crystals. These lamellae do not exhibit well-formed crystal faces but are disc-like in overall shape. At lower crystallization temperatures the crystals take the form of complex arrays of curved lamellae which are aggregated into, among others, watchglass-shaped or hollow spherical objects. The variation of the curvature of the crystals with crystallization temperature is discussed in the light of previous studies of the formation of curved crystals of poly(4-methylpentene-1) and polyoxymethylene.

Key words: Crystal morphology; crystallization; electron microscopy; optical microscopy; polychlorotrifluoroethylene; solution crystallization.

1. Introduction

This paper is the third in a series [1, 2] [1] of three dealing with the phenomenon of curved crystal formation in polymers. The investigation we report herein stemmed from our earlier study of the crystallization of poly(4-methylpentene-1) which, as we reported in the first paper of this series [1], led to the observation that lamellar crystals of that polymer were all the more pronouncedly curved the lower the temperature (higher supercooling) at which they were grown from solution. This observation led in turn to the speculation that the manifestation of this phenomenon, rather than being peculiar to P4MP,[2] might be of somewhat more general occurrence among polymers. In order to test this notion we decided to investigate other polymers. In the second paper in this series we reported that a similar phenomenon is manifested in the case of polyoxymethylene [2] crystals grown from solution.

As this paper will demonstrate folded-chain polychlorotrifluoroethylene crystals grown from solution indeed exhibit a habit-supercooling trend which, in its overall phenomenological aspects, parallels those which we have reported for P4MP and POM insofar as the manifestation of curvature and its variation in lamellar crystals grown at different temperatures is concerned. On the fine structural level, however, the character of PCTFE lamellae as a function of supercooling stands in marked contrast to those of P4MP and POM. This latter factor and its bearing on the origins of the dependence of the curvature of the PCTFE crystals on the conditions under which they are grown will be discussed in the light of the conjectures we have previously advanced concerning the origins of the curvature found in crystals of P4MP and POM.

By way of background to our choice of PCTFE for study it should be pointed out that we had no a priori reasons to expect curvature, or variations in curvature as a function of growth conditions, in PCTFE crystals. The choice of PCTFE was simply based on the following considerations. First, we envisaged that if curvature and variations of curvature as a function of growth conditions were manifested in crystals of a polymer, the phenomenon might be expected to manifest itself in a more complex fashion in the case of a polymer whose crystals exhibit several nonequivalent growth faces or which display a marked preference for growth along a crystallographically unique direction. Second, polymers which exist in more than one stable crystallographic phase might also be expected to exhibit more complex manifestations of this phenomenon. In line with this reasoning PCTFE which had been shown to crystallize in a hexagonal unit cell [3–7] and which does not seem to exhibit polymorphism appeared as a suitable candidate for further study, since we

[1] Figures in brackets indicate the literature references at the end of this paper.

[2] For the sake of brevity the names of polymers discussed in this paper will be referred to in an abbreviated form. Thus, the abbreviation for poly(4-methylpentene-1) will be P4MP, while polychlorotrifluoroethylene and polyoxymethylene will be referred to as PCTFE and POM, respectively.

533-558 OL - 74 - 4

could hope to avoid the above-mentioned complications. Third, the study of PCTFE provided the attraction of uncovering some new and more detailed morphological data on the crystallization of this polymer from solution which has hitherto been poorly characterized.

2. Experimental Details

2.1. Preparation of Polymer Solutions

The powdered PCTFE polymer used in this study had a molecular weight estimated at 76,000.[3] The solvent was low molecular weight PCTFE in the form of a light oil (Kel-F Polymer Oil Grade KF-1).[4] This PCTFE oil was vacuum distilled prior to use in order to remove particulate impurities.

In order to obtain solutions with a weight/volume concentration of 0.1 percent, ten milligram quantities of the powdered polymer were placed in test tubes with 10 cm^3 of the PCTFE oil. The tubes were then placed in a stirred oil bath maintained at a temperature of 195 °C for one-half hour. The resulting solutions were then quickly transferred to another bath maintained at the desired crystallization temperature. Crystallization temperatures of 110, 105, 100, and 90 °C were used. Minor variations in the above regimen were necessary in the case of crystallization at 110 °C. These will be described where appropriate in the text.

The onset of crystallization from the solutions (as judged by the initial appearance of cloudiness) occurred over a time span ranging from a day or two in the case of crystallization at 110 °C to a few minutes in the case of crystals precipitated from solutions placed in the 90 °C bath. After crystallization had proceeded for a long time, but before the suspensions were cooled to room temperature, the solvent containing uncrystallized polymer was isothermally replaced with fresh solvent. This replacement was accomplished as follows. First, the suspension was taken from the crystallization bath and quickly poured into a special filtration vessel akin to that described by Bassett et al. [8] situated in a bath which was maintained at the crystallization temperature. The solvent containing unprecipitated polymer was then drawn through the filter until the volume of the suspension was reduced to approximately one-fourth of its original value. Fresh solvent, preheated to the temperature of crystallization, was then added to restore the volume of the suspension to its original value. The process of reducing the volume and adding fresh solvent was then repeated at least three times. The vessel containing the crystals in suspension in fresh solvent could then be cooled to room temperature without any fear that the morphological details of the crystals would be obscured by further precipitation of polymer upon cooling the solution.

2.2. Optical Microscopy

Crystals were examined at room temperature using a phase-contrast optical microscope while they were in suspension in liquid as well as after being allowed to sediment and dry on flat glass slides. For examination of the crystals while in suspension in liquid, glass microscope slides with a shallow central depression were used. In the latter instance, liquids of appropriate refractive index (usually $n = 1.58$) were added to the crystal suspension in order to enhance contrast.

2.3. Electron Microscopy

After the washed suspensions had been cooled to room temperature, droplets containing crystals were deposited on carbon films supported on copper grids and the solvent was allowed to evaporate at room temperature. Electron microscopy and electron diffraction studies were carried out on both unshadowed and Pt : Pd shadowed crystals in a JEM 6A electron microscope. The effects of beam-induced structural changes were minimized by working at low beam intensities obtained using the double condenser system of the microscope with the second condenser lens appropriately defocused.

3. Observations

The morphologies of the various types of crystals formed on precipitation from 0.1 percent solutions at temperatures of 110, 105, 100, and 90 °C will now be described. We shall begin with the simplest crystals found, namely those formed on crystallization at 110 °C.

3.1. Crystals Formed at 110 °C

Crystallization in 0.1 percent solutions which were transferred directly to baths at 110 °C was observed to proceed very slowly. Furthermore, the crystals demonstrated a marked tendency to form an almost continuous coating of intergrowing multilayered crystals adhering to the walls of the crystallization vessel. Microscopic examination of crystals formed under these conditions was very difficult. It was, however, found that "seeding" the solutions resulted in well-dispersed suspensions of crystals which settled to the bottom of the crystallization vessel but could be readily stirred back into suspension and were thus more amenable to microscopic examination.

The seeding procedure which was adopted is similar in principle to that used by Blundell, Keller, and Kovacs in growing polyethylene crystals from dilute solutions at elevated temperatures [9]. Briefly, the procedure was as follows: A 0.1 percent solution of the polymer in PCTFE oil, after being held at 195 °C for one-half hour was transferred to a bath at 80 °C. At this temperature crystallization occurs extremely rapidly, the preparation yielding complex crystals. After 45 min this preparation was transferred to a bath at 123 °C. The cloudiness in the preparation disappeared within 5 min indicating that redissolution had occurred. The preparation was maintained at 123 °C for a total of 15 min, at the end of which time it was transferred to

[3] As estimated by the manufacturer on the basis of the correlation between zero-strength-time and molecular weight.

[4] The identification of the products of specific manufacturers is made only for the purpose of describing experimental conditions. Such identification does not, in any way, imply endorsement by the National Bureau of Standards.

a bath at 110 °C. Crystallization occurred within 2 days at this temperature.

The seeding procedure did not have any marked effect on the habit of the crystals grown at 110 °C, other than to provide for a higher incidence of monolayer crystals of a more uniform size. Seeding of solutions crystallized at 105 and 100 °C (at which temperature it was possible to obtain crystals in suspension without resorting to seeding) had no detectable effect on the habits of the crystals formed at these temperatures.

An example of the many monolayered lamellar crystals formed at 110 °C using the seeding procedure outlined above is shown in figure 1. The selected area electron diffraction pattern of figure 2 shows, through the presence of the six intense 10.0, and the much weaker 11.0 and 20.0 reflections (too weak to be seen in fig. 2) that the electron beam is incident along the c axis of the hexagonal unit cell. The unit cell parameter a was calculated from the (hk.0) reflections and found to be 6.42 ± 0.03 Å, in good agreement with values of other workers [3, 4, 7]. Since the length of a typical chain (on the basis of molecular weight) is of the order of 1700 Å and since the crystals are approximately only 130 Å thick along the chain direction, it is clear that the chain molecules are folded in these crystals.

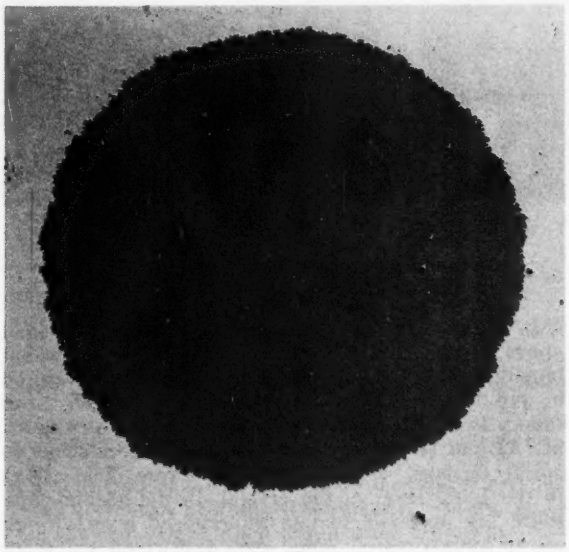

FIGURE 1. *Example of disk-shaped monolayer crystal formed at 110 °C.*

Note circular outline. Electron micrograph, magnification 7,900x.

Unlike chain-folded lamellar crystals of many polymers, these PCTFE crystals do not exhibit smooth, well developed, lateral growth faces. Even when formed under conditions of slow growth, as these were, chain-folded lamellae of PCTFE are essentially circular in overall shape. Furthermore, their periphery is very finely serrated.

This latter feature, which may be discerned in figures 1 and 2 and is illustrated at much higher magnification in figure 3 bears importantly on the nature of the fold domain structure in the interior of these crystals. A consideration of figure 3 clearly reveals that the fine structure of the periphery of these crystals is characterized by the profuse incidence of outgrowths (or "growth tips") (see arrow A in figure 3) of the order of 1000 Å wide, which protrude outwards from the interior of the lamellae. The outgrowths often display a vague semblance of hexagonality in their outline suggesting that, on this small scale, the lateral growth pattern of the crystals may possess some semblance of crystallographic regularity.

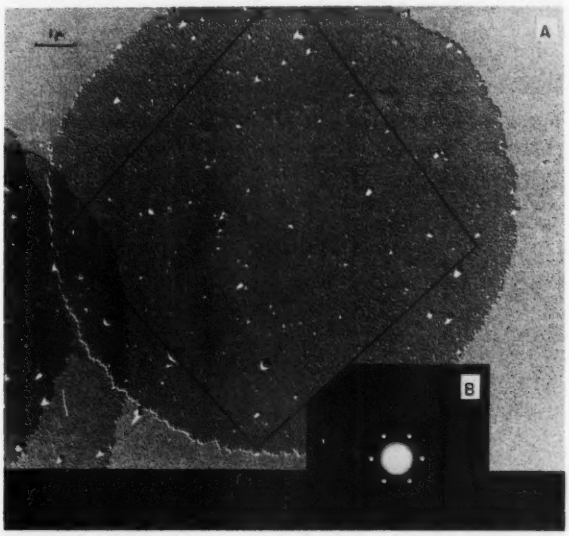

FIGURE 2. (a) *Electron micrograph of monolayer crystal formed at 110 °C.*

Gold shadowed. Magnification 5,700x.

(b) *Selected area diffraction pattern obtained from area outlined by the black lines in (a).*

The six spots are 10.0 reflections. Continuous outer ring is due to shadowing metal.

Between adjacent growth tips, as at B in figure 3, we find very narrow channels which can be traced, along meandering paths, for some distance into the interior of the crystal. In shadowed crystals the shadowing material accumulates on the sides of these channels which are away from the source, confirming that these features are indeed depressions and that they are present in the dried down crystal before it is irradiated. These channels arise because crystallizing polymer is preferentially deposited at the growth tips. Under these circumstances, the regions between the growth tips tend to become filled in more slowly. As the channels get narrower the likelihood that a molecule will diffuse into such a confined region and crystallize there becomes progressively less and the channels are never completely filled in. The unfilled channels which remain behind the growth front and become surrounded by crystalline polymer impart to

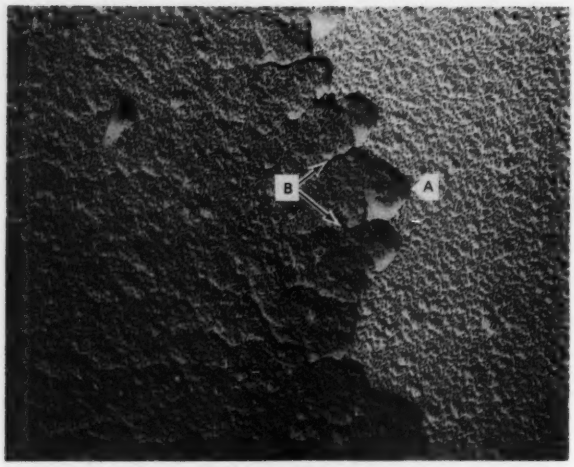

FIGURE 3. *High magnification view of edge of monolayered crystal formed at 110 °C.*

See text for explanation of arrows. Electron micrograph, Pt:Pd shadowed. Magnification 93,000x.

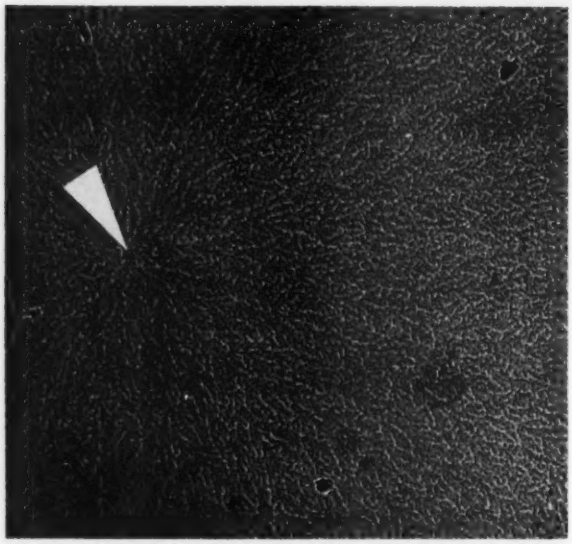

FIGURE 4. *High magnification view including center of crystal grown at 110 °C.*

Arrow indicates center. Note radiating appearance of fine structure. Electron micrograph. Magnification 17,400x.

the crystal an apparently radiating fine structure which emanates from its center. Figure 4 illustrates this feature.

This apparent radiating texture is, however, not to be interpreted as evidence for a radially symmetric internal structure. The electron diffraction pattern in figure 2b indicates the monocrystal character of these lamellae. The absence of any appreciable arcing in the 10.0 reflections (as well as in the 11.0 and 20.0 reflections) cleraly indicates that the orientation of the unit cell is essentially constant throughout the crystal.

Given that the lateral growth of the crystals involves the apposition of the chain molecules in a folded conformation at the periphery of the lamellae, that their periphery is finely serrated, that they exhibit a radiating fine texture, and that no appreciable deviations in lattice orientation are observed within the lamellae, it may be readily concluded that these crystals are multisectored and consist of a crystallographically coherent finely divided mosaic of fold domains.[5] The multisectored character of these crystals will be discussed in section 5.1, it may, however, be noted in anticipation of what follows that this feature and its manifestation in association with an overall essentially circular and finely serrated lateral mode of growth involving the lateral encapsulation of voids behind the growth front are characteristics of the constituent lamellae of all the crystals formed in the temperature range 110 °C–90 °C.

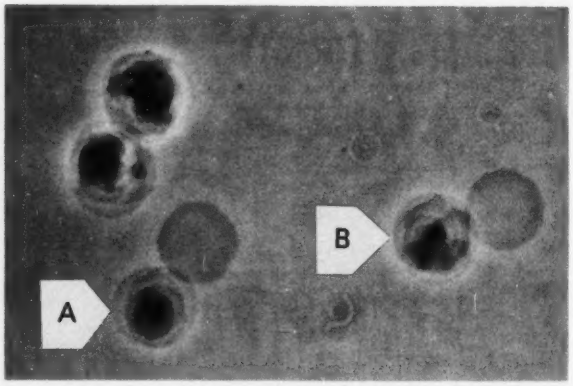

FIGURE 5. 110 °C *crystals sedimented and dried on microscope slide.*

Arrows A and B point to crystals which show development of additional layers on screw dislocations. Phase-contrast optical micrograph. Magnification 1,066x.

In addition to the monolayered crystals described above, multilayered crystals whose constituent lamellae exhibit similar fine structures are also formed at 110 °C. Two types of multilayered crystals were found. In the first type, examples of which are shown at (A) and (B) in figure 5, additional layers occur as spiral terraces originating from screw dislocations in the basal layer of the crystal. In the second type there are only two to four superposed layers which are of approximately equal size, and which are offset relative to one another as in the bilayer crystal shown in figure 6.

Electron diffraction patterns indicate that the superimposed layers in the bilayer crystals are rotated with respect to one another as may be seen in figure 6. The amount of this rotation was not fixed but varied from one case to another ranging up to 15° or so. It might be thought that these bilayered crystals with

[5] The term "fold domain" and "sector" are used synonymously throughout this paper even in the absence of direct evidence linking specific crystal faces and fold domain boundaries.

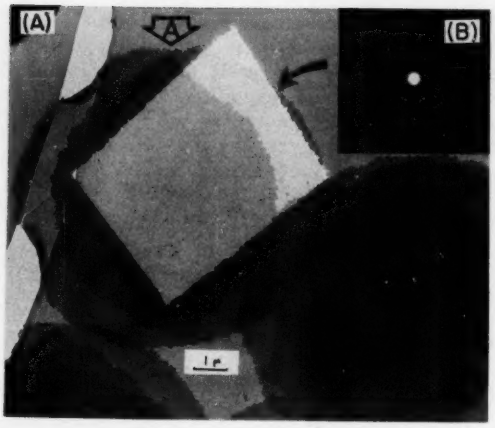

FIGURE 6. *Example of bilayer crystal with offset layers*
(a) *Example of a bilayer crystal (arrow) with offset layers.*
Electron micrograph, unshadowed. Magnification 5,000x.
(b) *Selected area diffraction pattern obtained from lighter area outlined in* (a).
Note misorientation between two sets of six 10.0 spots.
(c) *Magnified schematic trace of region* (A) *in crystals where two layers cross.*
Note that growth appears to be retarded at that portion of each lanella which is overlapped by the other layer as evidenced by the slight concavity in the vicinity of the crossover point.

apparently offset layers are merely monolayer crystals which accidently overlapped when they were deposited and allowed to dry upon a substrate. There are two features which suggest that these bilayered crystals genuinely grew as such or that they are the product of individual monolayers which impinged upon and adhered to one another (fold surface to fold surface) as they were developing in the mother liquor and subsequently proceeded to grow further in concert with one another thereafter. First, as may be seen in figure 6a and as shown schematically in figure 6c the respective peripheries of the superposed layers take on a slightly concave profile in the vicinity of the cross-over points (e.g. (A) in fig. 6a) between the overlapping layers. This feature indicates that the outward growth at the portion of the periphery of each lamella which is overlapped by the other layer tends to be slower than the outward growth at the "free" portion of the periphery of each lamella. This feature demonstrates that the two layers actually grew in concert for a substantial period of time. The second feature which confirms the specificity of this growth pattern is the frequency with which bilayered crystals occur with the two layers offset by approximately the same amount. The origins of this seemingly specific offset are at present unclear.

Having discussed the principal structural features of the 110 °C chain-folded lamellar crystals, as revealed by examination of sedimented and dried crystals, a further important aspect of their habit remains to be pointed out. This feature of these crystals, which relates to the three-dimensional character of their as-grown shapes, was investigated by examining the crystals while in suspension in liquid. They exhibit, when viewed edge-on in suspension, as are crystals A and B in figure 7, the essentially straight-line profile to be expected of planar crystals. There is, however, a suggestion revealed in some multilayered crystals that their constituent layers may be very slightly splayed.

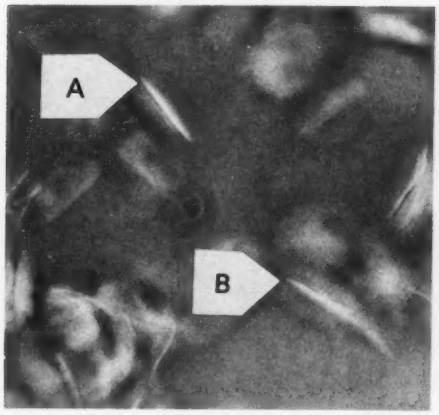

FIGURE 7. *110 °C crystals in suspension in liquid.*
Arrows A and B indicate crystals which are being viewed essentially edge-on. Phase-contrast optical micrograph. Magnification 1,040x.

The absence of collapse features (such as pleats, etc.) characteristic of collapsed nonplanar polymer crystals in the sedimented and dried crystals shown above, further substantiates the planar character of the chain-folded lamellae formed at 110 °C.

The planar or very nearly planar character of the crystals described above contrasts vividly with that of the crystals formed at temperatures of 105 °C and below.

3.2. Crystals Formed at 105 °C

A phase-contrast optical micrograph of a number of crystals formed at 105 °C as seen in suspension in liquid is shown in figure 8 in which the crescent-

shaped edge-on profile exhibited by many of the crystals in the field of view is evident. There are actually two related types of crystals formed at this temperature.

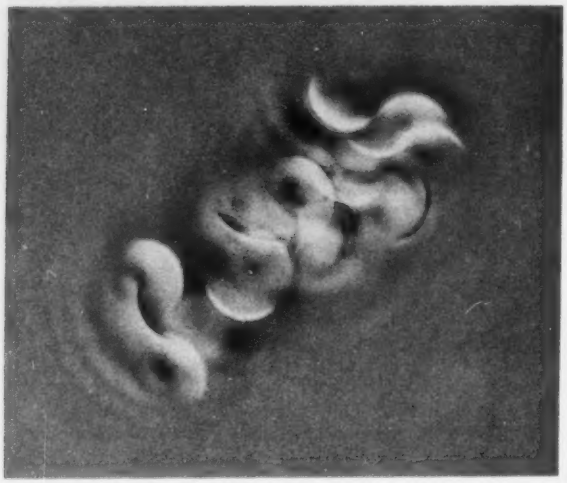

FIGURE 8. *105 °C crystals in suspension in liquid.*

Phase-contrast optical micrograph. Magnification 1,100x.

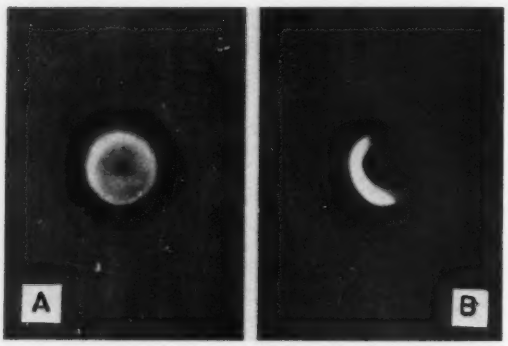

FIGURE 9. *105 °C crystal in suspension in liquid.*

Crystal has an overall shape approximating that of a watchglass. (a) view along central axis of crystal. (b) view perpendicular to central axis. Phase-contrast optical micrograph. Magnification 1,000x.

An example of the first, predominant, type as seen from two perspectives is shown in figure 9. This crystal exhibits, when viewed along its central axis, a circular profile as seen in figure 9a. This feature, in conjunction with the distinctly crescent-shaped profile exhibited by the same crystal when viewed edge-on, i.e., at a right angle to its central axis, as in figure 9b, demonstrates the pronouncedly curved overall shape of this species of crystal, whose shape is akin to that of a watchglass. An electron micrograph of such a crystal is shown in figure 10. These crystals consist of many superposed chain-folded lamellar layers, hence the opacity of their central regions to the electron beam; nevertheless, the lamellar character of these crystals is clearly evident in their thinner peripheral regions. The opacity of these crystals to the electron beam renders impossible the revelation, under the transmission electron microscope, of the buckling and/or folding of their constituent lamellae which occur in the central regions of the crystals as a result of their collapse upon sedimentation and drying.

The lamellar character of these crystals has already been seen in figure 10. The finely serrated character of the periphery of the constituent lamellae in these crystals can be seen more clearly at higher magnification as in figure 11. Here void-like channels extending into the interior of the crystals as well as entrapped void-like regions, both similar to those seen in the crystals formed at 110 °C, may be discerned.

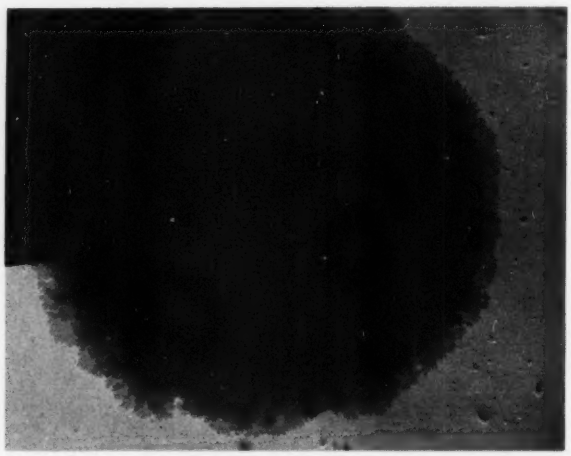

FIGURE 10. *105 °C crystal.*

Note lamellar character. Electron micrograph magnification 5,400x.

As mentioned earlier, a second species of crystal is formed at 105 °C. The as-grown shape of these crystals corresponds to that of two simple watchglass crystals such as those described above joined back-to-back such that their respective central axes are coaxial or nearly so. When viewed along their common central axis these crystals exhibit a circular periphery as is the case for the simple crystals. However, when viewed, while in suspension in liquid, along a direction normal to their common central axis, as shown in figure 12, (arrow) they exhibit the appearance of two crescents placed back-to-back.

These multilayer crystals consist of two sets of lamellae similar in character to the constituent lamellae of the watchglass shaped crystals described earlier, the two sets of lamellae, however, being curved in opposite directions.

For the purposes of the present discussion, the salient habit feature of the crystals formed at 105 °C, which we wish to reiterate, is their distinctly curved overall shapes as contrasted with the planar character of the crystals formed at 110 °C.

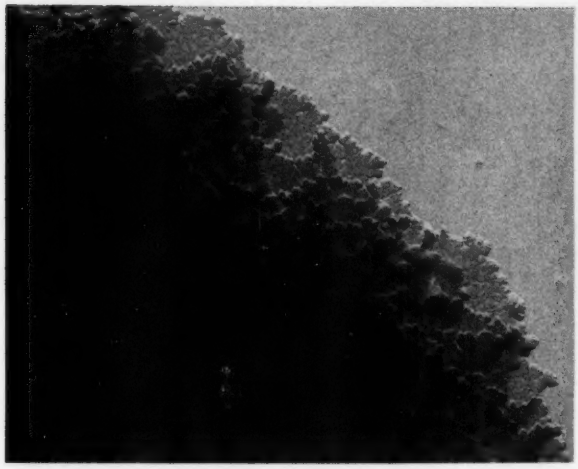

FIGURE 11. *High magnification view of edge of 105 °C crystal.*

Note the finely serrated character of the periphery. Electron micrograph. Magnification 17,700x.

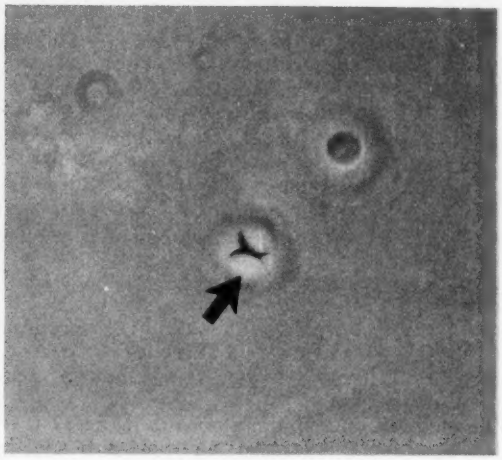

FIGURE 12. *Arrow points to an example of "double watchglass" type of crystal formed at 105 °C.*

Crystal in suspension in liquid. Phase-contrast optical micrograph. Magnification 520x.

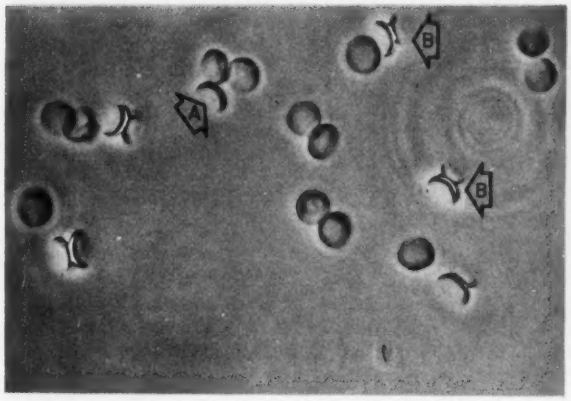

FIGURE 13. *Group of crystals formed at 100 °C in suspension in liquid.*

Arrow A points to simple watchglass-shaped crystal seen edge-on. Arrows B point to "double watchglass' crystal seen edge-on. Crystals which are edge-on in the field of view almost always have the appearance of two crescents placed back to back. Phase-contrast optical micrograph. Magnification 370x.

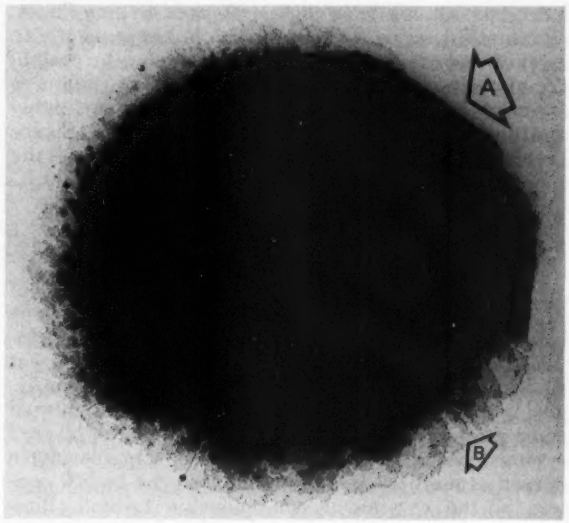

FIGURE 14. *100 °C crystal.*

Crystals formed at this temperature show a greater tendency to fold edges under on collapse as at A. Fracture (as at B) is also a common feature in collapsed crystals of this type. Electron micrograph. PtPd shadowed. Magnification 4,600x.

3.3. Crystals Formed at 100 °C

Multilayered crystals exhibiting nonplanar habits essentially similar to those of the two species grown at 105 °C are also formed when the polymer is crystallized from solution at 100 °C. Two additional features may, however, be noted. First, there is a somewhat higher incidence of the double watchglass species than was observed at 105 °C, indeed, these crystals were the predominant species formed at 100 °C. A phase-contrast optical micrograph depicting several such crystals (e.g., see arrows marked B) viewed edge-on or nearly so in suspension in liquid is shown in figure 13. An example of the simpler, single watchglass crystals as viewed edge-on may also be seen in figure 13 (arrow marked A). Second, the shape of the single watchglass crystals and the component halves of the more complex, double watchglass, species appear to be more hemispherical than watchglass-like. This feature, though to some extent subjective, is partially substantiated by the greater frequency with which the lamellae at the crystal periphery tend to fold inwards upon sedimentation and collapse as shown in region A in the electron micrograph of a collapsed crystal illustrated in figure 14. Fracture (see B in fig. 14) is a feature which often occurs when crystals of this type

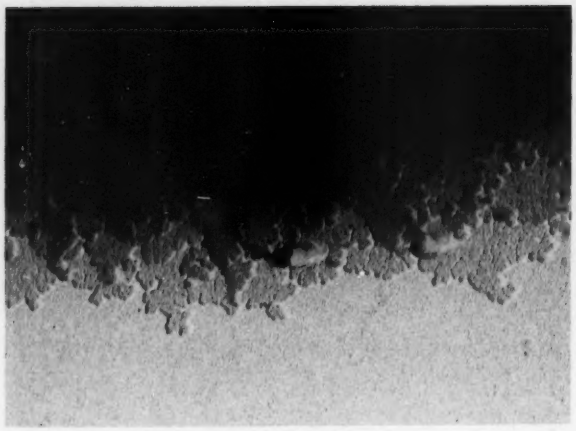

FIGURE 15. *High magnification view of periphery of 100 °C crystal showing highly reentrant character of the lamellae.*

Electron micrograph. magnification 19,700x.

collapse. The resulting cracks, when viewed at high magnification, are seen to be traversed by fine fibrils. Figure 14 reveals the lamellar character of these crystals and the finely serrated character of the periphery of their constituent lamellae. These two features are more clearly revealed in figure 15 which is a highly magnified view of the outer portion of a crystal. Figure 15 also reveals the similarity in the nature of the constituent lamellae in the crystals formed at 100 °C and those formed at 105 and 110 °C.

3.4. Crystals Grown at 90 °C

Because growth is very rapid at temperatures of 90 °C and below some crystallization takes place before temperature equilibrium is attained when solutions initially held at 195 °C are transferred to baths at 90 °C. The phase contrast micrograph shown in figure 16 illustrates the appearance of crystals formed when a solution is cooled to 90 °C. In the multilayered crystals, denoted A in figure 16, the lamellae have curved around to completely enclose the hollow centers of the crystals in an onionskin fashion. Birefringence observations show that the chain molecules are parallel to the radius vector in these hollow, essentially spherical, crystals.

More complex crystals, such as those denoted B in figure 16 are also formed under these conditions. These crystals are complex arrays of curved chain-folded lamellae. The origin of these arrays may readily be envisaged as the consequence of a pronounced tendency for fresh layers, initiated on a curved parent lamella. The origin of these arrays may readily be parent lamella at their point of origin. This effect is similar to that already observed on a more limited scale in the double watchglass crystals seen at 105 and 100 °C.

Since they consist of many chain-folded layers, the crystals formed at 90 °C are too thick to examine in direct transmission in the electron microscope. We

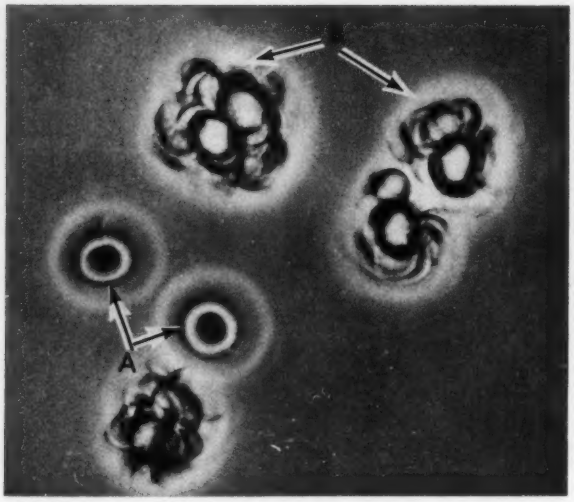

FIGURE 16. *Crystals formed at 90 °C in suspension in liquid.*

The arrows marked A indicate hollow spherical crystals in which curved lamellae completely enclose the centers. The arrows marked B point to examples of the many complex arrays of curved lamellae found at this temperature. Phase-contrast optical micrograph. Magnification 840x.

therefore resorted to replication techniques in order to examine the fine structure of these crystals. Figure 17 shows a replica of a crystal from a suspension cooled to 90 °C. These replicas were prepared by evaporating a Pt:Pd alloy onto crystals which had been sedimented onto a flat glass microscope slide and dried there. Carbon was then evaporated over the Pt:Pd layer to provide a backing. The film of Pt:Pd and carbon containing the crystals was then cut into small squares and floated off the glass slide onto a water surface. The small squares were then picked up and dried on electron microscope grids. After drying, the grids were immersed in a vessel containing PCTFE oil at room temperature. This vessel was then slowly heated up to 175 °C in order to dissolve the polymer and extract it from the replica.

The electron micrograph shown in figure 17 reveals the collapse features formed on sedimentation of these nonplanar structures. In order to see the fine structural characteristics of the lamellae the replica must be examined at higher magnification, as in figure 18. In figure 18 the serrated character of the periphery of the lamellae is clearly visible, thus showing the similarities between the lamellae of which these crystals are composed and those formed at the higher temperatures.

4. Summary of Results

The observations described above provide a detailed characterization of the crystals which are observed to form when PCTFE is precipitated from dilute solutions at a number of temperatures in the range from 110 to 90 °C. The habits of the crystals are observed to depend strongly on the degree of supercooling prevailing during their growth.

At 110 °C we find disk-like monolayered, chain folded lamellae exhibiting an essentially planar overall shape.

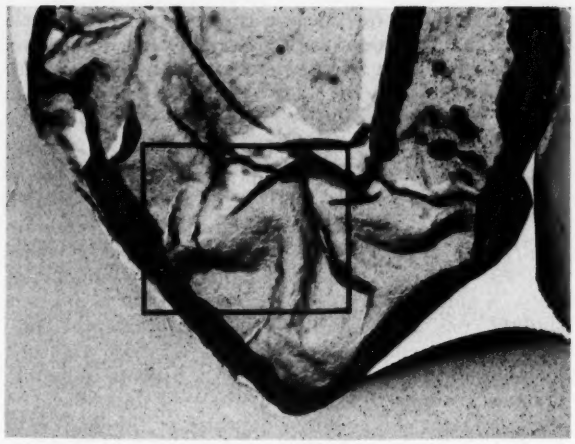

FIGURE 17. *Shadow-transfer replica of a portion of a crystal formed at 90 °C, permitting the observation of the buckling and pleating resulting from collapse of the crystals.*
Electron micrograph. Magnification 10,300x.

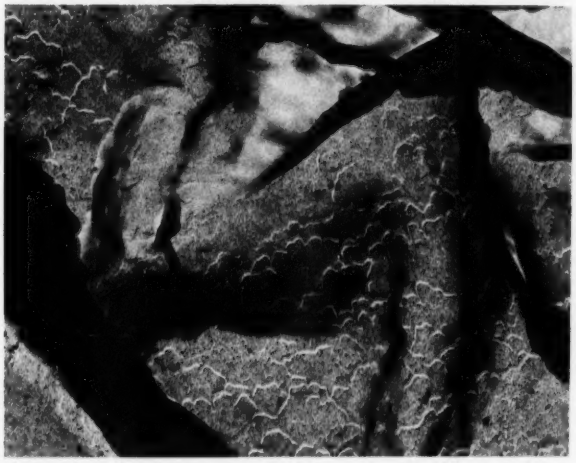

FIGURE 18. *Higher magnification view of region outlined in figure 17.*

Note the lamellar texture of the surface and the highly serrated character of the lamellae. Electron micrograph. Magnification 28,000x.

These unusual crystals are characterized by an absence of prismatic growth faces and the presence of a highly multisectored fine structure. Although this growth pattern suggests that the lamellae possess an irregular internal structure, electron diffraction reveals that these lamellae have a single-crystal character with the orientation of the unit cell remaining essentially constant throughout the crystal. Multilayered crystals are also formed at 110 °C. The constituent lamellae in these crystals are similar to the monolayered crystals.

The crystals which are formed at somewhat higher degrees of supercooling, i.e., upon crystallization at 105 °C and at 100 °C are of two types. The simpler ones possess a curved overall shape akin to that of a watchglass. The shape of the more complex corresponds to that of two watchglasses joined back to back. These structures are multilayered, consisting of stacks of curved lamellae. At even higher degrees of supercooling we find, along with other, more complex, structures, crystals in the form of hollow spheres where the curving lamellae completely enclose the hollow centers of the crystals in an onion-skin fashion.

Crystals formed at 105 °C have a radius of curvature in the range 5–6 μm. Those formed at 100 °C have a slightly smaller radius of curvature and those formed at 90 °C have a radius of curvature in the range 4–4.5 μm. This variation is much less than that found in our earlier studies [1, 2].

Paralleling the trend toward increasingly curved crystals as the degree of supercooling is increased we find an increasing tendency for new layers, initiated on a growing crystal, to adopt a sense of curvature opposite to that of the parent lamellae. This tendency leads to the formation, at high degrees of supercooling, of complex pseudospherulitic arrays of curved lamellae (see fig. 16).

5. Discussion

For the purposes of discussion we will group the results of our experiments into two classes. In the first instance we will discuss the fine structural features observed in the simple monolayered crystals formed at 110 °C. These features are representative of those exhibited by the lamellae of which crystals formed at other temperatures are composed. As a second area for discussion we will consider the observed effects of crystallization temperature on the overall shapes of PCTFE crystals.

5.1. Fine Structure of Lamellar Crystals of PCTFE

The important features of the fine structure of the PCTFE folded chain lamellae we have observed in this study are best exemplified in the monolayered chain-folded crystals formed at 110 °C. Turning our attention to the overall appearance of these crystals we see that, instead of being bounded by smooth crystallographic growth faces, they exhibit an essentially circular outline. This feature, together with the apparently radiating structure caused by channel-like voids in the interior of the crystals and the finely serrated character of the periphery, suggests that the crystals grow in an irregular manner. In characterizing and attempting to account for this irregular growth pattern, we must however, bear in mind that it leads to a structure which is crystallographically coherent; i.e., the unit cell orientation is essentially constant throughout the crystal.

If we examine the influence of crystallization temperature on crystal habit we see differences in behavior pattern between PCTFE and such "normal" polymers as P4MP and POM which require some comment. In these latter cases crystals with well-defined growth faces and consisting of only a few fold domains are formed under conditions where growth is slow. As crystals are formed at lower and lower temperatures, favoring increasingly rapid growth, the lamellae develop in a multisectored manner,

i.e., they are subdivided into an increasingly finer mosaic of fold domains due to microfaceting associated with the development of successive arrays of sectored outgrowths. In the case of PCTFE, however, the profile of the growing face remains essentially unchanged as growth becomes more rapid and the influence of growth rate on sector size is not nearly so marked as in P4MP and POM.

In order to discover whether the solvent was a factor influencing the fine structure of PCTFE crystals we attempted to crystallize the polymer from mesitylene and from 2,5-dichlorobenzotrifluoride. These experiments yielded morphologies essentially the same as those obtained on crystallization from PCTFE oil. Our experimentation in an attempt to obtain crystals of PCTFE with well-defined prismatic faces has been far from exhaustive and, since it is known that parameters such as solvent, molecular weight, concentration, and temperature affect morphology, it will be necessary to carry out further experiments in order to establish whether or not PCTFE can be induced to form regular prismatic crystals under suitably chosen conditions.

A factor in addition to those mentioned above which might influence the habits of PCTFE crystals can be found in the steric character of the molecules. This effect would be an intrinsic one arising from the molecular conformation and could be relatively unaffected by the coice of crystallization conditions. In the case of PCTFE the CF_2CFCl-groups follow each other in a random sequence with syndiotactic diads occurring approximately twice as frequently as isotactic ones [10]. This irregular placement of chlorine atoms may lead to an irregular lateral packing of the molecules.[5] We do not, as yet, have a model linking such an effect to the observed crystal habit and further experimentation is necessary to establish the importance of steric factors in regulating interchain packing and thereby possibly influencing crystal habits.

Having indicated some possible origins of the irregular lateral habit of crystals of PCTFE let us return for a moment to some questions relating to the process of chain folding in this polymer. From the fact that the length of any given molecule is, on the average, much greater than its extension in the crystal we must conclude that the molecular chains in these crystals are folded. Although one would suspect that the molecules could fold in a regular manner along (10.0) or possibly even (11.0) planes we have been unable, because of the lack of clearly distinguishable prismatic facets in these crystals, to identify any specific sets of planes as containing the molecular chain folds.

Lacking an answer to this question it is impossible to characterize the fine structure of these crystals in terms of specific fold domains (or sectors). This question could, or course, be resolved by characterizing well-formed crystals and observing the process of degeneration into the habit described above. Since we have not yet attained this goal we will content ourselves, in the following discussion, with using terms like "fold domain" and "domain structure" as a shorthand description for the fine structure of the crystals even though the relationship between this fine structure and the chain folding process is not clear.

[5] This question is investigated more fully in the recent study by Mencik [7].

5.2. Curved Crystal Formation in PCTFE

In our earlier papers [1, 2] we advanced, as a working hypothesis, a model which is presumed to account for curved crystal formation in P4MP and POM through the influence of two factors. First, detailed diffraction contrast observations on crystals of these two polymers indicate that individual fold domains are nonplanar. Thus, a simple four or six-sectored crystal is actually slightly conical in overall shape. This degree of conicalness is extremely small and is most readily assessed by means of diffraction contrast experiments on simple crystals composed of only a few fold domains. The second factor influencing curvature is the nature of the interconnection between adjoining fold domains in a multisectored crystal. We suppose that adjacent fold domains are joined together in a coherent manner such that their nonplanarity accumulates. On this basis we expect a multisectored crystal of a given size to be more highly curved than one possessing only a few fold domains. In actual fact the phenomenology of curved crystal formation is more complicated than this and we would strongly advise the interested reader to consult the more detailed discussion in reference [1].

From the phenomenological point of view this description fits the observed characteristics of the crystals rather well. In the case where crystals of P4MP and POM consisted of only a few fold domains we found essentially planar crystals whereas highly multisectored crystals were found to be curved. The crystals of PCTFE formed at temperatures below 110 °C also fit this pattern in that they are both strongly curved and highly multisectored.

PCTFE crystals formed at 110 °C do not fit into the previously established pattern for curved crystal formation because they are essentially planar in their overall shape in spite of the fact that they are highly multisectored. On the basis of this observation we might, within the hypothetical framework described above, surmise that fold domains in 110 °C crystals are planar or that there is insufficient connectivity between adjoining fold domains to allow neighboring non-planar fold domains to make a cumulative contribution to the overall curvature of the crystal.

On the basis of our experiments we cannot determine which, if either, of these effects is present. In the first place we have been unable to obtain diffraction contrast effects which allow an assessment of the nonplanarity of individual fold domains. Such an undertaking would be difficult, if not impossible, on crystals such as ours because of the very small size of the fold domain structure. It is even less likely that one could measure, by means of Moire patterns [11], lattice distortions which could give rise to nonplanar fold domains in such crystals.

Since such information is lacking we cannot assert with any positiveness that curved crystal formation is

a phenomenon which is caused by the same factors in the three polymers we have examined. The fact that crystals formed at lower temperatures are both curved and multisectored in all three cases does permit us to speculate that this is so. In this context and in order to fit the observations on PCTFE crystals formed at 110 °C into the phenomenological framework of our earlier work we would then further speculate that:

(1) Fold domains in PCTFE crystals formed at low supercoolings are more nearly planar than those in crystals formed at high supercoolings or, (2) that in PCTFE crystals formed at low supercoolings there is insufficient connectivity between neighboring nonplanar fold domains to allow for the propagation of a curved structure, while at high supercoolings the nonplanarity of neighboring fold domains contributes to overall curvature in a cumulative manner.

We can summarize our discussion of curved crystal formation in PCTFE by noting that, while PCTFE does indeed exhibit a habit-supercooling trend parallelling that exhibited by P4MP and POM, we are unable to characterize the possible origins of this trend in PCTFE. If suitable crystals were available it might be possible to make more affirmative statements about the origins of curvature in PCTFE crystals.

Finally, the observation that increasing supercooling tends to favor the development of arrays of lamellae which curve in opposite directions as in the double watchglass shaped crystals formed at 100 °C and the complex structures (e.g., B in fig. 16) formed at 90 °C, bears further comment. The conclusion we wish to point out in this connection is the following: The curvature of the constitutent lamellae in those crystals is an intrinsic feature of the lamellae and is not caused by repulsive interactions between superposed lamellae as might be invoked to account for the splaying of the lamellae in opposite directions. We base this conclusion on the fact that curvature is an intrinsic feature of the single watchglass shaped crystals formed at 105 and 100 °C as well as the hollow spherical shaped crystals formed at 90 °C which are curved in only one direction.

6. Conclusions

Crystals of PCTFE were obtained by crystallizing the polymer from 0.1 percent solutions of PCTFE at temperatures of 110, 105, 100, and 90 °C. At 110 °C both monolayered and multilayered chain-folded lamellar crystals were formed. The crystals were planar. The individual lamellae exhibited an essentially circular overall outline and their periphery was finely serrated. The internal fine structure of the lamellae is mosaic-like on a very fine scale. The irregular character of the lateral mode of propagation of the lamellae and their complex internal texture prevents any firm statements regarding the chain-folding process involved in the formation of these crystals.

At lower crystallization temperatures multilayered crystals exhibiting curved overall shapes were formed. The curvature of these crystals tended to be more pronounced the lower the crystallization temperature. This effect is not nearly as strong as those observed for P4MP and POM [2]. The fine structures of the lamellae in these curved crystals was however similar to that of those formed at 110 °C. The origins of the fact that the crystals of PCTFE tended to be all the more pronouncedly curved the lower the crystallization temperature remain obscure at this stage. Uncertainties regarding the nature of the fold domain structure in the crystals preclude us from making any connection between our present study and our previous ones on the formation of curved crystals of P4MP and POM other than the phenomenological one that (as was the case for P4MP and POM) the PCTFE crystals tended to be all the more pronouncedly curved the lower the crystallization temperature.

7. References

[1] Khoury, F., and Barnes, J. D., J. Res. Nat. Bur. Stands. (U.S.), **76A** (Phys. and Chem.), No. 3, 225–252 (May–June 1972).
[2] Khoury, F., and Varnes, J. D., J. Res. Nat. Bur. Stands. (U.S.), **78A** (Phys. and Chem.), No. 2, 95–127 (Mar.–Apr. 1974).
[3] Kaufman, J. S., J. Am. Chem. Soc. **75**, 1477 (1953).
[4] Ermolina, A. V., Markova, G. S., and Kargin, V. A., Soviet Physics–Crystallography **2**, 615 (1957).
[5] Roldan, L. G., and Kaufman, H. S., Norelco Reporter **10**, #1, 11 (1963).
[6] Miyamoto, Y., Nakafuku, C., and Takemura, T., Polymer Journal (Japan) **3**, 122 (1972).
[7] Mencik, Z., J. Polymer Sci. Pt. A-2, **11**, 1585 (1973).
[8] Bassett, D. C., and Keller, A., Phil. Mag. **7**, 1553 (1962).
[9] Blundell, D. J., Keller, A., and Kovacs, A. J., J. Polymer Sci. **B4**, 481 (1966).
[10] Bovey, F. A., and Tiers, G. V. D., Fortschr. Hochpolym. Forsch. **3**, 139 (1963).
[11] Bassett, D. C., Phil. Mag. Ser. VIII **10**, 595 (1964).

(Paper 78A3–817)

JOURNAL OF RESEARCH of the National Bureau of Standards—A. Physics and Chemistry
Vol. 78A, No. 3, May–June 1974

Enthalpy of Formation of Phosphorus Pentachloride; Derivation of the Enthalpy of Formation of Aqueous Orthophosphoric Acid

R. H. Schumm, E. J. Prosen, and D. D. Wagman

Institute for Materials Research, National Bureau of Standards, Washington, D.C. 20234

(February 1, 1974)

When chlorine (real gas, 980 mmHg) combines with white (α) phosphorus to form phosphorus pentachloride at 24.89 °C, 3986.3±2.7 J of heat are liberated per gram of stoichiometrically equivalent $Mg_2P_2O_7$. This value was determined by a dead-ended flow system in an electrically calibrated isoperibol calorimeter. Correction was made for the formation of up to one mol percent PCl_3 in the products; no other impurities were found. From this value, the standard (25 °C, ideal gas) enthalpy of formation of PCl_5(c) is calculated to be -443.85 ± 0.30 kJ/mol, -106.08 ± 0.07 kcal/mol. When this figure is combined with a recent determination of the enthalpy of hydrolysis of PCl_5(c), the standard enthalpy of formation of H_3PO_4 (aq, 100 H_2O) is calculated to be -1296.5 ± 1.5 kJ/mol, in good agreement with two other values which involve the formation and hydrolysis of P_4O_{10} (hex). A "best value" is suggested: $\Delta Hf°$ (H_3PO_4, 100 H_2O) $= -1295.8 \pm 1.3$ kJ/mol, -309.7 ± 0.3 kcal/mol.

Key words: Enthalpy of formation; phosphoric acid; phosphorus pentachloride.

1. Introduction

The direct chlorination of phosphorus, followed by dissolution in water of the resulting phosphorus pentachloride, provides a convenient thermochemical path to aqueous orthophosphoric acid. The most recent selection of the enthalpy of formation of the latter compound, given in NBS Technical Note 270–3 [1],[1] is based on the bomb combustion of phosphorus followed by dissolution of phosphorus pentoxide in water [2]. Both steps of this latter path are subject to certain difficulties (see sec. 9); therefore the present work was undertaken as an independent check.

A preliminary value of the enthalpy of formation of phosphorus pentachloride based on the present work was cited in [1]. No other values in that review publication were based on PCl_5. Since the completion of the present work a number of investigations related to the enthalpy of formation of aqueous orthophosphoric acid have been published; these are discussed following the description of our results. On the basis of our work and these recent investigations, we derive a value for the enthalpy of formation of aqueous orthophosphoric acid. Our laboratory work was carried out during the period May 1, 1963, through January 10, 1964.

2. Materials

The white (α) phosphorus employed in the present work was obtained by fractional sublimation, with continuous removal of impurities, at room temperature from the commercial form (yellow sticks under water) in the all-glass, greaseless apparatus shown to scale in figure 1. After the reaction ampoules (D) were flame-baked at 10^{-5} mmHg[2] and sealed off at S_1, the rest of the apparatus was pressurized with nitrogen and opened at A. The liquid yellow phosphorus was transferred under water against a stream of backflushing nitrogen through S_2. The apparatus was then sealed at S_2 and pumped down to 10^{-3} mm Hg to remove the water. After the solidified phosphorus was dry and had begun to sublime over at 25 °C (equilibrium vapor pressure = 0.04 mmHg [3]), an ice bath was placed around the condenser (C). During the next twenty hours, while the pumping continued at 10^{-3} mmHg, about ninety percent was trapped in the condenser (C) at 0 °C (equilibrium vapor pressure = 0.005 mmHg [3]) as colorless well-formed crystals, while some phosphorus vapor with impurities was continuously carried on to the liquid-nitrogen trap (E). The pressure was then reduced to less than 10^{-5}

[1] Figures in brackets indicate the literature references at the end of this paper.

[2] 1 mmHg = 133.322 N/m²

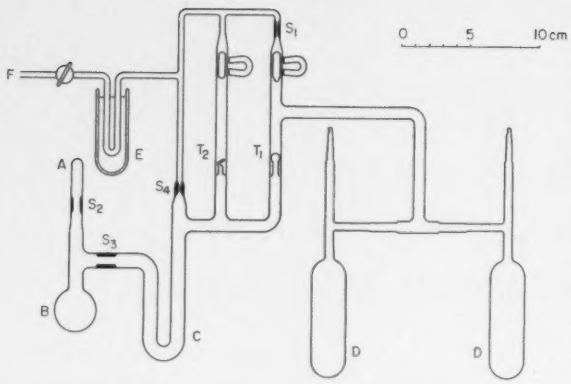

FIGURE 1. *The fractional sublimation line for phosphorus.*

A, Loading port for yellow P; B, Yellow-P chamber; C, White-P condenser; D, Reaction ampoules; E, Trap cooled in liquid nitrogen; F, High vacuum; S_1, S_2, Seal-off; S_3, Seal-off, 6 mm i.d.; S_4, Seal-off, 2 mm i.d.; T_1, T_2, Internal break seals.

mmHg by a mercury-diffusion pump, all parts containing phosphorus were cooled by liquid nitrogen, and the yellow-phosphorus chamber (B) was sealed at S_3. The previously baked, sealed reaction ampoules were opened to the line by breaking the internal break seal T_1 and then seal S_4 was made. The sublimed white phosphorus, now in an evacuated isolated system, was transferred at about 25 °C to the reaction ampoules (D) at 0 °C where it appeared as large, colorless, highly refractive, well-formed crystals. The apparatus was then connected to the high vacuum through T_2 and the reaction ampoules were sealed off at liquid-nitrogen temperature. The amount of material in the sealed ampoules (any convenient number of which could be accommodated though only two are shown) was readily maintained within 10 percent of a nominal value by measuring the amount of yellow phosphorus placed in the apparatus, with about 10 percent allowance for loss, and by keeping the vapor paths to the reaction ampoules approximately equal. All steps were carried out with moderate precautions to exclude daylight in order to avoid the UV-catalyzed reversion to the yellow form. Incandescent illumination did not seem to catalyze this transformation.

The chlorine gas was taken from a commercial 5-lb (net) cylinder of liquid chlorine with a stated purity of 99.5 percent minimum. The chlorine was dispensed by a halogen-gas-service pressure regulator through a short drying tower of $Mg(ClO_4)_2$ and P_4O_{10} into the chlorine delivery line. Below the regulator, the exposed parts of which were monel metal, borosilicate glass was used; some of the joints were made up with a hard laboratory wax which showed no deterioration after extensive exposure to the chlorine gas. Two needle valves made of borosilicate glass and fluorocarbon materials were also incorporated in the line.

After completion of the chlorination runs the purity of the chlorine remaining in the cylinder was determined by allowing it to react with mercury and analyzing the unreacted gas. A sample from the chlorine supply line was collected in a glass vessel provided with fluorocarbon-lubricated stopcocks. It was then connected to an all-glass line containing a reservoir of mercury which was provided with pressure and vacuum connections for regulation of the height of the mercury. Air was removed from the line by connection to a high-vacuum line, the mercury was permitted to rise to the lower cut-off stopcock of the sample vessel and the stopcock was opened. Reaction took place slowly in the absence of water vapor. Water vapor was found to accelerate the reaction, but was not used. Some seconds were required for the appearance of a tarnish on the mercury mirror, which gradually went over to a grey material. The reaction proceeded at this slow steady rate, even after the mercury had been thoroughly covered with the reaction product, and was complete in 6 to 10 h. In order to avoid the formation of an opaque mercury mirror on the interior glass surface, the mercury in the sample vessel was not agitated. Upon standing overnight, the mercury, covered with a large amount of the grey, irregularly shaped reaction product, rose to the top of the sample vessel which terminated in a capillary (1.3 mm i.d.) closed by the upper stopcock which communicated through another stopcock to a small, calibrated, evacuated receiver. The narrowness of the capillary prevented the rise of the mercury-chlorine reaction product so that a clean mirror-bright mercury surface appeared below the stopcock. The stopcock was opened and the unreacted gas together with clean mercury was pushed through into the calibrated receiver. The upper stopcock of the vessel was then closed, leaving some mercury in the receiver, and the mercury was brought back to the bottom of the sample vessel, thus permitting the release of unreacted gases trapped in the solid reaction product. The mercury was again permitted to rise, pushing additional gas above a mirror-clean mercury surface into the capillary. The upper stopcock of the vessel was opened, and the additional gas was added to the receiver. After a dozen passes of this kind, additional gas appearing in the capillary portion amounted to about 1 ppm of the original sample. The mercury was then raised for the final time into the calibrated portion of the receiver and the pressure and volume of the total gaseous nonreacting impurity were read.

The original Cl_2 sample (325 cm^3 at 1060 mmHg, 26 °C) contained 0.05 mol percent (4.5 cm^3 at 42 mm Hg, 25 °C) of gases which would not react with dry mercury. The unreacted gases were analyzed mass spectrometrically by the Analytical Chemistry Division and found to consist of, as ppm of the total sample: air, 20; CO_2, 274; CCl_4, 80; CH_3CHCl_2, 5; HCl, 55; and H_2O, 65.

3. Apparatus

The calorimeter that was used in the measurements is shown to scale in figure 2. It was designed to permit calorimetric hydrolysis of the reaction products but this step was not used in the present work.

All screw-threaded parts were constructed of brass except for the polymethylmethacrylate plug (L) and

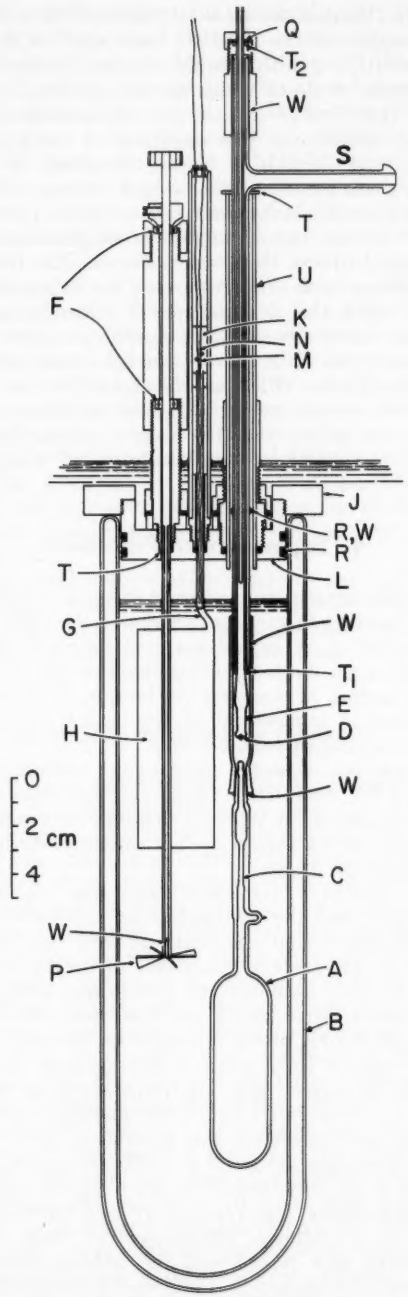

FIGURE 2. *The submarine isoperibol calorimeter.*

A, Reaction ampoule; B, Dewar vessel; C, 0.042-Inch i.d. glass tubing; D, Diamond mounted in wax; E, Bubble breaker; F, 1/8-Inch ball bearings; G, 0.10-Inch o.d. × 0.01-inch-wall platinum tubing; H, Heater encased in platinum; J, Aluminum flange; K, Beeswax; L, Machined polymethylmethacrylate plug; M, 30-Gage copper wire; N, 18-Gage copper wire; P, Platinum stirrer; Q, Brass washer; R, Rubber O-ring; S, Chlorine-inlet tube with spherical glass joint; T, Polytetrafluoroethylene washer; T_1, T_2, Polytetrafluoroethylene O-rings; U, Glass chimney; W, Hard laboratory wax.

the aluminum flange (J). The parts which pass through the plug (L) were made of borosilicate glass except for the platinum tubing (G). The glass chimney (U) was originally part of a device against which the reaction ampoule (A) was to be broken for the hydrolysis reaction.

The diamond-tipped ampoule opener (E) was manipulated from the top of the chlorine-inlet tube (S) through the brass stuffing box which contained a fluorocarbon O-ring (T_2) lubricated with fluorocarbon grease. A small area of the brass (Q) in the stuffing box, which was exposed to chlorine, suffered a discoloration during preliminary experiments but no further change occured on subsequent exposure to chlorine.

The fluorocarbon O-ring (T_1) fitted loosely at the upper portion of the flared bottom of the ampoule opener (E) and permitted communication to the top of the reaction ampoule (A) until the breaker (E) was raised at the end of the reaction period.

There was no exit from the reaction ampoule.

The Dewar vessel (B) was a standard 1-quart flask.

The calorimetric heater (H) was shaped as a flat blade, about 1.5 mm thick. It was made of 160 turns (noninductive) of No. 36 AWG enameled manganin wire, wrapped over a thin sheet of mica 82 mm long and 28 mm wide, and fixed with coil dope. Leads of No. 30 AWG copper wire (M) (enameled and silk-wound) were hard-soldered to ends of the heater winding which was then placed in the platinum sheath; the two No. 30 AWG copper leads protruded about 7 mm above the tube (G) that extended out from the top of the heater blade (that is, 93 mm above the estimated calorimetric boundary). The seams of the platinum sheath were soldered with gold. The No. 30 AWG copper leads (0.00339 Ω/cm, measured) were soft-soldered, each, to 537 mm of No. 18 AWG copper (N) (0.000222 Ω/cm, measured) which made demountable contacts through Hg amalgam to copper busbars (0.001 Ω for the sum of the resistances of the bars) which were connected to the current-carrying leads and the potential-measuring leads of the electrical measuring circuit. In order to determine the actual temperature of the heating coil during calibration runs, its resistance, with leads, was measured potentiometrically between 0 and 50 °C in series with a 1000-Ω standard resistor at a measuring current of 0.1 mA. Its resistance was found to be

$$R_t = 1068.167[1 + 5.69 \times 10^{-6}(t - 25) - 6.38 \times 10^{-7}(t - 25)^2]\ \Omega,$$

and

$$R_{max} = 1068.180\ \Omega \text{ at } 29.5\ °C,$$

where t is the temperature in °C of the stirred water bath in which the heater was immersed. The average resistance of the heater which carried 112 mA during heating periods of the calibration runs ranged between 1067.995 and 1067.945 Ω (with leads) corresponding to temperatures between 46 and 48 °C. The resistance of the leads between the estimated calorimetric boundary (± 5 mm) and the potential taps on the busbars was calculated from the above figures to be

0.088±0.004 Ω. The energy dissipated in the extra-calorimetric leads, about 0.008 percent of that measured, was subtracted from the total to obtain the amount added to the calorimetric system.

The stirrer (P) was turned at a rate of about 950 rpm by a belt drive from a synchronous motor.

The platinum-resistance thermometer (not shown; behind the plane of fig. 2), Cyril H. Meyers No. 274, was a single-helix coil of platinum,[3] about 4-cm long in a thin-wall 9-mm o.d. glass tube. The top of the Pt coil (i.e., the junctions of the gold leads) was 97 mm below the surface of the calorimetric liquid. At 24 °C, the thermometer had a resistance of 29.8966 Ω, and a temperature coefficient of 0.100767 Ω/°C.

The electrical energy was measured by a circuit basically the same as that described in [4, 5, and 6]. Steady current from a bank of large storage batteries was switched by a solenoid, as required, between the calorimeter heater and a dummy coil of similar resistance. A steady EMF of 120 V dc was applied to the busbars in all calibration experiments. A 0.1-Ω standard resistor (potential drop, 12 mV) was used for the current measurement; the voltage applied at the busbars was measured in a parallel-connected voltage divider consisting of a 10-Ω standard resistor (potential drop, 60 mV) in series with two 10,000-Ω standard resistors. Potential drops across the resistors were measured using a White double potentiometer [4] (range 0 to 100 mV), which, at the conclusion of the series of runs, was calibrated for internal consistency of steps on the two largest decades. The dial corrections (max: 1.3 μV) agreed well with an absolute calibration made in 1943 by the Resistance Section, NBS. An auxiliary circuit consisting of a 100-Ω and a 1,000-Ω standard resistor was used to establish a 100/1100 fraction of standard cell voltage for determination of potentiometer ratio [5] at the conclusion of each run. Interpolations of the last-dial readings to zero galvanometer deflection, correction for external parasitic emf (usually zero, sometimes barely detectable), dial corrections (from the present calibration), and potentiometer ratio (0.9998958 to 0.9999586) were applied. The solenoid switch, a common dc relay, was manually armed prior to a selected second, triggered by a second relay activated by an amplified pulse of the NBS time signal, and then promptly bypassed and rearmed for the reverse switching operation. (The arming process resets the electrical circuits so that in each relay the movement of the armature is the same in the forward and reverse switching operations.) The electrical elements used in the calibration had recently been certified by the Electricity Division, NBS: the saturated cadmium standard (i.e., Weston normal) cell, thermostated at 30.2 °C, had a voltage of 1.018091 V±3 μV and the standard resistors were certified to ±7 ppm. Additional small circuit resistances in connecting wires, where applicable, were measured to within 2 ppm of the total circuit resistance involved.

The masses of the $Mg_2P_2O_7$ (see sec. 5) in the crucibles (about 20 g with crucible) were obtained by the substitution mode of weighing on a balance of sensitivity of 5 div/mg (20-g load) and standard deviation of ±0.1 div (0.020 mg). The weighings of a crucible with and without $Mg_2P_2O_7$ always involved the same integral-gram pieces of the weight set, the difference being accounted for by the fractional-gram pieces only. The net change in the number of weights used never amounted to more than seven pieces. The fractional-gram pieces were intercompared in an internal calibration using the reversal mode of weighing. These weighing observations were found to agree within 0.020 mg of the differences given by an official Class-S calibration by the NBS Mass Section in 1961, which was used for corrections to the nominal values of the weights in calculating the masses of the $Mg_2P_2O_7$. Buoyancy corrections were made on all weighings of $Mg_2P_2O_7$ (sec. 7).

4. Experimental Procedure

The chlorination runs were carried out with about 0.6 g of white phosphorus, except in the case of Run No. 2 (0.97 g). A sealed reaction ampoule was first attached to the bottom of the chlorine inlet tube with a fresh portion of wax and the bottom of the ampoule was cooled to remove any phosphorus from the upper tubular portions by vaporization.

The amount of water used in the calorimeter was adjusted for each run, based on the measured external volume of the reaction ampoule, to maintain the same level in the Dewar flask throughout the series of runs and calibrations.

After assembly, the calorimeter was placed in the water bath and the spherical-joint connection to the chlorine supply line was made up with wax. The lines were then alternately evacuated to the break-bubble on the reaction ampoule and pressurized with chlorine a few times, after which the line was maintained at about 200 mmHg above atmospheric pressure with all supply valves fully open while spilling out a few cm^3/min to waste. After an initial warm-up to a temperature conveniently below the starting temperature, the calorimetric system was allowed to coast until the temperature rise assumed a steady foreperiod rate. At the end of the 20-minute foreperiod, during which time the temperature was read every two minutes on the platinum resistance thermometer, the chlorine-spill valve was closed and the bubble inlet on the ampoule was broken by depressing the breaker (E).

Reaction began spontaneously, proceeded at a steady rate as shown by the temperature rise (0.6 to 1.1°C/min, depending on the individual run) with a bright yellow-green flame of somewhat fluctuating intensity, and terminated abruptly. Reactions in preliminary experiments, conducted with well-evacuated thin wall ampoules, proceeded with a fluctuating slower rate, terminated with a gradually decreasing rate, and resulted in unreacted phosphorus in the products.

[3] Certain commercial materials and equipment are identified in this paper in order adequately to specify the experimental procedure. In no case does such identification imply the recommendation or endorsement of the National Bureau of Standards, nor does it imply that the material or equipment is best for the purpose.

Thick-wall ampoules (about 1.2 mm thick) were found to be essential for a good reaction. A separate study of the air-conductance of the line indicated that, at the rates of flow of chlorine gas during the reaction periods, all parts of the line remained at atmospheric pressure or greater. Temperature readings were taken every 0.2 °C during the fast part of the temperature rise, which amounted to about 2.5 °C. Reaction stopped abruptly after 4 min, whereupon the chlorine pressure was reduced to atmospheric and the chlorine inlet to the ampoule was closed by drawing up the breaker (E) so that the wide part of the glass sealed the chlorine inlet at the fluorocarbon O-ring (T_1). After the fast temperature rise, about 15 min were required for "equilibration." During this time the temperature was read every minute. After a total reaction period of 22 min, readings were taken every 2 min during a 20 min after-period.

The calorimeter was disassembled and the reaction ampoule was removed by warming the wax. The reaction ampoule was then broken open at the neck and the contents were immediately analyzed as described in section 5.

Electrical calibrations were carried out with an empty reaction ampoule. The chlorine inlet tube (S) was not connected to the chlorine-supply line. Heating times of 12 min and total reaction periods of 22 min were used.

5. Chemical Analysis of Products

The contents of the reaction ampoule, consisting of PCl_5, PCl_3, and unreacted chlorine gas, were hydrolyzed by aqueous hydrazine hydrochloride. This reduced the free chlorine to chloride ion and converted the PCl_5 and PCl_3 to phosphoric and phosphorous acids. Phosphorous acid was determined iodimetrically in one aliquot following a selective oxidation of the excess hydrazine by iodine. Total phosphorous was determined gravimetrically as orthophosphate in separate duplicate aliquots after the lower valence forms of phosphorus had been oxidized by bromine. The details of these procedures and examination of the reaction products for other phosphorus compounds are described in the remainder of this section.

The disengaged ampoule containing the reaction products was broken open at the neck, just above the reaction chamber, and the small amount of PCl_5 in the tubular portion was washed with water into approximately 200 cm^3 of water containing 100 mg of hydrazine dihydrochloride in a 500-cm^3 Erlenmeyer flask with fluorocarbon-gasketed glass-stoppered closure. The reaction chamber, containing nearly all the products of reaction, was then placed in the Erlenmeyer flask which was tightly closed and shaken. The first portion of water to enter the chamber caused a rapid evolution of HCl gas which violently expelled the unreacted chlorine and resulted in a momentary pressure rise in the Erlenmeyer flask. The chamber then immediately filled with the aqueous solution and the remaining PCl_5 was converted to liquid $POCl_3$ which, in a few minutes, was hydrolyzed to H_3PO_4 and more HCl. The contents of the Erlenmeyer were then washed through a No. 40 (Whatman) paper into a 1-litre volumetric flask. The total amount of phosphorus was determined in duplicate volumetric 200/1000 aliquots. Duplicate 50/1000 aliquots were also taken, diluted to approximately 200 cm^3, and treated in the same manner as the larger aliquots as a check of completeness of analytical recovery. The temperatures of the volumetric glassware were noted, where applicable, and corrections were made on the basis of recent calibrations. The aliquots, about 0.1 *N* in HCl, were exposed overnight to bromine [7] vapors in a closed space, acquiring a deep bromine color, and were then heated for a few hours to about 80 °C to drive off the excess bromine. The phosphorus was precipitated, dissolved, and reprecipitated as $MgNH_4PO_4$ [8], filtered on a crucible of Selas sintered procelain of porosity 10 and ignited to constant weight on the Selas crucible at 900 °C.

Analysis of the products of the preliminary experiments, in which the reprecipitated $MgNH_4PO_4$ on ashless filter paper in ordinary porcelain crucibles was ignited at 1050–1100 °C, was hindered by difficulty in obtaining constant weight. The ignited $Mg_2P_2O_7$ usually showed a persistent gray to black discoloration despite efforts to burn the paper off at a temperature below 900 °C before completing the ignition. The conversion to $Mg_2P_2O_7$ actually takes place at a relatively low temperature, at 250 °C [9] or at 477 °C [10], and filter paper, alone, can be ignited to a colorless ash at 675 °C [10]. Treatment of the precipitate with aqueous ammonium nitrate before and after ignition [11, 12] was ineffective in removing the discoloration.[4] Ignitions on Selas crucibles without paper yielded constant weight after 1 h at approximately 900 °C; prolonging the ignition overnight at this temperature did not result in further weight loss.

The unreacted hydrazine dihydrochloride and the trivalent phosphorus were determined iodimetrically according to the reactions:

$$N_2H_4 + 2I_2 + 4HCO_3^- \rightarrow N_2 + 4I^- + 4H_2O + 4CO_2 \quad (1)$$

and

$$HPO_3^{=} + I_2 + 2HCO_3^- \rightarrow HPO_4^{=} + 2I^- + H_2O + 2CO_2 . \quad (2)$$

Reaction (1) proceeds rapidly and quantitatively if the pH of the solution is between 7.0 and 7.4 [13]. Such solutions, however, are easily oxidized by air. Reaction (2) proceeds slowly but quantitatively [14] in sodium bicarbonate solution and is carried out with an excess of I_2 which is subsequently back titrated. A 200-ml aliquot was added to an iodine flask containing 5 g of KI and 12 g of $NaHCO_3$ while flushing with CO_2 (from "dry ice"). The solution, while being

[4] Treadwell and Hall [11] state that the precipitate can be whitened by moistening with strong acid and carefully reheating. McNabb [12] says that the unignited or ignited precipitate can be dissolved in HNO_3, but the acid solution must be neutralized with ammonia before heating, to yield white $Mg_2P_2O_7$ of correct weight.

533-558 OL - 74 - 5

vigorously agitated and flushed with CO_2, was titrated with 0.1 *N* I_2 in 0.25 *N* KI to the first permanent perceptible yellow of free iodine. Then 5 ml excess of the 0.1 *N* iodine solution was added by means of a pipette and the flask was capped, sealed with aqueous KI, and set aside to allow reaction (2) to occur. A blank, containing similar amounts of H_3PO_4, HCl and $NH_2NH_2 \cdot 2HCl$, was treated in a similar manner using the same volume of iodine solution. About 1 to 2 h later the excess iodine was back titrated with 0.0400 *N* sodium arsenite (NBS Standard Sample 83a). The difference in the back-titers was calculated as phosphite, according to eq (2).

While performing the direct iodine titration of hydrazine in the CO_2-blanketed neutral solutions containing phosphite ion, vigorous agitation was maintained, by magnetic stirrer, to prevent oxidation of phosphite ion by local concentrations of I_2. The method was tested on various mixtures containing known amounts of hydrazine and phosphorous acid. It gave values for both constituents which were estimated to be accurate to ± 0.004 milliequivalents in the aliquot.

The hydrolyzed products of the preliminary experiments, many of which contained unreacted phosphorus, were examined for various inorganic compounds of phosphorus. In one procedure, the orthophosphate in a 300/1000 aliquot was separated, before bromine treatment, from the other compounds of phosphorus by precipitation and reprecipitation under CO_2 as $MgNH_4PO_4$. The combined filtrates were then treated with bromine vapors and the converted forms of phosphorus were precipitated and reprecipitated as $MgNH_4PO_4$. The weight of the second precipitate from samples containing up to 7 percent phosphorous acid (based on total phosphorus) was in good agreement with the iodimetrically determined phosphite. The estimated uncertainty of the comparison, obtained from the combined uncertainties of the two methods, was ± 0.023 mmol phosphorus for the whole sample. The methods agreed within this range. Becker and Johnson [15] found that a double precipitation of $MgNH_4PO_4$ effects a complete separation of phosphite from orthophosphate.

The amount of hypophosphite in the hydrolyzed reaction products of the preliminary runs was found by another method to be negligible. In this procedure, the sum of hypophosphite plus phosphite was determined by iodimetric oxidation in acid solution to H_3PO_3, and then, in neutral solution, to H_3PO_4 [14]. When subtracting the values obtained for phosphite in separate iodimetric phosphite determinations (by the methods described above), small negative and positive values were obtained for the amount of hypophosphite present. These values were all within the limit of error of ± 0.033 mmol/run.

Three of the preliminary runs were examined for various phosphorus compounds by one-dimensional chromatography on Schleicher and Schuell Paper No. 589 GR. The hydrolyzed reaction products of these runs were diluted to 1 litre. Aliquots (10 cm^3) were neutralized with ammonia, evaporated at room temperature to 1 cm^3, and applied as single and triple spots. Some were irrigated by Ebel's basic solvent 1° [16] and others by Ebel's acid solvent 1°. The irrigated papers were first exposed to bromine vapor to convert the nonorthophosphate areas to orthophosphate, and then were sprayed with molybdic acid, heated, and sprayed with stannous chloride to develop the molybdenum blue color. Tests of the procedure with known mixtures of orthophosphate, phosphite, hypophosphite, pyrophosphate, triphosphate, trimetaphosphate, and tetrametaphosphate showed that these compounds migrated under both acid and alkaline conditions as described by Ebel, and that the lower limit of identification of each compound was about 100 ppm phosphorus in the solution applied to the paper. The applied spots of hydrolyzed products contained up to 15,000 ppm P (1.5 percent) as orthophosphate and 1100 ppm P as phosphite. At no time was overloading of the paper apparent. No phosphorus compounds other than orthosphosphate and phosphite were observed on the test papers irrigated by basic solution. Thus, since the lower limit of identification of any single species is 100 ppm, we may estimate, on the basis of results of the test with the product solution containing 1100 ppm of phosphite, that the concentration of any other form of phosphorus compound is less than 10 percent of the concentration of the phosphite. Acid irrigation of papers spotted similarly showed only one spot, that of the orthophosphate and phosphite (unseparated).

Two-dimensional chromatography of a synthetic mixture first with the alkaline and then with the acid solution, resulted in the expected array of individual compounds but with reduced sensitivity, the lower limit of detection being 300 ppm P in any compound. Two-dimensional chromatograms were not made of the test solutions.

One-dimensional chromatograms were made of one sample applied as stripes in two concentrations (3200 and 200 ppm P as phosphate and phosphite; 9500 and 600 ppm P as phosphate and phosphite). Here the sensitivity was increased (probably because of the cancellation of the effect of lateral diffusion of the phosphorus compounds during irrigation) to an estimated 50 ppm. No species other than phosphate and orthophosphate were evident. An acid irrigation of a similarly striped paper showed only the phosphate stripe (with phosphite not separated from the phosphate).

A review of the literature indicates that there is no reason to expect the formation of species other than PCl_5 and PCl_3 in the products of the chlorination reaction. P_2Cl_4 has been prepared only by electrical discharge [17, 18]; also it decomposes below 25 °C. No other chlorides of phosphorus have been described as existing under normal conditions.

6. Units and Physical Constants

The calorie (cal) used is the thermochemical calorie which is 4.184 J. The molecular weight of $Mg_2P_2O_7$

is 222.5534 ± 0.0014, from the 1969 Table of Atomic Weights [19].

7. Experimental Results

The results of the electrical calibrations are given in table 1. ΔR_c corresponds to the corrected temperature rise [20] measured on the platinum resistance thermometer. E_e is the quantity of electrical energy introduced into the system. E_s is the energy equivalent of the standard calorimetric system defined as the solid parts of the calorimeter (always wetted to the same height), 857.50 g water and 17.00 g glass reaction ampoule. ΔE_s is the increase in energy equivalent of the real system calculated from the specific heats of additional water used (4.1802 J/g), the additional glass of the reaction ampoule (0.20 cal/g), the wax to attach it (0.69 cal/g) and the amount of phosphorus used (none in the calibration runs; 0.19 cal/g). The large deviation in E_s for run 4 is attributed to a 1 s error in arming the switching circuit at the end of the heating period. The water used in the calorimeter accounts for 94.4 percent of the energy equivalent.

TABLE 1. *Results of the electrical calibrations*

Run No.	ΔR_c Ω	Mid temp. °C	E_e J	ΔE_s J/Ω	E_s J/Ω
1	0.240627	23.68	9,272.69	592.61	37,942.92
2	.251235	23.71	9,680.98	589.49	37,944.07
3	.251522	23.68	9,692.94	593.68	37,943.47
4	.246657	23.66	9,514.80	578.05	37,996.98
5	.245257	23.68	9,448.30	579.92	37,944.16
6	.258372	23.71	9,953.36	580.54	37,942.83
7	.246515	23.62	9,495.99	579.72	37,941.22
Mean of Runs 1–3, 5–7		23.68			37,943.11
Estimated standard deviation of the mean					±0.44

The results of the chlorination runs, all of which proceeded rapidly and terminated abruptly, are given in table 2. The heat produced by chlorination of the white phosphorus is expressed as joules per gram mass of $Mg_2P_2O_7$ precipitated from the bromine-treated products. This quantity, denoted h, is calculated by the formula:

$$h = \frac{f[(37{,}943.11 + \Delta E_s)\Delta R_c + 12.38\,v - 0.479(1.594\,w/f + 0.100)\Delta t]}{1.00032\,w}$$

f = the aliquot fraction of the total of the hydrolyzed products in which, after bromine treatment, the total phosphorus was determined as $Mg_2P_2O_7$. E_S is 37,943.11 J/Ω (see table 1).

v = the difference in back-titer, ml of 0.0400 N As^{3+}, between the blank and a 200-ml aliquot; the quantity 12.38 v is the heat which would have been liberated by chlorination of the PCl_3 in the products, obtained as[5]

$$\frac{v(\text{ml}) \times 0.0400\,N}{2\ \text{meq/mmol}} \times 5 \times 29.6 \frac{\text{cal}}{\text{mmol}} \times 4.184 \frac{\text{J}}{\text{cal}}$$

w = the weight of $Mg_2P_2O_7$ in air

Δt = the amount by which the calorimeter temperature at the end of the reaction period (the reaction temperature) is exceeded by the average room temperature.

1.594 $w/f + 0.100$ = the calculated mass of chlorine consumed by the reaction, plus that required to fill, in the average case, the internal volume of the ampoule less the volume of the PCl_5.

0.479 J/°C · g is the specific heat of chlorine gas [1].

1.00032 ± 0.00001 is the buoyancy factor for $Mg_2P_2O_7$, density = 2.56 g/cm³ weighed versus brass in air, density = 1.16 mg/cm³.

P^{3+}/P in table 2 is the mol ratio of trivalent phosphorus to total phosphorus in the products, equal to 0.00225 v/w).

The pressure of chlorine gas was about 980 mmHg; the average value of the temperature at the end of the reaction period was 24.87 °C.

The amount of $Mg_2P_2O_7$ obtained from the 50-ml aliquots (diluted to and treated as 200-ml aliquots), was very close to exactly one fourth of that obtained from the 200-ml aliquots. The average loss in the 50-ml aliquots was only 0.001 ± 0.051 (std devn) mg $Mg_2P_2O_7$, indicating that no correction is necessary

[5] The heat of chlorination of PCl_3 to PCl_5 is 29.6 kcal/mol [1].

TABLE 2. *Results of the phosphorus chlorinations*

Run	Final temp. °C	Mid temp. °C	f	ΔE_s J/Ω	ΔR_c Ω	v ml	Δt °C	w g	h J/g	P^{3+}/P
1	24.87	23.53	.1999782	99.19	.265957	1.74	2.63	.508285	3,985.787	.000762
2	24.83	23.00	.1999427	115.93	.366052	3.20	2.97	.700229	3,985.741	.01018
3	24.78	23.60	.2000179	404.70	.234310	0.81	−0.58	.451336	3,985.625	.00399
4	25.10	23.90	.1999860	476.87	.238413	.05	−0.50	.459166	3,988.871	.00024
5	24.96	23.69	.1999924	580.49	.252663	.08	3.24	.488012	3,985.489	.00036
6	24.77	23.50	.1999896	528.19	.253536	.30	2.73	.489102	3,986.393	.00136
Mean	24.89	23.54							3,986.32	
Estimated standard deviation of the mean									±0.53	

for loss of phosphorus during the double precipitation procedure.

Since there is no trend in the calculated value of h with increasing mole fraction of trivalent phosphorus in the products (up to 1%) we may conclude that the value taken for the molar heat correction for trivalent phosphorus contributes no appreciable systematic error. The heat calculated in this way is the enthalpy of reaction.

The estimated over-all standard deviation, taking into account other probable errors (see sec. 8), is ± 1.36 J/g $Mg_2P_2O_7$. Therefore, using an uncertainty level which is twice the overall standard deviation [22], we obtain a value −3,986.32 ± 2.72 J/g $Mg_2P_2O_7$ or −443.585 ± 0.303 kJ/mol PCl_5 (−106.019 ± 0.072 kcal/mol PCl_5) for the enthalpy of reaction, at 24.89 °C, of phosphorus with chlorine at 980 mmHg.

To adjust this value to the reaction taking place at 25 °C with chlorine gas in the ideal state we must apply small corrections for the relative enthalpy of the chlorine (real gas) and the $\Delta Cp°$ of the reaction. From the work of Ross and Maass [23] we can derive a value of −108 J/mol for $(H-H°)$ of chlorine gas at 298 K, 1.29 atm (980 mmHg). For 2 1/2 mol chlorine per g-atom phosphorus the enthalpy correction is −270 J/g-atom P.

The heat capacity at 25 °C of $P(c, \alpha)$ is 23.8 J/(g-atom K) and of chlorine gas (ideal) is 33.9 J/(mol K) [1]. There appears to be no value for the heat capacity of $PCl_5(c)$ in the literature. However, the absolute entropy of $PCl_5(c)$ at 298 K is estimated to be 39.8 ± 2.0 cal/(mol K) [24]. From this estimate, we may estimate that the specific heat is 120 ± 50 J/(mol K). Thus, the $\Delta Cp°$ of the reaction is 12 ± 50 J/(mol K) and, hence, the correction to 25 °C is 1 ± 2 J/mol.

The standard enthalpy of formation of PCl_5 at 25 °C, therefore, is

$$\Delta Hf°_{298.15}\,[PCl_5(c)] = -443.854 \pm 0.303 \text{ kJ/mol}$$

$$= -106.084 \pm 0.072 \text{ kcal/mol.}$$

This quantity corresponds to the reaction

$$P(c, \alpha) + Cl_2(g) \rightarrow PCl_5(c).$$

8. Uncertainties

The estimated maximum systematic error in the electrical calibration is ±39 ppm. The uncertainties which contribute chiefly to this estimate are in the measurement of the voltage drop across the total-current-measuring resistor (12 mV ± 0.2 μV, i.e., 17 ppm) and the operation of the switching device (750 s ± 0.02 s, i.e., 27 ppm).

The estimated standard deviation of the mean of the calibration runs calculated by the method of Rossini [22] is 0.44 J/Ω, which is 12 ppm.

The estimated maximum systematic error in the chemico-analytical determination of the amount of reaction is 312 ppm, obtained as the square root of the sum of the squares of the following probable errors:

aliquot factor (for total phosphorus determination): 200 ppm

phosphite determination

$$\frac{\pm 0.1 \text{ ml} \times 0.040N}{\text{aliquot}} \times \frac{1 \text{ mmol}}{2 \text{ mequiv}} \times \frac{1000 \text{ ml/run}}{200 \text{ ml/aliquot}} = \pm 0.010 \text{ mmol } PCl_3\text{/run}$$

$$\frac{\pm 0.010 \text{ mmol } PCl_3\text{/run}}{22 \text{ mmol total P/run}} \times \frac{29.7 \text{ cal/mmol } PCl_3}{106 \text{ cal/mmol } PCl_5} = \quad 117 \text{ ppm}$$

weight corrections for weighing $Mg_2P_2O_7$:

0.03 mg/0.5 g = 60 ppm

conversion of H_3PO_4(aq) to $Mg_2P_2O_7$:

0.1 mg $Mg_2P_2O_7$/0.5 g $Mg_2P_2O_7$ 200 ppm

presence of phosphorus-chlorine compounds other than PCl_3 and PCl_5 (assumed) 0 ppm.

The estimated standard deviation of the mean of the chlorination runs is 0.53 J/g $Mg_2P_2O_7$, i.e., 133 ppm.

The overall standard deviation assigned to the observed enthalpy of chlorination is taken as the square root of the sum of the squares of these four values according to the method of Rossini [22, p. 316]: 342 ppm × 3,986.32 J/g $Mg_2P_2O_7$ = ± 1.36 J/g $Mg_2P_2O_7$.

9. Discussion

The references to papers we discuss in this section are summarized in table 3. There are only two previous measurements of the enthalpy of chlorination of phosphorus; both measurements, carried out more than a hundred years ago, used white[6] phosphorus. Abria [25] obtained 3199 cal/g P (no details), i.e., 99.1 kcal/mol. Andrews [26] reacted in a closed glass vessel at about atmospheric pressure a known volume of chlorine, measured dry at 11.4 °C and 29.85 in Hg, with an excess of phosphorus. In two runs he obtained 1924.6 and 1926.1 g-cal/(1000 cm^3 Cl_2 at 0 °C, 1 atm). Average calorimeter temperature during the runs was 11.6 °C. The contribution of the reactants or products to the heat capacity of the system was about 0.1 percent of the total value and appears to have been neglected. Converting these values to conventional units we have:

[6] In the literature white phosphorus has consistently been regarded as the ordinary form; when the red form was used the investigator usually specified it as such. White phosphorus was also known as yellow phosphorus because of discoloration by an indeterminate though thermochemically negligible amount of the red variety.

$$\Delta U(11.6\,^{\circ}\mathrm{C}) = -1.9254 \times (22{,}413.6/1000) \times 1.0135 \times 5/2 \times (4.1899/4.184) = -109.499 \text{ kcal/mol P}$$

If we assign an optimistic uncertainty of ±50 cal to Andrews' value for the reaction with 1000 cm^3 Cl_2, we derive an uncertainty of 2.9 kcal/mol P in the above molar enthalpy of reaction. It carries a negative bias, however, in that a considerable undetermined amount of PCl_3, formed because of excess phosphorus, leads to a high value of liberated heat per mol Cl_2.

TABLE 3. *Important reactions in the thermochemistry of phosphorus*

Investigator, Year	Reference	Reaction	Stand · enthalpy change, kcal/g atom P
		Chlorination	
Abria, 1846	[25]	$P + 5/2\ Cl_2(g) = PCl_5$	−99.1 (temperature not stated).
Andrews, 1848	[26]	$P + 5/2\ Cl_2$(g, 29.85 in Hg, 11.4 °C) = PCl_5	−110.9 (too negative because of PCl_3).
This work, 1972		$P + 5/2\ Cl_2$(g, 980 mmHg)	−106.084.
		Hydrolysis of Chloride	
Favre, 1853	[29]	PCl_5 + [large excess H_2O] = [H_3PO_4 + 5HCl, aq]	−137 at 15 °C(?).
Berthelot and Louguinine, 1875	[30]	PCl_3 + [~1100 H_2O] = [H_3PO_4 5HCl + ~1096 H_2O]	−119.4.
Thomsen, 1882	[21]	PCl_5 + [~2000 H_2O] = [H_3PO_4 + 5HCl + ~1996 H_2O]	−123.8.
Birley and Skinner, 1968	[28]	PCl_5 + [x H_2O] = [H_3PO_4 + 100H_2O] + [5HCl + (x − 104)H_2O]	−129.21 when x = 4000. −130.14 when x = 8500.
		$\Delta Hf°$[H_3PO_4 in 100H_2O] = −309.88 ± 0.36 kcal, based on PCl_5 value of present work	
		Combustion, Hydrolysis	
Head and Lewis, 1970	[31]	[P] + 5/4 O_2(g) + [2.078 H_2O] = [H_3PO_4 + 0.578 H_2O]	−203.12 ± 0.07 at 52.1 °C.
		[H_3PO_4 + 0.578 H_2O] + [39.422 H_2O] = [H_3PO_4 + 40 H_2O]	−4.30 ± 0.03 at 52.1 °C.
		sum adjusted to 25 °C, 100 H_2O: $\Delta Hf°$[H_3PO_4 in 100H_2O] = −309.49 ± 0.40 kcal	
		Bomb Combustion (since 1900)	
Giran, 1903	[34]	$P + 5/4\ O_2$(g, 15–20 atm) = 1/4 P_4O_{10} (orthorh.)	−180.1 (for hexagonal P_4O_{10}).
Holmes, 1962	[2]	$P + 5/4\ O_2$(g, 25 atm) = 1/4 P_4O_{10}	−178.3 ± 0.25.
Egan and Luff, 1963	[33]	$P + 5/4\ O_2(g) = 1/4\ P_4P_{10}$	−179.84 ± 0.50.
		Hydrolysis of Oxide	
Holmes, 1962	[2]	1/4 P_4O_{10} + [1.5 H_2O] = H_3PO_4 (cryst.) (author's reactions 3, 4, 5)	−24.921 ± 0.15 (−25.035 at 33 °C).
		H_3PO_4 (cryst.) + [363H_2O] = [H_3PO_4 + 363H_2O] sum adjusted to 100 H_2O:	−2.65 ± 0.10.
		1/4 P_4O_{10} + [101.5 H_2O] = [H_3PO_4 + 100 H_2O]	−27.39 ± 0.19.
		1/4 P_4O_{10} + [1.5 H_2O] = [H_3PO_4] (author's reactions, 3, 4, 8)	−21.338 ± 0.15.
		[H_3PO_4] + [375 H_2O] = [H_3PO_4 + 375 H_2O] sum adjusted to 100 H_2O:	−5.51 ± 0.10.
		1/4 P_4O_{10} + [101.5 H_2O] = [H_3PO_4 + 100 H_2O]	−26.67 ± 0.19.
Irving and McKerrel, 1967	[35]	1/4 P_4O_{10} + [2.1416 H_2O] = [H_3PO_4 + 0.6416 H_2O] adjusted to [H_3PO_4 + 100 H_2O] at 25 °C: $\Delta Hf°$[H_3PO_4 in 100H_2O] = −309.88 ± 0.5 kcal using results of Egan and Luff	−23.702 at 58.96 °C

Unless otherwise specified, the states are crystalline (white P; hexagonal P_4O_{10}), temperature is 25 °C; the term cryst. is used redundantly for emphasis.

4.1899 J/g, °C is the heat capacity of water at 11.6 °C [27]. The value 1.0135 is the compressibility factor of chlorine at 11.4 °C and 29.85 in Hg, evaluated from the third equation of p. 62 of reference [23]. Whence,

$$\Delta H°(25\,^{\circ}\mathrm{C}) = -109{,}499 + (-(5/2)\ R\ (284.55)) + (25 - 11.6)(3)\ \text{cal} = -110.9 \text{ kcal/mol P.}$$

The enthalpy of hydrolysis has been measured in four investigations, only one of which is recent. Birley and Skinner [28] measured the heat liberated at 25 °C when crystalline vacuum-sublimed PCl_5 was hydrolyzed to orthosphoric acid, H_3PO_4, in 4000 to 8500 mol of water, in an isoperibol[7] solution calorimeter. Reac-

[7] An isoperibol calorimeter is a calorimeter in a constant-temperature environment.

tion times of up to 30 min were required for completion of the reaction. Separately measured values of the heat of mixing of H_3PO_4(aq) with HCl(aq) in the same apparatus enabled them to calculate each run as a reaction whose products were H_3PO_4 in 100 mol of water, separate from the HCl(aq) produced. In calculating the $\Delta Hf°(H_3PO_4$ in 100 $H_2O)$ from their calorimetric measurements they used our preliminary value [1], $\Delta Hf°(PCl_5, c) = -106.0$ kcal/mol based on the present work. Substituting our final value, we have, for the hydrolysis reaction of Birley and Skinner[8]

$$\Delta Hf°(H_3PO_4 \text{ in } 100\ H_2O) = -1296.6 \pm 1.5 \text{ kJ/mol}$$
$$= -309.88 \pm 0.36 \text{ kcal/mol.}$$

Here, the uncertainty in PCl_5 does not contribute appreciably to that assigned to H_3PO_4 (aq). The chief source of the uncertainty assigned by [28] is the slowness of the hydrolysis reaction. The hydrolysis of PCl_5 in water takes place in two steps:

$$PCl_5(c) + H_2O(l) \rightarrow POCl_3(l) + 2\ HCl(aq)$$

and

$$POCl_3(l) + 3H_2O(l) \rightarrow (H_3PO_4 + 3\ HCl)\ (aq).$$

Although we performed no calorimetric hydrolyses, "bench-top" experiments in this laboratory indicated that if the $PCl_5(c)$ is introduced into the water by breaking an evacuated ampoule, explosive evolution of HCl(g) occurs, according to the first reaction; if the ampoule contains air at about one atmosphere the initial step still is extremely rapid but not eruptive. The second step proceeds slowly at the interface between the two liquid phases with the moderate stirring which normally occurs in a calorimetric vessel, requiring up to 30 minutes as found by Birley and Skinner [28] and by Thomsen [21]. However, if the aqueous phase in the vicinity of the $POCl_3(l)$ can be kept in an unstirred condition for a short time the heat of the second step warms the $POCl_3(l)$ to its normal boiling point and the reaction is completed in about 5 min. We did not investigate the effect of using aqueous alkali or of increasing the stirring to break up the $POCl_3$ into small drops.

The enthalpy of hydrolysis was measured also by Thomsen [21], giving −123.2 kcal/mol at 22.6 °C in 2000 H_2O, when adjusted to 25 °C: −123.8 kcal/mol), and by Berthelot and Louguinine [30], giving −116.9 kcal/mol, in 1100 (?) H_2O probably at 15 °C (when adjusted to 25 °C: −119.4 kcal/mol). In citing these results we use an estimated $\Delta Cp = -250$ cal/°C for the reaction, correct the erroneous molecular weight used by Berthelot and Louguinine, and multiply their 0 °C-calories by 1.0076 to convert to thermochemical calories. Favre [29] reported $\Delta H = -136.9$ kcal/mol in a large excess of water, probably at 15 °C. A comparable result of Birley and Skinner at 25 °C in 4000 H_2O is −129.2 kcal/mol. Both Birley and Skinner [28] and Berthelot and Louguinine [30] found little dependence of the result on the H_2O/PCl_5 ratio.

Another thermochemical route to aqueous orthophosphoric acid lies through the combustion of white phosphorus and hydrolysis of the resulting phosphorus pentoxide,[9] P_4O_{10}, by a strong aqueous acid at an elevated temperature. The phosphorus is usually protected by a combustible material, such as polyethylene, against premature reaction with oxygen. The use of glass ampoules has not been reported. There is a strong likelihood of reaction of the P_4O_{10} with the glass; combustion reactions involving phosphorus are frequently accompanied by undesired interaction with other materials present [31, p. 702].

The most successful work along this line, and the most recent in the thermochemistry of aqueous orthophosphoric acid, seems to be that of Head and Lewis [31]. They measured the sum of the two steps as a single procedure burning polyethylene-encapsulated liquid phosphorus at 50 °C in oxygen, apparently at a pressure of 10 bar, in a platinum-lined rotating bomb containing 60 weight percent $HClO_4$ as a hydrolytic medium. By a judicious choice of two other reactions at 50 °C in the same apparatus, errors in the estimated corrections to standard states (the "Washburn corrections") for the products of the reactions were made to cancel, although there were some side reactions for which corrections were required. As the sum of three separate reactions in the bomb they reported for

$$P(l) + 5/4\ O_2(g) + 2.078\ H_2O(l) \rightarrow (H_3PO_4 + 0.578\ H_2O)$$
$$\Delta U°(52.1\ °C) = -846.51 \text{ kJ/mol},$$
$$\Delta H°(52.1\ °C) = -849.87 \text{ kJ/mol}.$$

In the same apparatus they measured the enthalpy evolved upon further dilution of the H_3PO_4 to the concentration in 40 mol of water:

$$\Delta H° = \Delta U° = -18.00 \pm 0.11 \text{ kJ/mol at } 50\ °C.$$

Finally, adjusting to 25 °C by previously published values they derived:

$$\Delta Hf°(H_3PO_4 \text{ in } 40\ H_2O) = -1294.3 \pm 1.6 \text{ kJ/mol}.$$

Diluting further [1], we can derive:

$$\Delta Hf°(H_3PO_4 \text{ in } 100\ H_2O) = -1294.9 \text{ kJ/mol}$$
$$= -309.49 \pm 0.40 \text{ kcal/mol}$$

in good agreement with the value based on the formation and hydrolysis of PCl_5.

Attempts at a direct measure of the combustion step alone have not been entirely satisfactory. The difficulty

[8] Here, and in instances to follow, we combine and compare our results, based on the 1969 Table of Atomic Weights, with other results, apparently based on the 1961 Table. However, it does not seem necessary to make adjustments for this change because all recently published results reviewed in this paper seem to be calculated for a mole of reaction defined by the directly measured mass of P or P_4O_{10} whose molecular weights were not changed. The decrease of 63 ppm for $Mg_2P_2O_7$, therefore, is not applicable here.

[9] Throughout this paper P_4O_{10} signifies the hexagonal form of phosphorous pentoxide described by Hill, et al. [32].

seems to be in the uncertainty in the final products arising from the presence of water as a product of the combustion of the material used to enclose the phosphorus in order to prevent premature reaction.

The most reliable work on the combustion of phosphorus (white) appears to be that of Egan and Luff [33] who obtained widely scattered results in a steel bomb, most of them with coated phosphorus. One series of runs was performed in a double-compartment bomb in which uncoated phosphorus under helium was isolated from the pressurized-oxygen compartment until the beginning of the reaction period; although in this case the formation of water was avoided, the reaction was not complete. On the basis of selected runs in the various series (less than two thirds of those reported) they obtained $\Delta Hf°[P_4O_{10}$ (*c*, hex.)] $= -719.4 \pm 2.0$ kcal/mol.

Holmes [2] carried out similar combustions of coated white phosphorus obtaining -713.2 ± 1.0 kcal/mol.

Ignoring the work of the nineteenth century on the combustion of phosphorus [25], [26], which is of considerable historical interest (it is interesting to note here that Berthelot does not seem to have performed any phosphorus combustion), we might consider the work of Giran [34] who appears to have been the only one ever to carry out calorimetric combustion of phosphorus without interfering foreign substances. Working under carbon dioxide, he covered a solid fused mass of white phosphorus in a porcelain crucible with a light compact layer of red phosphorus which prevented oxidation until combustion was triggered in 15 to 20 atm pressure of oxygen in a porcelain-lined bomb. The adverse criticism by Holmes [2] with regard to Giran's handling of the phosphorus is not considered valid; it seems to have arisen from a misreading of Giran's text. Giran found the energy ($-\Delta H$?) of combustion to be 184.7 kcal per 31 grams of phosphorus. This value should be multiplied by 0.9937 to correct for air buoyancy during weighing of the phosphorus and for change in the accepted values of the enthalpies of combustion of the materials with which Giran calibrated his apparatus. Giran's product seems to have been the orthorhombic form of P_4O_{10} (he called it amorphous) which is more stable than the common (hexagonal) form usually produced in bomb work and which has an enthalpy of formation which is 13.7 kcal more negative. The formation of orthorhombic P_4O_{10} can be attributed to the slower cooling of the combustion product on the enamelled walls. With an additional adjustment (from 15 to 25 °C) equal to -0.073 kcal we have

$$\Delta Hf°\ (P_4O_{10}, \text{hex.}) = (-184.7) \times 0.9937 \times 4 + 13.7 - 0.07 = -720.5 \text{ kcal/mol.}$$

The enthalpy of hydrolysis of P_4O_{10} has been measured at 58.96 °C by Irving and McKerrell [35] who used 62 percent (9.6 N) aq $HClO_4$ for hydrolysis in an isoperibol solution calorimeter. By combining these results with those for two other dissolution reactions in the same apparatus they found the enthalpy of hydrolysis of P_4O_{10} to form 4(H_3PO_4 in 0.6416 H_2O) is -94.807 kcal: adjusted to 25 °C [36] and to H_3PO_4 in 100 H_2O (25 °C) [1]: -110.260 ± 0.035 kcal. Holmes [2] measured the enthalpy of dissolution of P_4O_{10} in 10.2 *N* $HClO_4$ at 33 °C in an adiabatic calorimeter; the results he obtained, using auxiliary reactions involving crystalline H_3PO_4, adjusted to 25 °C and H_3PO_4 in 100 H_2O are -109.564 kcal; the use of auxiliary reactions involving liquid anhydrous H_3PO_4 led to values which were 0.7 kcal more positive per mol H_3PO_4.

If the selected combustion results of Egan and Luff [33] are combined with the hydrolysis results of Irving and McKerrell [35] and the enthalpy of formation of liquid water [1], we have a third, closely agreeing, value by way of the two-step P_4O_{10} route:

$$\Delta Hf°(H_3PO_4 \text{ in } 100\ H_2O) = -309.88 \pm 0.50 \text{ kcal/mol.}$$

On the basis of the present work and the other investigations cited above, we would recommend the following values, all at 298.15 K:

$$\Delta Hf°(PCl_5, c) = -443.87 \pm 0.20 \text{ kJ/mol} = -106.09 \pm 0.05 \text{ kcal/mol,}$$

$$\Delta Hf°(P_4O_{10}, \text{hex}) = -3008.3 \pm 5.2 \text{ kJ/mol} = -719.0 \pm 1.3 \text{ kcal/mol,}$$

$$\Delta Hf°(H_3PO_4 \text{ in } 100\ H_2O) = -1295.8 \pm 1.3 \text{ kJ/mol} = -309.7 \pm 0.3 \text{ kcal/mol.}$$

This recommendation is in consonance with those of references [28] and [31].

10. References

[1] Wagman, D. D., Evans, W. H., Parker, V. B., Halow, I., Bailey, S. M., and Schumm, R. H., Nat. Bur. Stand. (U.S.) Tech. Note 270–3, (January 1968).

[2] Holmes, W. S., Trans. Faraday Soc. **58,** 1916 (1962).

[3] MacRae, D., and Van Voorhis, C. C., J. Am. Chem. Soc. **43,** 547 (1921).

[4] Prosen, E. J., and Rossini, F. D., J. Res. Nat. Bur. Stand. (U.S.) **33,** 255 (1944).

[5] Prosen, E. J., Maron, F. W., and Rossini, F. D., J. Res. Nat. Bur. Stand. (U.S.) **46,** 106 (1951).

[6] Rossini, F. D., Chapter 4 in Experimental Thermochemistry, F. D. Rossini, Editor, (Interscience Publishers, Inc., New York, New York, 1956).

[7] Greenfield, S., Chapter 5b in Comprehensive Analytical Chemistry, Vol. 1c C. L. Wilson and D. W. Wilson, Editors, (Elsevier Publ. Co., New York, 1962).

[8] Hoffman, J. I., and Lundell, G. E. F., J. Res. Nat. Bur. Stand. (U.S.) **5,** 279 (1930).

[9] Hillebrand, W. F., Lundell, G. E. F., Bright, H. A., and Hoffman, J. I., Applied Inorganic Analysis, 2nd Edition, p. 638 (Wiley and Sons, New York, 1953).

[10] Duval, C., Inorganic Thermogravimetric Analysis, pp. 47, 99 (Elsevier Publ. Co., New York, 1953).

[11] Treadwell, F. P., and Hall, W. T., Analytical Chemistry, 9th English Edition, Vol. **II,** p. 258 (Wiley and Sons, New York, 1942).

[12] McNabb, W. C., J. Am. Chem. Soc. **49,** 891 (1927).

[13] Penneman, R. A., and Audrieth, L. F., Anal. Chem. **20,** 1058 (1948).

[14] Wolf, L., and Jung, W., Z. anorg. u. allgem. Chem. **201,** 337 (1931).
[15] Becker, W. E., and Johnson, R. E., J. Am. Chem. Soc. **79,** 5157 (1957).
[16] Ebel, J. P., Mikrochim, Acta **1954,** 679.
[17] Besson, A., and Fournier, Compt. rend. **150,** 102 (1910).
[18] Sandoval, A. A., Moser, H. C., Inorg. Chem. **2,** 27 (1963).
[19] Commission on Atomic Weights, IUPAC, Pure Appl. Chem. **21,** 91 (1970).
[20] Prosen, E. J., Chapter 6 in Experimental Thermochemistry, F. D. Rossini, Editor, (Interscience Publishers, Inc., New York, New York, 1956).
[21] Thomsen, J., Thermochemische Untersuchungen, Vol **2,** pp. 322, 323 (Barth, Leipzig, 1882).
[22] Rossini, F. D., Chapter 14 in Experimental Thermochemistry, F. D. Rossini, Editor, (Interscience Publishers, Inc., New York, 1956).
[23] Ross, A. S., and Maass, O., Can. J. Research **18B,** 55 (1940).
[24] Kelley, K. K., and King, E. G., U.S. Bur. Mines Bull. No. 592, p. 75, (U.S. Government Printing Office, Washington, D.C. 20402, 1961).
[25] Abria, Compt. rend. **22,** 372 (1846); his paper in Annali di Fisica, Chimica e Matematiche **24,** 269 (1846) is an Italian translation of this.
[26] Andrews, T., Phil. Mag. [3], **32,** 321–339, 426–434 (1848). This is considered to be the first bomb calorimeter, though compressed gas was not used—see Partington, J. R., The History of Chemistry, Vol. **4,** p. 609 (MacMillan and Co., London, 1964); Ostwald, W., Outlines of Gen. Chem., transl. by J. Walker, p. 215 (MacMillan and Co., London, 1890).
[27] Osborne, N. S., Stimson, H. F., and Ginnings, D.C., Nat. Bur. Stand. (U.S.) Handb. 77, Vol. **II,** p. 318.
[28] Birley, G. I., and Skinner, H. A., Trans. Faraday Soc. **64,** 3232 (1968).
[29] Favre, P.-A., J. pharm. chim. [3] **24,** 328 (1853).
[30] Berthelot and Louguinine, Ann. chim. et phys. [5] **6,** 305 (1875). (1875).
[31] Head, A. J., and Lewis, G. B., J. Chem. Thermodynamics **2,** 701 (1970).
[32] Hill, W. L., Faust, G. T., and Hendricks, S. B., J. Am. Chem. Soc. **65,** 794 (1943).
[33] Egan, E. P., Jr., and Luff, B. B., Progress Report, June 1–Nov. 30, 1963, Tennessee Valley Authority, AD 429008. (Natl. Tech. Info. Service, 5285 Port Royal Road, Springfield, VA 22151).
[34] Giran, H., Ann. chim. et phys. [7] **30,** 203 (1903).
[35] Irving, R. J., and McKerrell, H., Trans. Faraday Soc. **63,** 2582 (1967).
[36] Egan, E. P., Jr., Luff, B. B., and Wakefield, Z. T., J. Phys. Chem. **62,** 1091 (1958); the revisions published in J. Chem. Eng. Data **7,** 385 (1962) do not apply here.

(Paper 78A3–818)

JOURNAL OF RESEARCH of the National Bureau of Standards—A. Physics and Chemistry
Vol. 78A, No. 3, May–June 1974

Heat Capacities of Polyethylene from 2 to 360 K. II. Two High Density Linear Polyethylene Samples and Thermodynamic Properties of Crystalline Linear Polyethylene

S. S. Chang

Institute for Materials Research, National Bureau of Standards, Washington, D.C. 20234

(February 13, 1974)

Heat capacities of two high density linear polyethylene samples were measured from 2 to 360 K. By incorporating the results from the previous work of this series, thermodynamic properties of completely crystalline linear polyethylene may be estimated. C_p, $H - H_0$, S and $-(G - H_0)$ at 298.15 K for crystalline linear polyethylene are estimated to be 22.60 J K^{-1} mol^{-1}, 3544 J mol^{-1}, 23.02 J K^{-1} mol^{-1} and 3319 J mol^{-1}, respectively. Spontaneous adiabatic temperature drifts were observed in both samples near 240 K. These drifts may be attributed to the enthalpy relaxation phenomena occurring in the glass transformation region.

Key words: Amorphous polyethylene; calorimetry; crystalline polyethylene; extended chain crystals; glass transition temperature; heat capacity; linear polyethylene; polyethylene; thermodynamic properties.

1. Introduction

The heat capacity behaviors of two high density linear polyethylene samples were studied. These two samples were prepared from the same stock from which the standard reference material SRM 1475 for linear polyethylene whole polymer was established. By crystallizing slowly from the melt in vacuum, the degree of crystallinity of the sample was increased from the original value of 71 to 88 percent, as estimated from their densities. Another sample was crystallized under 5000 atm of pressure. The pressure-crystallized sample was composed mainly of extended-chain crystals and has a degree of crystallinity of 96 percent.

By combining the results from this work and from the previous work [1][1] on a sample of SRM 1475 in the condition as received, the thermodynamic properties of 100 percent crystalline linear polyethylene may be estimated.

Large spontaneous temperature drifts were observed in the temperature range centering around 235–240 K for both samples when quenched or annealed, as well as for the original sample of SRM 1475 after similar quenching and annealing procedures. These drifts, phenomenologically similar to that observed to occur in the glass transformation range of completely amorphous substances, are the basis of the assignment of the glass transition temperature in polyethylene.

[1]Figures in brackets indicate the literature references at the end of this paper.

2. Experimental Detail

2.1. Calorimetry

Heat capacity measurements on the two high density linear polyethylene samples were made with the same vacuum adiabatic calorimeter [2] as that used previously for the two samples of standard reference materials, SRM 1475 and SRM 1476 (linear and branched polyethylene whole polymers) in the conditions as received [1].

2.2. Samples

a. Slow Melt-Crystallized Linear Polyethylene

The density and the crystallinity of a sample of SRM 1475 linear polyethylene were increased by melting and recrystallizing the sample slowly in a mold in a vacuum oven. The sample was melted by heating to 170 °C and keeping it there for about 1 hr. It was then cooled to 150 °C in 1 hr. A rate of cooling of 0.75 K h^{-1} was maintained during the period when the sample was cooled from 150 to 90 °C. The sample was then cooled to room temperature at a rate of a few degrees per hour.

The finished sample from the mold was in the shape of a cylinder, 5-cm O.D. and 6.3-cm long, with a hole of 1.3-cm diam in the center. The density of the sample was 0.981 g cm^{-3} at 23 °C as determined in an ethanol-water density gradient column.

Small angle x-ray diffraction patterns were obtained from this sample. The long spacing of the sample

was increased to 24.7 nm by the slow melt crystallization process. The new value is about twice the original value, 12.1 nm. for the sample of SRM 1475 in the condition as received. The mass of the calorimetric sample was 93.105 g in vacuo. The density values of 0.981 and 0.00117 g cm^{-3} for the sample and for air, respectively, were used to estimate the buoyancy correction. No variation in the densities of the sample, before and after the calorimetric measurement, was detected beyond a range of 0.0005 g cm^{-3}. Helium gas at a pressure of 12.5 cm of Hg was sealed in to facilitate the thermal conduction within the sample container.

b. Pressure Crystallized Linear Polyethylene

The crystallization of linear polyethylene sample under high pressure [3] was carried out as follows. A sample of SRM 1475 linear polyethylene was placed in a steel pressure vessel, 2.5-cm I.D. and 2.5-cm wall thickness, and then pumped down to a pressure of about 1×10^{-4} mm of Hg. After 2 h, a sealing plug was forced into the bore and the vessel was disconnected from the vacuum line. A piston was used to push the plug in until the load reached 5000 lb. The whole vessel was then heated to 210 °C while the position of the piston was kept constant. To do this the load on the piston was increased to about 60,000 lb (equivalent to a pressure of 5150 atm). The piston load was reduced in order to melt the polymer and then increased in 2500 lb increments, followed by 5-min waiting periods, to crystallize the sample under high pressure. Inward creep of the piston during the waiting period, indicative of crystallization, became significant at 48,000 lb load but no apparently isobaric change in piston position occurred. The lack of such a change probably indicates that the pressure is not hydrostatic. At the same piston position, the load was 8000 lb less when being withdrawn then being advanced. If the force at the polymer-sealing plug interface is the average of these, the pressure was 4800 atm when the load applied to the advancing piston was 60,000 lb. After 20 min the heaters were switched off and the load on the advancing piston was kept between 60,000 and 65,000 lb as the vessel was cooled to 100 °C. After cooling to 25 °C over a 15 h period the load was 45,000 lb. The sealing plug was withdrawn and the sample removed.

In order to check the possibility that the increase in the density of the sample is not due to the oxidation of the polymer at elevated temperatures, the sample was subjected to infrared spectroscopic investigations. A film of 0.1 mm thick was prepared from the pressure-crystallized sample according to ASTM Method D–2238–64T. The IR spectrum of this film was examined in the region of 1700–1750 cm^{-1}. The recorded trace indicated only a smooth base line within 0.002 in the absorbancy scale in that region. When the IR spectrum of a film of 0.5 percent CO-ethylene copolymer, 0.04 mm thick and similarly prepared, was examined under the same operational conditions, the absorption peaks in the region 1700–1750 cm^{-1} reached nearly full-scale of the recorder at about 1.23 in absorbancy scale. The peaks of a 0.05 mm film made from 1 percent CO-ethylene copolymer went off-scale in the same frequency region. Hence the oxygen content of the pressure-crystallized sample is probably much less than 10 ppm and no significant oxidation has occurred during the high pressure and high temperature treatments in preparing the sample and the film.

The intrinsic viscosity of the pressure-crystallized sample in 1-chloronaphthalene at 130 °C is 0.915 dl/g. The intrinsic viscosity of the SRM 1475 is 0.890 dl/g as reported in the certificate. Gel-permeation chromatograph, GPC, was also taken for the pressure-crystallized sample in order to detect any changes in the molecular weight distribution. The result of a single GPC run on the pressure-crystallized sample indicates an 8 percent increase in the M_n, a 3 percent increase in the M_w and a 15 percent decrease in the M_z over that of a calibration run of the SRM 1475. Except for the M_z, the changes are within the estimated standard deviations of the molecular weight determinations by GPC for SRM 1475 [4]. Apparently no drastic change of the polymer had occurred during the preparation of the sample under high pressure and high temperature.

The mass of the calorimetric sample was 63.836 g corrected to vacuum. The density values of 0.993 and 0.00117 g cm^{-3} for the sample and for air, respectively, were used to estimate the buoyancy correction. Helium gas at a pressure of 85 mm of Hg at room temperature was sealed in the sample container to facilitate the thermal conduction. The molar mass refers to the mass of the repeating unit $-CH_2-$, 14.027 g.

c. DSC Observations

The melting behavior of the pressure-crystallized linear polyethylene sample was observed in a commercial dynamic differential scanning calorimeter (DSC). The extended-chain crystals of the pressure-crystallized sample melt at a higher temperature than the folded-chain crystals in either the as-received SRM 1475 or the slow melt-crystallized sample. However, just below the main melting peak, there is a small peak or shoulder which occurs at a temperature corresponding to the melting peak of the folded-chain crystals. The ratio of the energies involved for the first (lower temperatures) peak to the main peak varies varies between 2 to 10 percent from sample to sample, indicating some inhomogeneous distribution of small amount of folded-chain crystal in the pressure crystallized sample. Similar behavior in the pressure-crystallized linear polyethylene samples has also been observed by other investigators using differential thermal analysis [3, 5] and DSC [6] techniques. Once the pressure-crystallized sample was melted and then recrystallized at atmospheric pressure, it behaved just like the ordinary linear polyethylene sample.

The energy required to melt the three linear polyethylene samples (as received, slow melt-crystallized, and pressure-crystallized) appears to be a linear function of the degree of crystallinity which is assumed to have a linear relationship with the specific volume of the sample. The heat of fusion for completely crystalline polyethylene is estimated at about 4100 J mol^{-1} from the DSC experiment, if the value of 1.00

cm^3g^{-1} is adopted as the specific volume for 100 percent crystalline polyethylene.

3. Results

3.1. Representation of Data

The results of the heat capacity measurement are tabulated in Table 1 and shown graphically in figure 1. Also shown in figure 1 are the results from the previous work [1] for the linear polyethylene sample SRM 1475 in the condition as received and the branched polyethylene sample SRM 1476 in various conditions. Table 1 is arranged in the order of increasing initial temperature of a series of heat capacity determinations. The series are numbered in chronological sequence in order to facilitate the tracing of thermal history of the sample.

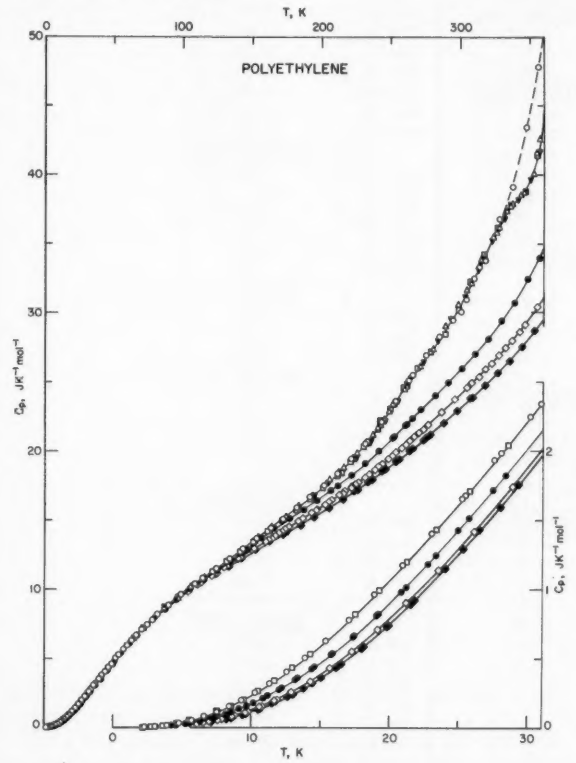

FIGURE 1. *Heat capacities of polyethylene.*

Linear, SRM 1475: ● as received [1], ◇ slow melt-crystallized, ◆ pressure-crystallized. Branched, SRM 1476 [1]: ○ as received, △ stabilized at 360 K and then quenched, □ annealed at 230 K, ▼ slow-cooled.

Quenched samples are produced in the cryostat at a fast cooling rate of 4–5 K/min. Annealed samples are either produced by a slow cooling rate of 1–2 K/h, or by holding at 220 to 225 K for one to three days followed by slow cooling. Series I of both samples represent measurements before any refrigerant being introduced into the cryostat. For the slow melt-crystallized sample, Series II–VI and XI represent heat capacity determinations after a quenching procedure, with the rest of the series represent that following an annealing procedure. For the pressured crystallized sample, Series II and VII–IX represent the measurement on the sample after quenching, while Series III and IV–VII represent that after slow cooling and annealing procedures.

The temperature increment for a heat capacity determination may be inferred from the differences in the mean temperatures of the adjacent determination within the series. Curvature corrections have been added to correct for the effect of the finite temperature rise of a determination. The precision of the measurement above 25 K is in the order of 0.05 percent. Below 25 K, the precision graduately changes to 1 percent at 5 K and about 5 percent at 2 K. The accuracy over most of the temperature range of the measurement is believed to be comparable to the precision as seen from the result of the heat capacity measurement on a Calorimetry Conference standard sample of sapphire [2].

Smoothed heat capacity values at rounded temperatures along with values of other derived thermodynamic functions are listed in table 2. H_0 and S_0 refers to the zero point enthalpy and the residual entropy of the individual samples. Since these samples are expected to have undetermined residual entropies at 0 K. Gibbs free energies for these samples are not given in table 2.

3.2. Estimation of C_p of Crystalline Linear Polyethylene

Heat capacities of linear and branched polyethylene samples from several literature sources as well as those from this research are plotted at selected temperatures as a function of specific volume at room temperature in figure 2. Literature values [7–12] included in figure 2 are those where the densities of the samples are given. The degrees of crystallinity of the samples are interpolated linearly between the specific volume of 1.00 $cm^3\ g^{-1}$ for the crystalline part and 1.17 $cm^{-3}\ g^{-1}$ for the amorphous part.

In order to minimize the effects due to the differences in chemical compositions and due to the differences in the laboratory techniques, the heat capacity of 100 percent crystalline linear polyethylene was estimated only from the results obtained in this laboratory for the three linear polyethylene samples which are derived from the same stock as that used to establish the SRM–1475. The heat capacities of these three samples ranging from 71 to 96 percent crystallinity are represented by the filled circles. The temperatures are denoted by the numbers nearby the straight lines. The straight lines are obtained by a least-squares fitting procedure through the data for the three samples. From 30 to 360 K, the maximum deviations of the data points from the generated lines are less than 0.4 percent. Apparently the two-phase additive model is applicable at high crystalline contents. Since the extrapolated range of crystallinity is only 4 percent, it is believed that the heat capacity of 100 percent crystalline linear polyethylene may be estimated to

TABLE 1. *Heat capacity of linear polyethylene*

(base mole [—CH_2—] = 14.027)

Slow melt-crystallized SRM 1475 ($\rho_{23\,°C}$ = 0.981 g cm^{-3})

T	C_p, J K^{-1}mol^{-1}	T	C_p, J K^{-1}mol^{-1}	T	C_p, J K^{-1}mol^{-1}
	SERIES VIII		SERIES VII		SERIES XI
2.29	0.0014	38.49	2.998	196.07	15.78
2.96	.0034	42.13	3.485	204.96	16.36
3.72	.0070	46.12	4.016	212.83	16.88
4.55	.0132	50.62	4.607	221.64	17.48
5.49	.0234	55.96	5.282	231.38	18.15
6.51	.0385		SERIES XII	241.13	18.87
7.56	.0593	84.99	8.319	250.98	19.64
8.56	.0844	94.24	9.091	260.81	20.48
9.52	.115	104.10	9.839	270.52	21.33
10.51	.151	113.77	10.516		SERIES X
11.60	.198	123.47	11.156	205.49	16.33
12.82	.260		SERIES II	215.02	16.96
	SERIES IX	86.10	8.347	224.57	17.61
6.03	.0304	94.53	9.117	234.13	18.32
6.91	.0457	104.02	9.837	243.78	19.10
7.82	.0654		SERIES III	253.50	19.89
8.75	.0901	110.67	10.31	263.30	20.73
9.67	.120	120.20	10.95	273.08	21.58
10.62	.156	129.91	11.58		SERIES XIV
11.68	.202	139.85	12.22	221.53	17.40
12.88	.263	149.80	12.85	231.27	18.11
14.21	.339	159.70	13.48	241.00	18.87
15.61	.434	169.57	14.10	250.71	19.65
17.21	.553		SERIES XIII	260.41	20.47
19.09	.711	122.61	11.11	270.19	21.33
21.17	.903	131.47	11.69		SERIES V
23.47	1.138	141.44	12.31	238.47	18.68
26.02	1.421	151.55	12.96	248.09	19.44
28.81	1.748	161.60	13.59	258.08	20.25
31.90	2.133	171.51	14.20		SERIES VI
35.32	2.579		SERIES XV	266.89	21.03
39.10	3.081	164.06	13.66	276.47	21.93
45.55	3.940	173.61	14.32	286.14	22.82
52.17	4.806	183.16	14.92	295.87	23.75
57.23	5.438	192.82	15.52	305.58	24.67
63.02	6.118	202.70	16.15		SERIES I
69.24	6.799		SERIES IV	304.88	24.59
76.40	7.523	166.34	13.89	313.62	25.47
84.18	8.246	176.19	14.52	322.76	26.39
		186.23	15.15	332.43	27.42
		196.47	15.81	342.43	28.66
		206.71	16.48		SERIES XVI
		216.75	17.14	308.36	24.92
		226.53	17.81	318.13	25.92
				327.79	26.91
				337.17	27.98
				346.27	29.13
				355.08	30.43

TABLE 1. *Heat capacity of linear polyethylene*—Continued

Pressure-crystallized SRM 1475 ($\rho_{23\,°C} = 0.993$ g cm^{-3})					
T	C_p, J K^{-1}mol^{-1}	T	C_p, J K^{-1}mol^{-1}	T	C_p, J K^{-1}mol^{-1}
	SERIES VIII		SERIES IV		SERIES III
2.74	.0034	2.32	0.0019	175.30	14.13
3.62	.0061	3.00	.0038	184.83	14.69
4.61	.0126	3.92	.0080	194.77	15.28
5.54	.0210	4.97	.0152	205.11	15.91
6.51	.0335	6.01	.0262	215.51	16.56
7.51	.0513	7.00	.0413	225.65	17.24
8.55	.0744	8.14	.0636		SERIES II
9.58	.1040	9.33	.0956	203.73	15.86
10.63	.1399	10.41	.1310	213.51	16.47
11.74	.1855	11.47	.1718	223.48	17.11
12.96	.2456	12.55	.2250	233.53	17.80
14.38	.3243	13.70	.2841	243.53	18.52
16.06	.4364	15.00	.3625	253.49	19.25
17.90	.5761	16.45	.4638	263.41	20.04
19.77	.7375	18.08	.5903	273.28	20.82
21.75	.9240	19.85	.7424		SERIES VII
23.95	1.152	21.45	.8933	206.68	16.02
26.46	1.433	23.11	1.061	216.39	16.63
29.26	1.763	25.24	1.292	226.32	17.28
32.27	2.144	27.94	1.604	236.31	17.98
35.46	2.562	31.06	1.987	246.22	18.73
38.98	3.032	34.28	2.414	255.99	19.46
43.04	3.576	37.84	2.873	265.62	20.23
47.54	4.178	41.92	3.425	275.31	21.03
52.42	4.818	46.44	4.030		SERIES IX
		51.32	4.674	278.29	21.22
		56.71	5.356	287.99	22.08
			SERIES V	297.74	22.96
		60.51	5.814	307.63	23.85
		66.55	6.497		SERIES I
		73.07	7.185	309.03	23.90
		80.32	7.887	318.10	24.79
		88.58	8.619	326.96	25.64
		97.74	9.352	335.80	26.58
		107.60	10.07	344.60	27.59
		117.99	10.77	353.35	28.71
		128.28	11.41		
			SERIES VI		
		133.00	11.70		
		142.79	12.28		
		152.70	12.86		
		162.63	13.43		
		172.50	13.99		

within 1–2 percent over the majority of the temperature range investigated.

The extrapolated heat capacity values for 100 percent crystalline polyethylene are listed in table 3 along with calculated thermodynamic functions. Also listed in table 3 are linearly extrapolated heat capacity values for amorphous linear polyethylene. The reliability of such an extrapolation for the amorphous phase, especially at temperatures above 250 K, is less certain than that for its crystalline counterpart, not only because the range of extrapolation is much longer than that of the measurement, but also due to the uncertainty in applying the simple two phase additive model over a long extrapolation region. The heat capacity curves for the three linear samples, figure 1, show curvatures concaved upward at temperatures above 300 K. These features are probably caused by premelting or melting of small crystallites. Gibbs free energy functions for the amorphous phase are not included in table 3 because of the existence of an undetermined residual entropy.

The extrapolated heat capacity for crystalline linear polyethylene is a relatively smooth function of temperature. The smoothness may be visualized in the C_p/T, dC_p/dT and $d \ln C_p/dT$ versus T plots, as shown in figure 3. Similar functions for SRM 1475 and SRM 1476 in the condition as received [1] are also shown in figure 3 for comparison. The slight irregularities observed around 290 K in the extrapolated crystalline heat capacity are probably the result of some experimental uncertainties. However, pronounced features centering around 150 and 250 K show up in the behavior of the linear and branched polyethylene samples.

TABLE 2. *Thermodynamic functions of polyethylene*
(units in J, K and mol; base mole [$-CH_2-$] = 14.027)

	Slow melt-crystallized SRM 1475			Pressure-crystallized SRM 1475		
T	C_p	$H-H_0^s$	$S-S_0^s$	C_p	$H-H_0^p$	$S-S_0^p$
5	0.018	0.021	0.006	0.015	0.020	0.005
10	.131	.339	.045	.117	.298	.040
15	.391	1.583	.143	.363	1.434	.129
20	.793	4.490	.307	.757	4.177	.284
25	1.305	9.696	.537	1.265	9.191	.506
30	1.895	17.67	.826	1.854	16.96	.787
35	2.536	28.73	1.166	2.499	27.83	1.121
40	3.202	43.07	1.548	3.168	41.99	1.498
45	3.870	60.75	1.964	3.841	59.52	1.910
50	4.526	81.75	2.406	4.502	80.38	2.349
60	5.766	133.3	3.342	5.750	131.7	3.282
70	6.882	196.7	4.317	6.870	195.0	4.255
80	7.871	270.5	5.301	7.860	268.7	5.238
90	8.747	353.7	6.280	8.736	351.8	6.215
100	9.535	445.2	7.243	9.522	443.1	7.177
110	10.26	544.2	8.186	10.24	542.0	8.119
120	10.94	650.2	9.108	10.90	647.7	9.038
130	11.59	762.8	10.01	11.52	759.8	9.935
140	12.22	881.9	10.89	12.11	878.0	10.81
150	12.86	1007.	11.76	12.70	1002.	11.67
160	13.49	1139.	12.61	13.27	1132.	12.50
170	14.12	1277.	13.44	13.84	1267.	13.33
180	14.74	1421.	14.27	14.42	1409.	14.13
190	15.37	1572.	15.08	15.00	1556.	14.93
200	16.01	1729.	15.89	15.60	1709.	15.71
210	16.66	1892.	16.68	16.22	1868.	16.49
220	17.33	2062.	17.47	16.86	2033.	17.26
230	18.04	2239.	18.26	17.54	2205.	18.02
240	18.79	2423.	19.04	18.26	2384.	18.78
250	19.59	2615.	19.83	19.00	2571.	19.55
260	20.42	2815.	20.61	19.76	2765.	20.31
270	21.31	3023.	21.40	20.56	2966.	21.07
280	22.24	3241.	22.19	21.39	3176.	21.83
290	23.18	3468.	22.99	22.26	3394.	22.59
300	24.14	3705.	23.79	23.14	3621.	23.36
310	25.10	3951.	24.60	24.05	3857.	24.14
320	26.10	4207.	25.41	24.99	4102.	24.92
330	27.16	4473.	26.23	25.97	4357.	25.70
340	28.33	4750.	27.06	27.04	4621.	26.49
350	29.67	5040.	27.90	28.26	4898.	27.29
360	31.23	5345.	28.75	29.72	5188.	28.11
273.15	21.60	3091.	21.65	20.82	3031.	21.31
298.15	23.96	3660.	23.64	22.98	3578.	23.22

The superscripts of *s* and *p* for the zero-point enthalpy and entropy values denote the reference states of slow melt-crystallized and pressure-crystallized polyethylene, respectively.

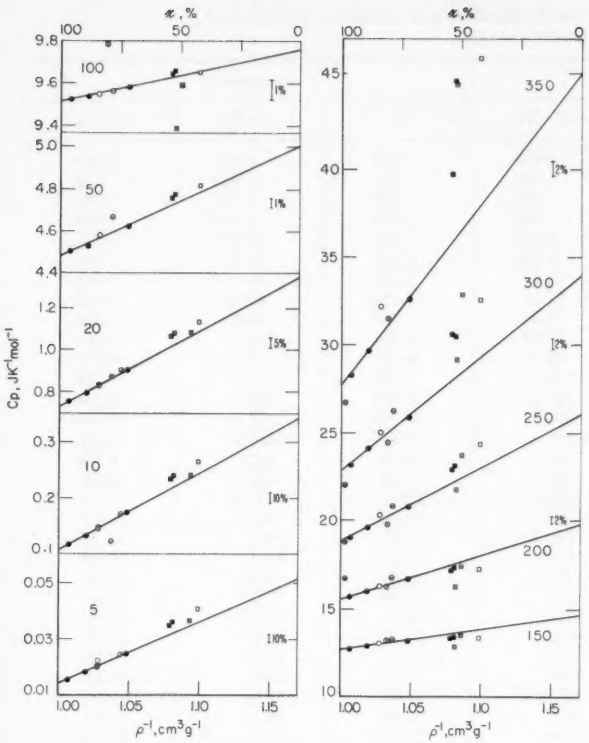

FIGURE 2. *Heat capacity of polyethylene as a function of specific volume.*

Circles—linear polyethylene. Squres—Branched polyethylene. ● ■ This work and previous work [1], ⊖ ⊟ Dainton et al. [7], ○ Isaacs et al. [8], ○□ Passaglia et al. [9], ⊘⊠ Tucker et al. [10], ○ □ Westrum [11], ⊗ Wunderlich [12].

The extrapolated values of crystalline and amorphous linear polyethylene from this investigation are plotted in figure 4 along with estimated values of crystalline, amorphous and liquid polyethylene from other sources. The C_p of ideal CH_2 chain crystal estimated by Broadhurst [13] from the *n*-paraffin data is in general higher than those obtained from this investigation, although the experimental *n*-paraffin values up to 200 K are slightly lower. Between 2 and 30 K, Tucker and Reese's values for the crystalline phase based on their measurements, are very close to ours, and is therefore not shown in figure 4. However, their estimated values from 30 to 150 K, with identical heat capacity for the crystalline and the amorphous phases from 60 to 150 K, lie inbetween our values for the two phases, but closer to our values for the crystalline phase. In an earlier estimate by Wunderlich [14] the values for the crystalline phase is identical to that of the amorphous phase for temperatures below 110 K. These values are somewhat higher than the estimated crystalline heat capacity from this research. At higher temperatures the values for the crystalline heat capacity are also higher than that from this research. The more recent estimate by Wunderlich [15] is based upon Tucker and Reese's estimate up to 150 K and is then made to join at 210 K the results of a differential scanning calorimetric work on extended chain crystals from 180 K [12]. The results of the DSC work are lower than the values for crystalline phase from this research at temperatures above 250 K. In both Wunderlich's estimates, there is a pronounced dip in heat capacity around 250 K. However Wunderlich's calculated values [12] based on a spectrum assigned earlier [16] agree relatively well with the result from this research over a wide temperature range.

For the amorphous phase, the estimation of Tucker and Reese [10] below 30 K agrees relatively well with our estimation for the amorphous phase. Because of the closeness of the two estimations, their values are not shown in figure 4. However their estimation to 150 K and the conclusion that the amorphous and the crystalline phases have identical heat capacity do not agree with the findings from this investigation. Two estimates of heat capacity of amorphous polyethylene have been made by Wunderlich. The earlier one [14] assumes identical heat capacity behavior for the amorphous and crystalline phases for temperatures below 110 K. The more recent one [15] incorporates the estimate by Tucker and Reese for temperatures below 150 K and assumes identical heat capacity values for the two phases between 60 and 210 K. Both Wunderlich's estimates for the amorphous phase are terminated around 250 K by the linear extrapolation of the liquid heat capacity above the melting point.

Heat capacity of the liquid and the supercooled liquid polyethylene from 200 K up has been estimated by many authors. Broadhurst [13] has estimated the C_p of ideal CH_2 chain liquid from *n*-paraffin data from 200 to 370 K. Atkinson, Larkin, and Richardson [17] have based their estimates on their measurement of liquid polyethylene above the melting point and *n*-paraffin data at lower temperatures. Wunderlich's earlier estimates [14] of liquid polyethylene C_p are the linear extrapolations from the liquid heat capacity of a sample of Marlex [2] 50 above the melting point in reference [18]. The more recent estimates [15] of Wunderlich were extrapolated from the average values of a collection of liquid polyethylene data.

3.3. Comparison of Results of Different Polyethylene Samples

Low temperature heat capacity behavior of various polyethylene samples are plotted in figure 5. As mentioned earlier [1], the heat capacities of the linear SRM 1475 sample and the branched SRM 1476 sample in conditions as received agree within 1–2 percent of the values reported for M2 and low density samples, respectively, studied by Tucker and Reese [10]. The reason for the closeness in agreement

[2] A commercial material is identified in this paper in order to adequately specify the experimental procedure. Such identification does not imply recommendation or endorsement by the National Bureau of Standards.

TABLE 3. *Thermodynamic properties of extrapolated crystalline and amorphous polyethylene*
(units in J, K, and mol; $-CH_2-=14.027$)

	Crystalline				Amorphous		
T	C_p	$H-H_0^c$	S	$-(G-H_0^c)$	C_p	$H-H_0^a$	$S-S_0^a$
5	0.014	0.018	0.005	0.006	0.051	0.057	0.014
10	.106	.267	.036	.092	.341	.943	.126
15	.342	1.323	.118	.451	.800	3.747	.347
20	.727	3.939	.266	1.384	1.346	9.088	.650
25	1.231	8.794	.481	3.225	1.937	17.28	1.014
30	1.819	16.39	.756	6.293	2.547	28.49	1.421
35	2.465	27.08	1.084	10.87	3.167	42.76	1.860
40	3.135	41.07	1.457	17.21	3.788	60.15	2.323
45	3.811	58.44	1.865	25.51	4.398	80.62	2.805
50	4.475	79.16	2.302	35.91	4.991	104.1	3.299
60	5.730	130.3	3.230	63.52	6.115	159.7	4.309
70	6.855	193.3	4.200	100.7	7.144	226.1	5.330
80	7.847	266.9	5.181	147.6	8.079	302.3	6.346
90	8.725	349.9	6.157	204.3	8.934	387.4	7.348
100	9.511	441.1	7.118	270.6	9.737	480.8	8.331
110	10.23	539.9	8.058	346.5	10.53	582.1	9.296
120	10.88	645.4	8.976	431.7	11.35	691.4	10.25
130	11.49	757.3	9.872	526.0	12.27	809.4	11.19
140	12.07	875.1	10.75	629.1	13.38	937.4	12.14
150	12.62	998.6	11.60	740.8	14.60	1077.	13.10
160	13.17	1128.	12.43	861.0	15.78	1229.	14.08
170	13.73	1262.	13.24	989.3	16.88	1393.	15.07
180	14.30	1402.	14.04	1126.	17.89	1567.	16.07
190	14.87	1548.	14.83	1270.	18.81	1750.	17.06
200	15.47	1700.	15.61	1422.	19.72	1943.	18.05
210	16.08	1857.	16.38	1582.	20.66	2145.	19.03
220	16.70	2021.	17.14	1750.	21.70	2356.	20.02
230	17.35	2192.	17.90	1925.	22.91	2579.	21.01
240	18.03	2368.	18.65	2108.	24.32	2815.	22.01
250	18.72	2552.	19.40	2298.	25.95	3066.	23.04
260	19.45	2743.	20.15	2496.	27.64	3334.	24.09
270	20.23	2941.	20.90	2701.	29.29	3619.	25.16
280	21.04	3148.	21.65	2914.	30.86	3920.	26.26
290	21.89	3362.	22.40	3134.	32.36	4236.	27.37
300	22.76	3586.	23.16	3362.	33.85	4567.	28.49
310	23.64	3618.	23.92	3597.	35.45	4913.	29.62
320	24.54	4058.	24.68	3841.	37.26	5277.	30.78
330	25.46	4308.	25.45	4091.	39.43	5660.	31.95
340	26.46	4568.	26.23	4350.	42.09	6067.	33.17
350	27.57	4838.	27.01	4616.	45.33	6503.	34.44
360	28.90	5120.	27.81	4890.	49.21	6975.	35.76
273.15	20.48	3006.	21.14	2768.	29.79	3712.	25.51
298.15	22.60	3544.	23.02	3319.	33.57	4504.	28.28

The superscripts of a and c for the zero-point enthalpy and entropy values denote the reference states of amorphous and crystalline polyethylene respectively.

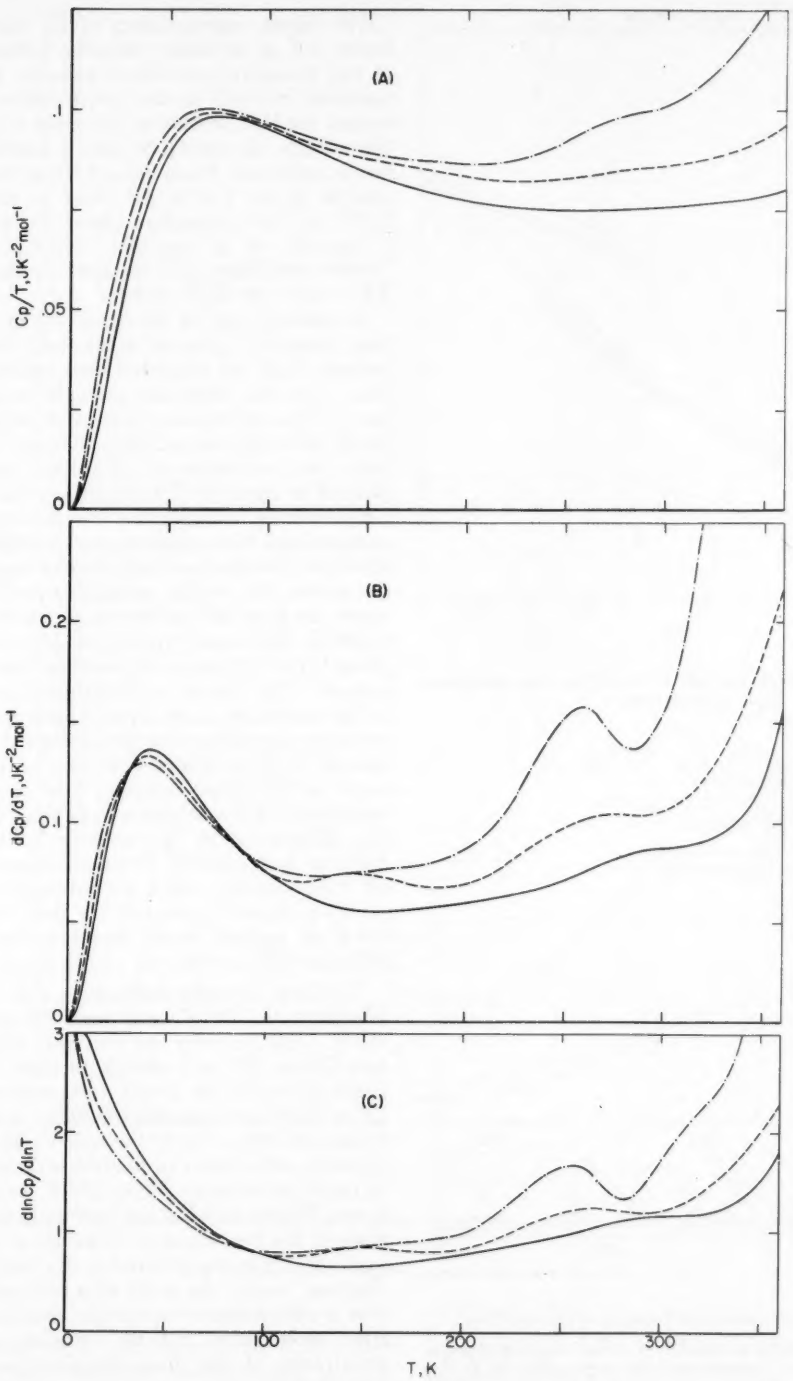

FIGURE 3. (A) C_p/T versus T Plot for Polyethylene.
(B) dC_p/dT versus T Plot for Polyethylene.
(C) $d \ln C_p/dT$ versus T Plot for Polyethylene.
——— estimated crystalline, — — — linear (SRM 1475 as received), —— · —— branched (SRM 1476 as received)

533-558 OL - 74 - 6

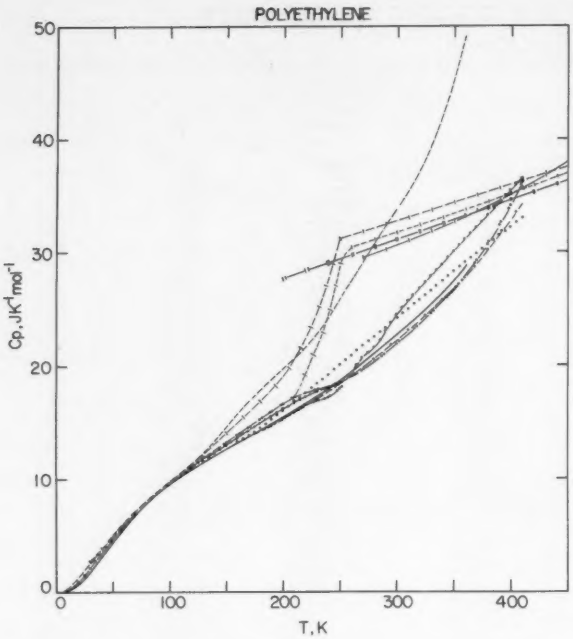

FIGURE 4. *Estimated heat capacity of crystalline and amorphous linear polyethylene.*

Crystalline: This research ——;
Broadhurst [13] · · · · calc., · · · —— · · · exptl.;
Wunderlich · — · [14], · — — · [12], · · —— · · [15];
Tucker and Reese [10], not shown.
Amorphous: This research —— ——;
Wunderlich | — — | [14], | — — — | [15];
Tucker and Reese [10], not shown.
Liquid: Broadhurst [13] || — ||;
Wunderlich | — — | [14], | — — — | [15];
Atkinson, Larkin and Richardson [17] | —— |.

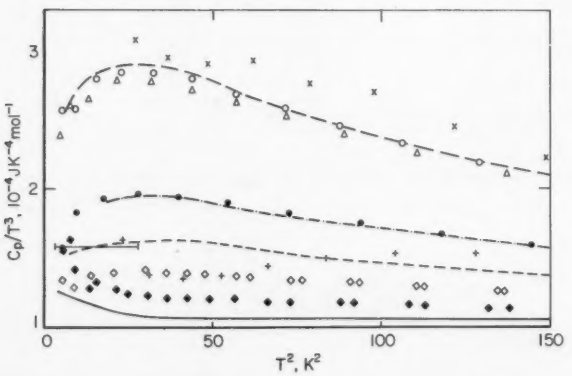

FIGURE 5. *Low temperature heat capacity of polyethylene.*

This work. Linear (SRM 1475): ● as received [1], ◇ slow-melt crystallized, ◆ pressure crystallized, ——— estimated 100 percent crystalline; Branched (SRM 1476) [1]: ○ as received. △ annealed. Isaacs et al. [8]: —— |—— |. Tucker et al. [10]: ——— ——— branched. ——· —— linear (M1), — — — (M2). Westrum [11]: × branched (DYNH), + linear (Marlex 50).

is probably due to their respective similarities in densities. The difference in the densities for the linear polyethylene samples is about 0.004 g cm^{-1} and that for the branched samples is about 0.01 g cm^{-1}.

The linear extrapolation of C_p versus crystallinity below 5 K is probably strongly influenced by the C_p of the pressure-crystallized sample, which shows an upsweep in C_p/T^3 as the temperature is lowered. The reason for this particular behavior to show up only in the sample consisting of mainly extended chain crystals is unknown. If the data of the pressure-crystallized sample below 5 K is not used in the extrapolation, C_p/T^3 for the crystalline phase below 15 K is within 5 percent of a constant 1.05×10^{-4} J K^{-4} mol^{-1}. Tucker and Reese [10] obtained a value of 1.104×10^{-4} J K^{-4} mol^{-1} for C_p/T^3 at 0 K.

A sensitive way of detecting any irregularities in the heat capacity behavior of an individual sample is to remove from the observed heat capacity the contribution from the relatively smooth crystalline heat capacity. The differences in the heat capacity of the three linear polyethylene samples, derived from SRM 1475, from the extrapolated crystalline heat capacity are plotted in figure 6. The short vertical bars at various temperatures indicate the magnitude of 1 percent of extrapolated heat capacity for crystalline linear polyethylene. For the two high density samples, systematic deviations due to the quenching and annealing processes are noticable in the temperature region from 170 to 240 K. The heat capacity of the annealed sample is about 0.1 to 0.2 percent lower than that of the quenched sample. The linear polyethylene sample SRM 1475 in the condition as received [1] has not been subjected to similar annealing and quenching treatments. A hump around 25 K is observed in the heat capacity differences of all three samples. The occurrence and the magnitude of the humps can generally be attributed to the differences in the specific volumes among the different samples [24]. The heat capacity differences of all three samples reach a minimum around 100 K. As shown in figure 2, most of the heat capacity values at 100 K of various linear and branched samples from different laboratories are within a spread of 1 percent.

The heat capacity differences rise sharply after the minimum at 100 K, and level off somewhat around 160 K. This behavior has also been observed by Beatty and Karasz [25] in a sample of high molecular weight linear polyethylene in the temperature region around 130 to 160 K and was considered by them to be the glass transition region for polyethylene. However, the heat capacity differences in figure 6 indicate another region of rapid rise around 230 to 270 K. In this temperature range, Beatty and Karasz have only noted a change of slope in the heat capacity behavior of their sample. Because the changes involved in the heat capacity "irregularities" are in the order of a few percent and spread over a wide temperature range, heat capacity determination alone may not be sufficient to indicate the occurrence of the glass transition in semicrystalline polyethylene.

Heat capacities of linear polyethylene from various literature sources are compared in figure 7 with the extrapolated heat capacity for crystalline linear polyethylene as the base line. The comparisons of branched polyethylene data, including the study of SRM 1476

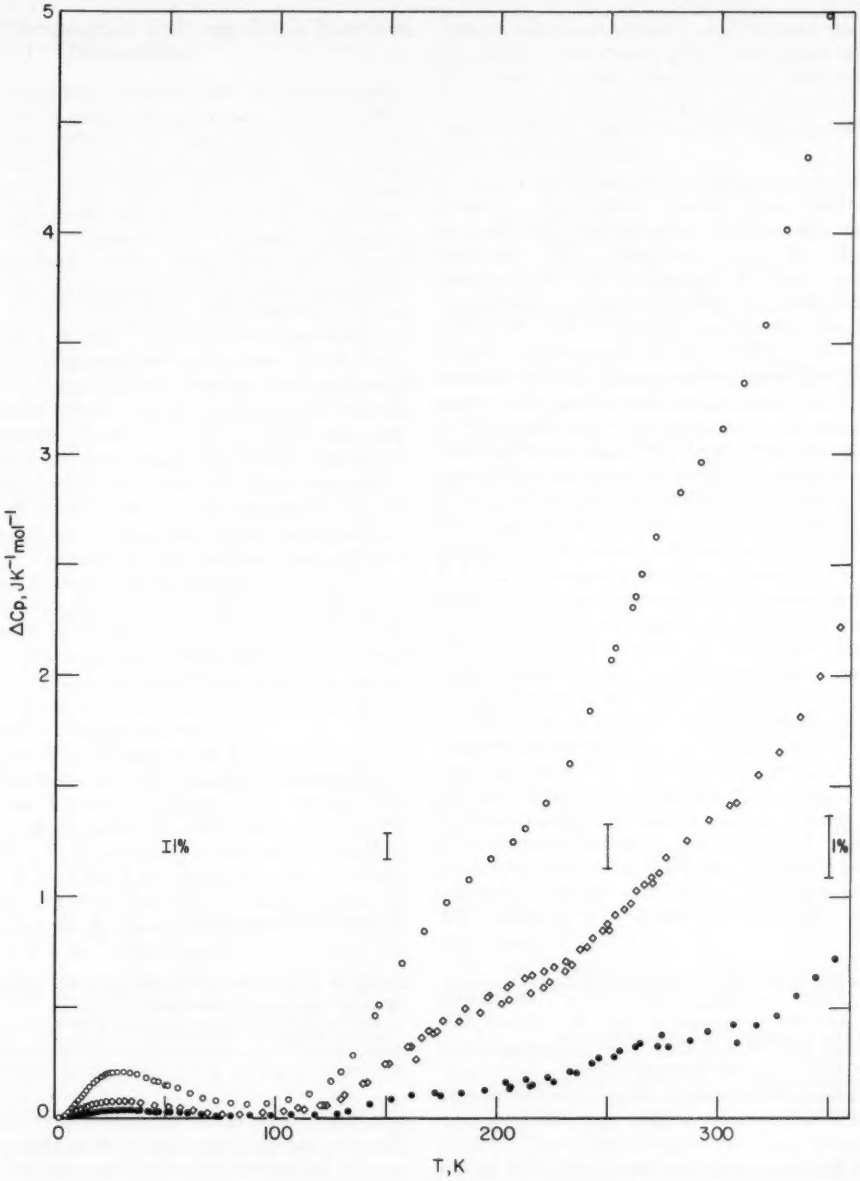

FIGURE 6. *Comparison of heat capacities of linear polyethylene samples versus estimated crystalline heat capacity.*

SRM 1475: ○ as received [1], ◇ slow crystallized, ● pressure crystallized.

from this laboratory [1] are shown in figure 8. The data are included in the comparison only if they are reported in tabular or analytical form. Data reported in graphical form are not included. When heat capacity values are reported at rounded temperatures, the curves shown in figures 7 and 8 may have been arbitrarily smoothed within the limits of the roundoff error of the reported values.

The results of the comparison shown in figures 7 and 8 are in general self-explanatory. A hump around 25 K in the difference curves, similar to that shown in figure 6, appears in all low temperature measurements. Two regions of more abrupt rise in heat capacity around 150 and 250 K may be noticed in the studies of linear polyethylene samples by Dainton et al. [7], and by Westrum [11], similar to the findings from this

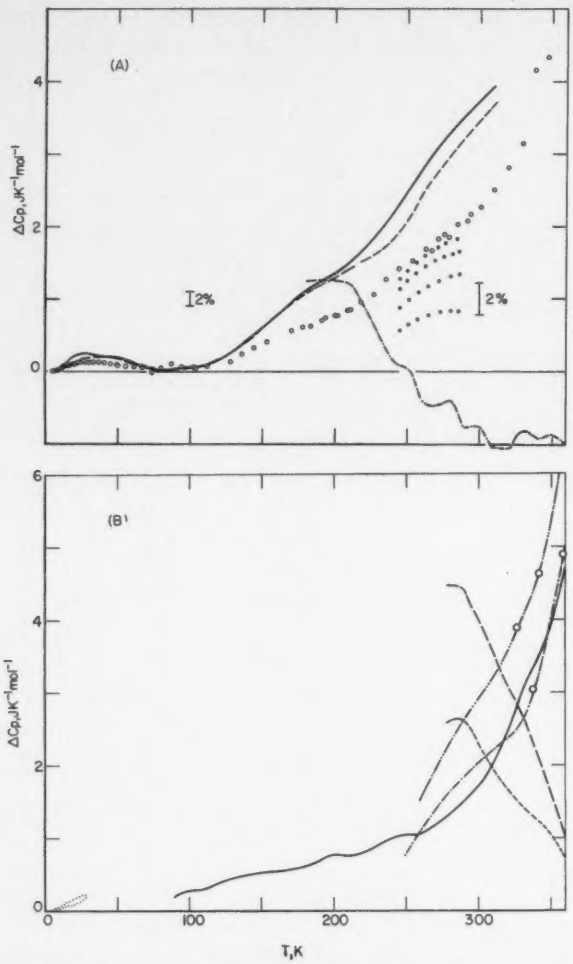

FIGURE 7. *Comparison of literature linear polyethylene heat capacity values.*

Baseline: crystalline linear polyethylene heat capacity from this work.
A. ○ Marlex 50, Westrum [11]; ——— Marlex 50, — — — Rigidex 50, Dainton et al. [7]; ——·—— Wunderlich [12]; · · · · · single crystals, Richardson [19].
B. —— Linear, Passaglia et al. [9] · · · · M1 and M2, Tucker et al. [10]; ——·—— Annealed, ——··—— Granular, Dole et al. [13]; ——— GD, — — — GC, Wilski [14].

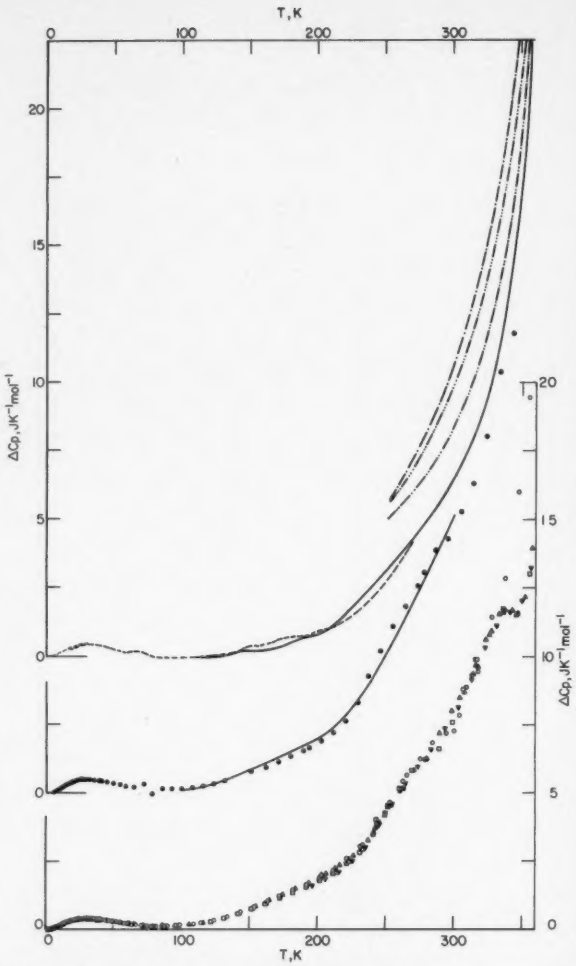

FIGURE 8. *Comparison of branched polyethylene heat capacity values.*

Baseline: crystalline linear polyethylene from this work.
Lower curves: SRM 1476 [1]. same legend as in figure 1.
Middle curves: ● E. F. Westrum [11]; ——— Dainton [7].
Upper curves: · · · Tucker and Reese [10]; — — — Sochava [20, 21]; —— Passaglia and Kevorkian [9]; ——·——, ——··——, ——···—— Dole [19].

laboratory [1]. Similar behaviors are noticeable in the measurements on branched samples by Westrum and by this laboratory. The dip around 300 K in Westrum's heat capacity curve for branched polyethylene is probably effected by long storage of the sample near room temperature. Similar features have been noticed in the branched polyethylene sample studied in this laboratory. The irregularities in Westrum's data around 80 to 90 K is presumably due to the temperature scales used. The effect of joining the International Practical Temperature Scale of 1948 and the NBS 1955 Provisional Temperature Scale at 90 K have been noted elsewhere [26, 27].

Sochava's sample [22, 23] is probably a branched polyethylene since its heat capacity behavior follows the pattern of other branched polyethylene samples. The low temperature behavior of this sample is similar to the branched polyethylene studied by Tucker and Reese [10], Westrum [11] and this laboratory [1]. The high temperature behavior of this sample is very similar to that of the branched polyethylene studied by Passaglia and Kevorkian [9]. Passaglia and Kevorkian's result on linear and branched polyethylene indicates that the heat capacity of the higher density linear sample is about 3–4 percent higher than that of the lower density branched sample at temperatures below 180 K. This indication is probably not real. The authors have pointed out in the paper that there have been experimental difficulties, and they have cited an uncertainty of 3–4 percent in the branched polyethylene and about 1 percent in the linear polyethylene measurements.

3.4. Adiabatic Temperature Drift and Glass Transition Temperature

The glass transition temperature of polyethylene has been assigned a value ranging from 130 to 250 K depending on the method of observation and on the investigators. The classical calorimetric and dilatometric methods of observing a break in the enthalpy or volume versus temperature curves, or a discontinuity in the heat capacity or thermal expansion coefficient behaviors, have difficulties in clearly demonstrating the occurrence of the glass transition phenomena in highly crystalline polyethylene. In the more sensitive ΔC_p versus T plot, figure 6, one observes two areas where irregularities occur over a relatively wide temperature range. In both regions the magnitude of the irregularity seems to be proportional to the amorphous content. However, only in the high temperature region, spontaneous thermal relaxation behavior, similar to the behavior of other completely amorphous substances, has been observed for the polyethylene samples. Thus the glass transition of polyethylene is limited to the higher temperature region of the heat capacity irregularities.

The detection of the kinetic nature of the glass transition phenomena in polyethylene by means of the observations of spontaneous adiabatic temperature drift in the glass transition region has been discussed in more detail elsewhere [28]. The following serves as a summary as well as a supplement.

The drift observation is enhanced by quenching and annealing treatments of the sample. In adiabatic calorimetry, the average heating rate during the heat capacity measurement is relatively constant, in the order of 10 K h^{-1}. Quenching is defined as a cooling rate to produce a glass at a much greater rate than the normal rate of observation. The cooling rates for quenching the sample in the calorimeter is generally in the order of 5 K min^{-1}. The annealing of a glass can either be achieved by a very slow rate of cooling in comparison to the rate of observation, or by holding for a couple of days at temperatures somewhat below the glass transition temperature of the quenched glass. A slow cooling rate of less than 1 K h^{-1} can easily be achieved. When a quenched glass is heated to temperatures near the glass transition region, sufficient mobility in the quenched glass allows it to relax toward the configurations of the supercooled liquid. If the sample is kept in an adiabatic environment, this relaxation shows up as a spontaneous temperature rise of the sample. This phenomena can usually be detected from some 50 K below the glass transition temperature, for materials having T_g around 200 to 300 K. Annealed glass can easily be overheated to temperatures above its glass transition temperature before its viscosity decreases to a low enough level to allow significant configurational relaxation to occur. Therefore the over-heated annealed glass relaxes toward the supercooled liquid state by spontaneously lowering its temperature under adiabatic conditions. The spontaneous heating and cooling of the quenched and annealed vitreous sample near the glass transition region have been observed for many vitreous materials as cited in reference [28]. Drifts have also been noted in some recent calorimetric studies on vitreous substances [29, 30]. The drift method has also been applied to the locating of the T_g of partially crystalline poly-1-pentene [31].

The total observed temperature in adiabatic calorimetry may come from three different sources, namely, the thermometer current, the heat transferred between the calorimeter and the shield, and the thermal effects generated by the sample itself. A steady thermometer current of 2 mA flowing through a 25-Ω (0 °C) platinum resistance thermometer produces approximately 0.1 T/273 mW of power. At around 250 K, under strict adiabatic conditions this power dissipation will cause a positive drift of the order of 0.03 mK min^{-1} to appear for the calorimeter loaded with polyethylene. The heat transfer coefficient for the loaded calorimeter at 250 K is about 1 mK min^{-1} per kelvin of temperature difference between the calorimeter and the adiabatic shield. With the short term temperature difference settable and controllable to within 1 mK, the positive drift produced by the thermometer current can be detected. Long term systematic variation in the drift has been observed to occur in the order of 0.05 mK min^{-1} per hour. The drift observable at the same temperature on different days may be different due to the residual emf in the differential thermocouple circuit. The residual emf in the heater and in the thermometer circuits is always less than 1 μV and varies slowly in time and temperature. Assuming a similar order of magnitude of the residual emf in the differential thermocouple circuit, a temperature difference in the order of 20 mK may exist between the adiabatic shield and the sample container. Coupled with the thermal transfer coefficient, a long term variation in the drift in the order of 0.05 mK min^{-1} may be expected.

In the temperature region around 150 K, some irregularity shows up in the ΔC_p plot, figure 6. The magnitude of the irregularity seems to be more pronounced in the linear sample than that in the branched sample, figure 8, it also seems to be proportional to the amorphous content. However no significant and long thermal drift is observed in this temperature region. One might associate this irregularity to the onset of the so-called crankshaft motion or other forms of segmental motion of the polyethylene chain in the amorphous phase. Branching of the chain increases the volume to be swept by this kind of motion and thus may hinder or move the onset to much higher temperature. A more pronounced C_p irregularity has been observed in a high molecular weight linear polyethylene sample [25].

Near 250 K, heat capacity irregularities show up in all three linear polyethylene samples, figure 6. The magnitude of the irregularity seems to be proportional to the amorphous content of the sample. Similar behavior may be seen in branched samples, figure 8. Significant spontaneous warming and cooling of the sample after quenching and annealing, respectively,

also show up in this temperature region. The calorimetric temperature drift, observed at 30 min after the termination of each energy input for the three linear polyethylene samples under both quenched and annealed conditions, are shown in figure 9. The drift

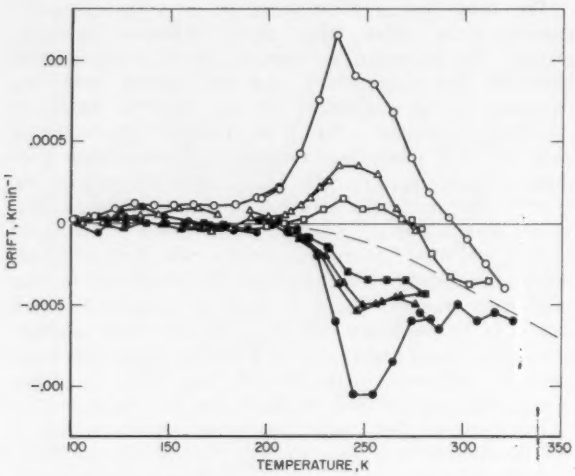

FIGURE 9. *Spontaneous adiabatic temperature drift of linear polyethylene.*

○ ● SRM 1475 as received, △ ▲ slow melt-crystallized, □ ■ pressure crystallized. Open symbols, quenched samples; filled symbols, annealed samples. Dashed line represents drift due to heat exchange alone under similar operational conditions.

behavior for the branched polyethylene sample was shown in reference [1]. Although the maximum magnitude of the observed drift is about one order of magnitude smaller than that observed in completely vitreous materials, the observed magnitude is still one order of magnitude greater than the contribution from the thermometer current and from the heat leak in the calorimeteric system. The magnitude of the maximum observed drift seems to be proportional to the amorphous content of the sample. However, the temperature at which the maximum drift occurs does not vary significantly as a function of the crystallinity of the sample. All three quenched samples show spontaneous warming drift peaks at temperatures around 235 K, and the annealed samples indicate cooling peaks near 245 K. Therefore in analogy with the behaviors observed for completely vitreous materials as cited in reference [28] and elsewhere, the glass transition temperature for the linear polyethylene sample may be assigned a value of 240 ± 5 K. This assignment is in good accord with a recent volume relaxation study on polyethylene samples [32]. The drifts for the two densified samples have been observed along with the heat capacity measurements reported in this paper. During the heat capacity measurements for the SRM 1475 in the condition as received [1], no annealing and quenching treatments were applied. Therefore the same sample was reloaded in the calorimeter and the drift behavior was observed following similar annealing and quenching treatments to those for the two high density samples.

The author wishes to thank C. H. Pearson in assisting in the calorimetric measurements and D. W. Brown for the preparation of the pressure-crystallized sample. He also wishes to thank G. T. Davis, Cheng-Hsiung Hsieh,[3] R. G. Christensen and G. Ross for the characterization of the samples by small-angle X-ray diffraction, IR spectroscopy, viscosity and gel-permeation chromatography, respectively.

4. References

[1] Chang, S. S., and Bestul, A. B., J. Res. Nat. Bur. Stand. (U.S.), **77A** (Phys. and Chem.), No. 4, 395–405 (July–Aug. 1973).
[2] Sterrett, K. F., Blackburn, D. H., Bestul, A. B., Chang, S. S., and Horman, J. A., J. Res. Nat. Bur. Stand. (U.S.), **69C** (Eng. and Instr.), No. 1, 19–26 (Jan.–Mar. 1965).
[3] Wunderlich, B., and Arakawa, T., J. Polymer Sci. A–2, 3697 (1964).
[4] Ross, G., and Frolen, L., J. Res. Nat. Bur. Stand. (U.S.), **76A** (Phys. and Chem.), No. 2, 163–170 (Mar.–Apr. 1972).
[5] Kardos, J. L., Baer, E., Geil, P. H., and Koenig, J. L., Kolloid Z. **204,** 1 (1965).
[6] Calvert, P. D., and Uhlmann, D. R., J. Polymer Sci. A–2, **10,** 1811 (1972).
[7] Dainton, F. S., Evans, D. M., Hoare, F. E., and Melia, T. P., Polymer **3,** 277 (1962).
[8] Isaacs, L. L., and Garland, C. W., J. Phys. Chem. Solids **23,** 311 (1962).
[9] Passaglia, E., and Kevorkian, H. K., J. Appl. Polymer Sci. **7,** 119 (1963).
[10] Tucker, J. E., and Reese, W., J. Chem. Phys. **46,** 1388 (1967).
[11] Westrum, E. F., Jr., unpublished.
[12] Wunderlich, B., J. Phys. Chem. **69,** 2078 (1965).
[13] Broadhurst, M. G., J. Res., Nat. Bur. Stand. (U.S.), **67A** (Phys. and Chem.), No. 3, 233–240 (May–June 1963).
[14] Wunderlich, B., J. Chem. Phys. **37,** 1203 (1962).
[15] Wunderlich, B., and Baur, H., Adv. Polymer Sci. **7,** 261 (1970).
[16] Wunderlich, B., J. Chem. Phys. **37,** 1207 (1962).
[17] Atkinson, C. M. L., Larkin, J. A., Richardson, Y. M. J., J. Chem. Therm. **1,** 435 (1969).
[18] Wunderlich, B., and Dole, M., J. Polymer Sci. **24,** 201 (1957).
[19] Richardson, M. J., Trans. Faraday Soc. **61,** 1876 (1965).
[20] Wilski, H., Kunstoffe **50,** 281 (1960).
[21] Dole, M., Hettinger, W. P., Jr., Larson, N. R., and Wethington, J. A., Jr., J. Chem. Phys. **20,** 781 (1952).
[22] Sochava, I. V., Doklady Akad. Nauk SSSR **130,** 126 (1960).
[23] Sochava, I. V., and Trapeznikova, O. N., Soviet Phys. Doklady **2,** 164 (1957).
[24] Guttman, C. M., J. Chem. Phys. **56,** 627 (1972).
[25] Beatty, C. L., and Karasz, F. E., Bull. Am. Phys. Soc. Ser. II, **16,** 1391 (1971).
[26] Furukawa, G. T., and Reilly, M., J. Res. Nat. Bur. Stand. (U.S.), **69A** (Phys. and Chem.), No. 1, 5–12 (Jan.–Feb. 1965).
[27] Roder, H. M., J. Res. Nat. Bur. Stand. (U.S.), **69A** (Phys. and Chem.), No. 6, 527–530 (Nov.–Dec. 1965).
[28] Chang, S. S., J. Polymer Sci. Part C, 43, (1973).
[29] Matsuo, T., Oguni, M., Suga, H., and Seki, S., Proc. Japan Acad. **48,** 237 (1972).
[30] Haida, O., Matsuo, T., Suga, H., and Seki, S., Proc. Japan Acad. **48,** 489 (1972).
[31] Bourdariat, J., Isnard, R., and Odin, J., IUPAC Intl. Sym. Macromol., Aberdeen, September 1973.
[32] Davis, G. T., and Eby, R. K., J. Appl. Phys. **44,** 4274 (1973).

(Paper 78A3–819)

[3] Guest Worker at NBS from the Union Industrial Research Institute, Hsing-Chu, Taiwan, Republic of China.

JOURNAL OF RESEARCH of the National Bureau of Standards—A. Physics and Chemistry
Vol. 78A, No. 3, May–June 1974

The Specific Heats, C_σ, and C_V, of Compressed and Liquefied Methane*

B. A. Younglove**

Institute for Basic Standards, National Bureau of Standards, Boulder, Colorado 80302

(January 30, 1974)

The specific heats, C_σ, of saturated liquid methane have been measured at 66 temperatures in the temperature range 95–187 K. The specific heats at constant volume, C_V, have been measured at 20 densities ranging from 0.8 to 2.8 times the critical density, at temperatures between 91 and 300 K, and at pressures to 330 bar (at 280 *PVT* states in all). The uncertainty of most of the measurements is estimated to be less than 0.5 percent, except near the critical point. These measurements were performed primarily to provide input data for accurate thermodynamic properties data calculations for liquid methane. They are believed to be the most comprehensive specific heat measurements available for pure compressed gaseous and liquid methane.

Key words: Constant volume; heat capacity; liquid; saturated liquid; specific heat; methane.

1. Introduction

For the calculation of fluid thermodynamic properties such as internal energy, enthalpy, entropy, and velocity of sound, at temperatures less than the critical point, one needs either the latent heat of vaporization or specific heat along a path traversing the temperatures of interest. Heat capacity measurements are much easier than latent heat measurements and the specific heat measurements are not restricted to the liquid-vapor curve but can be made covering temperatures and densities in the single phase fluid region as well.

For methane, specific heat of the saturated liquid, C_σ, was measured from 95 to 187 K, and specific heat at constant volume, C_V, was measured on 20 isochores with densities ranging from 8 mol/l to 28 mol/l, temperatures from 90 to 300 K, and pressures to 330 bar [1].[1]

2. Apparatus

The specific heats were obtained using a constant volume adiabatic calorimeter, as described previously by Goodwin [2]. Basically, it consists of a thin spherical stainless-steel sample holder bearing a heater and platinum resistance thermometer and enclosed in an adiabatic shield. The calorimeter and cryostat are shown in figure 1. The refrigerant was liquid nitrogen.

The versatility of this instrument is demonstrated in that it has been used with very minor modifications for the C_V and C_σ measurements of hydrogen [3, 4], oxygen [5, 6], fluorine [7, 8], and in this work on methane. These measurements cover temperatures from 14 to 300 K and pressures to 330 bar.

The thermometer was calibrated by the NBS Temperature Section. Temperatures are on the IPTS–68 scale. The temperature of the adiabatic shield and guard ring are controlled to the sample temperature with difference thermocouples and automatic power regulation. Heat exchange to the sample holder is considered negligible.

The sample used was 99.99 percent methane. Impurities as analyzed by the supplier in ppm were $CO_2 < 10$; O_2, 4; N_2, 12. A molecular sieve in an ice bath served to ensure removal of water vapor present in the sample.

3. Procedure

In essence, the specific heat C_V is calculated from the measured parameters as follows. The total heat capacity is determined as the ratio of the heat input ΔQ to the temperature increase ΔT brought about by applying a very stable power source to a resistor attached to the calorimeter sample holder, for an elapsed time Δt. The heat capacity of the empty sample holder Co is then subtracted off. It, of course, was previously measured in exactly the same way except with the sample space pumped to a vacuum. The difference of these two quantities is the heat capacity of the methane sample. The specific heat is

*This work was carried out at the National Bureau of Standards under the sponsorship of The American Gas Association.

**Present address: Cryogenics Division, National Bureau of Standards, Boulder, CO 80302.

[1] Figures in brackets indicate the literature references at the end of this paper.

TABLE 1. *Specific heat of saturated liquid methane,* C_σ *or* C_{SAT}*; specific heat at constant volume of saturated liquid calculated,* C_V*; specific heat of the two phase (liquid-vapor) system,* C_2*; heat capacity of the calorimeter (empty)* C_0*, and heat capacity of the calorimeter (full)* $\Delta Q/\Delta T$ *or* DQ/DT*, with temperature, pressure, density, and temperature increment,* DT

ID	Temp K	Press bar	Dens mol/l	DT K	*DQ/DT* J/K	C_0 J/K	C_2 J/mol · K	C_V J/mol · K	C_{sat} J/mol · K
201	95.402	0.209	27.755	3.657	133.482	46.671	54.418	34.274	54.240
401	95.846	.219	27.718	5.799	139.159	46.881	54.252	34.103	54.131
202	99.021	.311	27.450	3.574	135.870	48.348	54.864	34.169	54.647
302	101.651	.409	27.224	6.638	141.300	49.520	55.058	34.016	54.877
402	101.961	.422	27.198	6.420	143.111	49.656	54.943	33.883	54.790
203	102.574	.448	27.145	3.524	137.905	49.923	55.152	33.898	54.896
204	106.891	.673	26.767	5.110	140.924	51.750	55.899	33.941	55.602
303	108.219	.758	26.649	6.495	145.302	52.293	55.794	33.710	55.583
403	108.800	.797	26.597	7.236	146.902	52.528	55.483	33.349	55.315
205	112.604	1.097	26.254	6.273	144.013	54.022	56.410	33.478	56.075
304	115.165	1.343	26.019	7.386	149.404	54.988	56.638	33.391	56.434
206	119.117	1.802	25.649	6.702	147.576	56.412	57.144	33.041	56.810
305	122.474	2.278	25.327	7.194	153.257	57.561	57.404	32.862	57.287
405	123.367	2.419	25.240	7.498	154.829	57.858	57.008	32.389	56.996
207	125.766	2.830	25.005	6.568	151.006	58.636	57.899	32.534	57.645
406	130.765	3.852	24.500	7.297	158.819	60.171	57.992	32.000	58.245
208	132.274	4.209	24.343	6.430	154.477	60.612	58.834	32.162	58.774
1001	132.751	4.326	24.293	5.117	122.552	60.750	62.894	32.148	58.879
902	135.455	5.038	24.007	4.538	137.072	61.512	60.813	31.499	58.930
1002	137.805	5.723	23.752	4.973	125.195	62.151	64.157	31.650	59.729
903	139.970	6.412	23.513	4.476	139.223	62.720	61.570	30.986	59.698
801	144.305	7.971	23.017	4.019	141.250	63.808	62.323	30.460	60.560
904	144.401	8.009	23.005	4.386	141.728	63.831	62.689	30.797	60.929
802	148.500	9.725	22.514	4.371	143.789	64.800	63.565	30.407	62.033
905	148.881	9.896	22.467	4.316	143.807	64.888	63.509	30.230	62.005
1003	150.824	10.807	22.224	4.332	133.134	65.326	68.994	31.449	64.014
803	152.809	11.798	21.969	4.247	146.566	65.763	65.022	30.468	63.898
906	153.157	11.978	21.924	4.229	146.775	65.838	65.129	30.459	64.048
1004	155.542	13.267	21.606	4.941	135.238	66.345	70.092	30.518	65.246
804	157.043	14.128	21.401	4.180	148.588	66.657	65.926	29.932	65.435
907	157.355	14.312	21.358	4.167	148.747	66.721	66.001	29.899	65.569
1005	159.127	15.388	21.107	4.035	137.307	67.080	71.446	30.244	66.905
805	161.181	16.707	20.808	4.095	151.123	67.486	67.294	29.823	67.733
908	161.483	16.908	20.763	4.088	151.284	67.545	67.375	29.793	67.898
1006	163.136	18.036	20.512	3.982	138.917	67.864	72.280	29.161	68.379
1402	163.782	18.492	20.412	5.441	153.354	67.987	68.702	30.257	69.936
806	165.249	19.556	20.179	4.036	153.713	68.263	68.749	29.746	70.534
1407	165.128	19.467	20.199	5.131	154.144	68.240	69.132	30.171	70.865
909	165.548	19.779	20.131	4.043	153.880	68.318	68.838	29.719	70.745
1007	166.549	20.536	19.967	2.738	141.994	68.503	74.756	29.907	71.756
807	169.253	22.687	19.505	3.963	156.273	68.991	70.216	29.609	73.960
910	169.565	22.945	19.450	3.949	156.656	69.047	70.480	29.743	74.411
1220	170.157	23.440	19.344	7.335	138.896	69.151	79.614	29.404	74.696
1008	170.197	23.474	19.336	4.297	144.726	69.159	76.862	30.033	75.369
1408	170.251	23.520	19.327	5.020	157.666	69.168	71.213	30.181	75.575
1403	171.097	24.243	19.172	5.271	158.018	69.316	71.376	29.980	76.320
808	173.180	26.094	18.773	3.890	159.054	69.675	71.898	29.577	78.540
911	173.480	26.369	18.714	3.873	159.572	69.727	72.273	29.813	79.194
701	173.505	26.392	18.709	5.002	141.928	69.731	81.284	29.262	78.678
1216	174.032	26.880	18.603	7.180	141.932	69.820	82.310	29.445	79.623
1009	174.429	27.252	18.522	4.167	148.478	69.887	79.930	30.556	81.334
1409	175.228	28.012	18.355	4.900	161.213	70.021	73.374	30.069	82.128
1404	176.295	29.051	18.125	5.118	162.367	70.198	74.158	30.312	84.253
809	177.029	29.782	17.961	3.811	162.720	70.318	74.323	30.097	85.466
1221	177.420	30.177	17.872	6.968	146.364	70.382	86.720	31.201	87.382
702	177.902	30.670	17.760	3.799	145.938	70.461	84.967	29.552	86.790
1010	178.557	31.349	17.603	4.090	151.355	70.567	82.156	29.861	88.641
1200	180.613	33.553	17.078	5.694	148.814	70.895	88.923	30.420	95.067
1217	181.034	34.018	16.963	6.825	149.125	70.961	89.202	30.254	96.349
703	181.645	34.702	16.790	3.688	150.564	71.057	89.496	30.451	98.844
1011	182.572	35.759	16.516	3.940	156.745	71.201	86.983	31.025	103.442
1222	184.222	37.703	15.976	6.616	154.219	71.454	94.445	31.451	113.330
704	185.271	38.982	15.588	3.549	156.464	71.613	95.503	31.421	121.769
1201	186.127	40.050	15.236	5.329	158.456	71.742	98.948	32.509	132.153
1012	187.577	41.915	14.530	6.026	151.278	71.957	80.630	16.306	141.359
1218	187.633	41.988	14.499	6.358	160.079	71.965	100.540	30.050	156.489

obtained by dividing the heat capacity by the amount of methane, N.

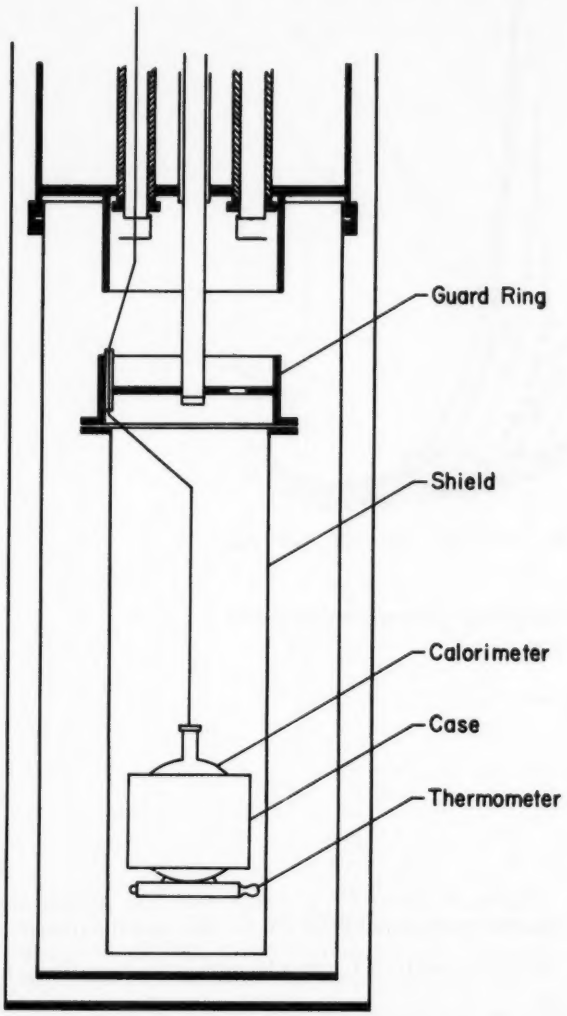

FIGURE 1. *Calorimeter and cryostat.*

Actually, several corrections are made to the above. Since the sample holder is a thin stainless steel sphere (~ 0.16 mm wall thickness and 5 cm diam), it stretches as the pressure increases. This allows work to be done by the methane due to the increase of the sample volume. This correction [4, 5, 6], developed by Walker [9], ranges from 0.5 to 5 percent of the resulting C_V value. However, it can be made accurately.

Of the three variables, pressure, temperature, and density, only temperature is measured during the measurement of an isochore. The pressure and temperature are measured at filling and the density calculated from the *PVT* surface [10]. The amount of methane, N, is calculated from the volume $V(T, P)$ as previously determined [3, 5]. The density for each C_V measurement is calculated from the filling density after correcting for sample holder expansion and the amount compressed into the filling capillary [6].

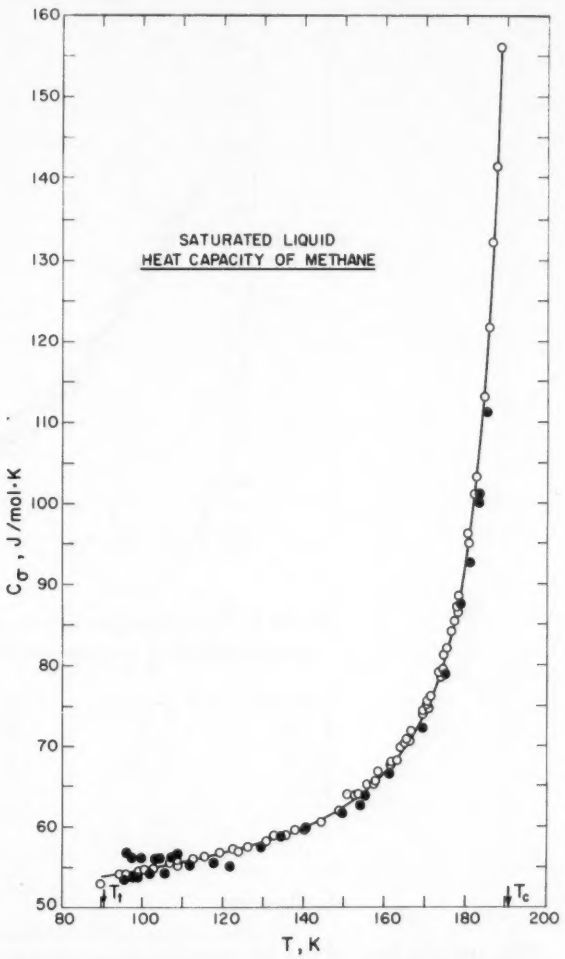

FIGURE 2. *Specific heat of the saturated liquid for methane, this work,* ○, *the measurements of Wiebe and Breevort* ● [12].

In the case of the C_σ measurement, the two phase heat capacity (liquid and gas) is first determined as the difference of the total heat capacity (DQ/DT, column 6 of table 1) and the empty heat capacity (Co, column 7) and the result divided by the total amount of sample (C_2, column 8). Then the effects of the latent heat of vaporization and heat absorbed by the vapor are subtracted [3, 5, 7] to give C_σ (column 10). This type of correction is derived by Hoge [11].

The temperature increment, resulting from a constant power input over a time Δt, is evaluated at the middle of the heating interval by extrapolating the temperature drift rates evaluated just before heating and after an equilibrating time has elapsed (about 20 min). Care was taken to reduce the effects of noise on drift rate by taking many (10 to 20) measurements of time and temperature.

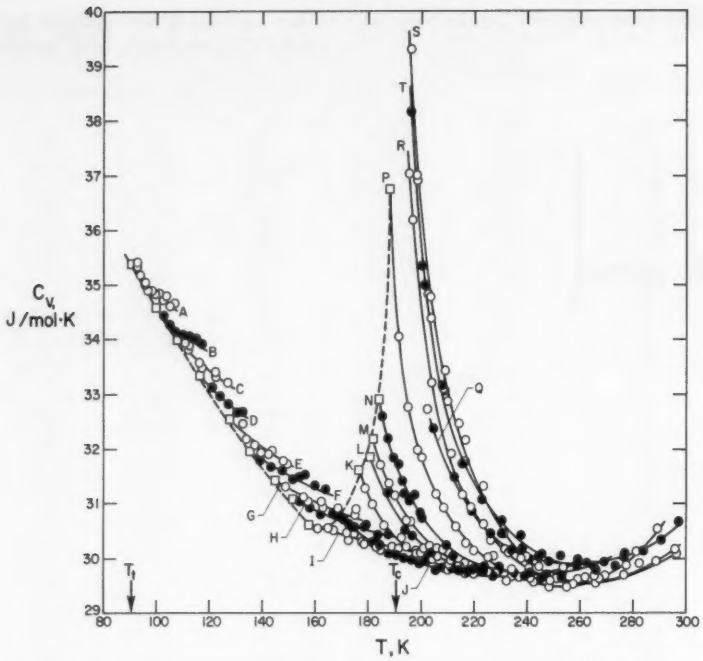

FIGURE 3. *Specific heat at constant volume of methane on isochores versus temperature.*

Open and closed circles on alternate isochores are for clarity.

A–28.0 mol/l,	B–27.4 mol/l	C–26.7 mol/l
D–25.8	E–24.7	F–24.0
G–23.0	H–22.1	I–21.3
J–19.5	K–18.0	L–17.0
M–16.7	N–16.0	P–14.4
Q–13.1	R–13.1	S–11.8
T–7.9		

4. Results

The specific heat of the saturated liquid was measured for 66 temperatures. The lowest was 95 K (triple point, 90.68 K) and the highest 187 K (see fig. 2 and table 1). The estimated uncertainty in the measured value of C_σ is about 0.5 percent generally but increasing to about 5 percent within a few Kelvin of the critical point. The data of Weibe and Breevort [12] are shown for comparison as the closed circles. Their measurements agree remarkably well with the new data, considering the state of the art at that time.

Figure 3 and table 2 show C_V as a function of temperature for the various isochores. The dashed line is the locus of C_V for saturated liquid as extrapolated from the C_V measurements. The uncertainties in C_V are the same as for C_σ. Densities Q, R, S, and T have uncertainties as large as 5 percent near critical temperature, indicated as T_c on figure 3. Density T is 22 percent less than critical density.

Figure 4 shows C_V at saturation. The circles are values extrapolated from the C_V data and the triangles are computed from C_σ data by adding the term $T\left(\frac{\partial P}{\partial T}\right)_v \frac{dV}{dT}$. These derivatives, evaluated analytically from a representation of the PVT surface [2], introduce the scatter and the lowering of the values from the extrapolated values which have essentially the same accuracy as the measured C_V values.

Comparison was made with the C_p data of Jones et al. [17] on their 2000 lb/in² (136.7 bar) by interpolation of the C_V data and adding the PVT contribution. Figure 5 shows the close agreement of the two sets of data. The other curve is calculated from spectroscopic heat capacities together with the PVT term above critical temperature, (T_c). Below the critical temperature, latent heats must also be used. The discontinuity is, of course, at T_c.

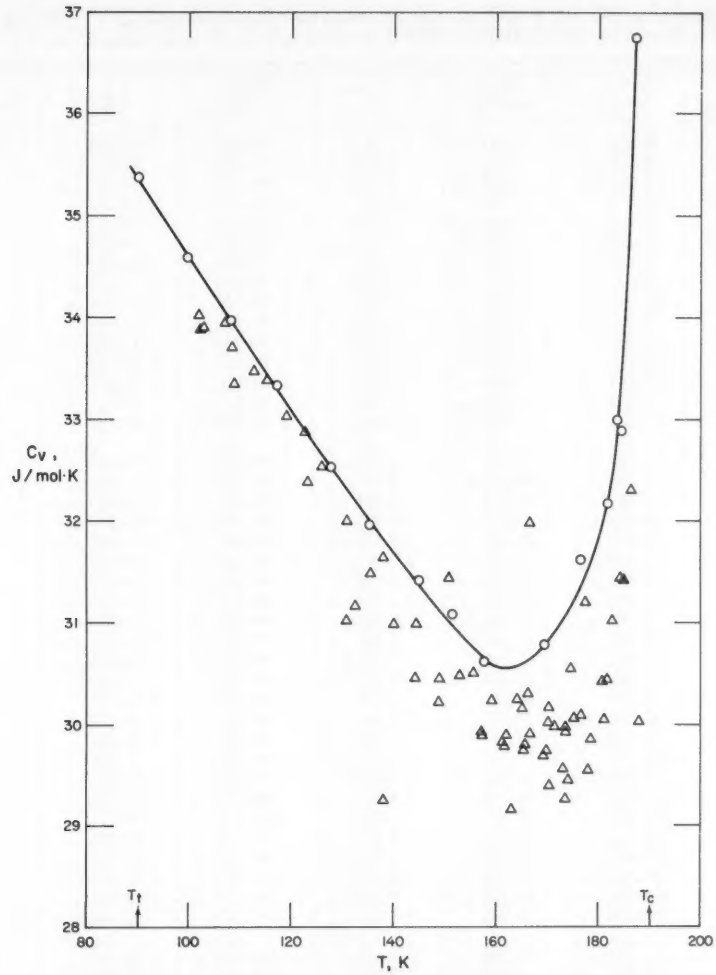

FIGURE 4. C_v *of liquid methane evaluated at the liquid-gas boundary.*
Extrapolation of C_v(○), calculation from C_σ using *PVT* surface (△).

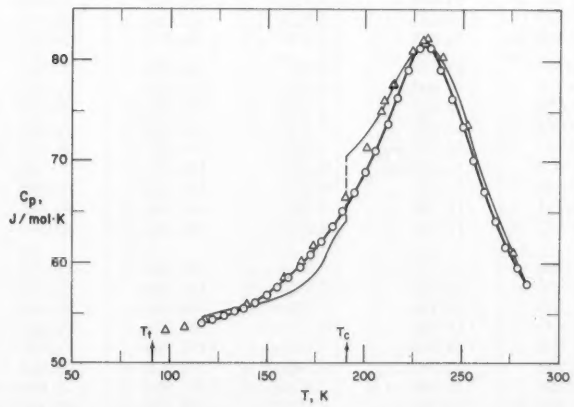

FIGURE 5. *Comparison of methane* C_p *from Jones, et al.* (–○–); *to* C_p *calculated from* C_v *data, this work* (△), *and to* C_p *calculated from* PVT *data* (—).

TABLE 2. *Specific heat at constant volume,* C_V, *of methane; heat correction for calorimeter expansion* Cl, *heat capacity of empty calorimeter,* CO, *total heat capacity of calorimeter (full)* $\Delta Q/\Delta T$ *or* DQ/DT, *with temperature, pressure, density, and temperature increment,* DT

ID	Temp K	Press bar	Den mol/l	*DT* K	*DQ/DT* J/K	Co J/K	Cl J/mol · *K*	C_V J/mol · K
2209	200.342	56.917	7.991	7.542	94.477	73.734	0.166	35.351
2203	201.339	58.027	7.991	5.459	94.406	73.865	.167	35.004
2210	207.854	65.217	7.988	7.559	94.152	74.691	.170	33.153
2204	208.168	65.562	7.988	7.419	94.184	74.729	.170	33.141
2211	215.402	73.451	7.984	7.554	94.227	75.593	.175	31.732
2212	222.937	81.598	7.980	7.511	94.677	76.439	.182	31.046
2205	222.993	81.658	7.980	7.361	94.691	76.445	.182	31.059
2206	230.373	89.583	7.977	7.387	95.264	77.226	.189	30.698
2213	230.453	89.668	7.977	7.484	95.130	77.234	.189	30.455
2207	237.534	97.229	7.973	7.324	95.819	77.940	.195	30.419
2214	238.128	97.862	7.973	7.382	95.748	77.998	.196	30.198
2208	244.733	104.881	7.970	7.292	96.283	78.619	.202	30.045
2215	245.476	105.669	7.969	7.369	96.374	78.687	.203	30.084
2216	252.815	113.433	7.966	7.332	97.017	79.335	.210	30.067
2218	266.349	127.671	7.959	7.246	97.960	80.436	.222	29.785
1505	195.780	53.853	10.176	6.728	102.498	73.123	.185	39.325
1523	198.095	57.310	10.175	5.257	101.084	73.436	.189	36.999
1521	198.426	57.804	10.174	5.284	101.071	73.480	.189	36.921
1506	202.601	64.048	10.171	6.923	100.060	74.028	.194	34.818
1502	203.142	64.857	10.171	6.470	106.980	74.098	.195	44.032
1524	203.375	65.206	10.171	5.301	100.142	74.128	.196	34.793
1522	203.731	65.739	10.171	5.320	99.881	74.173	.197	34.382
1525	208.704	73.193	10.167	5.334	99.538	74.795	.203	33.078
1523	209.057	73.722	10.167	5.326	99.856	74.838	.204	33.447
1507	209.526	74.426	10.166	6.942	99.491	74.895	.203	32.879
1503	209.853	74.915	10.166	6.955	99.636	74.935	.204	33.020
1526	214.044	81.206	10.164	5.346	99.736	75.434	.211	32.476
1508	216.467	84.845	10.161	6.956	99.479	75.715	.213	31.750
1504	216.813	85.365	10.161	6.945	99.842	75.755	.214	32.185
1509	223.396	95.256	10.157	6.923	99.937	76.489	.223	31.318
1510	230.790	106.373	10.151	6.920	100.066	77.268	.233	30.432
1511	237.756	116.844	10.147	6.901	100.443	77.962	.242	29.998
1512	244.636	127.181	10.142	6.864	100.993	78.610	.251	29.857
1513	251.488	137.466	10.137	6.819	101.457	79.221	.261	29.650
1514	259.403	149.331	10.131	6.782	102.116	79.886	.271	29.632
1515	266.154	159.433	10.126	6.725	102.604	80.421	.280	29.560
1517	282.516	183.843	10.114	6.617	104.067	81.599	.301	29.922
1518	289.146	193.696	10.110	6.625	104.538	82.032	.310	29.964
1519	295.822	203.596	10.105	6.556	105.109	82.444	.319	30.170
219	195.627	55.318	11.838	9.621	105.430	73.102	.204	37.165
223	196.581	57.055	11.839	7.285	104.709	73.232	.209	36.177
224	203.924	70.601	11.832	7.393	103.134	74.198	.226	33.223
225	211.370	84.550	11.826	7.394	102.930	75.118	.242	31.908
205	215.626	92.584	11.822	8.023	102.779	75.618	.250	31.148
226	218.787	98.572	11.819	7.411	102.950	75.979	.256	30.922
206	223.653	107.819	11.815	8.022	103.224	76.517	.265	30.609
227	226.191	112.653	11.813	7.374	103.274	76.789	.270	30.347
207	231.675	123.117	11.808	7.947	103.685	77.359	0.279	30.155
228	233.566	126.729	11.806	7.338	103.858	77.549	.283	30.130
208	239.625	138.319	11.801	7.906	104.383	78.141	.293	30.043
229	204.923	140.803	11.800	7.311	104.171	78.264	.296	29.653
209	248.734	155.761	11.792	7.882	104.855	78.979	.309	29.604
210	257.453	172.459	11.784	9.556	105.552	79.726	.323	29.534
211	266.957	190.643	11.775	9.438	106.408	80.482	.339	29.632
212	276.534	208.934	11.766	9.341	107.186	81.187	.355	29.702
214	296.364	246.647	11.748	9.271	108.845	82.476	.388	30.098
301	204.751	77.746	13.088	7.244	105.556	74.303	.264	32.393
302	212.016	93.924	13.080	7.229	105.596	75.195	.282	31.485
303	219.265	110.242	13.073	7.214	105.859	76.033	.299	30.868
304	226.524	126.697	13.065	7.179	106.293	76.824	.315	30.478
305	234.072	143.881	13.057	7.166	106.784	77.600	.331	30.165
306	241.245	160.256	13.050	7.146	107.321	78.295	.347	29.985
307	248.387	176.580	13.042	7.078	107.969	78.948	.362	29.965
309	262.566	208.987	13.026	7.007	109.144	80.140	.391	29.918
310	276.780	241.398	13.011	6.874	110.608	81.204	.419	30.309
313	276.944	241.772	13.010	6.908	110.434	81.216	.419	30.114

TABLE 2. *Specific heat at constant volume,* C_v, *of methane; heat correction for calorimeter expansion* Cl, *heat capacity of empty calorimeter,* CO, *total heat capacity of calorimeter (full)* $\Delta Q/\Delta T$ *or* DQ/DT, *with temperature, pressure, density, and temperature increment,* DT— *Continued*

ID	Temp K	Press bar	Den mol/l	*DT* K	*DQ/DT* J/K	Co J/K	Cl J/mol · K	C_v J/mol · K
314	283.783	257.318	13.003	6.854	110.947	81.684	.433	30.147
311	290.591	272.756	12.995	6.847	111.617	82.124	.446	30.375
312	297.427	288.216	12.987	6.788	112.344	82.540	.460	30.687
501	191.539	52.228	14.388	7.056	108.595	72.531	.268	34.042
528	195.039	61.226	14.383	8.352	107.756	73.021	.281	32.765
502	198.638	70.602	14.379	7.127	107.453	73.509	.295	32.000
520	200.323	75.028	14.377	8.432	107.534	73.732	.299	31.860
503	205.816	89.577	14.371	7.131	107.532	74.437	.315	31.171
521	208.733	97.366	14.366	8.358	107.655	74.799	.321	30.940
504	212.954	108.696	14.362	7.102	107.804	75.306	.334	30.585
522	217.103	119.884	14.356	8.319	107.990	75.788	.347	30.292
505	220.066	127.901	14.353	7.075	108.187	76.123	.356	30.152
523	225.394	142.360	14.346	8.245	108.656	76.704	.369	30.032
506	227.167	147.180	14.344	7.039	108.887	76.892	.375	30.067
524	234.287	166.574	14.334	8.234	109.380	77.621	.392	29.826
507	234.417	166.928	14.335	6.969	109.372	77.634	.393	29.805
508	241.372	185.902	14.326	6.927	109.898	78.307	.411	29.647
525	242.493	188.962	14.324	8.159	109.939	78.412	.412	29.585
509	248.293	204.791	14.317	6.910	110.378	78.940	.428	29.485
510	255.197	223.622	14.308	6.870	111.009	79.538	.445	29.500
511	262.143	242.543	14.299	6.820	111.759	80.107	.461	29.656
514	265.537	251.779	14.294	7.970	112.059	80.373	.468	29.681
512	269.538	262.650	14.289	7.971	112.383	80.678	.478	29.689
515	273.495	273.386	14.284	7.928	112.890	80.969	.487	29.885
513	277.494	284.223	14.278	7.914	113.176	81.255	.497	29.877
516	281.439	294.892	14.273	7.875	113.651	81.527	.506	30.061
517	289.349	316.229	14.262	7.793	114.710	82.045	.524	30.557
701	187.947	51.088	16.104	7.172	110.110	72.012	0.350	32.038
707	188.669	53.498	16.103	6.957	110.164	72.118	.353	31.990
721	191.577	63.245	16.098	6.895	110.072	72.537	.367	31.543
702	195.118	75.188	16.093	7.178	110.019	73.032	.378	31.066
708	195.637	76.943	16.092	6.947	110.062	73.103	.380	31.040
720	199.140	88.833	16.087	6.859	110.111	73.576	.390	30.670
703	202.277	99.525	16.082	7.135	110.530	73.987	.397	30.670
709	202.632	100.738	16.082	6.943	110.308	74.032	.399	30.441
704	209.408	123.943	16.071	7.112	110.909	74.881	.426	30.204
710	209.569	124.495	16.071	6.933	110.994	74.901	.427	30.258
711	216.494	148.306	16.060	6.873	111.429	75.718	.450	29.911
705	216.509	148.360	16.060	7.078	111.388	75.720	.450	29.875
712	223.352	171.937	16.049	6.816	112.095	76.484	.472	29.805
706	223.900	173.825	16.048	7.007	112.128	76.544	.473	29.780
713	230.437	196.359	16.038	6.824	112.675	77.232	.494	29.639
714	237.251	219.833	16.027	6.791	113.485	77.913	.515	29.729
715	244.048	243.213	16.016	6.758	113.994	78.556	.536	29.594
716	250.777	266.302	16.005	6.660	114.660	79.159	.557	29.627
717	257.424	289.044	15.994	6.627	115.322	79.724	.577	29.689
718	264.035	311.587	15.983	6.571	116.177	80.256	.597	29.944
719	270.623	333.970	15.972	6.544	116.590	80.759	.616	29.849
1601	185.501	42.477	16.038	2.172	110.226	71.648	.337	32.608
1602	187.587	49.323	16.035	2.006	110.069	71.959	.348	32.198
1603	189.591	55.934	16.032	2.009	109.944	72.252	.358	31.832
1604	191.595	62.582	16.029	2.004	110.119	72.539	.361	31.732
1618	192.871	66.824	16.024	6.135	109.928	72.719	.367	31.410
1605	193.605	69.272	16.026	2.010	109.753	72.822	.377	31.163
1606	195.615	75.989	16.023	2.012	109.895	73.100	.383	31.041
1607	197.622	82.719	16.020	2.003	110.311	73.373	.389	31.157
1608	199.628	89.464	16.017	2.005	110.203	73.640	.396	30.831
1619	200.031	90.821	16.011	8.252	110.152	73.693	.391	30.746
1620	209.230	121.946	15.996	10.164	110.765	74.859	.419	30.246
1609	217.884	151.399	15.986	6.097	111.290	75.877	.452	29.793
1611	223.224	169.616	15.977	6.069	111.946	76.470	.469	29.830
1610	223.903	171.930	15.976	6.052	112.026	76.544	.471	29.834
1622	229.421	190.764	15.964	10.032	112.633	77.128	.484	29.842
1612	229.453	190.871	15.967	6.063	112.588	77.131	.488	29.795
1623	239.424	224.878	15.948	9.937	113.475	78.122	.515	29.681
1613	241.503	231.959	15.948	5.956	113.763	78.319	.525	29.748
1614	247.521	252.433	15.939	5.898	114.298	78.871	.544	29.715

TABLE 2. *Specific heat at constant volume, C_V, of methane; heat correction for calorimeter expansion* Cl, *heat capacity of empty calorimeter,* CO, *total heat capacity of calorimeter (full)* $\Delta Q/\Delta T$ *or* DQ/DT, *with temperature, pressure, density, and temperature increment,* DT— *Continued*

ID	Temp K	Press bar	Den mol/l	*DT* K	*DQ/DT* J/K	Co J/K	Cl J/mol · K	C_V J/mol · K
1615	253.443	272.535	15.929	5.912	114.868	79.389	.562	29.742
1616	259.333	292.473	15.919	5.842	115.529	79.880	.579	29.869
1617	265.198	312.270	15.910	5.849	116.001	80.347	.597	29.856
1309	184.764	45.449	16.723	5.354	110.741	71.537	0.381	31.721
1301	187.826	56.698	16.717	6.932	110.769	71.994	.394	31.357
1310	190.103	65.099	16.714	5.347	110.862	72.326	.406	31.150
1302	194.733	82.255	16.706	6.892	110.968	72.979	.423	30.685
1311	195.445	84.904	16.706	5.344	111.063	73.077	.427	30.679
1303	201.094	105.956	16.696	5.855	111.252	73.833	.446	30.196
1323	202.937	112.841	16.693	6.031	111.551	74.072	.453	30.239
1312	206.062	124.532	16.688	5.287	111.919	74.468	.465	30.204
1304	206.122	124.756	16.689	4.249	111.707	74.475	.466	30.023
1324	208.680	134.336	16.683	5.477	112.228	74.792	.473	30.184
1305	210.401	140.788	16.681	4.330	112.079	75.001	.481	29.882
1313	211.348	144.339	16.679	5.286	112.322	75.115	.483	29.987
1325	214.143	154.818	16.674	5.464	112.494	75.446	.492	29.847
1306	215.024	158.123	16.673	4.934	112.592	75.549	.496	29.840
1314	216.658	164.252	16.670	5.219	112.889	75.737	.501	29.924
1326	219.582	175.218	16.665	5.433	112.992	76.069	.511	29.727
1327	225.003	195.545	16.655	5.423	113.635	76.662	.530	29.749
1317	232.337	223.009	16.643	5.178	114.228	77.426	.555	29.585
1318	237.657	242.891	16.633	5.448	114.856	77.952	.572	29.651
1319	243.097	263.174	16.624	5.401	115.579	78.468	.590	29.802
1320	248.519	283.339	16.614	5.387	115.951	78.960	.608	29.686
1321	253.921	303.370	16.604	5.359	116.619	79.430	.626	29.831
1322	259.304	323.264	16.595	5.339	117.189	79.878	.644	29.913
411	187.325	58.469	17.007	8.019	111.229	71.920	.416	31.221
401	193.924	83.993	16.997	6.900	111.328	72.867	.443	30.513
406	196.587	94.337	16.992	7.437	111.563	73.233	.452	30.399
413	203.953	123.025	16.978	7.970	112.216	74.202	.478	30.119
414	211.988	154.390	16.964	7.898	113.134	75.192	.507	30.033
415	219.901	185.282	16.950	7.850	113.769	76.104	.535	29.782
416	227.768	215.952	16.936	7.807	114.550	76.955	.562	29.698
417	235.598	246.397	16.922	7.735	115.435	77.751	.590	29.743
418	245.293	283.931	16.904	7.650	116.261	78.670	.623	29.635
419	252.926	313.338	16.890	7.598	117.007	79.345	.649	29.667
1801	178.581	37.972	18.086	3.069	112.484	70.571	.469	31.280
1802	181.649	51.836	18.080	3.085	112.625	71.057	.496	30.991
1803	186.224	72.545	18.068	6.089	112.813	71.756	.503	30.598
1804	192.299	100.083	18.056	6.060	113.438	72.639	.530	30.377
1805	198.354	127.540	18.044	6.039	113.922	73.471	.554	30.090
1806	204.379	154.828	18.032	6.010	114.564	74.256	.578	29.958
1807	210.370	181.915	18.019	5.964	115.132	74.998	.602	29.803
1808	216.641	210.187	18.006	5.923	115.821	75.735	.627	29.741
1809	222.620	237.053	17.994	5.886	116.615	76.404	.651	29.812
1810	228.488	263.318	17.982	5.854	117.179	77.031	.674	29.742
1811	234.304	289.242	17.970	5.825	117.723	77.623	.697	29.683
1812	240.990	318.901	17.955	5.797	118.614	78.271	.723	29.841
1709	172.603	40.302	19.500	6.087	114.035	69.577	0.596	30.637
1710	178.550	73.409	19.486	6.101	114.965	70.566	.608	30.586
1701	181.613	90.419	19.479	6.082	115.092	71.052	.636	30.306
1711	184.637	107.182	19.472	6.065	115.515	71.517	.650	30.262
1702	187.628	123.725	19.465	6.054	115.740	71.965	.663	30.094
1712	190.680	140.564	19.457	6.039	116.187	72.408	.676	30.082
1703	193.640	156.857	19.450	6.008	116.537	72.827	.690	30.021
1713	196.693	173.622	19.443	5.997	116.917	73.247	.704	29.980
1704	199.616	189.630	19.435	5.980	117.239	73.639	.717	29.918
1714	202.661	206.260	19.428	5.946	117.740	74.036	.731	29.976
1705	205.568	222.086	19.421	5.941	117.875	74.406	.745	29.798
1715	208.615	238.633	19.413	5.927	118.353	74.784	.759	29.854
1706	211.480	254.140	19.406	5.895	118.705	75.131	.772	29.844
1716	214.522	270.555	19.398	5.886	118.998	75.490	.787	29.783
1707	217.573	286.970	19.391	5.857	119.326	75.842	.801	29.752
1717	220.387	302.058	19.384	5.842	119.782	76.158	.814	29.837
1708	223.411	318.216	19.376	5.818	120.066	76.491	.829	29.789

TABLE 2. *Specific heat at constant volume, C_V, of methane; heat correction for calorimeter expansion* Cl, *heat capacity of empty calorimeter,* CO, *total heat capacity of calorimeter (full)* $\Delta Q/\Delta T$ *or* DQ/DT, *with temperature, pressure, density, and temperature increment,* DT— *Continued*

ID	Temp K	Press bar	Den mol/l	*DT* K	*DQ/DT* J/K	Co J/K	Cl J/mol · K	C_V J/mol · K
807	161.140	39.441	21.313	5.723	116.134	67.478	.746	30.544
801	165.189	68.515	21.299	6.791	116.981	68.251	.772	30.565
808	166.828	80.226	21.296	5.647	117.232	68.554	.798	30.507
802	171.921	116.429	21.279	6.676	118.171	69.459	.833	30.495
809	172.488	120.439	21.279	5.633	118.018	69.557	.831	30.336
810	178.091	159.906	21.262	5.566	118.950	70.491	.859	30.307
803	178.582	163.345	21.258	6.640	118.980	70.571	.859	30.275
811	183.640	198-640	21.244	5.532	119.742	71.365	.890	30.224
804	185.182	209.346	21.238	6.587	119.938	71.600	.896	30.193
812	189.153	236.787	21.227	5.487	120.631	72.188	.921	30.236
805	191.734	254.532	21.218	6.521	120.927	72.559	.933	30.175
813	194.626	274.322	21.210	5.456	121.445	72.964	.953	30.229
806	198.229	298.849	21.197	6.467	121.824	73.454	.971	30.139
814	200.078	311.376	21.193	5.439	122.044	73.700	.985	30.109
2109	153.984	30.846	22.126	4.385	117.420	66.016	.818	31.040
2101	157.876	62.103	22.113	4.327	118.099	66.827	.845	30.931
2102	162.200	96.526	22.098	4.314	118.875	67.684	.927	30.800
2103	166.497	130.432	22.083	4.273	119.755	68.493	.940	30.832
2104	170.767	163.847	22.069	4.251	120.349	69.259	.951	30.716
2105	175.011	196.789	22-054	4.233	120.874	69.985	.976	30.567
2106	179.314	229.914	22.040	4.211	121.698	70.688	1.003	30.615
2107	183.514	261.982	22.025	4.186	122.103	71.346	1.029	30.432
2108	187.701	293.689	22.011	4.164	122.834	71.976	1.056	30.468
1406	148.828	44.459	22.933	6.789	118.758	64.875	0.899	31.314
1407	155.536	104.131	22.907	6.633	120.057	66.344	1.015	31.098
1402	155.969	107.942	22.906	6.629	120.154	66.435	1.017	31.100
1401	156.936	116.449	22.900	7.882	120.264	66.635	1.020	31.042
1408	162.130	161.805	22.883	6.560	121.193	67.671	1.042	30.958
1403	162.555	165.498	22.881	6.564	121.222	67.753	1.043	30.925
1409	168.648	217.963	22.858	6.496	122.400	68.883	1.075	30.923
1404	169.076	221.618	22.856	6.499	122.320	68.960	1.078	30.826
1410	175.122	272.905	22.834	6.458	123.385	70.003	1.120	30.798
1405	175.530	276.347	22.832	6.440	123.626	70.071	1.123	30.898
2001	139.073	45.399	24.008	4.195	119.866	62.486	0.988	31.796
2002	143.270	88.569	23.990	4.184	120.961	63.554	1.146	31.655
2003	147.448	130.924	23.972	4.155	121.919	64.557	1.165	31.612
2004	151.599	172.491	23.954	4.133	122.597	65.498	1.191	31.437
2005	155.908	215.104	23.935	4.091	123.742	66.422	1.205	31.550
2006	160.011	255.209	23.917	4.084	124.120	67.256	1.236	31.258
2007	164.072	294.445	23.900	4.052	124.977	68.042	1.268	31.267
901	130.508	34.766	24.785	2.255	121.056	60.095	1.097	32.662
909	131.693	48.379	24.772	5.484	121.045	60.443	1.106	32.454
904	132.694	59.842	24.767	5.557	121.433	60.734	1.136	32.479
902	134.136	76.278	24.761	4.991	121.346	61.144	1.174	32.166
910	137.159	110.410	24.746	5.421	122.150	61.977	1.245	32.080
903	139.337	134.756	24.735	5.473	122.514	62.555	1.258	31.949
911	142.547	170.300	24.720	5.356	123.309	63.375	1.283	31.911
906	143.713	183.112	24.715	5.439	123.701	63.663	1.287	31.964
912	147.886	228.554	24.695	5.336	124.401	64.659	1.303	31.785
907	149.124	241.915	24.689	5.389	124.607	64.943	1.313	31.732
913	153.185	285.371	24.670	5.287	125.563	65.844	1.348	31.728
908	154.473	299.029	24.664	5.310	126.059	66.120	1.359	31.839
1201	121.160	64.484	25.872	3.070	122.005	57.118	1.274	33.145
1202	124.223	104.694	25.855	3.048	122.909	58.138	1.400	32.958
1203	127.262	144.001	25.838	3.035	123.532	59.107	1.420	32.757
1204	130.274	182,414	25.822	3.013	124.390	60.025	1.455	32.691
1101	110.867	44.963	26.655	5.194	121.731	53.349	1.309	33.910
1106	111.917	60.514	26.649	5.165	121.991	53.758	1.354	33.789
1103	111.855	59.603	26.649	5.215	121.835	53.734	1.351	33.724
1102	116.030	120.523	26.624	5.136	123.377	55.306	1.503	33.557
1107	117.051	135.181	26.618	5.109	123.607	55.677	1.510	33.478
1104	122.089	206.386	26.588	5.057	125.308	57.432	1.546	33.415
1108	122.094	206.453	26.588	5.051	125.107	57.434	1.546	33.311

TABLE 2. *Specific heat at constant volume,* C_V, *of methane; heat correction for calorimeter expansion* Cl, *heat capacity of empty calorimeter,* CO, *total heat capacity of calorimeter (full)* $\Delta Q/\Delta T$ *or* DQ/DT, *with temperature, pressure, density, and temperature increment,* DT—Continued

ID	Temp K	Press bar	Den mol/l	*DT* K	*DQ/DT* J/K	Co J/K	Cl J/mol·K	C_V J/mol · K
1109	127.100	275.451	26.559	4.981	126.527	59.056	1.574	33.180
1105	127.123	275.769	26.558	5.028	126.592	59.064	1.574	33.210
1004	102.424	48.414	27.388	5.069	121.472	49.858	1.475	34.428
1001	105.029	90.948	27.371	5.078	122.552	50.974	1.619	34.267
1005	107.466	129.912	27.355	5.035	123.275	51.986	1.613	34.129
1002	110.058	170.735	27.338	4.981	124.205	53.030	1.637	34.049
1006	112.446	207,806	27.322	4.941	125.126	53.962	1.646	34.035
1003	115.142	249.013	27.305	4.914	126.082	54.979	1.652	33.999
1007	117.361	282.491	27.290	4.903	126.695	55.789	1.673	33.879
1912	92.592	40.274	28.164	3.061	120.491	45.311	1.351	35.326
1901	92.609	40.540	28.164	2.871	120.603	45.319	1.313	35.415
1907	93.793	62.384	28.155	2.873	121.008	45.899	1.458	35.186
1902	95.465	92.859	28.143	2.842	122.072	46.701	1.769	35.003
1913	95.634	95.885	28.141	3.022	122.178	46.780	1.765	35.020
1908	96.675	114.525	28.134	2.824	122.424	47.269	1.769	34.898
1903	98.301	143.313	28.122	2.807	123.144	48.020	1.740	34.913
1909	99.505	164.435	28.114	2.821	123.531	48.566	1.745	34.830
1904	101.123	192.506	28.102	2.793	124.316	49.288	1.768	34.839
1910	102.319	213.085	28.093	2.791	124.573	49.812	1.767	34.710
1905	103.902	240.032	28.082	2.749	125.401	50.495	1.755	34.793
1911	105.104	260.314	28.074	2.766	125.538	51.005	1.766	34.600
1906	106.655	286.252	28.063	2.751	126.307	51.653	1.781	34.644

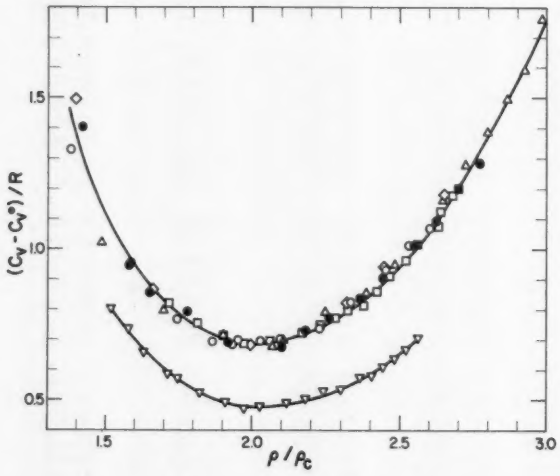

FIGURE 6. *Reduced specific heats versus reduced density for* CH_4 (●), F_2 (◊), O_2 (Δ), Kr (□), Ar (○), *and* Ne (▽).

Comparison of C_V methane extrapolated to saturation to several other liquids: F_2 [8], O_2[6], Kr [13], Ar [14], and Ne [15] is shown if figure 6. The density is reduced by the critical density. The spectroscopic heat capacity, C_v^0 is subtracted in each case. Molar specific heats are independent of reducing parameters [16]. All of the data except that for Ne correlate quite well. Presumably this departure of Ne is a result of its being more of a quantum fluid. H_2 and He also depart markedly from this grouping as shown by Diller [16].

I would like to acknowledge the support of the American Gas Association. R. D. Goodwin's data of the *PVT* of methane were essential and his computer programs calculating the various functions and derivatives were of great help. I thank D. E. Diller for his numerous contributions. The data shown in figure 6 are from his work.

5. References

[1] The S. I. (international system) unit of pressure is the Pascal (1 Pa = 1 N/m²). The bar is 10^5 Pa, also 1 atm = 1.01325 × 10^5 Pa, 1 lb/in² = 6894.757 Pa, 1 dyne/cm² = 10^{-1} Pa. Also one mole methane = 16.0430 g, based on the ^{12}C scale and the natural isotopic abundance averages: see Remy, H., Chem. Berichte **101,** I (1968).
[2] Goodwin, R. D., J. Res. Nat. Bur. Stand. (U.S.) **65C,** (Eng. and Instr.), No. 4, 231–243 (Oct.–Dec. 1961).
[3] Younglove, B. A. and Diller, D. E., Cryogenics **2,** 1 (1962).
[4] Younglove, B. A. and Diller, D. E., Cryogenics **6,** 1 (1962).
[5] Goodwin, R. D. and Weber, L. A., J. Res. Nat. Bur. Stand. (U.S.), **73A,** (Phys. and Chem.), No. 1, 1–13 (Jan.–Feb. 1969).
[6] Goodwin, R. D. and Weber, L. A., J. Res. Nat. Bur. Stand. (U.S.), **73A,** (Phys. and Chem.), No. 1, 15–24 (Jan.–Feb. 1969).
[7] Goodwin, R. D. and Prydz, R., J. Res. Nat. Bur. Stand. (U.S.), **74A,** (Phys. and Chem.), No. 4, 499–505 (July–Aug. 1970).
[8] Prydz, R. and Goodwin, R. D., J. Res. Nat. Bur. Stand. (U.S.), **74A,** (Phys. and Chem.), No. 5, 661–665 (Sept.–Oct. 1970).
[9] Walker, P. A., Dissertation (University of London, 1956).
[10] Goodwin, R. D. and Prydz, R., J. Res. Nat. Bur. Stand. (U.S.), **76A,** (Phys. and Chem.), No. 2, 81–101 (Mar.–Apr. 1972).
[11] Hoge, H. J., J. Res. Nat. Bur. Stand. (U.S.), **36,** 111 (1946).
[12] Weibe, R. and Breevort, M. J., J. Am. Chem. Soc. **52,** 622 (1930).
[13] Gladun, C. and Menzel, F., Cryogenics **10,** 210 (1970).
[14] Gladun, C., Cryogenics **11,** 205 (1971).
[15] Gladun, C., Cryogenics **7,** 78 (1967).
[16] Diller, D. E., Cryogenics **11,** 166 (1971).
[17] Jones, M. L., Jr., Mage, D. T., Faulkner, R. C., Jr., and Katz, D. L., Chem. Eng. Progress Symposium Series **59,** 52 (1960).

(Paper 78A3–820)

JOURNAL OF RESEARCH of the National Bureau of Standards—A. Physics and Chemistry
Vol. 78A, No. 3, May–June 1974

An Improved Procedure for Synthesis of DL-4-Hydroxy-3-methoxymandelic Acid (DL-"Vanillyl"-mandelic Acid, VMA)

Alexander J. Fatiadi and Robert Schaffer

Institute for Materials Research, National Bureau of Standards, Washington, D.C. 20234

(January 23, 1974)

An improved procedure for synthesis of DL-4-Hydroxy-3-methoxymandelic Acid (DL-Vanillyl-mandelic Acid, VMA) entails slow addition of an ice-cold, aqueous solution of glyoxylic acid to an ice-cold alkaline solution of guaiacol, with efficient mechanical stirring. This one-step condensation procedure provides VMA in 68–75 percent yield.

Key words: Alkaline condensation; glyoxylic acid; quaiocol; synthesis; vanillyl-mandelic acid; VMA.

1. Introduction

In connection with a program on clinical standards being conducted at the National Bureau of Standards, there was need for a simple, practical method for the large-scale preparation of pure DL-4-hydroxy-3-methoxymandelic acid (IV) in high yield. The D-enantiomorph of IV is one of the major metabolites of epinephrine and norepinephrine found in normal human urine [1],[1] but abnormally high concentrations of IV are found in the urine of patients having pheochromocytoma [2].

A literature survey revealed that IV has been prepared in low (19%) to moderate (45%) yield by a multiple-step procedure from vanillin *via* the cyanohydrin intermediate [3–5]. An alternative route for the synthesis is the procedure of Goodman and co-workers [6], who made use of a reaction, previously employed in a synthesis of vanillin [7], in which guaiacol (I) was added to glyoxylic acid (II), and without isolation the intermediate product (III) was directly oxidized *via* IV to vanillin.

The authors [6] demonstrated that IV was, indeed, produced in this reaction by showing that mixing (68 h at 25°) of I (1.14 mol) with II (1.35 mol) in basic media gave IV in 28 percent yield. Because of its simplicity, this one-step process for the synthesis of IV was examined to seek improvement in its yield.

Our procedure for preparation of IV (developed for use with two moles of the reagents) utilizes *slow* addition of an ice-cold, aqueous solution of II to a cold alkaline solution of I, with efficient mechanical stirring. By this procedure, the intermolecular reaction between glyoxylate ions that promotes a competitive Cannizzaro reaction of II (a kinetically controlled process) is lessened, permitting normal addition to II (or its ion) of the phenoxide ion from I (*para* position activated due to resonance) by a thermodynamically controlled process, and this contributes to an increase in the yield of IV. The normal reaction between I and II to yield III is rather fast considering the low temperature at which it is conducted. Reaction of I with II for 5 h (4 h for addition of II at −5 to 0° and 1 h for additional stirring at 0–15°) gave IV in 40 percent yield, and condensation

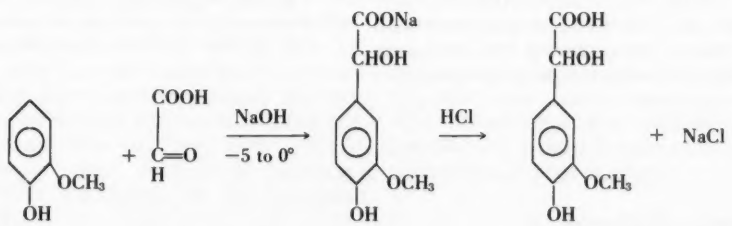

[1] Figures in brackets indicate the literature references at the end of this paper.

533-558 OL - 74 - 7

for 7 h (3 h of stirring at 0–15°) after introduction of II, gave IV in 45 percent yield. Recovered unreacted I at this stage was 0.76 mol.

The importance of slow introduction of I is evident from the fact that, when the reaction was performed at 25° (total stirring for 24 h), the yield of IV was 54 percent (nearly twice that previously reported), but raising the reaction temperature to 35–40° or 50° reduced the yield of IV to 42 and 32 percent, respectively. The condensation provided a maximum yield of IV after 18 h, and the product was usually recovered after 24 h to give IV in an overall yield of 65 percent. A longer time (8 h) for introduction of II and 16 h for stirring or longer condensation time (120 h) did not improve the yield further. Replacement of sodium carbonate by sodium hydroxide did not improve the yield of IV. However, conducting the condensation in dilute solution was found advantageous; for example, on increasing the volume used by 50 percent and 100 percent, the yield of IV was increased by 10 and 15 percent, respectively. In view of the large volume of solution that would have had to have been processed, this was not practical as a laboratory procedure. Salting out before extraction improved the yield of IV considerably.

2. Experimental Procedure

Thin layer chromatography (T.L.C.) was performed either on nonactivated silica gel G plates with 4:4:1 (v/v) chloroform–acetic acid–water followed by spraying with 3*M* sulfuric acid in methanol and heating for 2 min in an oven at 110 °C or on silica gel GF plates (254-nm irradiation).

DL-*4-Hydroxy-3-methoxymandelic Acid*—A solution of 176 g (4.4 mol) of sodium hydroxide in 100 ml of water (precooled to 15°) was combined with 1 kg of crushed ice, and to this mixture, surrounded by an ice-salt bath, was added with efficient stirring, 250 g (2.014 mol) of guaiacol (I) (solution temperature, −7°). While stirring, an ice-cold solution of 225 g (2.5 mol) of glyoxylic acid monohydrate (II) in 400 ml of water was introduced dropwise during 4 h, the reaction temperature being kept at 0 to −5°. If II is added too fast, an undesirable white precipitate appears at the end of the addition period, but this dissolves on further stirring. The solution was stirred for an additional 20 h (total 24 h) while the temperature slowly rose to ~ 20°. The dark-brown solution was acidified with 375 ml of concentrated hydrochloric acid, saturated with salt (700 g), and extracted with benzene (3 × 100 ml). After drying the benzene extract (sodium sulfate), concentration to a syrup gave unreacted I (10 g). The aqueous layer was next extracted with ethyl acetate (15 × 250 ml); the next extract (250 ml) usually gives less than 1.2 g of IV on evaporation. The extracts were combined, dried (Na_2SO_4), treated with acid-washed charcoal (3g), and carefully concentrated to a syrup in a rotary evaporator. The pink syrup was cooled, and the product crystallized. This was filtered and washed with cold ethyl acetate to give almost colorless crystals of IV 260 g, (65%) in several crops; mp 128–130°. Crude IV can be recrystallized from 1:2 (v/v) ethyl acetate-cyclohexane, 1:3 (v/v) 2-butanone-cyclohexane, 1:3 (v/v) ether-benzene, or acetonitrile. The analytical sample was recrystallized from ethyl acetate (charcoal and concentration) and then from 1:3 (v/v) 2-butanone-cyclohexane (with stirring at room temperature to prevent formation of clusters); colorless crystals; mp 132–133° (dried *in vacuo* over concentrated sulfuric acid); lit mp 133° (ref. [3]), 131–133° (refs. [4] and [5]) 134–135° (ref. [6]); ν_{max}^{KBr} 1870, 1748, and 1745 cm^{-1} (C=O stretch); n.m.r. (methyl sulfoxide-d_6): singlet at δ3.70 ($-OCH_3$), at δ4.95 (−C−H), multiplet at δ6.8 (aromatic protons), broad peak at δ8.65 (changed on treatment with a drop of pyridine-d_5 to a sharp singlet at δ8.73). T.L.C.; R_F 0.63; λ_{max} of IV in *M* K_2CO_3) was at 251 nm (ϵ_{nM} 1.022) and 293 nm (0.429). Samples of IV were titrated with standardized sodium hydroxide using a pH meter to the first inflection point of the titration curve; pK_1 3.75 (carboxyl group) and pK_2 9.80 (phenolic group). The sample contained a carboxylic acid equivalent of 99.83 percent.

The authors are most pleased to acknowledge the partial support of this work by the National Institute of General Medical Sciences (NIH); the authors also thank J. K. Taylor, R. A. Durst, and E. R. Deardorff of this Division for titration measurements.

3. References

[1] Shaw, K. N. F., McMillan, A., and Armstrong, M. D., Fed. Proc. **15**, 353 (1956); J. Biol. Chem., **226**, 255 (1957).
[2] Armstrong, M. D., McMilland, A., and Shaw, K. N. F., Biochim. Biophys. Acta **25**, 422 (1957).
[3] Gardner, J. A. F., and Hibbert, H., J. Amer. Chem. Soc. **66**, 607 (1944).
[4] Shaw, K. N. F., McMillan, A., and Armstrong, M. D., J. Org. Chem. **23**, 27 (1958).
[5] Recondo, E. F., and Rinderknecht, H., J. Org. Chem. **25**, 2248 (1960).
[6] Goodman I., Olenczak, A. P., Scherrer, J. W., and Hiatt, R. B., Biochim. Biophys. Acta **156**, 364 (1968).
[7] Boedecker, F., and Volk, H., U. S. Patent 2,062,205; J. Kamlet, U. S. Patent 2,640,083 [Chem. Abstr. **48**, 5884 (1954)].

(Paper 78A3–821)

JOURNAL OF RESEARCH of the National Bureau of Standards—A. Physics and Chemistry
Vol. 78A, No. 3, May–June 1974

Single Particle Motions in Liquids: Qualitative Features of Memory Functions

Raymond D. Mountain

Institute for Basic Standards, National Bureau of Standards, Washington, D.C. 20234

(February 1, 1974)

Memory functions, which enter into the equations of motion for time correlation functions, are constructed from neutron scattering, infrared absorption and light scattering data involving single particle motions in liquids. The qualitative features of these memory functions are related to the shape of the corresponding time correlation functions. It is found that a negative portion to the memory function is indicative of a rapid loss of correlation in time while strong temporal correlations imply a memory function which does not go negative. The mathematical structure of a memory function is examined for the case of the ideal gas by expanding and evaluating the projection operator representation of the function. The resulting expression has a rich mathematical structure and can be expressed in a closed form only for its Laplace transform.

Key words: Depolarized Rayleigh scattering; ideal gas; incoherent neutron scattering; infrared absorption; liquid state; memory function; projection operator; Raman scattering; time correlation function.

1. Introduction

The time correlation of molecular quantities has proven to be a useful way of describing molecular motions in liquids. These time correlation functions, which are obtained as Fourier transforms of data, can be investigated using recently developed techniques of time dependent statistical mechanics [1]. Exact equations of motion for the time correlation functions have been derived which involve memory functions, quantities which characterize the history of the fluid [1, 2]. While time correlation functions are now widely used to represent molecular motions [3], only a few studies of memory functions have appeared [4–9]. In this paper we examine some properties of memory functions as derived from data and from model correlation functions. Our results, combined with other results obtained from computer simulations, enable us to make some qualitative observations about the general features of these important quantities.

A motivation for studying memory functions is the hope that these quantities will have simpler structure than the time correlation functions. Should this be true, it would be possible to model molecular motions in liquids in terms of a relatively simple memory function once the qualitative features of the memory functions are understood. Indeed, this has been done empirically for the velocity time correlation functions obtained by computer simulation of the Lennard-Jones model fluid [10].

The mathematical structure of memory functions has been studied in the short time and long time limits [4–6]. We present here a calculation for all times of the memory function for the incoherent neutron scattering by an ideal gas. The mathematical structure of this quantity is found to involve even powers of the velocity of a particle in terms of deviations of the even powers from their average values. This structure is more complex than the structure of the time correlation function. Thus we have examples which suggest the existence of a rich underlying mathematical structure which yields relatively simple functional forms for the memory functions.

It is plausible to expect that future studies will find a whole range of cases and that for as yet to be determined physical situations, the memory functions are comparatively simple quantities.

The paper is organized in the following way. First we introduce some notation and outline briefly the relation connecting a time correlation function and a memory function. In section 3 we construct memory functions from data and discuss the structural features of these quantities. The mathematical structure of memory functions is probed in section 4 where the memory function for the incoherent scattering from an ideal gas is calculated from the microscopic definition of a memory function. The structure discovered in this analysis is found to have some unexpected features. The discussion of the qualitative features of memory functions in section 5 makes use of both our results and the results of other studies.

2. Formal Preliminaries

Molecular motions in liquids may be studied experimentally in a number of ways. For example, the

translational motion of a single atom is probed by incoherent neutron scattering and the changes in orientation of a single molecule is probed by depolarized Rayleigh scattering. Infrared absorption and certain types of depolarized Raman scattering also probe orientational motions. In each case one can obtain from the data, a time correlation function which describes some aspect of the motion of a typical molecule in the fluid.

The notation we shall employ for a time correlation function is $\psi(t)$ with $\psi(0)=1$ where

$$\psi(t)=\langle u^*(0)u(t)\rangle/\langle\,|\,u\,|^2\rangle. \tag{2.1}$$

Here the angular brackets $\langle\ \ldots\ \rangle$ indicate an ensemble average and the phase function

$$u(t)=\exp\,(-iLt)u(0) \tag{2.2}$$

evolves in time as determined by the Liouville operator, L, for the system. The phase functions associated with various experimental probes are described elsewhere [11].

A formally exact equation of motion for $\psi(t)$ may be derived using the projection operator formalism of Zwanzig [1, 2]. The equation is

$$\frac{\partial\psi(t)}{\partial t}=-\int_0^t dt'K(t-t')\psi(t') \tag{2.3}$$

with

$$\left.\frac{\partial\psi}{\partial t}\right|_{t=0}=0. \tag{2.4}$$

The memory function $K(t)$ is specified as

$$K(t)=\langle\dot{u}^*(0)\,\exp\,[-(1-\mathrm{P})iLt]\dot{u}(0)\rangle \tag{2.5}$$

where the projection operator P has the property

$$Pg=u\langle u^*g\rangle \tag{2.6}$$

for any phase function g and

$$\dot{u}=-iLu. \tag{2.7}$$

3. Memory Functions

In this paper we examine memory functions obtained by recursively solving eq (2.3) for $K(t)$ when $\psi(t)$ is known from experiment. The numerical procedures are discussed in the appendix. We use incoherent neutron scattering data for liquid argon [12] as an example of translational motion. Infrared absorption data and depolarized Raman scattering data for neopentane [13] and depolarized Rayleigh scattering data for benzene [14] are used as examples of orientational motion.

The results are displayed in figures 1–4. There the correlation function, $\psi(t)$, and the normalized memory function, $K(t)/K(0)$, are shown as functions of time. These memory functions are characterized by a rapid initial decrease to negative values followed by an approach to zero which is prompt when compared with the decay of the correlation function. This appears to be a fairly common situation as evidenced by its presence in the memory function for the incoherent neutron scattering from an ideal gas as shown in figure 5. It is not a universal feature as counter examples may be constructed.

The results for $K(t)$ become erratic for long times. This is a result of the sensitivity to irregularities in $\psi(t)$ of the numerical procedure used to obtain $K(t)$. The uncertainty of $K(t)$ in figure 1 is on the order of ± 0.02 for times greater than 10^{-12}s. The pair of dashed lines in figure 3 indicate the range of values assumed by $K(t)$. In figure 4 the solid horizontal lines

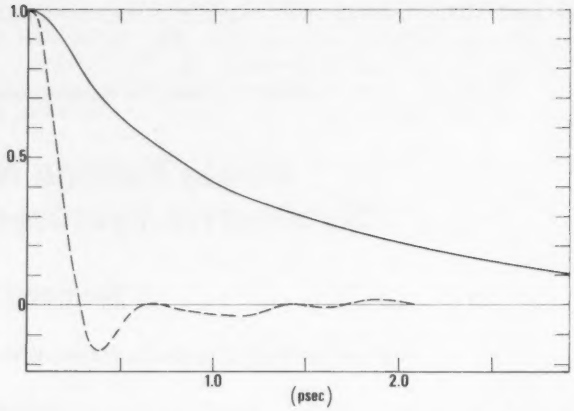

FIGURE 1. *Single particle translation motion for liquid argon at* T = 85.2 K.

The time correlation function (——) and normalized memory function (– – –) for $Q = 2.0\text{Å}^{-1}$ are pictured.

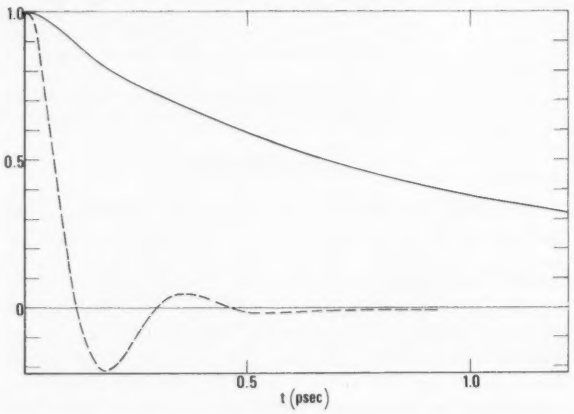

FIGURE 2. *Reorientation of liquid benzene molecules at* t = 59 °C *studied via depolarized Rayleigh scattering.*

The $l=2$ component of reorientation motion is pictured. The time correlation function (——) and the normalized memory function (– – –) are shown as functions of time.

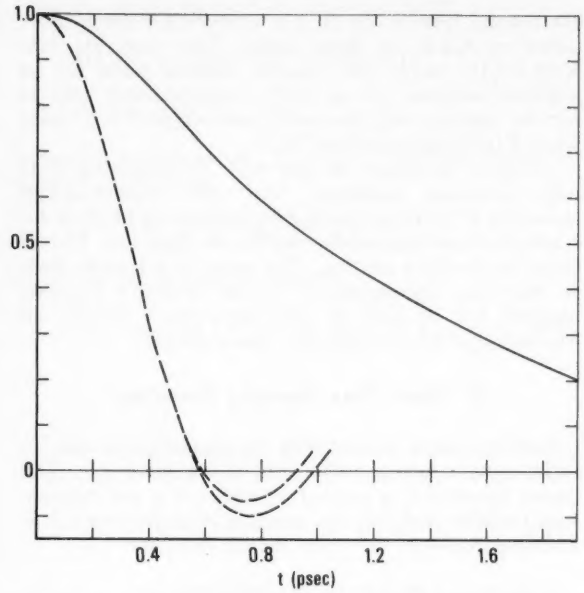

FIGURE 3. *Reorientation of neopentane at 241 K studied by infrared absorbtion.*

The $l = 1$ component of reorientation motion is pictured. The solid line (——) is the time correlation function and the dashed line (– – –) is the normalized memory function.

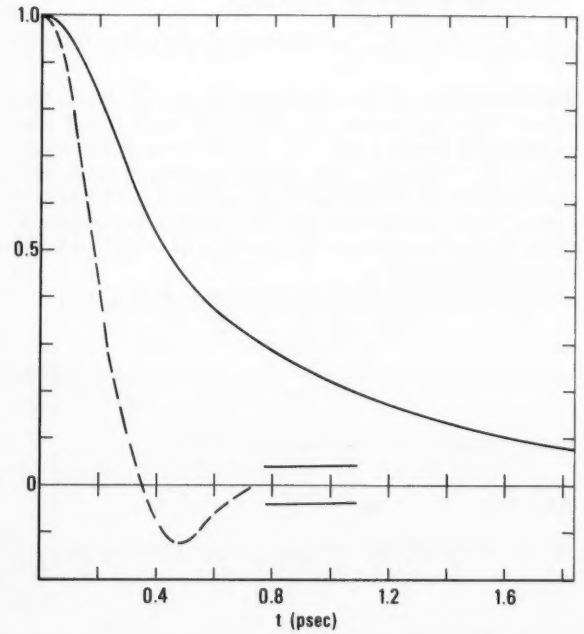

FIGURE 4. *Reorientation of neopentane at 239 K studied by Raman scattering from the 924 cm^{-1} band.*

The time correlation function (——) and the normalized memory function (– – –) for the $l = 2$ component of reorientation motion are displayed as functions of time.

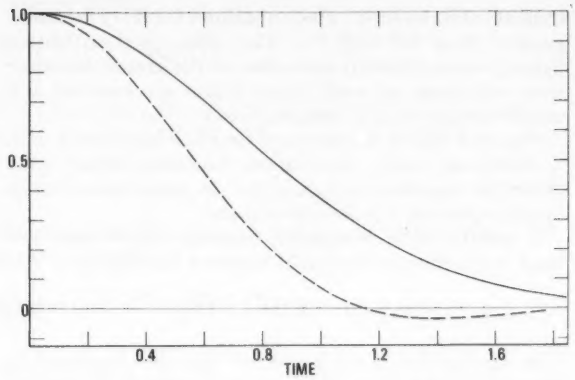

FIGURE 5. *The time correlation function (——) and normalized memory function (– – –) for incoherent neutron scattering from an ideal gas.*

The time is measured in units of $q^2/2\beta m$.

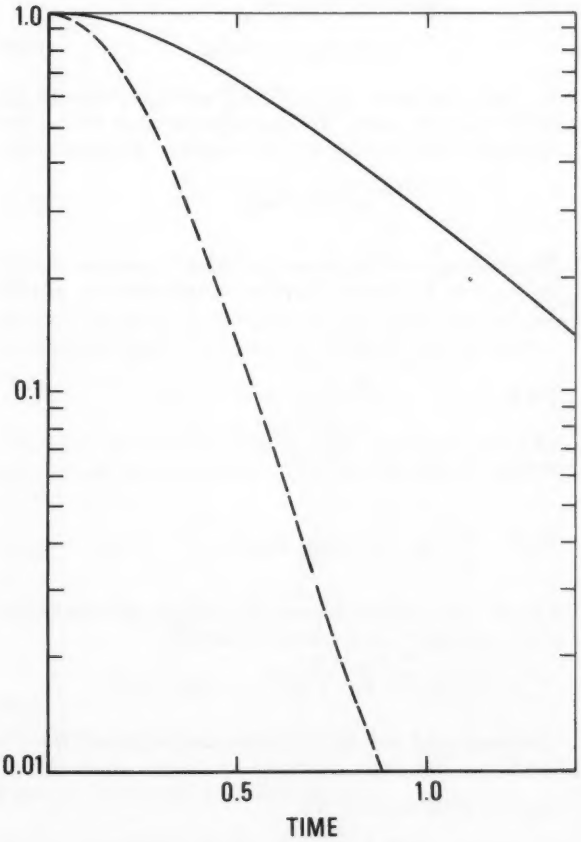

FIGURE 6. *The model time correlation function (——) and the corresponding normalized memory function (– – –) of eq (3.1) are displayed.*

This shows that memory functions need not have negative regions.

indicate the range of values obtained for $K(t)$ for times greater than 0.8×10^{-12}s. The data used to obtain figure 2 were carefully smoothed so the erratic behavior does not show up until longer times are reached and would not be visible with this scale.

Figure 5 shows the memory function associated with a Gaussian time correlation function (ideal gas). Here the negative region is not as pronounced as in liquid argon but it is definitely there.

A model time correlation function which does not have a negative portion to its memory function is

$$\psi(t) = \exp\,[A - \sqrt{A^2 + t^2/\tau^2}]. \tag{3.1}$$

The results for $A=1.0$ and $\tau=0.5$ are displayed in figure 6. The tail of the memory function is approximately exponential.

The existence of a negative portion in the memory function is not surprising. From eq (2.5) we observe that $C(t)$, the negative of the second time derivative of $\psi(t)$, is not dissimilar to $K(t)$ since

$$\begin{aligned} C(t) &= -\partial^2\psi(t)/\partial t^2 \\ &= \langle \dot{u}^* \exp\,[-iLt]u\rangle. \end{aligned} \tag{3.2}$$

At least for short times, $K(t)$ and $C(t)$ should be fairly close in value. They are identical at $t=0$. The function $C(t)$ necessarily has negative portions since

$$\int_0^\infty dt\, C(t) = 0. \tag{3.3}$$

This follows readily from the initial condition $\partial\psi(t)/\partial t\,|_{t=0}=0$. By taking Laplace transforms we obtain

$$\begin{aligned} \hat{C}(z) &= \int_0^\infty dt e^{-zt} C(t) \\ &= -z^2\hat{\psi}(z) + z \end{aligned} \tag{3.4}$$

so that

$$\int_0^\infty dt\, C(t) = \lim_{z\to 0} \hat{C}(z) = 0. \tag{3.5}$$

Let us now examine further the relationships between $C(t)$ and $K(t)$. The operator identity

$$\begin{aligned} &\exp[-(1-P)iLt] = \exp[-iLt] \\ &+ \int_0^t dt' \exp[-iL(t-t')]iPL\, \exp[-i(1-P)Lt'] \end{aligned} \tag{3.6}$$

may be used to show that

$$K(t) = C(t) - \int_0^t dt' K(t-t')\partial\psi(t')/\partial t' \,. \tag{3.7}$$

This equation may also be obtained directly from eq (2.3). In some of the cases considered in this article, the second term in eq (3.7) is numerically small compared to $K(t)$ for short times. This suggests that $K(t) \approx C(t)$ might be a useful starting point for an iterative solution of eq (2.3). Unfortunately this is not the case as only the trivial solution $\psi(t)=1$ exists when $K(t)$ is replaced by $C(t)$.

Another limitation of this way of examining $K(t)$ only becomes apparent after the mathematical structure of $K(t)$ is studied by evaluating eq (2.5) for incoherent neutron scattering by an ideal gas. This is done in the next section. The point to be made here is that the decomposition of the memory function implied by eq (3.7) is not particularly useful for evaluating $K(t)$, at least for this example.

4. Ideal Gas Memory Function

In this section we examine the memory function for incoherent neutron scattering by an ideal gas. The phase function u is $\exp(i\mathbf{q}\cdot\mathbf{r})$ where $\mathbf{q}$ is the momentum transfer and $\mathbf{r}$ is the position of a gas atom. It is a simple matter to show that for the ideal gas

$$\begin{aligned} \psi(t) &= \langle e^{-i\mathbf{q}\cdot\mathbf{r}} e^{-iLt} e^{i\mathbf{q}\cdot\mathbf{r}}\rangle \\ &= \langle \cos\,(\mathbf{q}\cdot\mathbf{v}t)\rangle = \exp\,[-q^2t^2/2\beta m] \end{aligned} \tag{4.1}$$

where m is the mass of the gas atom and $\beta = 1/k_B T$, the inverse of Boltzmann's constant k_B times the absolute temperature T.

The memory function is formally

$$K(t) = \langle e^{-i\mathbf{q}\cdot\mathbf{r}}(-i\mathbf{q}\cdot v) e^{-(1-P)iLt}(i\mathbf{q}\cdot\mathbf{v}) e^{i\mathbf{q}\cdot\mathbf{r}}\rangle. \tag{4.2}$$

The evaluation of this expression is now to be undertaken. The procedure we follow is to expand the exponential factor $\exp[-i(1-P)Lt]$, apply the operator $-i(1-P)L$ the appropriate number of times and then collect the resulting terms in such a way that a closed form is obtained for the Laplace transform of $K(t)$. It does not seem to be possible to obtain a closed form for $K(t)$ itself.

For the ideal gas, the dynamics are trivial;

$$\begin{aligned} -iL\mathbf{r} &= \mathbf{v} \\ -iL\mathbf{v} &= 0. \end{aligned} \tag{4.3}$$

Let us consider first the expansion of $K(t)$:

$$\begin{aligned} K(t) = \Big\langle e^{-i\mathbf{q}\cdot\mathbf{r}}(-i\mathbf{q}\cdot\mathbf{v}) \sum_{n=0}^{\infty} \\ \frac{(-t)^n[(1-P)iL]^n}{n!}(i\mathbf{q}\cdot\mathbf{v}) e^{i\mathbf{q}\cdot\mathbf{r}} \Big\rangle \end{aligned} \tag{4.4}$$

We note that the odd terms in t will vanish when the expectation value is taken. First consider the $n=2$ coefficient.

$$[(1-P)iL]^2(i\mathbf{q}\cdot\mathbf{v}) e^{i\mathbf{q}\cdot\mathbf{r}}$$

$$= (1-P)iL[(\mathbf{q}\cdot\mathbf{v})^2 - \langle(\mathbf{q}\cdot\mathbf{v})^2\rangle]e^{i\mathbf{q}\cdot\mathbf{r}}$$

$$= [(\mathbf{q}\cdot\mathbf{v})^2 - \langle(\mathbf{q}\cdot\mathbf{v})^2\rangle](-i\mathbf{q}\cdot\mathbf{v})e^{i\mathbf{q}\cdot\mathbf{r}} \tag{4.5}$$

$$= k_2(-i\mathbf{q}\cdot\mathbf{v})e^{i\mathbf{q}\cdot\mathbf{r}}.$$

Repeated application of $[(1-P)iL]^2$ yields a sequence of terms of the type

$$(-1)^n k_{2n}(i\mathbf{q}\cdot\mathbf{v})e^{i\mathbf{q}\cdot\mathbf{r}}$$

where the coefficients k_{2n} satisfy

$$k_{2n+2} = k_{2n}(\mathbf{q}\cdot\mathbf{v})^2 - \langle k_{2n}(\mathbf{q}\cdot\mathbf{v})^2\rangle \tag{4.6}$$

and

$$k_0 = 1.$$

A more useful grouping of terms is achieved by introducing another set of coefficients $\{C_j\}$ defined by

$$k_{2n} = \sum_{j=0}^{n-1} C_j(x^{2n-2j} - \langle x^{2n-2j}\rangle) \tag{4.7}$$

with $C_0 = 1$. The notation $x = \mathbf{q}\cdot\mathbf{v}$ has been introduced to simplify the writing. The C_j's satisfy the recursion relation

$$C_n = -\sum_{j=0}^{n-1} C_j\langle x^{2n-2j}\rangle. \tag{4.8}$$

Now let us express $K(t)$ in terms of the C_j's. The factors $\exp(i\mathbf{q}\cdot\mathbf{r})$ yield 1 when the expectation value is taken so we drop those terms.

$$K(t) = \left\langle x^2 \sum_{n=0}^{\infty} \frac{(-t^2)^n}{(2n)!} k_{2n} \right\rangle$$

$$= \langle x^2\rangle + \left\langle x^2 \sum_{n=1}^{\infty} \frac{(-t^2)^n}{(2n)!} \sum_{j=0}^{n-1} C_j(x^{2n-2j} - \langle x^{2n-2j}\rangle) \right\rangle \tag{4.9}$$

$$= \langle x^2\rangle + \left\langle (x^2 - \langle x^2\rangle) \sum_{n=1}^{\infty} \sum_{j=0}^{n-1} \frac{(-t^2)^n}{(2n)!} C_j x^{2n-2j} \right\rangle.$$

It will prove convenient to reorder the double sum in eq (4.9) so that

$$K(t) = \langle x^2\rangle + \left\langle (x^2 - \langle x^2\rangle) \sum_{j=0}^{\infty} \sum_{n=j+1}^{\infty} C_j \frac{(-t^2)^n}{(2n)!} x^{2n-2j} \right\rangle$$

$$= \langle x^2\rangle + C_0 \left\langle (x^2 - \langle x^2\rangle) \sum_{n=1}^{\infty} \frac{(-t^2)^n}{(2n)!} x^{2n} \right\rangle \tag{4.10}$$

$$+ \left\langle (x^2 - \langle x^2\rangle) \sum_{j=1}^{\infty} \sum_{n=j+1}^{\infty} C_j \frac{(-t^2)^n}{(2n)!} x^{2n-2j} \right\rangle.$$

The next step in the analysis involves the use of eq (4.8) to systematically replace the C_j's in eq (4.10) with C_0.

Thus we find

$$K(t) = \langle x^2\rangle + C_0 g_1(t)$$

$$- \left\langle (x^2 - \langle x^2\rangle) \sum_{j=1}^{\infty} \sum_{n=j+1}^{\infty} \sum_{k=0}^{j-1} C_k\langle x^{2j-2k}\rangle \frac{(-t^2)^n}{(2n)!} x^{2n-2j} \right\rangle. \tag{4.11}$$

Now reorder the j and k sums and extract the $k=0$ term to obtain

$$K(t) = \langle x^2\rangle + C_0 g_1(t) - C_0 g_2(t)$$

$$- \left\langle (x^2 - \langle x^2\rangle) \sum_{k=1}^{\infty} \sum_{j=k+1}^{\infty} \sum_{n=j+1}^{\infty} C_k\langle x^{2j-2k}\rangle \frac{(-t^2)^n}{(2n)!} x^{2n-2j} \right\rangle. \tag{4.12}$$

This process can be repeated with the result

$$K(t) = \langle x^2\rangle - C_0 \sum_{N=1}^{\infty} (-1)^N g_N(t) \tag{4.13}$$

where

$$g_N(t) = \left\langle (x^2 - \langle x^2\rangle) \sum_{k_1=1}^{\infty} \sum_{k_2=k_1+1}^{\infty} \right.$$

$$\cdots \sum_{n=k_{N-1}+1}^{\infty} \frac{(-t^2)^n}{(2n)!} \langle x^{2k_1}\rangle\langle x^{2k_2-2k_1}\rangle$$

$$\left. \cdots \langle x^{2k_{N-1}-2k_{N-2}}\rangle\langle x^{2n-2k_{N-1}}\rangle \right\rangle. \tag{4.14}$$

Further progress is possible if we make use of the moment property of the x's for the ideal gas, namely

$$\langle x^{2j}\rangle = (2j-1)!!\langle x^2\rangle^j. \tag{4.15}$$

The $(2n)!$ term in the denominator can be removed by taking Laplace transforms [15]. For the case $N=1$, we obtain

$$\hat{g}_1(z) = \int_0^{\infty} dt\, e^{-zt} g_1(t) \tag{4.16}$$

$$= \left\langle x^2 - \langle x^2\rangle \right) \sum_{n=1}^{\infty} \frac{(-1)^n x^{2n}}{z^{2n+1}} \Big\rangle$$

$$= \left\langle \frac{x^4 - x^2\langle x^2\rangle}{z^3} \frac{1}{1 + x^2/z^2} \right\rangle.$$

Closed forms for the other $\hat{g}_j(z)$ are also possible. We evaluate $\hat{g}_2(z)$ to illustrate how this is done. First we use eqs (4.14, 4.15) to obtain

$$\hat{g}_2(z) = \left\langle (x^2 - \langle x^2\rangle) \sum_{j=1}^{\infty} \sum_{n=j+1}^{\infty} (2j-1)!! \right.$$

$$\left. \frac{\langle x^2\rangle^j (-1)^n x^{2n-2j}}{z^{2n+1}} \right\rangle$$

$$= \left\langle \frac{(x^2 - \langle x^2 \rangle)}{z} \sum_{j=1}^{\infty} (2j-1)!! \left[\frac{\langle x^2 \rangle}{x^2} \right]^j \frac{(-x^2/z^2)^{j+1}}{1 + x^2/z^2} \right\rangle$$

$$= \left\langle \frac{x^4 - x^2\langle x^2 \rangle}{z^3(1 + x^2/z^2)} \right\rangle \sum_{j=1}^{\infty} (2j-1)!!(-1)^{j+1}[\langle x^2 \rangle / z^2]^j . \tag{4.17}$$

Next we make use of the result

$$(2j-1)!! = \sqrt{\frac{2}{\pi}} \int_0^{\infty} dq\, q^{2j} \exp(-q^2/2) \tag{4.18}$$

to obtain

$$\hat{g}_2(z) = \left\langle \frac{x^4 - x^2\langle x^2 \rangle}{z(z^2 + x^2)} \right\rangle \hat{I}(z) \tag{4.19}$$

where

$$\hat{I}(z) = \sqrt{\frac{2}{\pi}} \int_0^{\infty} dq \frac{e^{-q^2/2}\langle x^2 \rangle q^2}{z^2 + \langle x^2 \rangle q^2}. \tag{4.20}$$

It is a straightforward task using these techniques to show that

$$\hat{g}_N(z) = (-1)^{N+1} \hat{g}_1(z) [\hat{I}(z)]^{N-1}. \tag{4.21}$$

Next, the Laplace transform of the memory function is found to be

$$\hat{K}(z) = \frac{\langle x^2 \rangle}{z} + \frac{\hat{g}_1(z)}{1 - \hat{I}(z)} \tag{4.22}$$

This in turn is shown to be

$$\hat{K}(z) = -z + \left[\sqrt{\frac{2}{\pi \langle x^2 \rangle}} \times \exp\,(z^2/2\langle x^2 \rangle)\, \operatorname{erfc}\,(z/\sqrt{2\langle x^2 \rangle}) \right]^{-1}. \tag{4.23}$$

One may also express $\hat{K}(z)$ in terms of $\hat{\psi}(z)$ as

$$\hat{K}(z) = -z + 1/\hat{\psi}(z) \tag{4.24}$$

by taking Laplace transforms of eq (2.3) and solving for $\hat{K}(z)$. In terms of $\langle x^2 \rangle$, it follows from eq (4.1) that

$$\psi(t) = \exp\,(-\langle x^2 \rangle t^2/2) \tag{4.25}$$

since

$$\langle x^2 \rangle = \frac{\int_0^{\infty} dv (qv)^2 e^{-\beta m v^2/2}}{\int_0^{\infty} dv e^{-\beta m v^2/2}} = q^2/\beta m \tag{4.26}$$

and thus

$$\hat{\psi}(z) = \sqrt{\frac{\pi}{2\langle x^2 \rangle}} \exp(z^2/2\langle x^2 \rangle)\, \operatorname{erfc}\,(z/\sqrt{2\langle x^2 \rangle}) \tag{4.27}$$

in agreement with the result of summing $\hat{K}(z)$.

Although a closed form for $K(t)$ has not been found, we have determined the underlying structure of the memory function. How it compares with the structure implied by eq (3.7) is worth noting. From eqs (4.21) and (4.22) it is evident that

$$\hat{K}(z) = \frac{\langle x^2 \rangle}{z} + g_1(z) \sum_{n=0}^{\infty} [-\hat{I}(z)]^n. \tag{4.28}$$

A simple calculation shows that

$$g_1(t) = C(t) - \langle x^2 \rangle \psi(t) \tag{4.29}$$

and

$$I(t) = \partial \psi(t)/\partial t. \tag{4.30}$$

An iterative solution of eq (3.7) yields

$$\hat{K}(z) = \hat{C}(z) \sum_{n=0}^{\infty} [-\hat{I}(z)]^n. \tag{4.31}$$

Consistency requires that

$$\hat{\psi}(z) \sum_{n=0}^{\infty} [-\hat{I}(z)]^n = 1/z. \tag{4.32}$$

Since $\hat{I}(z) = z\hat{\psi}(z) - 1$, eq (4.32) is satisfied and the two solutions are equivalent. The mathematical structure which was found to be useful for summing the memory function expansion may appear in retrospect to be inconvenient because of the extensive cancellations which necessarily occur. However, attempts to impose the structure of eq (3.7) on the expansion were unsuccessful in achieving a form which could be completely summed.

In order to see just what sort of structure we have developed, let us review the steps followed in summing the expansion of $K(t)$. The set of coefficients $\{k_{2n}\}$ resulted from grouping the sum in terms of powers of the time. Next. the sum was arranged in terms of the deviations of x^{2l} from the average $\langle x^{2l} \rangle$ and resulted in the set of coefficients $\{C_j\}$. This was the crucial step in the analysis as it exhibited the underlying structure of the memory function. Clearly this way of arranging the sum is different from the structure implied by eq (3.7) since $C(t)$ does not involve the projection operator. Next we eliminated all C_j's except C_0 from the expansion through repeated use of eq (4.8). The closed form obtained in eq (4.23) required an explicit relation among the moments of x, namely eq (4.15) which follows from the Boltzmann distribution for the velocities. It would be interesting to see if this type of structure could usefully be imposed on $K(t)$ for an interacting system. This topic is not considered here.

5. Discussion

The time correlation functions, $\psi(t)$, shown in figures 1–4 are typical of the ones obtained from

liquid state scattering and absorption data. The curves initially exhibit a rapid falloff and then go over to an approximately exponential function for long times. The functions, $\psi(t)$, are everywhere positive and, except for the short time part, the curves are concave upward. The memory functions $K(t)$ exhibit a rapid initial falloff which carries them to negative values. The negative portion of $K(t)$ has the effect of decreasing the magnitude of $\partial\psi/\partial t$ and thereby reducing the slope of $\psi(t)$ so that $\psi(t)$ remains positive for all times.

It is interesting to compare this situation with that found from computer simulations for the velocity time correlation functions in Lennard-Jones liquids [9, 10]. There the time correlation functions achieve negative values. This implies that the initial state is "strongly remembered" by the system, a viewpoint consistent with the behavior of $K(t)$ since $K(t)$ remains positive. At higher temperatures, where the kinetic energy is large compared with the strength of the pairwise interaction energy, the time correlation functions do not go negative while the memory functions do.

This suggests that the persistence of the memory function is closely related to the time evolution of the cage-like many body structure described by Rahman [16]. He found from his molecular dynamics calculations that a liquid atom undergoes a strong, velocity reversing collision and then "rattles" about in a loose cage of neighboring atoms until it escapes when the cage breaks down. The rattling motion leads to negative values of the velocity time correlation function. However, if the cage breaks up too rapidly, as it would at high temperatures or low densities, no rattling motion, coherent with the initial condition, occurs and $\psi(t)$ remains positive.

The calculation of the memory function for the ideal gas shows that this function has an extensive mathematical structure. This is expressed in the properties of the coefficients $\{k_{2n}\}$ and $\{C_j\}$. The memory functions constructed from data show more structure than the memory function determined numerically from the ideal gas time correlation function.

This comparison is the basis for the following conjecture. The mathematical structure of the memory function for an interacting system should exhibit two parts, in contrast with the one part exhibited by the ideal gas. There should be a "short-time" part which dominates the initial behavior of $K(t)$ and then goes rapidly to zero. The second part of the memory function should dominate the remainder of the time interval. This part can be either positive or negative depending on the type of correlation involved and is dominated by many-body effects which are only poorly understood. The testing of this conjecture is a subject for further work.

6. Appendix

The numerical inversion of eq (2.3) to obtain $K(t)$ from $\psi(t)$ is accomplished by replacing the integro-differential equation by a set of coupled difference equations defined on a discrete set of evenly spaced time points t_i with $t_{i+1}-t_i=\Delta t$. For simplicity, a subscript notation is used so $\psi(t_i)$ becomes ψ_i and $\psi(0)=\psi_0$. The trapezoidal rule and simple difference expressions are used to replace integral and differential operations. A typical member of this set of difference equations is

$$\frac{1}{2\Delta t}[\psi_{i+1}-\psi_{i-1}]=-\Delta t\left[\frac{1}{2}(K_0\psi_i+K_i\psi_0)+\sum_{j=1}^{i-1}K_{i-j}\psi_j\right]. \tag{6.1}$$

These equations for K_i are solved recursively in terms of the $\{\psi_j\}$ subject to the initial conditions

$$\begin{aligned}&\psi_0=1,\ \psi_1=\psi_{-1}\\ &K_0=2(\psi_1-\psi_0)/(\Delta t)^2.\end{aligned} \tag{6.2}$$

The last condition follows from eqs (2.5 and 3.2) which indicate that

$$K(0)=-\partial^2\psi(t)/\partial t^2\,|_{t=0}. \tag{6.3}$$

The solution has the form

$$\begin{aligned}K_1&=-K_0\psi_1-[\psi_2-\psi_0]/(\Delta t)^2\\ K_i&=-K_0\psi_i-2\sum_{j=1}^{i-1}K_{i-j}\,\psi_j \qquad i>1\\ &\quad-[\psi_{i+1}-\psi_{i-1}]/(\Delta t)^2.\end{aligned} \tag{6.4}$$

These expressions were used to obtain the $K(t)$ curves discussed in the text.

It is necessary that $\psi(t)$ be a smooth function of t if this technique is to yield useful results for $K(t)$. Figures 1–4 indicate the kinds of uncertainties which show up in $K(t)$. Some care is needed in the selection of the time increment Δt. If it is too large the difference expression for the first derivative is inaccurate. If Δt is too small, the noise in $\psi(t)$ governs the outcome rather than $\psi(t)$ itself.

Another procedure for solving for $K(t)$ is described in appendix B of reference [6]. This procedure is more accurate than the one described here in that it uses spline fits to $\psi(t)$ to estimate derivatives and it uses a more accurate integration scheme. However, when the procedure we use is stable, the results of the two methods agree closely.

I wish to thank Drs. Livingston and Dardy for making their data available to me prior to publication.

7. References

[1] Zwanzig, R., in Lectures in Theoretical Physics, Eds. W. E. Brittin, W. B. Downs and J. Downs, (Interscience, New York, 1961), p. 106.

[2] Berne, B. J., Boon, J. P. and Rice, S. A., J. Chem. Phys. **45,** 1086 (1966).

[3] van Konynenburg, P. and Steele, W. A., J. Chem. Phys. **56,** 4776 (1972). This article contains numerous references to other work employing time correlation functions.

[4] Résibois, P., Brocas, J. and Decan, G., J. Math. Phys. **10,** 964 (1969).

[5] Corngold, N., and Duderstadt, J. J., Phys. Rev. A **2,** 836 (1970).

[6] Berne, B. J., and Harp, G. D., Adv. in Chem. Phys. **XVII,** 63 (1970).

[7] Harp, G. D., and Berne, B. J., Phys. Rev. A **2,** 975 (1970).

[8] Rahman, A. in Statistical Mechanics, New Concepts, New Problems, New Applications, Eds. S. A. Rice, K. F. Freed and J. C. Light (U. of Chicago Press, Chicago, Ill., 1972), pp. 177–199.

[9] Kushick, J., and Berne, B. J., J. Chem. Phys. **59,** 3732 (1973).

[10] Levesque, D. and Verlet, L., Phys. Rev. A **2,** 2514 (1970).

[11] See for example, Table I of Ref. [7].

[12] Sköld, K., Rowe, J. M., and Ostrowski, G., and Randolph, P. D., Phys. Rev. A **6,** 1107 (1972).

[13] Livingston, R. C., Rothschild, W. G., and Rush, J. J., J. Chem. Phys. **59,** 2498 (1973).

[14] Dardy, H. D., Volterra, V., and Litovitz, T. A., J. Chem. Phys. **59,** 4491 (1973).

[15] Wheelon, A. D., J. Math. and Phys. **34,** 182 (1955).

[16] Ragman, A., J. Chem. Phys. **45,** 2585 (1966).

(Paper 78A3–822)

JOURNAL OF RESEARCH of the National Bureau of Standards—A. Physics and Chemistry
Vol. 78A, No. 3, May–June 1974

The Infrared Spectra of Matrix Isolated Uranium Oxide Species*

S. Abramowitz and N. Acquista

Institute for Materials Research, National Bureau of Standards, Washington, D.C. 20234

(February 13, 1974)

The infrared spectra of matrix isolated products of the interaction of uranium and oxygen have been investigated at high temperatures. By use of collateral available data on the various uranium oxide species, plus employment of oxygen 16 and 18 isotopes, peak assignments were verified for many of the neutral metal oxide species.

Key words: Infrared spectra; mass spectrophotometry; matrix isolated; oxides of uranium.

1. Introduction

The infrared spectra of matrix isolated uranium oxides have been studied by several investigators [1–6].[1] Although the spectra were similar, these workers differed in their interpretation and assignment of the observed bands. In particular, Abramowitz et al. [1, 2]; and Leary et al. [3]; assigned two absorption bands at 873 and 776 cm^{-1} to UO_2 and UO while Carstens et al. [4], and Gabelnick et al. [5, 6], assigned the features at 776 and 820 cm^{-1} to UO_2 and UO respectively. All workers with the exception of Carstens et al. [4] used oxygen isotopically enriched urania to support their assignments. The uranium oxides were prepared by vaporization of the solid oxides from Knudsen effusion cells [1–3, 5, 6]. Carstens et al. prepared uranium oxides by chemically sputtering a uranium metal cathode with an argon-oxygen mixture by means of a discharge in a hollow cathode device [4]. By the latter technique, it was possible to monitor the $UO/UO_2/UO_3$ ratio by changing the oxygen/argon concentration.

It has been shown that the reaction of U(g), and oxygen species O, O_2, and O_3 yield the ionic species UO^+ and UO_2^+ in addition to the neutral products. Because of the uncertainty inherent in the sputtering technique as to the state of the oxygen species and/or uranium atoms it was felt worthwhile to perform these experiments with well characterized uranium beams obtainable from Knudsen cells. The reaction products were deposited on gold plated OFHC copper discs so that the ionic species that are produced in these reactions will be neutralized. The products of the reaction of an uranium beam with varying dilutions of argon-oxygen and argon-nitrous oxide mixtures were studied. In this way one could in principle produce different relative concentrations of UO, UO_2, and UO_3 by varying the O/U ratio. In addition, the matrix-mixtures could be passed through a microwave discharge to determine what effect an increase in O and O_3 species would have on the uranium oxides spectra.

2. Experimental Procedure

The apparatus and procedure used to prepare matrices have been described [1]. Unlike the sputtering method used by Carstens et al. [4], the uranium atoms were produced by vaporization of the metal from a single crystal tungsten cup placed inside a polycrystalline tungsten crucible capped with a 0.005 in tantalum foil with a 1 mm orifice. The temperature of the Knudsen crucible was measured with a W 25 percent Re versus W 3 percent Re thermocouple inserted in an 0.040 in hole drilled up the side of the cell. An electron beam furnace mounted directly beneath the deposition plate was used to vaporize the uranium to temperatures of about 1950 °C. Matrices were formed in 1–2 h. The matrix jet was 45° relative to the effusing atom beam. Beams of O, O_2, O_3 and N_2O diluted in argon were codeposited with the uranium atoms onto a gold plated OFHC copper disc mounted in the crystal holder of an Air Products closed cycle helium refrigerator [7] operated at 10 to 15 °K. Temperatures of the deposition plate were measured with a hydrogen bulb thermometer and a gold-iron versus chromel thermocouple. Deposition on a metallic surface was chosen so as that ionic species which are produced by these reactions will be neutralized [8]. Some previous experiments, as yet unpublished, have suggested the presence of trapped ionic species in an argon matrix.

The uranium used in these experiments was an NBS standard sample, while the argon was of research grade purity. The oxygen, nitrous oxide and isotopic mixtures of oxygen were obtained from com-

*Work supported in part by the Defense Nuclear Agency, Washington, D.C. 20305.
[1]Figures in brackets indicate the literature references at the end of this paper.

mercial sources and used without further purification.

The concentration of uranium oxides in argon was estimated using the standard effusion formula and the geometry of the system. During deposition the crucible was maintained at 1900 to 2100 °C to give a uranium vapor pressure in the range of 0.001 to 0.003 torr [9]. The rare-gas to oxygen mixture whose concentration varied from 1000 to 50 was deposited at the rate of 3–6 mmol/h. Using this data, the concentrations of rare gas to total uranium oxides were estimated to be from 5000 to 50,000.

Infrared spectra were observed using a Perkin Elmer Model 99G [7] with a grating blazed for 12 μm. An interference filter was used to block out the higher order radiation. Atmospheric water and ammonia lines were used to calibrate the spectra. It is estimated that the wave numbers are accurate to ± 0.5 cm^{-1} in the 700–900 cm^{-1} region.

3. Experimental Results

Representative infrared spectra obtained by reacting uranium atoms with varying concentration of argon-oxygen solutions are shown in figure 1. At the highest dilution of oxygen used ($Ar/O_2 = 1000$) two features appear at 820 and 776 cm^{-1}. These have been assigned to UO and UO_2 respectively by Carstens et al. [4] and Gabelnick et al. [5, 6]. As the concentration of O_2 is increased ($Ar/O_2 = 50$), the intensity of the band at 776 cm^{-1} relative to the band at 820 cm^{-1} is increased. As the concentration is further increased, the 820 cm^{-1} feature disappears and new bands appear at 853 and 745 cm^{-1}. These new features have been assigned to the two stretching modes of UO_3 [4, 6]. Finally, in pure oxygen only features assignable to UO_3 are observed. These results are shown in curves a, b, c in figure 1.

In another series of experiments, Ar/O_2 was passed through a microwave discharge prior to reacting them with the uranium beam. The resulting ozone and oxygen atoms react with the uranium to produce a small increase of the 820 cm^{-1} peak relative to the 776 cm^{-1} band.

Figure 2 shows the spectra of the reaction products of uranium atoms with different mixtures of Ar/N_2O at cryogenic temperatures. The spectra show a similar concentration dependence as those obtained with Ar/O_2 mixtures, and the similar spectra. At the highest concentrations of N_2O used ($Ar/N_2O = 50$) UO_2 and UO_3 peaks are much more intense than UO (curve a, fig. 2). At the lowest concentration used, the 820 cm^{-1} UO, band, was more intense than the 776 cm^{-1}, UO_2 band. A significant increase in the UO feature is obtained by passing Ar/N_2O mixtures through a microwave discharge, producing oxygen atoms and nitrogen. Another peak at 804 cm^{-1} is comparable in intensity with UO (see fig. 2). The species responsible for this peak may be a uranium nitrogen species. However, more experiments are needed to elucidate this.

Further experiments were performed using $Ar/^{18}O_2$ and a mixture of 2 parts $^{16}O^{18}O$ to 1 part each of $^{16}O_2$ and $^{18}O_2$ also in argon. These experiments yield vibrational frequencies for mixed isotopes of UO_2 and UO_3. The results of these isotopic experiments are shown in figure 3. Curve "b" is the spectrum obtained by reacting $Ar/^{18}O_2$ (= 100) with uranium atoms. The isotopic $^{18}O_2$ contains very little $^{16}O_2$ (~ 1%) and this is reflected in the spectra by the absence of $U^{16}O$ at 820 cm^{-1} and $U^{16}O_3$ at 853 cm^{-1} and 745 cm^{-1}. Therefore this spectrum shows bands due to $^{18}O_2$ and the mixed $^{16,18}O_2$. The band at 776 cm^{-1} is $U^{18}O$, while the band at 772 cm^{-1} is $U^{16}O^{18}O$. The others peaks are due to isotopic UO_3. Spectrum "a", where the single isotope $^{16}O_2$ is used, is included in figure 3 for comparison.

Curve "c" is representative of the spectra obtained when uranium atoms react with an isotopic mixture of Ar/O_2 (= 350) of ($^{16}O_2 : 2^{16}O^{18}O : {}^{18}O_2$). All the isotopic variations of UO, UO_2 and UO_3 are present in varying degrees of intensity. The band at 776 cm^{-1} is present, its intensity due to $U^{18}O$ and $U^{16}O_2$. Below this band, is the mixed isotope band ν_3 at 772 cm^{-1}, $U^{16}O^{18}O$. The band at 728.8 cm^{-1}, which is not present in spectrum "a" or "b" is the mixed isotopic $U^{16}O^{18}O$ fundamental ν_1 the symmetric stretch-

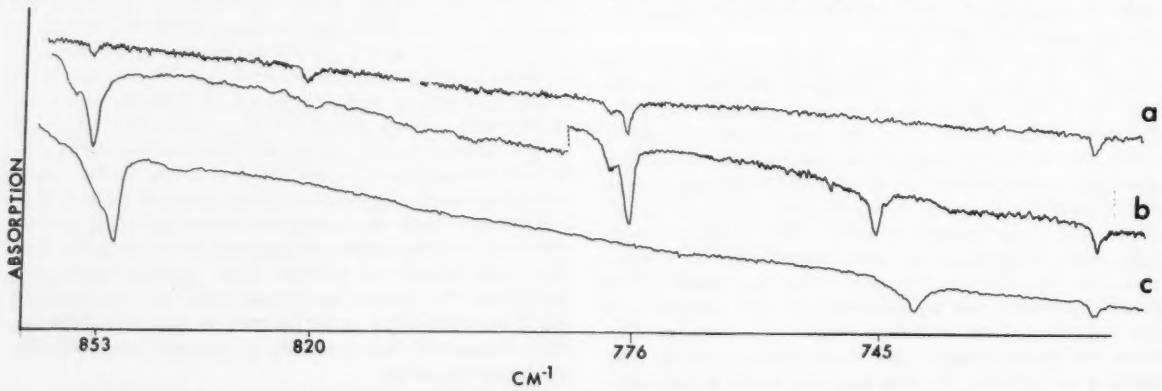

FIGURE 1. *The infrared spectrum of uranium oxides in argon matrices. (Note CO_2 at about 720 cm^{-1} in all spectra.)*

(a) Uranium vapor reacted with $Ar/O_2 = 1000$
(b) Uranium vapor reacted with $Ar/O_2 = 50$
(c) Uranium vapor reacted with pure O_2

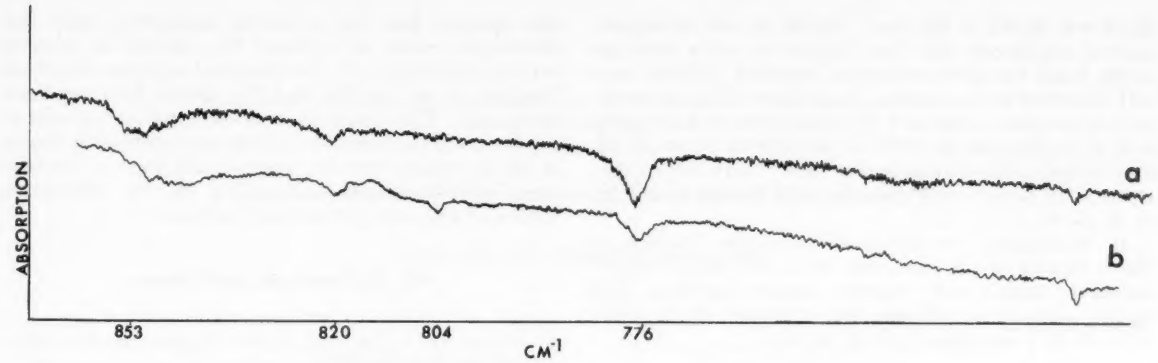

FIGURE 2. *The infrared spectrum of uranium oxides in argon matrix.*

(a) Uranium atoms reacted with $Ar/N_2O = 50$
(b) Uranium atoms reacted with $Ar/N_2O = 100$ passed through a microwave discharge

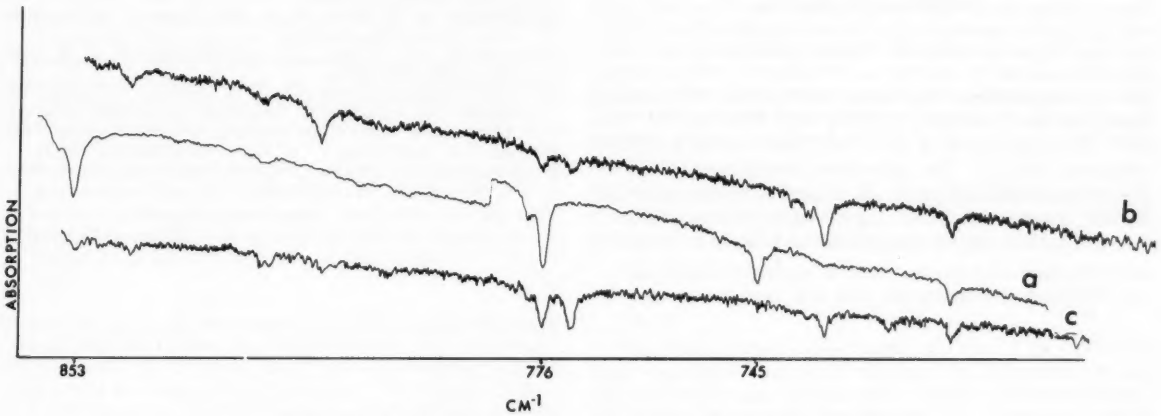

FIGURE 3. *The infrared spectrum of uranium oxides in argon matrices.*

(a) Spectrum obtained when uranium vapor reacts with $Ar/^{16}O_2 = 50$.
(b) Spectrum of $U^{16}O$, $U^{18}O_2$, and $U^{18}O^{18}O$ obtained when uranium is codeposited with $Ar/^{18}O_2 = 100$ (about 15% $^{16}O^{18}O$ in $^{18}O_2$ is present).
(c) Spectrum obtained when uranium vapor reacts with a mixture in argon of $^{16}O_2$, $^{16}O^{18}O$, $^{18}O_2$ in ratio of 1:2:1 (=350).

ing mode of UO_2. This band is observed because it is now infrared active. In the symmetrical molecules $U^{18}O_2$ and $U^{16}O_2$. ν_1 bands are infrared inactive. The other bands present in the mixed isotope experiment are due to UO_3. Curve "c" shows the spectrum. It is clear from the above experiments that the same spectra are obtained by condensing the vapors over urania in argon and also by codepositing a uranium atom beam with an oxygen argon mixture. The bands are all listed in table 1 with their assignment together with Gabelnick's results [4, 5].

In a final experiment, the spectrum of the matrix isolated vapors above UO_2(s) effusing from a single crystal tungsten cup (which in turn was placed inside of polycrystalline tungsten cell, covered with a tantalum foil with a 1 mm hole) was observed. Bands were observed at 853 and 776 cm^{-1} due to UO_3 and UO_2 but none at 873 and at 820 cm^{-1}. It was apparent from this experiment and those involving reactions between uranium atoms and O_2 molecules where no

TABLE 1. *Observed bands and assignments of uranium oxides in argon matrices*

Wave number	Wave number	Assignment
cm^{-1} [a]	cm^{-1} [b]	
819.6	820.0	$U^{16}O$
776.1	776.1	$U^{18}O$
776.1	776.1	$U^{16}O_2$
737.2	737.1	$U^{18}O_2$
771.7	771.1	$U^{16}O^{18}O$
728.8	728.4	$U^{16}O^{18}O$
809.9	809.9	$U^{18}O_3$
705.2	705.2	$U^{18}O_3$
852.5	852.5	$U^{16}O_3$
745.4	745.6	$U^{16}O_3$
847.7	847.5	$U^{16,18}O_3$
842.4	842.5	$U^{16,18}O_3$
731.9	731.8	$U^{16,18}O_3$
720.5		CO_2
804.2		UN_x

[a] This work.
[b] Reference [5].

band was found at 873 cm^{-1} under any of our experimental conditions that this feature is not a uranium oxide band but some unknown impurity. Neither was UO observed in the matrix. To produce UO, it is necessary to prepare a mixture of uranium metal and urania and to equilibrate at 1900 °C for several hours [5, 6]. Our results are summarized in table 1 and the assignment is in accord with Gabelnick et al. and Carstens et al. [4–6].

In conclusion, we have observed the spectra of the products of the reactions of a well characterized uranium beam with various oxygen species. The results appear to indicate that uranium atoms react with O_2 in a stepwise fashion such as

$$U + O_2 \rightarrow UO + O$$

$$UO + O_2 \rightarrow UO_2 + O$$

$$UO_2 + O_2 \rightarrow UO_3 + O,$$

$$O + O_2 \rightarrow O_3$$

In our experiments to date, we cannot differentiate between the formation of UO_2^+ and UO_2 or UO^+ and UO. The reactions of $U + N_2O$ proceed in a similar stepwise fashion. The vibrational assignment for UO_2 given by Gabelnick et al. [5, 6] and Carstens et al. [4] is the correct one. The appearance of two bands in the stretching region assignable to UO_3 indicates that this species has C_{3v} or lower symmetry (only one vibrational mode of a planar D_{3h} species is infrared active). Attempts to fit the observed isotopic stretching frequencies of $U^{16,18}O_3$ to a C_{3v} model have not been successful. This suggests a lower symmetry (perhaps C_{2v} for the UO_3 molecule). However a definitive choice of the geometry for this species will have to await a complete vibrational analysis of all the vibrational modes of UO_3 and its isotopic variants.

4. References and Note

[1] Abramowitz, S., Acquista, N., and Thompson, K. R., J. Phys. Chem. **75,** 2281 (1971).

[2] Abramowitz, S., and Acquista, N., J. Phys. Chem. **76,** 648 (1972).

[3] Leary, H. J., Rooney, T. A., Cater, E. D., and Friedrick, H. B., High Temp. Sci. **3,** 433 (1971).

[4] Carstens, D. H. W., Gruen, D. M., and Kozlowski, J. F., High Temp. Sci. **4,** 436 (1972).

[5] Gabelnick, S. D., Reedy, G. T., and Chasanov, M. G., Chem. Phys. Letters **19,** 90 (1973).

[6] Gabelnick, S. D., Reedy, G. T., and Chasanov, M. G., J. Chem. Phys. **58,** 4468 (1973).

[7] Certain commercial apparatus are identified to specify adequately the experimental procedure. In no case does such identification imply recommendation or endorsement by NBS.

[8] Fite, W. L., and Irving, P., J. Chem. Phys. **56,** 4227 (1972).

[9] Ackermann, R. J., Rauh, E. G., and Chandrasekharaiah, N. S., J. Phys. Chem. **73,** 762 (1969).

(Paper 78A3–823)

JOURNAL OF RESEARCH of the National Bureau of Standards — A. Physics and Chemistry
Vol. 78A, No. 3, May-June 1974

Publications of the National Bureau of Standards*

Citations with Selected Abstracts

J. Res. Nat. Bur. Stand. (U.S.), **78A** *(Phys. and Chem.)*, No. 2, (Mar.-Apr. 1974), SD Catalog No. C13.22/sec.A:78/2.

The formation of curved polymer crystals: Polyoxymethylene, F. Khoury and J. D. Barnes.

Solid-phase behavior of several long-chain n-paraffins, esters, and a ketone, Peter K. Sullivan.

Simultaneous measurements of heat capacity, electrical resistivity, and hemispherical total emittance by a pulse heating technique: Vanadium, 1500 to 2100 K, A. Cezairliyan, F. Righini, and J. L. McClure.

The shape of idealized grain boundaries, S. R. Coriell.

Reactions of fluorocarbon ions in C_2F_6. Implications for the radiolysis, L. W. Sieck, R. Gorden, Jr., and P. Ausloos.

A simple technique for the generation of dilute mixtures of pollutant gases, W. Tsang.

Energy levels and classified lines in the second spectrum of thorium (Th II), R. Zalubas and C. H. Corliss.

Proposed secondary wavelength standards and line classifications in thorium spectra between 0.9 and 3 μm, A. Giacchetti, J. Blaise, C. H. Corliss, and R. Zalubas.

Monogr. 25, Section 11. **Standard x-ray diffraction powder patterns. Section 11-data for 70 substances,** H. E. Swanson, H. F. McMurdie, M. C. Morris, E. H. Evans, B. Paretzkin, J. H. de Groot, and S. J. Carmel, Nat. Bur. Stand. (U.S.), Monogr. 25-Sec. 11, 134 pages (Feb. 1974) SD Catalog No. C13.44:25/Sec. 11, $1.55.

Key words: Crystal structure; integrated intensities; lattice constants; peak intensities, powder patterns; reference intensities; standard; x-ray diffraction.

Standard x-ray diffraction patterns are presented for 70 substances. Fifty-two of these patterns represent experimental data and 18 are calculated. The experimental x-ray powder diffraction patterns were obtained with an x-ray diffractometer. All d-values were assigned Miller indices determined by comparison with computer interplanar spacings consistent with space group extinctions. The densities and lattice constants were calculated, and the refractive indices were measured whenever possible. The calculated x-ray powder diffraction patterns were computed from published crystal structure data. Both peak height and integrated intensities are reported for the calculated patterns.

Monogr. 133. **Mass and mass values,** P. E. Pontius, Nat. Bur. Stand. (U.S.), Monogr. 133, 39 pages (Jan. 1974) SD Catalog No. C13.44:133, 70 cents.

Key words: Apparent mass; buoyancy corrections; mass comparison; mass value; true mass; weighing.

There are several bases for assigning mass values to weights to be used as mass standards. As a consequence a given weight may have several assigned mass values depending on the basis used. In many cases, the differences between these assigned values, although easily detectable with precise weighing equipment, are of no practical concern. However, in some instances these differences may be crucial. The first part of this paper is a historical summary of weighing, standards, and the assignment of value; and the interfacing of mass measurements with civilization. The second part of this paper discusses in detail the methods of assigning mass values. Ways to convert from values on one basis to values on another basis are discussed. Sample problems relating to the buoyant effect of the air are presented in the appendices.

H113. **CODASYL data description language. Journal of Development, June 1973,** Nat. Bur. Stand. (U.S.), Handb. 113, 155 pages (Jan. 1974) SD Catalog No. C13.6/2:113, $1.70.

Key words: COBOL; CODASYL; data base administration; data base management; data base task group; data description language.

This Journal of Development reports the work of the CODASYL Data Description Language Committee. The Committee was assigned the tasks of establishing "ways to aid the functions of data administration and systems administration." The Committee's charter included, "the provision of specifications for the declarations required to establish and maintain data base structures." As a step towards this purpose, the Journal contains three sections which treat the Background and History of the Data Description Language Committee, Major Concepts, and the specifications of the Data Description Language. The Committee based its work, in part, on the 1971 report of the Data Base Task Group Report.

The approved Data Description Language specifications contain the syntax and semantic rules that permit the description of the structure and contents of a data base in a language independent of, but common to, many other high level programming languages. The language specifications will have a significant impact on the development of functionally compatible data base management systems and will increase the portability of programs between different computer systems.

Though not part of the approved language specifications, the presentation of the major concepts will help in the understanding of the specifications. Similarly, the background and history information will help explain the evolutionary growth of the Data Description Language.

SP260-47. **Standard reference materials: Electrical resistivity of electrolytic iron, SRM 797, and austenitic stainless steel, SRM 798, from 5 to 280 K,** J. G. Hust, Nat. Bur. Stand. (U.S.), Spec. Publ. 260-47, 20 pages (Feb. 1974) SD Catalog No. C13.10:260-47, 55 cents.

Key words: Austenitic stainless steel; cryogenics; electrical re-

---

**Publications with prices and SD Catalog numbers may be purchased directly from the Superintendent of Documents, U.S. Government Printing Office, Washington, D.C. 20402 (foreign: one-fourth additional). Microfiche copies are available from the National Technical Information Service (NTIS), Springfield, Va. 22151. Reprints from outside journals and the NBS Journal of Research may often be obtained directly from the authors.*

sistivity; electrolytic iron; Lorenz ratio; standard reference material.

Electrical resistivity data are presented for characterized electrolytic iron, SRM 797, and austenitic stainless steel, SRM 798, at temperatures from 5 to 280 K. Resistivities at ice and liquid helium temperatures were determined for 22 randomly selected iron specimens and the same number of steel specimens. These data indicate that the effect of material variability is about 1 percent for each of these SRM's.

SP366. Supplement 1. **Bibliography on atomic line shapes and shifts (April 1972 through June 1973),** J. R. Fuhr, L. J. Roszman, and W. L. Wiese, Nat. Bur. Stand. (U.S.), Spec. Publ. 366 Suppl. 1, 73 pages (Jan. 1974) SD Catalog No. C13.10:366, Suppl. 1, $1.05.

Key words: Atomic; instrumental broadening; line shapes; line shifts; pressure broadening; resonance broadening; Stark broadening; Van der Waals broadening.

This is the first supplement to the NBS Special Publication 366, "Bibliography on Atomic Line Shapes and Shifts (1889 through March 1972)." It contains about 350 references and covers the literature from April 1972 through June 1973. The bibliography contains five major parts: (1) All general interest papers are cataloged according to the broadening mechanisms (and, further, according to special topics under several of the mechanisms) and as to whether the work is a general theory, a general review, a table of profiles or parameters, a comment on existing work, a study of general experimental measurement techniques, or an experimental effort of general importance. Also included are selected papers on important applications of line broadening and on miscellaneous topics relating to atomic spectral line shapes and shifts. (2) In Part 2, all papers containing numerical data are ordered as to element, ionization stage, broadening mechanism (in the case of foreign gas broadening the perturbing species are listed), and it is indicated whether the data are experimentally or theoretically derived. (3) While in the two preceding parts of the bibliography the references are listed for brevity by identification numbers only, in Part 3 all references are listed completely by journal, authors, and title and are arranged chronologically and alphabetically within each year according to the principal author. (4) This section contains a list of all authors and their papers. (5) A final section provides corrections or additions to our first bibliography.

SP400-2. **Semiconductor measurement technology: Microelectronic ultrasonic bonding,** G. G. Harman, Ed., Nat. Bur. Stand. (U.S.), Spec. Publ. 400-2, 109 pages (Jan. 1974) SD Catalog No. C13.10:400-2, $1.25.

Key words: Bonding; degradation (wire bond); discrete devices; electrical interconnection; fabrication (wire bond); failure (wire bond); hybrid circuits; integrated circuits; microelectronics; reliability; semiconductor devices; testing (wire bond); ultrasonic bonding; wire bond.

This report primarily comprises excerpts of the work done under the NBS ultrasonic wire bonding program that was previously published in 17 quarterly and other reports. The material is organized into subject groupings with the intention of presenting in convenient form sufficient information for making high quality ultrasonic wire bonds as well as imparting a basic understanding of the ultrasonic systems used. The work emphasizes problems and methods of solving them. To accomplish this, the required measurement equipment is first introduced. This is followed by procedures and techniques used in setting up a bonding machine, and then various machine- or operator-induced reliability problems are discussed. The characterization of the ultrasonic system and its problems are followed by in-process bonding studies and work on the ultrasonic bonding (welding) mechanism. The report concludes with a discussion of various effects of bond geometry and wire metallurgical characteristics. Where appropriate, the latest, most accurate value of a particular measurement has been substituted for an earlier reported one. Thus all of the included material is up to date.

SP400-3. **Semiconductor measurement technology: ARPA/NBS workshop I. Measurement problems in integrated circuit processing and assembly,** H. A. Schafft, Nat. Bur. Stand. (U.S.), Spec. Publ. 400-3, 24 pages (Feb. 1974) SD Catalog No. C13.10:400-3, 60 cents.

Key words: Die bonding; hermeticity; integrated circuits; measurement methods; microelectronics; oxides; photolithography; process control; reliability; semiconductor devices; silicon; wire bonding.

The dual purpose of the workshop was (1) to announce and describe the new effort, "Advancement of Reliability, Processing, and Automation for Integrated Circuits with the National Bureau of Standards," sponsored by the Defense Advanced Research Projects Agency (ARPA), and (2) to obtain additional input on critical measurement problems in integrated circuit processing and assembly to assist in planning future work in the effort. More than 130 engineers representing 61 organizations from the electronics industry and government participated in the workshop. The measurement problems in silicon, oxides, photolithography, and assembly and the problems in information dissemination that were identified by the participants are summarized. Included as appendices are summaries of two talks given: one which described the results of earlier direct contacts with a cross section of industrial representatives on major measurement problems in integrated circuit processing and assembly and the other which described the initial plans for work in the new effort.

BSS48. **Design, siting, and construction of low-cost housing and community buildings to better withstand earthquakes and windstorms,** W. F. Reps and E. Simiu, Eds., Nat. Bur. Stand. (U.S.), Bldg. Sci. Ser. 48, 152 pages (Jan. 1974) SD Catalog No. C13.29/2:48, $4.85.

Key words: Buildings; construction; design; developing countries; earthquakes; low-cost housing; natural disasters; structures; windstorms.

The extensive loss of life and property caused in developing countries by earthquakes and windstorms (hurricanes, typhoons and tropical cyclones) may be reduced to a considerable degree by the adoption and implementation of improved design, siting and construction procedures practicable within the context of the cultural and socioeconomic constraints prevailing in these countries.

The report provides technical information regarding characteristics of materials and building systems, and discusses the structural performance of buildings subjected to the action of earthquakes and wind forces with specific reference to structures typical of developing countries. Potential ways are described in which structures can be made more resistant to such action. Siting considerations are discussed from a geological, seismic and climatological viewpoint, and recommendations relating to siting problems are made. Techniques of housing construction, both traditional and industrialized, are described and improvements resulting in better earthquake or windstorm resistance are suggested. Building codes, their improvement and their enforcement are also discussed.

The report discusses cultural and socio-economic constraints influencing the adoption of improved practices, describes various feasible technical improvements of construction materials, composite systems and building systems, identifies mechanisms for stimulating technical improvements and discusses the role of institutions in this regard. Throughout the report, specific references are made to Peru, the Philippines and Turkey, countries which suffer from frequent devastation from natural disasters such as earthquakes and typhoons and which were selected as case studies for the purpose of this report.

TN648. Thermophysical properties of nitrogen from the fusion line to 3500 R (1944 K) for pressures to 150,000 psia (10342×10^5 N/m²), R. T. Jacobsen, R. B. Stewart, R. D. McCarty, and H. J. M. Hanley, Nat. Bur. Stand. (U.S.), Tech. Note 648, 162 pages (Dec. 1973) SD Catalog No. C13.46:648, $1.25.

Key words: Density; dielectric constant; enthalpy; entropy; equation of state; fixed points; heat transfer coefficients; index of refraction; Joule-Thomson; latent heat; melting point; nitrogen; Prandtl number; specific heat; speed of sound; surface tension; thermal conductivity; thermal diffusivity; vapor pressure; viscosity; volume.

Tables of thermophysical properties of nitrogen are presented for temperatures from the fusion line to 3500 R for pressures to 3000 psia, and from the fusion line to 1500 R for pressures above 3000 psia to 150,000 psia. The tables include values of entropy, enthalpy, internal energy, density, specific volume, velocity of sound, specific heats (C_v and C_p), thermal conductivity, viscosity, thermal diffusivity, Prandtl number, and the dielectric constant for selected isobars. Additional tables are included for values of: $(\partial P/\partial V)_T$, $(\partial P/\partial T)_\rho$, $V(\partial H/\partial V)_\rho$, $(\partial P/\partial U)_v$, $V(\partial P/\partial V)_T$, and $(\partial V/\partial T)_p$, which have special utility in heat transfer calculations. Tables of selected isobars for the liquid and vapor phases, and for the saturated vapor and saturated liquid are included.

An equation of state is presented for liquid and gaseous nitrogen for the temperature and pressure ranges of these tables. In the determination of the equation of state, all of the P-ρ-T (pressure-density-temperature) data available from the published literature were reviewed, and appropriate corrections made to bring experimental temperatures into accord with the International Practical Temperature Scale of 1968. The coefficients of the equation of state were determined by a weighted least squares fit to selected P-ρ-T data and simultaneously to C_v data determined by corresponding states analysis from oxygen data, and to data which defined the phase equilibrium criteria for the saturated liquid and saturated vapor. A vapor pressure equation, melting curve equation, and an equation to represent the ideal gas heat capacity of nitrogen are also presented. The equation of state is estimated to be accurate to within 0.5 percent in the liquid region, to within 0.1 percent for supercritical isotherms up to 15,000 psia, and to within 0.3 percent from 15,000 to 150,000 psia. The vapor pressure equation is accurate to within ± 0.01 K between the triple point and the critical point.

TN800. Computer networking: Approaches to quality service assurance, R. B. Stillman, Nat. Bur. Stand. (U.S.), Tech. Note 800, 26 pages (Jan. 1974) SD Catalog No. C13.46:800, 60 cents.

Key words: Compiler; computer network; documentation; dynamic software analysis; interpreter; quality control; software testing; software verification; static software analysis; structured programming; system errors; system performance; theorem-proving.

The problem of quality service assurance in a (generalized) computer networking environment is addressed. In the absence of any direct, well-defined, quantitative measure of service quality and reliability, error collection and analysis is the only basis for service quality control. Therefore, mechanisms are described which facilitate reporting of operational errors, documentation of error corrections, and collection of system performance data. Since techniques for hardware quality control are well known, these mechanisms focus on collecting data which can be used to assess and control software quality. Finally, specific network facilities are described which support research in the area of software quality, and potential areas of new research using the network are identified.

TN804. Review of computer networking technology, R. P. Blanc, Nat. Bur. Stand. (U.S.), Tech. Note 804, 135 pages (Jan. 1974) SD Catalog No. C13.46:804, $1.55.

Key words: Computer networks; computer-to-computer transfers; interactive terminals; minicomputer-based systems; network configuration; remote job entry; resource sharing.

This report gives a descriptive summary of the technical characteristics of existing computer networks, including data communication technology and configuration related to support of resource sharing services for a computer network. Included are discussions of terminal support capabilities for the communications network and a development of relevant network terminology. The report concludes with a comparative evaluation of existing technological approaches to networking.

TN805. Network management survey, I. W. Cotton, Nat. Bur. Stand. (U.S.), Tech. Note 805, 91 pages (Feb. 1974) SD Catalog No. C13.46:805, $1.20.

Key words: Computer network; management; network, network management.

This report presents the results of a study of management practices in different computer networks. Five networks were chosen as typical of different approaches to network implementation and management: Defense Advanced Research Projects Agency (ARPA) Network, MERIT Network, Triangle Universities Computation Center (TUCC), Oregon State Regional Network and Tymnet, a commercial network. A common format is employed to survey each network. While the report is not intended to be prescriptive, some empirical observations are presented for each topic covered.

TN809. Government looks at privacy and security in computer systems. A summary of a conference held at the National Bureau of Standards, Gaithersburg, Maryland, November 19-20, 1973, C. R. Renninger and D. K. Branstad, Eds., Nat. Bur. Stand. (U.S.), Tech. Note 809, 47 pages (Feb. 1974) SD Catalog No. C13.46:809, 85 cents.

Key words: Computer systems, privacy and security; confidentiality; privacy; security.

This publication summarizes the proceedings of a conference held for the purpose of highlighting the needs and problems of Federal, State and local government in safeguarding individual privacy and protecting confidential data contained in computer systems from loss or misuse. The Conference was held at the National Bureau of Standards on November 19-20, 1973.

The origin of governmental problems is discussed in the context of the public's concern for privacy arising out of computer-based recordkeeping, the diverse legislative actions now being taken to safeguard privacy, the threats to the security of computer-based information systems and the technological problems associated with protecting against such threats. Useful distinctions are drawn between privacy, confidentiality and security to clarify the issues and allocate responsibilities for solving the problem among lawmakers, technologists and management.

Major needs are described. These include the need for cohesive Federal, State and local legislation, technological guidelines and standards for assuring uniform compliance with legislative requirements; management guidelines for identifying and evaluating threats to security; and improved technological mechanisms for controlling access to computer systems and networks. Cost implications of providing security measures are discussed.

TN813. NBS Reactor: Summary of activities July 1972 to June 1973, R. S. Carter, Nat. Bur. Stand. (U.S.), Tech. Note 813, 135 pages (Feb. 1974) SD Catalog No. C13.46:813, $1.55.

Key words: Activation analysis; crystal structure; diffraction; isotopes; molecular dynamics; neutron; nuclear reactor; radiation.

This report summarizes all those programs which depend on the NBS reactor. It covers the period from July 1972 through June 1973. The programs range from the use of neutron beams to study the structure and dynamics of materials through nuclear physics and neutron standards to sample irradiations for activation analysis, isotope production and radiation effects studies.

TN814. **A mechanized information services catalog,** B. Marron, E. Fong, and D. Fife, Nat. Bur. Stand. (U.S.), Tech. Note 814, 56 pages (Feb. 1974) SD Catalog No. C13.46:814, 90 cents.

Key words: Bibliographic data bases; computer-based systems; information services; information systems.

NBS is mechanizing a catalog of currently available information sources and services. Information from recent surveys of machine-readable, commercially-available bibliographic data bases, and the various current awareness, batch retrospective, and interactive retrospective services which can access them, has been correlated and converted into a machine-readable data base. A prototype searching capability has been established on an operational interactive retrieval system. Reasons for establishing the catalog and the choice of the initial information are detailed and the prototype implementation is described. Sample queries are included, as well as a to-date listing of the catalog. Plans for future development are discussed.

TN815. **Fire accidents involving the ignition of sleepwear worn by children under the age of three,** E. A. Tyrrell, Nat. Bur. Stand. (U.S.), Tech. Note 815, 23 pages (Feb. 1974) SD Catalog No. C13.46:815, 60 cents.

Key words: Accidents; burn injuries; case histories; children's sleepwear; fabric fires; FFACTS; fires; flammable fabrics; garment fires; ignition sources; standards.

Accident case histories of children under age 3 involved in sleepwear fires are examined in detail. Of 434 persons involved in sleepwear ignition incidents in the NBS Flammable Fabrics Accident Case and Testing System as of January 1973, 101 were children under age 6; 22 of these were children under age 3. In 15 of these 22 accidents, the child was a victim of his own actions, while in 7 more accidents, the child played a passive role in the ignition sequence. Matches and kitchen ranges were the most frequent ignition sources found for this group of children. Seven of these small children died; the remaining 15 victims sustained burn injuries covering from one to 65 percent of their bodies. Most of the sleepwear items involved in these 22 accidents were made of cotton and 14 of these 22 items were pajamas. Children under age 3 were most frequently involved in fire accidents during the morning hours in the kitchen or bedroom. Only one child was under the supervision of an adult at the time of the accident. From the information found in the case history reports, an analysis of the severity of the injuries received by the victims was made and it was determined that the severity of the injuries received by one of the 3 infants under the age of one and 15 of the remaining 19 one- and two-year-olds probably would have been reduced if they had been afforded the protection of a flammability standard.

TN816. **Engineering and construction manual for an instrument to make burn hazard measurements in consumer products,** L. A. Marzetta, Nat. Bur. Stand. (U.S.), Tech. Note 816, 48 pages (Feb. 1974) SD Catalog No. C13.46:816, 85 cents.

Key words: Consumer products; contact temperature; thermesthesiometer; thermometry.

Surface temperature measurement alone is insufficient to establish the hazard of human contact with a hot or cold object. A metal surface is more likely to cause thermal injury than a plastic surface at the same temperature. An instrument equipped with a measuring probe has been developed for indicating the tissue temperature that would be experienced if human contact were made with the hot surface in question. The correct value of interface contact temperature can be read for a selected contact time without knowing the composition or temperature of the heated material under test.

A detailed set of instructions and drawings for assisting in the construction of the device is included in the manual. Several test procedures are described for use in checking the performance of the measuring probe and instrument.

TN818. **Occupant behavior in building fires,** A. I. Rubin and A. Cohen, Nat. Bur. Stand. (U.S.), Tech. Note 818, 28 pages (Feb. 1974) SD Catalog No. C13.46:818, 60 cents.

Key words: Disaster research; high rise building fires; occupant safety.

Fire safety in buildings is important in building design and the formulation of codes and standards. However, an examination of the information concerning the *needs* of occupants in fire emergencies (as opposed to ensuring a degree of structural integrity for the building) indicates that the scientific information base is woefully inadequate. The increasing prominence of high rise buildings having many occupants intensifies the need for better information about the behavior of occupants during fire emergencies. Fire researchers have indicated that it is often not feasible to evacuate buildings because of time constraints. Instead, designers use techniques such as safe areas within buildings and requiring people to respond differentially, based on their particular location. This approach emphasizes communications and warning systems to transmit messages. These systems such as loud noises or blinking lights should be designed to "take advantage" of the usual responses made by people. Occupants can actively be a part of the fire warning and fighting system instead of being unwilling victims. This possibility is pursued and a human factors approach is taken to suggest some means of better understanding the capabilities of occupants.

NBSIR 73-202. **Conservation via effective use of energy at the point of consumption,** C. A. Berg, 37 pages (Apr. 1973). Order from NTIS as COM 74-10479.

Key words: Buildings; energy conservation; industrial equipment.

The practices and equipment employed at the point of energy consumption in buildings and in industrial processes permit excessive consumption of energy. It is estimated that if full application of the economically justifiable technical improvements presently available were made to equipment and practices in buildings and industry, as much as 25 percent of the total primary fuel consumption in the U.S.A. could be conserved. The reasons why economically justifiable application of effective technology at the point of energy consumption has not been widely adopted in the past are considered. The needs to facilitate adoption of effective equipment and practices in the future are discussed.

NBSIR 73-287. **Procedures for the calibration of volumetric test measures,** J. F. Houser, 24 pages (Aug. 1973). Order from NTIS as COM 73-11928/1GA.

Key words: Air density; calibration; gravimetric; neck; volumetric;

The values for graduated neck type volumetric vessels may be obtained by either gravimetric or volumetric calibrations. This text describes the two methods of calibration and the data reduction associated with each method. Procedures for preparing these vessels for test are discussed. Also included are illustrations for data recording.

NBSIR 73-304. **Reference-waveform generation using Debye dielectric dispersion,** N. S. Nahman, R. M. Jickling, and D. R. Holt, 98 pages (Dec. 1972). Order from NTIS as COM 74-10281.

Key words: Pulse distortion in transmission lines; pulse techniques; reference waveform generation; time domain mea-

surements; transient response Debye dielectric.

This report discusses the theory, construction, and operation of Reference-Waveform Generators using a tunnel diode transition-waveform generator driving 4.65 meter (15 foot), 3.10 meter (10 foot), and 1.55 meter (5 foot) liquid-dielectric uniform lossy coaxial lines to produce known 0.2 volt transition waveforms across 50 ohms with (10-90%) transition times from 205 to 560 picosecond. Each resultant Available-Waveform is characterized in terms of its departure from the step response of the uniform lossy coaxial line operating into a 50 ohm load. The liquid dielectric solutions are dispersive with relaxation times of the order of 4 picoseconds in which heptane is the solvent and the ketones, butanone, heptanone and octanone are the solutes in concentrations ranging from 0.25- to 2-molal.

NBSIR 73-316. **Liquid helium pumps,** P. M. McConnell, 90 pages (June 1973). Order from NTIS as AD 769542.

Key words: Cavitation; helium; pump performance; pumps; superfluid.

This report summarizes studies of pump characteristics and performance in supercritical, normally boiling, and superfluid helium, and also presents results on a survey of commercially available pumps for helium service. Experimental measurements were made on a centrifugal pump which produced a maximum head of about 15 meters and a maximum flow of about 2.5×10^{-4} m^3/s. Performance agreed approximately with classical affinity laws, but cavitation appeared to provide less of a performance limitation than expected. The survey turned up several pumps which have been used in helium, though relevant performance data is lacking.

NBSIR 73-331. **Refrigeration of superconducting rotating machinery,** V. D. Arp, 75 pages (June 1973). Order from NTIS as COM 74-10238.

Key words: Equation of state; helium; hydrodynamics; near-critical flow; refrigeration; superconductors; thermodynamics.

Recent work at the NBS Cryogenics Division in three areas related to helium refrigeration is summarized: (1) Analysis is given of a possible high pressure refrigeration cycle which offers in principle a reduced component size, but which turns out to be impractical because of expansion engine inefficiencies. (2) Exact equations for flow of a real fluid are derived and applied to problems of fluid flow near the critical point, as may occur with some helium-cooled superconducting systems, and (3) Three new equations of state for helium are given, each using different state variables, to eliminate the need for iterative techniques in helium refrigeration cycle and fluid flow analysis.

NBSIR 73-339. **Preliminary hydrogen freezing studies,** D. E. Daney, W. G. Steward, and R. O. Voth, 281 pages (Oct. 1973). Order from NTIS as COM 73-11985/1GA.

Key words: Freezing rates; solid hydrogen; thawing; thermal conductivity.

The study summarized in this report is aimed at developing the technology required to fill space vehicle propellant tanks with solid hydrogen by in-place freezing. Planned continuation of this work was terminated with the loss of NERVA funding by the NASA. Therefore, progress to-date is summarized but substantial experimental results have not yet been obtained.

The program was to have been carried out in two phases: a mathematical analysis and experimental verification of the analysis. Freezing times and heat flux have been calculated for four geometrical shapes, and a range of sizes, refrigerant temperatures, ortho-para concentrations, and heat transfer coefficients. The results of these calculations are presented in generalized graphical form, in a total of 240 graphs.

The freezing experimental apparatus has been built and a preliminary test performed which generally demonstrates the validity of the analytical and experimental approaches. With only minor modifications the apparatus is ready for a full test program of hydrogen freezing and melting techniques.

NBSIR 73-345. **Combustion of metals in oxygen phase II: Bulk burning experiments,** A. H. Tench, H. M. Roder, and A. F. Clark, 49 pages (Dec. 1973). Order from NTIS as COM 74-10239.

Key words: Alloys; aluminum; combustion; ignition; oxygen; safety; stainless steel; steel, titanium.

This program was started to study combustion of the ordinary metals in oxygen, to provide information useful to designers of bulk oxygen handling equipment, particularly from the point of view of safety. We have studied the ignitability and combustability of carbon steels, stainless steels, aluminum alloys, titanium and copper metals, in oxygen atmospheres up to 60 psig. We encountered a violent reaction involving burning stainless steel and aluminum, a thermite reaction apparently, and have investigated this from a quantitative point of view. We have tried throughout to study the quantitative aspects of the combustion processes, and related quenching effects. Ordinary steel and stainless steel burn quite readily at these low oxygen pressures, and the stainless steel-aluminum reaction produces intense heat, with severe damage to neighboring structures. We are at the stage where further investigations could be carried out quite expeditiously and on a sound statistical basis.

NBSIR 73-346. **RF total mass gauging in large storage containers: Empty tank modes,** R. S. Collier and D. Ellerbruch, 28 pages (Oct. 1973). Order from NTIS as COM 74-10240.

Key words: LOX storage container; radio frequency; total mass gauging.

This report describes experiments to determine the feasibility of radio frequency (RF) mass gauging for fluids stored in large containers. The experiments were done at the NASA Mississippi Test Facility using the 460,000 gallon LOX Storage Tank as an electromagnetic resonant cavity. The results show that the RF gauging technique is feasible for large containers.

NBSIR 73-348. **An engineering feasibility study for one-way time transfer using the GOES satellite ranging system,** J. B. Milton and W. F. Hamilton, 38 pages (Dec. 1973). Order from NTIS as COM 74-10241.

Key words: Clock synchronization; one-way time transfer; satellite timing; synchronous satellite.

The Time and Frequency Division of the National Bureau of Standards has conducted an engineering study to determine the feasibility of using the GOES satellite ranging system for precise (0.1 microsecond, one-sigma) time transfer to a receiving-only timing site. The GOES satellite ranging system, termed a trilateration system, will accurately locate this satellite within some coordinate structure. The sources of time transfer errors have been studied in some detail. These errors can be caused by satellite location errors, ground station location errors, unknown delays caused by the troposphere, the ionosphere, and the various equipments. Simplified designs for an automatic and a manually operated timing site are presented. Some technical problems found in the associated equipment are discussed. The study indicates that a secondary, or slave site, clock could be synchronized to within 0.1 microsecond, one-sigma, of some master clock utilizing a one-way, or receiving-only system.

NBSIR 73-402. **NBS materials science and manufacturing in space research,** E. Passaglia and R. L. Parker, 127 pages (Nov. 1973). Order from NTIS as COM 74-10472.

Key words: Materials processing; perfection; purity; space manufacturing; space processing; zero-g.

This report describes NBS work for NASA in support of NASA's Materials Science and Manufacturing in Space (MS/MS) (now Space

Processing) program, covering the period November 1, 1972 to October 31, 1973. The objectives of the NBS program are to perform ground-based studies of those aspects of space that could possibly provide a unique environment for making materials more perfect or more pure. The approach taken deals primarily with experimental and theoretical studies of the possible effects of the absence of gravitational forces on those materials preparation processes where the presence of gravity may be important in reducing perfection or purity. The materials preparation processes studied comprise 5 tasks in the areas of crystal growth, purification and chemical processing, and the preparation of composites.

NBSIR 73-403. **Development and analysis of techniques for calibration of Kerr cell pulse-voltage measuring systems VII,** E. C. Cassidy, R. E. Hebner, R. J. Sojka, and M. Zahn, 129 pages (Nov. 1, 1973). Order from NTIS as COM 74-10016/5GA.

Key words: Electric field measurement; electro-optic Kerr effect; high voltage measurement; impulse measurement; Kerr constant; liquid insulants; nitrobenzene; peak reading voltmeter; space charge.

To improve the accuracy of pulse voltage systems using the electro-optic Kerr effect, it is necessary to improve the accuracy of calibration of Kerr cells. In the past this has been attempted by calibrating the cell under direct voltage and relying on the frequency independence of the Kerr coefficient (below 10^8 Hz) to insure that the calibration was valid under high voltage pulses. Space charge effects, however, modify the electric field distribution in the liquid under direct high voltage. The electric field and space charge behavior in nitrobenzene have therefore been documented as functions of the level and frequency of the applied voltage. In addition, to improve the efficiency of cell design and to facilitate the investigation of other liquids for use in Kerr cells, the electro-optic Kerr coefficient of nitrobenzene has been measured as a function of temperature and wavelength. Finally a new peak reading voltmeter based on the Kerr effect is described and the results of using the electro-optic Kerr effect to measure the voltage pulses in medical x-ray machines are presented.

NBSIR 73-417. **Evaluation of commercial integrating-type noise exposure meters,** W. A. Leasure, Jr., R. L. Fisher, and M. A. Cadoff, 33 pages (Dec. 1973). Order from NTIS as COM 74-10477.

Key words: Acoustics (sound); dosimeter; environmental acoustics; instrumentation; noise exposure; noise exposure meters.

As a result of the promulgation of occupational noise exposure regulations by the Federal government, there are a number of commercial noise exposure meters on the market today that provide a measure of noise integrated (with appropriate weighting) over a time interval. This report presents the results of an evaluation of such instruments by the National Bureau of Standards (under the sponsorship of the U.S. Environmental Protection Agency) as to their usefulness in monitoring compliance with occupational noise regulations as well as their applicability as instruments for use in achieving the broader goals of the EPA. Tests were designed and conducted to evaluate microphone and system response to sound of random incidence, frequency response, crest factor capability, accuracy of the exchange rate circuitry, performance of the noise exposure meter as a function of temperature, and the dependence of the device on battery voltage. The rationale of the test procedures utilized to evaluate overall system as well as specific performance attributes, details of the measurement techniques, and results obtained are discussed.

NBSIR 74-442. **High temperature slow crack growth in ceramic materials,** A. G. Evans, 48 pages (Feb. 1974). Order from NTIS as COM 74-10476.

Key words: Ceramics; crack healing; crack propagation; cyclic fatigue; failure prediction; high temperature; static fatigue.

High temperature slow crack growth processes in several ceramic materials are examined under static and cyclic loading conditions. Data obtained at temperatures up to 1400 °C are used for purposes of failure prediction and for analysis of the slow crack growth phenomena. It is shown that purity plays a major role in slow crack growth resistance, particularly in the hot pressed materials, and that cycling in the low frequency regime does not significantly increase the rate of slow crack growth. The slow crack growth mechanisms appear to be primarily plasticity related. Two semi-quantitative mechanisms are presented, one due to dislocation motion and the other due to grain boundary sliding.

This column lists all outside publications by the NBS staff, as soon after issuance as practical. For completeness, earlier references not previously reported may be included from time to time.

Arni, H. T., **Precision of air-permeability, turbidimeter, and No. 325 sieve fineness data,** *Amer. Soc. Testing Mater. Spec. Tech. Publ.* **473,** pp. 20-44 (1970).

Key words: Air-permeability; cements; fineness; No. 325 sieve; portland cements; precision; tests; Wagner turbidimeter.

Data on air-permeability and turbidimeter fineness from an interlaboratory test program involving eight different portland cements and from about 80 to 150 laboratories over a period of a year and a half are presented and analyzed from the standpoint of between-laboratory and within-laboratory precision. Scatter diagrams for the four pairs of samples are presented and used as an aid in the analysis. For six of the cements, results of determinations of fineness by the No. 325 sieve are also analyzed and scatter diagrams shown. The effect on the calculated standard deviation of the elimination of some outlying results is assessed. A method of determining within-laboratory or single-laboratory precision without the use of duplicate determinations is presented. Laboratory bias was found to be significantly larger than the random error for all three tests. There was no indication of any significant difference in precision or in laboratory bias between the Type I and Type IA cements for any of the tests.

Bagus, P. S., Krauss, M., LaVilla, R. E., **The threshold region of the methane carbon K-absorption spectrum,** *Chem. Phys. Lett.* **23,** No. 1, 13-17 (Nov. 1, 1973).

Key words: Carbon-K-absorption threshold; first Rydberg transition; $1a_1^{-1}$ hole state calculation; methane; vibronic transition.

The carbon K-absorption of CH_4 is analyzed with the help of an ab initio calculation of the Rydberg states of $1a_1^{-1}$ hole state. The strong absorption peak at 288.3 eV is identified as the first Rydberg $2t^* \leftarrow 1a_1$, whose calculated ionization potential is in good agreement with experiment. Also, the oscillator strength for this transition was calculated to be $f = 1.9 \times 10^{-2}$, which is within the estimated margin of error of the experimental $f = 0.6 \times 10^{-2}$. The weak peak at 287.2 eV is interpreted as a vibronic transition to the $3a_1(3s)$ Rydberg. An estimate of its oscillator strength as 10 percent of the allowed 2t(3p) Rydberg line is consistent with experiment. For the case of CD_4, this weak forbidden transition was estimated to be 20 percent of the allowed 2t(3p) Rydberg line.

Ballard, D. B., **A resolution test sample for the scanning electron microscope,** (Proc. 30th Annual Meeting on Electron Microscopy Society of America, Los Angeles, Calif., Aug. 14-18, 1972), Paper in *8th Annual Proceedings Electron Microscopy Society of America,* C. J. Arceneaux, Ed., pp. 446-447 (Claitor's Publishing Division, Baton Rouge, La., Aug. 1972).

Key words: Al-W alloy; resolution test specimen; SEM; specimen criteria.

A test sample that satisfies the restrictive specimen criteria discussed previously [1] for a resolution determination of the SEM is essential. At present, the use of a resolution sample made from a specimen well-known to the particular operator who carries out measurements on the subsequent photomicrograph is the usual

procedure. The aluminum-tungsten (Al-W) dendritic structure (located at arrow) in figure 1 that remains on the crystal surface of the bead resulting from the melting of aluminum on a hot tungsten filament, provides such a specimen.

Bass, A. M., Laufer, A. H., **The methyl radical combination rate constant as determined by kinetic spectroscopy,** *Int. J. Chem. Kinet.* **V,** 1053-1065 (1973).

Key words: Absorption spectroscopy; combination; f-number; methyl; radical; rate constant.

The rate constant for the reaction

$$CH_3 + CH_3 + M \xrightarrow{k_1} C_2H_6 + M \quad (M = He)$$

has been determined by means of vacuum ultraviolet flash photolysis and time-resolved kinetic spectroscopic observations of the 1504-Å absorption band of CH_3. The measurements made using three different sources of methyl radicals (azomethane, dimethylmercury, and ketene-hydrogen) were in accord and yielded a value for the rate constant of $k_1 = (9.53 \pm 1.17) \times 10^{-11}$ cc molec^{-1} sec^{-1}. A detailed error analysis is presented. The *f*-value for the 1504-Å band of CH_3 is determined to be $(2.5 \pm 0.7) \times 10^{-2}$.

Bender, P. L., Currie, D. G., Dicke, R. H., Eckhardt, D. H., Faller, J. E., Kaula, W. M., Mulholland, J. D., Plotkin, H. H., Poultney, S. K., Silverberg, E. C., Wilkinson, D. T., Williams, J. G., Alley, C. O., **The lunar laser ranging experiment,** *Science* **182,** 229-238 (Oct. 1973).

Key words: Celestial mechanics; crustal movements; earth rotation; geophysics; laser; moon; polar motion; selenodosy.

The data obtained so far by the McDonald Observatory have been used to generate a new lunar ephemeris based on direct numerical integration of the equations of motion for the moon and planets. With this ephemeris, the range to the three Apollo retroreflectors can be fit to an accuracy of 5 meters by adjusting the differences in momenta of inertia of the moon about its principal axes, the selenocentric coordinates of the reflectors, and the McDonald longitude. The accuracy of fitting the results is limited currently by errors of a few arc sec in the angular orientation of the moon, as derived from the best available theory of how the moon rotates in response to the torques acting on it. A new calculation of the moon's orientation as a function of time based on direct numerical integration of the torque equations is expected to considerably improve the accuracy of fitting the data.

Bennett, L. H., Swartzendruber, L. J., McNeil, M. B., **On the electron-configuration theory of marine corrosion,** (Proc. 3d Int. Congress on Marine Corrosion and Fouling, Gaithersburg, Md., Oct. 2-6, 1972), Paper in *Proceedings: Third International Congress on Marine Corrosion and Fouling,* pp. 410-426 (Northwestern University Press, Evanston, Ill., Oct. 1973).

Key words: Alloy theory; catalysis; chemisorption; Cu-Ni alloys; d-bands; electron-configuration; metallurgy; passivity; rigid-band model; saltwater corrosion; surfaces.

The electron-configuration theory of corrosion introduced by Uhlig relates chemisorption and passivity to alloy compositions having favorable d-electron configurations. This theory postulates a critical composition for passivity which coincides with a theoretical filling of the d-band in a "rigid-band" description of these alloys. Recently, detailed knowledge of the electronic structure of Cu-Ni alloys has been greatly increased, and it no longer appears that a strict band model alone can give an adequate description of the disordered alloys. Recent theories and modern spectroscopic methods, including soft x-ray and photoelectron spectroscopy and other techniques, have provided a great deal of new knowledge concerning the electronic structure of Cu-Ni alloys. In light of these experimental and theoretical developments, this paper investigates whether or not there is any evidence to support an electron-configuration theory of corrosion, without regard to the question of passivity, for Cu-Ni alloys in saltwater. The addition of small amounts of Fe has important effects on the corrosion rate in the copper-rich alloys and the relevance of this to the electron-configuration theory is considered. Effects of metallurgical variables and of film properties are noted. The related topic of heterogeneous catalysis is discussed.

Berger, M. J., **Beta-ray dose in tissue-equivalent material immersed in a radioactive cloud,** *Health Phys.* **26,** 1-12 (Jan. 1974).

Key words: Beta-rays; depth-dose; dosimetry; electrons; immersion problem; radioactive cloud.

The radioactive-cloud immersion problem for beta-radiation has been treated schematically by assuming a semi-infinite air medium (source region) located adjacent to a semi-infinite water medium (tissue-equivalent target). The source region has been assumed to contain a uniform concentration of beta-emitting radionuclide, and calculations have been made of the absorbed-dose distribution (depth dose) in the water target. A leakage correction has also been made to estimate the reduction of absorbed dose that would occur if the target had lateral dimensions small compared to the beta-particle range in air. Depth-dose calculations have been carried out for various source spectra (including beta-ray as well as discrete electron spectra) for 15 radionuclides (rare gases) emitted by nuclear power plants into the atmosphere, and for 12 other commonly used radionulides.

Billingsley, F. P. II, **Calculation of the absolute infrared intensities for the 0-1, 0-2 and 1-2 vibration-rotation transitions in the ground state of NO^+,** *Chem. Phys. Lett.* **23,** No. 2, 160-166 (Nov. 15, 1973).

Key words: Dipole moment function; infrared intensities; multiconfiguration; NO^+.

The absolute infrared intensities of the 0-1, 0-2 and 1-2 vibration-rotation bands in the $^1\Sigma^+$ ground state have been calculated from first principles. The dipole moment function for NO^+ was determined in the region of the equilibrium internuclear separation by an accurate multi-configuration self-consistent-field procedure. The dipole matrix elements over vibration states were solved exactly using numerical techniques. The ratio of the calculated integrated absorption coefficients for the fundamental and first overtone (88.8 cm^{-2} atm^{-1} and 0.6 cm^{-2} atm^{-1}, respectively, at 273.16 K) is in reasonable agreement with an estimate based on observation of these bands in NO^+ at high altitudes in the upper atmosphere.

Blevin, W. R., **Sinusoidal radiation chopper,** *Appl. Opt.* **12,** No. 12, 2802 (Dec. 1973).

Key words: Radiation chopper; sinusoidal modulation.

A description is given of a simple method for modulating a beam of optical radiation sinusoidally.

Bur, A. J., Fetters, L. J., **Intrinsic viscosity measurements on rodlike poly(*n*-butyl isocyanate) and poly(*n*-octyl isocyanate),** *Macromolecules* **6,** No. 6, 874-879 (Nov.-Dec. 1973).

Key words: Intrinsic viscosity; poly(*n*-butyl isocyanate); poly(*n*-octyl isocyanate); rodlike.

Previous calculations of the molecular length of rodlike poly(*n*-butyl isocyanate), $(-CO-NC_4H_9-)_n$, from dielectric relaxation time measurements have not shown satisfactory agreement with the results from x-ray and light-scattering measurements. Here, we examine this conflict by extending our hydrodynamic experiments to include intrinsic viscosity measurements on well-characterized low molecular weight samples of poly(*n*-butyl isocyanate) (PBIC) and poly(*n*-octyl isocyanate) (POIC), $(-CO-NC_8H_{17}-)_n$. Using the Kirkwood-Auer-Riseman equation relating intrinsic viscosity and rod dimensions, the intermonomer translation along the rod axis is calculated to be 1.66 ± 0.12 Å. This is lower than the 1.94-Å result from x-ray measurements, but higher than the 1.33 ± 0.12 Å result from dielectric relaxation time measurements. The root of the problem ap-

pears to be the application of hydrodynamic equations to a physical situation which does not satisfy the model assumptions.

Cameron, J. M., Plumb, H., **Traceability—with special reference to temperature measurement,** *Soc. Automot. Eng. Trans.* **78,** Section 3, 1586-1590 (1969).

Key words: Calibration; temperature, traceability.

The requirement that measurements be traceable to national standards arose in response to needs for consistency between different parts of the measurement system. There is one single agreed-upon definition for traceability, but it has been taken to mean the existence of some chain of intercomparisons or calibrations leading back to the National Bureau of Standards. Like all procedural or material requirements, its presence or absence may bear little relation to the performance characteristic one is really interested in. The scientific problem of expressing the desired performance requirements in terms of the amount and type of evidence needed to determine the degree of consistency of measurement processes is discussed and illustrated for the measurement of temperature. The importance of the study of measurement as a production process and the need for a program for the surveillance of the measurement process is discussed and plans for a new service for transfer of measurement capability in thermometry are presented.

Carrington, C. G., Drummond, D., Gallagher, A., Phelps, A. V., **Oscillations in continuum molecular spectra of alkali-metal—noble-gas molecules,** *Chem. Phys. Lett.* **22,** No. 3, 511-514(Oct. 15, 1973).

Key words: Alkali-metal; continuum; molecules; rare-gas; spectra.

Regular intensity undulations in the continuum spectra of heavy diatomic molecules are reported. In particular, the AII–XΣ transition of the Rb—noble-gas Cs—noble-gas molecules has been studied. Calculations as well as experimental observations of absorption and emission spectra are reported.

Cassidy, E. C., Anderson, W. E., Booker, S. R., **Recent refinements and developments in Kerr system electrical measurement techniques,** *IEEE Trans. Inst. Meas.* **IM-21,** No. 4, 504-510 (Nov. 1972).

Key words: Electric fields; electrical measurements; electro-optics; high-speed photography; high-speed techniques; high-voltage measurements; Kerr effect; laser applications.

Kerr system electrical measurement techniques are improved by progress in two important areas: 1) in the development of methods for visualizing and measuring pulsed (microsecond) electric fields and high voltages from time-varying electro-optical fringe patterns recorded using high-speed photographic techniques, and 2) in the development of convenient experimental methods for evaluating and correcting path-dependent errors in Kerr system response. Results demonstrate use of fringe-pattern measurements in achieving accurate pulse voltage measurements and in correction of errors resulting from sizeable end-field variations in existing 300-kV Kerr cells.

Cassidy, E. C., Hebner, R. E., **Experimental study of the behavior of nitrobenzene under varied high voltage conditions,** (Proc. Electrical Insulation and Dielectric Phenomena, Buck Hill Falls, Pa., Oct. 23-25, 1972), Chapter 1972 Annual Report of the *Conference Electrical Insulation and Dielectric Phenomena,* pp. 37-44 (National Research Council, National Academy of Sciences, Washington, D.C., 1973).

Key words: Dielectric liquid; electrical properties of liquids; electro-optics; high voltage measurement; Kerr effect; laser applications; nitrobenzene; optical properties of liquids.

Recently developed fringe-pattern methods are employed for visualizing time and space variations in electric fields between electrodes immersed in nitrobenzene. Investigations are conducted with operation under high direct, pulsed (μs), and 60 Hz voltage. With minimization of effects resulting from variations in the fringing fields at the electrode ends, the fringe-pattern "mappings" of the field distribution enable observation of space-charge behavior. Applied voltages are measured simultaneously using calibrated (with state-of-the-art accuracy) devices. Results enable computation and plotting of electric field distribution and intensity, of charge distribution, and of the Kerr constant of nitrobenzene.

Cezairliyan, A., **Change in normal spectral emittance (at 650 nm) of niobium during melting and its relation to surface roughness,** *Surface Sci.* **40,** 429-432 (1973).

Key words: High temperature; melting; niobium; normal spectral emittance; surface roughness.

Investigations on the normal spectral emittance (at 650 nm) of niobium during melting are reported. An attempt is made to relate the difference between the emittance of solid and liquid niobium at the melting point to the roughness of the solid surface. The results indicate that this difference is primarily due to conditions of the solid surface.

Chandler, H. H., Bowen, R. L., Paffenbarger, G. C., Mullineaux, A. L., **Clinical evaluation of a radiopaque composite restorative material after three and a half years,** *J. Dent. Res.* **52,** No. 5, 1128-1137 (Sept.-Oct. 1973).

Key words: Clinical evaluation; clinical research; composite restorations; dental restorations; dentistry; monomers; operative dentistry; reinforcements.

A clinical comparison was made of an experimental radiopaque composite restorative material and Addent 35. The radiopaque experimental formulation contained a novel ternary eutectic dimethacrylate as the resin binder and fused silica and a novel BaF_2-containing glass as the reinforcing fillers. Evaluation of restorations indicate that the experimental material compared favorably with the commercial material.

Chow, L. C., Brown, W. E., **Phosphoric acid conditioning of teeth for pit and fissure sealants,** *J. Dent. Res.* 52, No. 5, 1158 (Sept.-Oct. 1973).

Key words: Enamel; hydroxyapatite; monocalcium phosphate monohydrate; pit and fissure sealant; phosphoric acid.

It is shown that monocalcium phosphate monohydrate, $Ca(H_2PO_4)_2 \cdot H_2O$, forms on enamel surface during the H_3PO_4 conditioning of teeth administered prior to application of pit and fissure sealants. The $Ca(H_2PO_4)_2 \cdot H_2O$ coating appears to protect teeth from excessive dissolution during the pretreatment and is washed away subsequently to provide a clean surface available for adhesion to sealant. These phenomena are in complete accord with the phase diagram for the ternary system $Ca(OH)_2OH_3PO_4 - H_2O$.

Chow, L. C., Brown, W. E., **Reaction of dicalcium phosphate dihydrate with fluoride,** *J. Dent. Res.* **52,** No. 6, 1220-1227 (Nov.-Dec. 1973).

Key words: Calcium phosphates; dental caries; fluoride; fluorapatite; tooth enamel.

The intermediate formation of $CaHPO_4 \cdot 2H_2O$ and its subsequent conversion to $Ca_5(PO_4)_3F$ or CaF_2 may be a major factor in increased fluoride uptake when tooth enamel is pretreated with acid solutions before being exposed to fluoride. To obtain information concerning the form of fluoride incorporation, the reactions of $CaHPO_4 \cdot 2H_2O$ with solutions containing various amounts of F^- and PO_4^{3-} ions were studied.

Clough, S. A., Beers, Y., Klein, G. P., Rothman, L. S., **Dipole moment of water from Stark measurements of H_2O, HDO, and D_2O,** *J. Chem. Phys.* **59,** No. 5, 2254-2259 (Sept. 1, 1973).

Key words: Dipole moment; Stark effect; water.

The equilibrium dipole moment of the water molecule has been determined from Stark effect measurements on two H_2O, one D_2O, and six HDO rotational transitions. The variation of the dipole moment projection operator with rotational state is taken into account and expressions are given for this operator evaluated in the ground vibrational states of the three isotopes. The value obtained for the equilibrium dipole moment is $|^0\mu_x| = 1.8473 \pm 0.0010$ D. The effective dipole moments in the principal axis energy representation are $|\mu_b$ (HOH)$| = 1.8546 \pm 0.0006$ D, $|\mu_b$ (DOD)$| = 1.8558 \pm 0.0021$ D and $|\mu_b$ (DOH)$| = 1.7318 \pm 0.0009$ D, $|\mu_a$ (DOH)$| = 0.6567 \pm 0.0004$ D.

Colson, J. P., Reneker, D. H., **Growth direction of polyoxymethylene crystals inside irradiated trioxane crystals,** *J. Appl. Phys.* **44,** No. 10, 4293-4302 (Oct. 1973).

Key words: Electret domains; polyoxymethylene crystals; radiation damage; solid state polymerization; trioxane.

The long slender crystals of polyoxymethylene that grew in irradiated trioxane crystals all grew toward the negative end of the trioxane crystal. The observed direction of growth was consistent with the assumption that the ion at the growing end of the polyoxymethylene chain was a cation. Certain morphological features such as facets and direction of taper of these polyoxymethylene crystals indicated the direction in which the crystals grew. Incidental observations of polyoxymethylene precursor crystals, electret domains in trioxane, and the effects of electron irradiation on polyoxymethylene crystals were made.

Colwell, J. H., **Thermal contacts in a low temperature cryostat,** *Cryogenics* **13,** No. 11, 674-675 (Nov. 1973).

Key words: Cryogenics; electrical leads; low temperature; thermal conductivity; thermal contact.

The thermal conductances of an assembly used for thermally anchoring electrical leads in a low temperature cryostat are reported. Measurements were made between 0.3 and 4 K of the conductance across the contacts of miniature gold-plated electrical connectors, insulated copper wires varnished to a copper mounting, and its copper mounting bolted to a copper support.

Cook, R. K., **The use of modulated reverberation for measurement of absorption and sound power,** (Proc. 1973 National Noise Control Engineering Conf., Washington, D. C., Oct. 15-17, 1973), Paper in *Noise-Con 73 Proceedings*, D. R. Tree, Ed., pp. 303-308 (Institute of Noise Control Engineering, Noise/News, Poughkeepsie, N.Y., Oct. 1973).

Key words: Noise control; acoustical measurement; sound power.

A source of sound power modulated in amplitude 100 percent at a very low sinusoidal frequency F is introduced into a reverberation chamber. The total acoustical energy in the sound field will have an amplitude modulation at the same frequency F, but lagging in phase by ϕ due to the absorption in the chamber. An analysis of the differential equation for energy and sound power balance yields (1) the absolute cross-section A for absorption, and (2) the time-averaged absolute sound power W_o of the source. Measurements A and W_o have been made at various audio frequencies in the 425 m^3 reverberation chamber of the Bureau. The modulated source of sound power was electroacoustical—an array of four loudspeakers having their audio input voltage waveforms amplitude-modulated at $F = 0.1$ to 0.4 Hz. The sound pressure $|p^2|$ was measured with an array of four microphones. The phase ϕ was obtained by means of an analog computer based on a least squares principle of design. For a steady source of sound power, e.g., a noisy machine, a modulated sound field can be produced by modulating (as a function of time) the absorption cross-section of the reverberation chamber. We present the analysis for energy and sound power balance, and examine some methods for achieving modulated absorption cross-sections.

Corley, D. M., **Test of a proposed method for vehicle noise measurement,** (Proc. 1973 National Noise Control Engineering Conf., Washington, D. C., Oct. 15-17, 1973), Paper in *Noise-Con 73 Proceedings*, D. R. Tree, Ed., pp. 230-235 (Institute of Noise Control Engineering, Noise/News, Poughkeepsie, N.Y., Oct. 1973).

Key words: Noise source level; sound pressure level; truck tire; directivity.

If a spherical pulsating source radiates into a infinite medium, the sound pressure is inversely proportional to the distance from the source. No real source exactly fulfills these conditions but it is generally assumed that far enough away from the source, spherical spreading will result. It has been proposed [Hixon, Inter-Noise 72, Washington, D.C.] that a measurement independent of distance results if both sound pressure level and distance from the source are monitored and the sound pressure level is normalized to a constant distance, e.g., 1 meter, from the source. This measurement is deemed Noise Source Level. Data exist for tires which can indicate the merit of this approach [W. Leasure et al, DOT-OST-ONA 71-9]. These data consist of sound pressure level and distance from the source simultaneously monitored as unpowered trucks coast past an array of microphones. The A-weighted Noise Source Level from three types of truck tires with tread designs representative of tread patterns in common use today are presented. It is concluded that spherical spreading is generally not the case even 500 feet from the source. The r-dependence is not satisfactorily removed by this method of analysis. Therefore considerable care should be exercised if Noise Source Level is used to characterize truck tire noise levels. Noise Source Level does appear to be useful for presenting source directivity.

Currie, L. A., **The evaluation of radiocarbon measurements and inherent statistical limitations in age resolution,** (Proc. 8th International Conference on Radiocarbon Dating, Wellington, New Zealand, Oct. 18-25, 1972), Paper in *Proceedings 8th International Conference on Radiocarbon Dating*, T. A. Rafter and T. Grant-Taylor, Eds., **2,** 598-611 (Royal Society of New Zealand, Wellington, New Zealand, 1973).

Key words: Age resolution; extraneous random errors; factor of merit components; method performance characteristics; minimum and maximum detectable ages; radiocarbon dating; statistical limitations.

A uniform approach, based upon the statistical behavior of random measurement errors, is suggested for assessing the relative merit of alternative methods of measuring radiocarbon and for interpreting and reporting the results of such measurements. The need for an objective, uniform approach is manifest because of the increasing concern with results which are close to the limits of precision or detection of the dating procedures.

The standard deviation of the estimated net signal (sample counts) is first examined in terms of its dependence upon random errors arising in observations of background and gross sample counts. Because of the high precision characterizing such observations, it becomes vital to evaluate random errors additional to the Poisson (counting) errors. The ability to discriminate between samples of similar age, and minimum and maximum detectable ages are discussed in terms of the statistical theory of hypothesis testing. An explicit approach results for the uniform treatment of detection, detectability and age limits.

The performance characteristics of alternative measurement methods cannot simply be stated in terms of a single "figure of merit," because of the rather complex dependence upon counting times, sample, background and modern standard counting rates, and non-Poisson sources of random errors. A "reduced activity" (sample activity/background equivalent activity) plot is offered as a means for planning experiments and for rapidly assessing the capabilities of any specific measurement procedure. As a result of the particular choice of variables for this plot, alternative procedures may be represented

by points in a fixed, two-dimensional array, where simple translations of the entire array correspond to changes in counting time or sample age.

Davis, D. D., Klemm, R. B., Braun, W., Pilling, M., **A flash photolysis-resonance fluorescence kinetics study of ground-state sulfur atoms. II. Rate parameters for reaction of $S(^3P)$ with C_2H_4,** *Int. J. Chem. Kinet.* **4,** 383-394 (1972).

Key words: Chemistry; ethylene; flash-photolysis; kinetics; resonance-fluorescence; sulfur atoms.

Absolute rate constants for the reaction of $S(^3P)$ with ethylene were measured over an ethylene concentration range of 7, a total pressure of 50 to 400 torr, and a flash intensity range of 10. At 298 °K, the bimolecular rate constant was found to be invariant over this range of variables and had a measured value of 4.96×10^{-13} cm^3 molec^{-1} s^{-1}. Over the temperature range of 218° to 442 K, the rate data could be fit to a simple Arrhenius equation of the form

$$k_1 = (7.13 \pm 0.74) \times 10^{-12} \exp\left(\frac{-1.58 \pm 0.08 \text{ kcal/mole}}{RT}\right).$$

Units are cm^3 molec^{-1} s^{-1}. The dependence of the measured value of k_1 on the concentration of the reaction product ethylene episulfide is discussed.

deWit, R., **Continuous distribution of disclination loops,** *Phys. Status Solidi (a)* **18,** 669-681 (Aug. 1973).

Key words: Burgers vector; continuous defect distribution; disclination; dislocation; distortion elasticity; Frank vector; loop; plasticity.

Kroupa's theory of a continuous distribution of dislocation loops is extended to include disclination loops. The relation of the loop densities to the plastic strain and bend-twist are derived. This provides the connection with the theory of the continuous distribution of dislocations and disclinations. Mura has recently introduced the new concepts of "plastic distortion" and "plastic rotation," and they are identified in this paper as the dislocation- and disclination-loop density tensors. The significance of these quantities for a finite loop is discussed.

Dickens, B., Prince, E., Schroeder, L. W., Brown, W. E., **$Ca(H_2PO_4)_2$, a crystal structure containing unusual hydrogen bonding,** *Acta Crystallogr.* **B29,** Part 10, 2057-2070 (Oct. 1973).

Key words: Calcium phosphate; centered hydrogen bonds; hydrogen bonding; single crystal neutron diffraction; single crystal x-ray diffraction.

$Ca(H_2PO_4)_2$ crystallizes in the triclinic unit cell $a = 7.5577$ (5), $b = 8.2531$ (6), $c = 5.5504$ (3) Å, $\alpha = 109.87$ (1)°, $\beta = 93.68$ (1)° and $\gamma = 109.15$ (1)° at 25 °C with $Z = 2$. The structure was determined by an automated Σ_2 method from x-ray data and refined by least-squares analysis to $R_w(F) = 0.048$, $R(F) = 0.020$ using 3678 observed x-ray data and to $R_w(F) = 0.055$, $R(F) = 0.048$ using 843 observed neutron data. Corrections were made for absorption, isotropic secondary extinction and anomalous dispersion in the x-ray case and for anisotropic secondary extinction in the neutron case. Least-squares refinements proceeded to the limits of the data sets in space group $P\bar{1}$. Rudimentary chains $Ca\cdots[P(1)O_4]-H(1)\cdots[P(2)O_4]\cdots$ run parallel to $[1\bar{1}0]$. Adjacent chains are joined by Ca...O bonds on one side and by O(8)–H(5)–O(8′) hydrogen bonds on the other. Alternatively, the structure may be considered to contain hydrogen-bonded layers of PO_4 groups; these layers are held together by hydrogen bonds on one side and by Ca···O bonds on the other. There are two very strong hydrogen bonds in the structure; O(7)– –H(4)– –O(7′), O(7)···O(7′) = 2.434 (2) Å and O(8)– –H(5)– –O(8′), O(8)···O(8′) = 2.423 (2) Å. These hydrogen bonds join the $P(2)O_4$ groups together to form and infinite chain. The very strong hydrogen bonds are across nominal centers of symmetry, and diffraction results indicate that each of the H(4) and H(5) protons is effectively centered in a broad symmetric potential well, possibly with a central barrier. A combination of diffraction and infrared spectral considerations suggests that the central barriers in the wells, if they exist, probably lie below the zero-point energy of the hydrogens.

Domalski, E. S., **Selected values of heats of combustion and heats of formation of organic compounds containing the elements C, H, N, O, P, and S,** *J. Phys. Chem. Ref. Data* **1,** No. 2, 221-277 (1972).

Key words: CHNOPS compounds; heat of combustion; heat of formation; selected values.

Selected values of the heats of combustion and heats of formation of 719 organic compounds are reported here. The data tabulated pertain to compounds containing the elements carbon, hydrogen, nitrogen, oxygen, phosphorus, and sulfur (CHNOPS). The information is arranged according to classes of compounds and within each class, compounds are arranged by empirical formula. The general classes covered are: hydrocarbons, alcohols, phenols, polyols, ethers, aldehydes, ketones, acids, acid anhydrides, esters, steroids, lactones, carbohydrates, heterocyclic oxygen compounds, amines, amides, urea derivatives, guanidine derivatives, amino acids, peptides, alkaloids, heterocyclic nitrogen compounds, porphyrins, organic sulfur compounds, and organic phosphorus compounds. When a selection was made from among several investigators, commentary is provided to indicate the choice, and usually some relevant data. The number of references cited is 596. An alphabetical compound index is provided which gives the name, page number, empirical formula, and the Wiswesser Line Notation (WLN), for each compound.

Drullinger, R. E., Zare, R. N., **Optical pumping of molecules II. Relaxation studies,** *J. Chem. Phys.* **59,** No. 8, 4225-4234 (Oct. 15, 1973).

Key words: Molecules; optical pumping.

The ($v'' = 3$, $J'' = 43$) level of Na_2 has been optically aligned using the 4880-Å line of a cw argon ion laser as a light source. The relaxation of this alignment is measured upon addition of foreign gas. In a low-pressure regime, where the mean free path exceeds the diameter of the light beam which both pumps and samples the alignment, the relaxation of the alignment versus pressure shows a "dog-leg shape" consisting of two linear regions. The first linear region corresponds to both elastic (velocity-changing) and inelastic (primarily rotational transfer) collisional relaxation whereas the second corresponds purely to inelastic collisional relaxation. The former process is dependent on the mode structure of the laser and shows saturation with increased pressure. In this low-pressure regime, the measured cross sections are shown to be lower bounds to the true cross sections and excitation by a multimode laser is shown to be inequivalent to excitation by a white light source when the width of the holes in the velocity distribution of the absorber molecules are nonoverlapping.

Erez, A., **Low-frequency electrical signal measurement by electrooptical methods,** *IEEE Trans. Instr. Meas.* **IM-21,** No. 4, 358-360 (Nov. 1972).

Key words: Electrooptical coupling; feedback amplifiers; light emitting diodes; photodetectors.

An analog system for the optical telemetry of voltage or current information using light-emitting diodes (LED) is described. Errors resulting from variations in the optical coupling efficiency are minimized because the light emitted by the LED contains the signal to be measured superimposed on a fixed intensity beam controlled by a reference zener diode. The nonlinearity of the LED is overcome by using part of its emitted light to control the feedback current of an operational amplifier that supplies the signal to the LED. The prototype system developed has a total error of approximately 0.2 percent of the input signal.

Ferguson, E. E., Fehsenfeld, F. C., Phelps, A. V., **Comment on photodetachment cross sections for CO_3^- and its first hydrate,** *J. Chem. Phys.* **59,** No. 3, 1565-1566 (Aug. 1, 1973).

Key words: CO_3^-; negative ions; photodetachment cross section; photodissociation.

Burt recently reported the photodetachment threshold energies for $CO_3^- + h\nu \rightarrow CO_3 + e$ and $CO_3^- \cdot H_2O + h\nu \rightarrow CO_3 \cdot H_2O + e$ to be 1.8 and 2.1 eV, respectively. It can be shown from previously established thermochemistry that these reported threshold energies are substantially too low unless the dissociation energy $D(CO_2 - O)$ is much larger (> 1.5 eV) than has been previously reported.

Flatto, L., Haber, S., **A quadrature formula of degree three,** *J. Approximation Theory* **9,** No. 1, 44-52 (Sept. 1973).

Key words: Hilbert basis; integration; invariants; multiple integrals; numerical integration; quadrature; reflection groups; symmetric groups; symmetries.

Let R be a region in n-space and Q a linear quadrature formula for R of the form

$$Q(f) = \sum_{r=1}^{k} a_r f(x_r).$$

It is known that if $Q(f) = \int_R f$ whenever f is a polynomial of degree 3 or lower, then $k \geq n+1$. It is known that the minimum possible value of k depends on the region R, being $2n$ for the n-cube and $n+2$ for the n-simplex ($n > 1$). In 1956 Hammer and Stroud conjectured that $k \geq n + 2$ for every R, when $n > 1$. In this paper we construct an R, and a Q with the required property, with $k = n+1$.

Flynn, D. R., Leasure, W. A., Jr., **Machinery noise: Measurement standards and test codes,** (Proc. 1973 National Noise Control Engineering Conf., Washington, D.C., Oct. 15-17, 1973), Paper in *Noise-Con 73 Proceedings,* D. R. Tree, Ed., pp. 257-260 (Institute of Noise Control Engineering, Noise/News, Poughkeepsie, N.Y., Oct. 1973).

Key words: Acoustics; noise; soundpower.

Measurements of the sound power emitted by machinery, or of the sound pressure at specific locations, are needed for a variety of purposes. These include measurements for diagnostic and control purposes, measurements for labeling (explicitly or implicitly) the noise emission from a product, and measurements to determine compliance with specifications or regulations. A brief discussion is given of the general items which should be included in noise measurement standards and test codes. An example of standards addressing these points is the series of basic documents on sound power level measurements being prepared under the auspices of the International Organization for Standardization.

Gubser, D. U., Soulen, R. J., Jr., **Thermodynamic properties of superconducting iridium,** *J. Low Temp. Phys.* **13,** No. 3/4, 211-226 (1973).

Key words: Critical magnetic field; iridium; superconductivity; transition temperatures.

The superconducting transition temperature of pure Ir is found to be 0.1125 K (±0.0005 K). The critical magnetic field as a function of temperature $H_c(T)$ has also been measured. From these data it is determined that $H_c(O)$ is 16.00 G (1 G corresponds to 10^{-4} T), $(dH_c/dT)_{T=T_c}$ is 235 G/K, the linear coefficient of normal state electronic specific heat γ is 3.19 mJ/mole-K², and the energy gap anisotropy parameter $\langle a^2 \rangle$ is 0.048. This value for $\langle a^2 \rangle$ is the largest of any superconducting element so far observed, and its significance in determining the superconducting properties of Ir is discussed. By using the large supercooling effects noticed near T_c, the Ginzburg-Landau parameter χ_0 is found to be 8.6×10^{-3}. The effects of impurities on T_c and on the magnetic behavior of Ir are also discussed.

Haber, S., Shisha, O., **An integral related to numerical integration,** *Bull. Amer. Math. Soc.* **79,** No. 5, 930-932 (Sept. 1973).

Key words: Bounded variation; improper integral; monotonicity; numerical integration; quadrature; Reimann integral.

The question of the convergence of numerical integration formulas (of Riemann sum type) to the improper Riemann integral $\int_0^\infty f(x)dx$ is studied. A new integral over $[0,\infty)$, more restrictive than the improper Riemann integral but not absolutely convergent, is introduced. Necessary and sufficient conditions are found for a function to be integrable in the new sense; they are stated in terms of property of functions similar to the property of being of bounded variation. A convergence theorem for the numerical integration of such functions is given.

Hamer, W. J., Wu, Y-C., **Osmotic coefficients and mean activity coefficients of uni-univalent electrolytes in water at 25 °C,** *J. Phys. Chem. Ref. Data* **1,** No. 4, 1047-1099 (1972).

Key words: Activity coefficients; activity coefficients of uni-univalent electrolytes; excess Gibbs energy for electrolytes; experimental methods for determining activity coefficients; osmotic coefficients.

This paper gives values for the osmotic coefficients and mean activity coefficients of uni-univalent electrolytes in aqueous solutions at 25 °C. The values are expressed on the molality or weight basis. Literature data have, for the most part, been critically evaluated through the excess Gibbs energy, ΔG^{ex}, which relates the osmotic coefficient, ϕ, and the mean activity coefficient, γ, by the expression: $\Delta G^{ex} = 2\ m\ R\ T\ (1 - \phi + \ln \gamma)$ where m is molality, R the gas constant, and T the Kelvin temperature. General relations for chemical potentials, activities, activities coefficients and osmotic coefficients are presented and five experimental methods for determining activity coefficients are described.

Hampson, R. F., Editor, Braun, W., Brown, R. L., Garvin, D., Herron, J. T., Huie, R. E., Kurylo, M. J., Laufer, A. H., McKinley, J. D., Okabe, H., Scheer, M. D., Tsang, W., Stedman, D. H., **Survey of photochemical and rate data for twenty-eight reactions of interest in atmospheric chemistry,** *J. Phys. Chem. Ref. Data* **2,** No. 2, 267-311 (1973).

Key words: Atmospheric chemistry; chemical kinetics; data evaluation; gas phase reactions; optical absorption coefficients; photochemistry; quantum yields; rate constants.

Photochemical and rate data have been evaluated for twenty-eight gas phase reactions of interest for the chemistry of the stratosphere. The results are presented on data sheets, one per reaction. For each reaction, the available data are summarized. Where possible there is given a preferred value for the rate constant or, for the photochemical reactions, preferred values for primary quantum yields and optical absorption coefficients.

Hanley, H. J. M., Prydz, R., **The viscosity and thermal conductivity coefficients of gaseous and liquid fluorine,** *J. Phys. Chem. Ref. Data* **1,** No. 4, 1101-1113 (1972).

Key words: Fluorine; kinetic theory; modified Enskog Theory; thermal conductivity; viscosity.

Tables of values for the viscosity and thermal conductivity of fluorine are presented in the range 70-300 K for pressures up to 200 atmospheres. Dilute gas values were determined from Kinetic Theory using the m-6-8 potential. Dense gas and liquid values were obtained from the modified Enskog Theory. The critical point anomoly in the thermal conductivity coefficient is also discussed.

Hardy, S. C., Coriell, S. R., **Surface tension and interface kinetics of ice crystals freezing and melting in sodium chloride solutions,** *J. Cryst. Growth* **20,** 292-300 (1973).

Key words: Crystal growth; ice; interface kinetics; morphological stability; sodium chloride; surface tension.

Cylindrical ice crystals growing into supercooled 0.1 M sodium chloride solutions develop approximately sinusoidal perturbations parallel to the cylinder axis. Using a previously developed non-linear morphological stability theory, an analysis of the growth and melting rates of these perturbations yields values of the solid-liquid surface tension and linear interface kinetic coefficient. In contrast to previous results in 0.1 M hydrochloric acid solutions, the melting behavior in sodium chloride solutions is different from the growth behavior. From the growth data, the solid-liquid surface tension is 30 mJ/m^2 and the linear interface kinetic coefficient is 2.2×10^{-4} m/s K for solutions with pH > 6. For solutions with pH < 5.5 and for all solutions on melting, the kinetic coefficients is too large (> 10^{-3} m/s K) to measurably affect the perturbation velocities. From the melting data, the surface tension is 38 mJ/m^2. The difference in surface tension on melting and growth is attributed to ionic adsorption during growth. Experiments in which the crystal is grown in one solution and is melted in a different solution indicate that the surface tension depends on the chloride content of the ice.

Haynes, W. M., **Viscosity of gaseous and liquid argon,** *Physica* **67,** No. 3, 440-470 (Aug. 1973).

Key words: Argon; compressed gas and liquid; dilute gas; saturated liquid; torsional crystal viscometer; viscosity.

The coefficient of shear vicosity of fluid argon has been measured at temperatures from 85 to 298 K and at pressures up to 34 MN/m^2 using the torsional crystal viscometer. The precision and accuracy of these measurements were estimated to be 0.5 and 2 percent, respectively. A detailed description of the apparatus and experimental measuring techniques is presented. Viscosity data for the compressed gas were represented and analyzed using density expansions. An empirical relation was developed to represent the data over the entire fluid range as a function of density and temperature. Also included is a comprehensive comparison of the present results with previous experimental data and theoretical predictions.

Hayward, E., Barber, W. C., Sazama, J., **Nuclear scattering of plane-polarized photons,** *Phys. Rev. C* **8,** No. 3, 1065-1073 (Sept. 1973).

Key words: Dynamic collective model; giant resonance; nuclear surface oscillations; photon scattering; polarized photons; tensor polarizability.

A beam of plane-polarized monochromatic photons has been produced by the resonance fluorescence of the well-known 1^+ state at 15.1 MeV in ^{12}C. These have been scattered a second time from natural targets of Cd, Sn, Ta, W, Pt, Au, and Bi. Measurements were made with poor energy resolution of the relative number of photons scattered at 90° parallel and perpendicular to the polarization vector in the incident 15.1-MeV beam. The observation of photons scattered along the polarization vector reflects the contribution of incoherent scattering to the dominant coherent-scattering process and results either from permanent nuclear deformation or from the dynamic deformation produced by the coupling of the giant dipole resonance with the quadrupole oscillations of the nuclear surface. The observed intensities of incoherent scattering are of the same order of magnitude for the deformed nuclei and the spherical vibrators and agree roughly with the predictions of the dynamic collective model. No incoherent scattering was observed from the rigid sphere ^{209}Bi.

Hebner, R. E., Jr., Cassidy, E. C., **Measurement of 60 Hz voltages using the Kerr effect,** *Rev. Sci. Instrum.* **43,** No. 12, 1839-1841 (Dec. 1972).

Key words: Electrical measurements; electro-optics; high voltage measurements; Kerr effect; laser applications; optical techniques.

The Kerr effect has been used to measure 60 Hz alternating voltage up to 30 kV peak. The system behaves much as it does under the influence of a short high-voltage pulse except that in this case the frequency of the applied voltage is sufficiently low that the space charge effects in the liquid are not negligible.

Helminger, P., De Lucia, F. C., Kirchhoff, W. H., **Microwave spectra of molecules of astrophysical interest. IV. Hydrogen sulfide,** *J. Phys. Chem. Ref. Data* **2,** No. 2, 215-223 (1973).

Key words: Hydrogen sulfide; hyperfine structure; interstellar molecules; microwave spectra; molecular parameters; radio astronomy; rotational transitions.

The available data on the microwave spectrum of hydrogen sulfide are critically reviewed for information applicable to radio astronomy. Molecular data such as rotational constants, centrifugal distortion constants, hyperfine coupling parameters, and dipole moments are tabulated. A detailed centrifugal distortion calculation has been carried out for the most abundant isotopic form of this molecule, $H_2{}^{32}S$, as well as for $HD^{32}S$. Transitions have been predicted and tabulated for the frequency range 1 MHz to 1000 GHz for $H_2{}^{32}S$ and 1 MHz to 700 GHz for $HD^{32}S$. All predicted transitions include 95 percent confidence limits; estimated error limits have been reported for all measured transitions. Observed transitions of $H_2{}^{33}S$ and $H_2{}^{34}S$ are also listed.

Hougen, J. T., **A modified ladder operator formalism for molecule-fixed components of the total angular momentum operator in linear molecules,** *J. Mol. Spectrosc. Notes* **48,** No. 3, 609-611 (Dec. 1973).

Key words: Commutation relations; Eulerian angles; ladder operators; linear molecules; molecule-fixed components; total angular momentum.

Because molecule-fixed components of the total angular momentum operator for linear molecules do not obey angular momentum commutation relations (either with or without the anomalous sign of i), the traditional angular momentum ladder operator formalism cannot be applied. It is known that this difficulty can be overcome by introducing into the linear molecule problem an extra rotational angle, which has no physical significance, but which does lead to a formalism isomorphic with the normal formalism for nonlinear molecules. It is shown that the linear molecule angular-momentum problem is susceptible to treatment, without introduction of an extraneous variable, by a relatively straightforward extension of the conventional formalism, in which angular momentum operators are taken to be functions of an integral or half-integral parameter representing the projection of the total angular momentum along the linear axis.

Hummer, D. G., Seaton, M. J., **Interpretation of the spectra of planetary nebulae.** Introductory Report, *Mem. Soc. Roy. Sci. Liege* **V,** 225-238 (1973).

Key words: Forbidden lines; nebular spectra; planetary nebulae; recombination spectra.

Progress since 1967 in the interpretation of nebular spectra is reviewed.

Hunt, C. M., **An analysis of roll filter operation based on panel filter measurements,** *ASHRAE Trans.* **78,** Part 2, 227-234 (1972).

Key words: Air conditioning filters; air filters; particulate filters; roll filters.

The pressure drop across an air filter can usually be expressed as a linear function of the face velocity in a log-log plot. This is true for both clean and dirty filters. Use of this fact has been made to develop a descriptive model to predict the dust holding capacity of a roll filter from parameters measured with a panel filter of the same medium when the movement of the roll filter is controlled by a pressure switch. The model is applied to some test data obtained with a panel filter to explore the possible effect of varying pressure switch

settings, air velocity, and other parameters on the predicted performance of a roll filter.

Iverson, W. P., **The corrosion of mild steel by a marine strain of *Desulfovibrio*,** (Proc. 3d Int. Congress on Marine Corrosion and Fouling, Gaithersburg, Md., Oct. 2-6, 1972), Paper in *Proceedings: Third International Congress on Marine Corrosion and Fouling*, pp. 61-82 (Northwestern University Press, Evanston, Ill., Oct. 1973).

Key words: Anaerobic corrosion; depolarizing agent; ferrous ions; marine corrosion; *marine Desulfovibrio*; polarization techniques.

A marine strain of *Desulfovibrio* was isolated from steel piling detritus at Dam Neck, Va. A medium which provided good surface growth on 2 percent agar plates in a hydrogen atmosphere was developed (Trypticase, 15 gm; Phytone, 5 gm; NaCl, 5 gm; seawater, 1000 ml). The corrosion rate of mild steel in this medium, with and without the addition of Fe^{++} ions, was investigated using polarization techniques. In the absence of added Fe^{++} ions, the corrosion rate was found to decrease and then either increase or remain at a low level. In one corrosion cell a high rate of corrosion was accompanied by the formation of a corrosion product or products in the shape of "stalactite" formations. Analysis indicated free sulfur and an iron sulfur compound with iron in the Fe^{+++} state.

In the presence of added Fe^{++} ions, the corrosion rate was found to increase to 255 mdd in one corrosion cell and then decrease. Chemically prepared FeS produced little change in the potential or the corrosion rate. Corrosion of mild steel in a bacteria-free culture filtrate, to which Fe^{++} ions were added in excess to remove the $S^{=}$ ions was extremely high. After an induction period of 3 days, the corrosion rate increased to a maximum of 1130 mdd 8 days after the start of the corrosion process. During the period of extensive corrosion, the potential of the steel dropped to more noble values.

When the black precipitate, formed upon the addition of Fe^{++} ions, was removed, the resulting filtrate was still highly corrosive, indicating that the depolarizing agent was water soluble and not the precipitate. The depolarizing agent appears to act as an electron carrier, removing electrons from the iron and transferring them to an acceptor which is thereby reduced. The action of this depolarizing agent could account for the high anaerobic corrosion rates observed in the field.

Inhibition of corrosion in cultures of *Desulfovibrio* appears to be due to the action of H_2S which reacts with the iron to form a protective film and prevents the actions of the soluble depolarizer.

Jacob, E. J., Lide, D. R., Jr., **Structural implications of the microwave spectrum of hexafluoropropene,** *J. Chem. Phys.* **59,** No. 11, 5877-5881 (Dec. 1, 1973).

Key words: Ground vibrational state; microwave spectrum of hexafluoropropene; rotational constants.

Analysis of the microwave spectrum of hexafluoropropene, C_3F_6, has yielded rotational constants for the ground vibrational state of 2557.88, 1255.033, and 987.082 MHz. Assignments have also been made on the first four excited states of the CF_3 torsional mode and on the first excited state of another low-lying skeletal mode. A rough estimate of 350 cm^{-1} has been obtained for the barrier to internal rotation of the CF_3 group. The ground-state moments of inertia are consistent with the expected geometry of the molecule, in which all atoms are coplanar except for two equivalent F atoms in the CF_3 group.

Jacox, M. E., Milligan, D. E., **Matrix-isolation study of the reaction of H atoms with NO. The infrared spectrum of HNO,** *J. Mol. Spectrosc.* **48,** No. 3, 536-559 (Dec. 1973).

Key words: Force constants; H + NO reaction; HNO; infrared spectrum; matrix isolation; thermodynamic properties.

Studies of the reaction with NO in an argon or a nitrogen matrix at 4° or 14 K of H and D atoms produced either photolytically or in a microwave discharge have confirmed the previous identification of the ground-state NO stretching fundamental of HNO and of DNO but have dictated a reassignment of the deformation fundamental of these two species. An absorption at 1153 cm^{-1} has been assigned as the deformation fundamental of DNO, and evidence is presented suggesting that the deformation fundamental of HNO lies very close to 1500 cm^{-1}. The assignment of an absorption at 2717 cm^{-1} as the NH stretching fundamental of HNO and of an absorption at 2043 cm^{-1} as the corresponding fundamental of DNO is consistent with the previous report of an exceptionally long NH bond for ground-state HNO. Detailed isotopic studies support this revised vibrational assignment, which is shown to be consistent with previous gas-phase studies. The force constants and thermodynamic properties of ground-state HNO derived from the matrix data are presented.

Jennings, D. A., Braun, W., Broida, H. P., **Vibrational relaxation of hydrogen by direct detection of electronic and vibrational energy transfer with alkali metals,** *J. Chem. Phys.* **59,** No. 8, 4305-4308 (Oct. 15, 1973).

Key words: Apparatus; energy transfer; metals; method; photochemistry; resonance fluorescence; vibrational relaxation.

A technique has been developed to measure the rate constant for vibrational relaxation of $H_2^{v=3,4}$ by $H_2^{v=0}$. The technique uses a mechanically chopped, tunable, cw dye laser coincident with either of the Na resonance lines at 589.6 or 589.0 nm. Sodium vapor is contained in a glass cell along with Cs atoms and H_2. Sodium atoms, excited by the dye laser radiation, collisionally transfer electronic energy to H_2 producing some H_2^v. Only vibrational energy in H_2^v from levels $v = 3,4$ can transfer to Cs as electronic energy and cause Cs resonance line emission at 894 and 852 nm. In this manner, using the observed emission as a detector of $H_2^{v=3,4}$, the vibrational relaxation rate constant was determined to be 3.9×10^{-14} cm^3 sec^{-1}. Similar rate constants were measured, with somewhat less accuracy, for D_2^v colliding with D_2 and for H_2^v colliding with He. It was found that N_2, Na, and Cs also undergo electronic to vibration and vibration to electronic energy exchange.

Johnson, C. R., **A Geršgorin inclusion set for the field of values of a finite matrix,** *Proc. Amer. Math. Soc.* **41,** No. 1, 57-60 (Nov. 1973).

Key words: Eigenvalues; field of values; Geršgorin set; numerical radius; spectrum; subadditive set valued function.

An easily computed Geršgorin type inclusion set for the field of values of an n by n complex matrix is presented. Some functional properties of this inclusion set parallel those of the field of values, and illustrative examples are given.

Johnson, D. R., Lovas, F. J., Kirchhoff, W. H., **Microwave spectra of molecules of astrophysical interest. I. Formaldehyde, formamide, and thioformaldehyde,** *J. Phys. Chem. Ref. Data* **1,** No. 4, 1011-1045 (1972).

Key words: Formaldehyde; formamide; interstellar molecules; microwave spectra; molecular parameters; radio astronomy; rotational transitions.

The available data on the microwave spectrum of formaldehyde, formamide, and thioformaldehyde is critically reviewed for information applicable to radio astronomy. Molecular data such as rotational constants, centrifugal distortion parameters, dipole moments, hyperfine coupling constants, and structural parameters are tabulated. Observed rotational transitions are presented for the astronomically interesting isotopic forms of these molecules when available. Detailed centrifugal distortion calculations have been carried out for the most abundant isotopic forms of these molecules, namely, $H_2{}^{12}C^{16}O$, $H_2{}^{13}C^{16}O$, $^{14}NH_2{}^{12}CH^{16}O$, and $H_2{}^{12}C^{32}S$. Transitions have been predicted and tabulated for the frequency ranges

1 MHz to 300 GHz for $H_2{}^{12}C^{16}O$,

100 MHz to 300 GHz for $H_2{}^{13}C^{16}O$,

500 MHz to 180 GHz for $^{14}NH_2{}^{12}CH^{16}O$,

and

100 MHz to 300 GHz for $H_2{}^{12}C^{32}S$.

All predicted transitions include 95 percent confidence limits; measured transition error limits have been reproduced from the original literature. References are given for all data included.

Johnson, V. J., **Thermodynamic and transport properties of cryogenic propellants and related fluids,** (Proc. American Society for Testing and Materials Symp. on Cryogens and Gases: Testing Methods and Standards Development, Los Angeles, Calif., June 25-30, 1972), *Amer. Soc. Test. Mater. Spec. Tech. Publ.* **537,** pp. 64-78 (1973).

Key words: Argon; bibliography; compilations; critical evaluation; cryogens; experimental measurement; fluorine; helium; hydrogen; methane; nitrogen; oxygen; properties of fluids; review; thermodynamic.

Significant advances have been made in recent years in the quality and range of thermophysical data for the cryogenic propellants, pressurants, and inertants. These advances have resulted from improved evaluation and compilation techniques coupled with better and more extensive experimental data and from a better theoretical understanding of the physical properties of gases. A review of recently completed and current data compilation projects for helium, hydrogen, argon, nitrogen, oxygen, fluorine, and methane will be given as well as recommended references for thermodynamic and transport property data tables for these fluids. Modern techniques in the plotting of thermodynamic charts from tabular data (or from functions such as the equation of state) have greatly improved their precision and value. A list of such charts is included.

Julienne, P. S., **Nonadiabatic effects in the B, C, B', and D states of H_2,** *J. Mol. Spectrosc.* **48,** No. 3, 508-529 (Dec. 1973).

Key words: Λ-doubling; heterogeneous interaction; molecular hydrogen; nonadiabatic; pure precession; RKR potentials.

The Kolos-Wolniewicz potentials for the H_2 $B^1\Sigma_u^+$ and $C^1\Pi_u$ states were used together with the hypothesis of pure precession for the rotation-electronic interaction, to calculate the nonadiabatic energy levels of these states for $J=1$ to 5. The complete coupling matrix was computed using accurate numerical vibrational wavefunctions. The calculated Λ-doubling of the $v=0$ to 12 C vibrational levels generally agrees well with experimental values, and the nonadiabatic shifts in the B rotational constants qualitatively explain the difference between the theoretical and RKR potentials for this state.

The interaction of the B' $^1\Sigma_u^+$ and D $^1\Pi_u$ states was also investigated, but only qualitatively since adiabatic potentials of sufficient accuracy do not exist for these states. The Λ-doubling of the $Dv=0$ rotational levels agrees well with the experimental values. An appreciable "background" nonadiabatic shift in the B' rotational constants was found. This shift, which is nearly 5 percent of B_v, is in addition to that of strong local two-level interactions and was not "deperturbed" in constructing the B' RKR potential. The result is that the RKR turning points differ by about 0.04 au from the "true" adiabatic turning points. This conclusion is supported by a Hartree-Fock calculation of the B' potential to the left of R_e.

Kearsley, E. A., **Measurement of normal stress by means of hole pressure,** *Trans. Soc. Rheol.* **17,** No. 4, 617-628 (1973).

Key words: Hole pressure; normal stress; pressure hole errors; shearing flows.

A measurement of normal stress differences in a shearing elastic liquid is accomplished through direct measurement of hole pressure. Gravity flow down an inclined channel is used and hole pressure is measured for slots perpendicular and parallel to the flow, as well as for a circular hole. The first and second normal stress differences are calculated under the assumption of second-order fluid behavior. Dynamic data are compared and a discrepancy noted.

Keller, R. A., **Tunable lasers for chemists,** *Chem. Technol.*, 626-634 (Oct. 1973).

Key words: Dye laser; isotope separation; photochemistry; review; saturation spectroscopy; spectroscopic analysis.

A general review of organic dye lasers and their use in the fields of: analytical chemistry, chemical synthesis and separation, photobiology, and spectroscopy is presented. The text includes 47 references.

Keller, R. A., Simmons, J. D., Jennings, D. A., **Enhancement of absorption spectra by dye-laser quenching, III: Quantitative aspects and a comparison of flash-lamp-pumped and cw systems under high resolution,** *J. Opt. Soc. Amer.* **63,** No. 12, 1552-1555 (Dec. 1973).

Key words: Dye laser; intra-cavity absorption; iodine detection; laser quenching; trace absorption detection; visible molecular absorption.

The enhancement of the detectability for trace absorptions by placing samples inside the laser cavity was found to be a factor of 100 for a flash-lamp-pumped dye laser and one thousand for a cw dye laser. High-resolution spectra showed that the holes in the laser output were as narrow as the absorptions that caused them. An approximately linear relationship (rather than the step-function behavior often associated with threshold phenomena) exists between pressures necessary to produce visually identical absorption spectra from samples placed inside and outside of the laser cavity. If such a relationship is of general occurrence, it will greatly facilitate the use of intracavity absorption for quantitative analysis, determination of relative absorption cross section, and for the study of the kinetics of appearance and disappearance of transient species.

Kirchhoff, W. H., Johnson, D. R., Lovas, F. J., **Microwave spectra of molecules of astrophysical interest II. Methylenimine,** *J. Phys. Chem. Ref. Data* **2,** No. 1, 1-10 (1973).

Key words: Hyperfine structure; interstellar molecules; methylenimine; microwave spectra; molecular parameters; radio astronomy; rotational transitions.

The available data on the microwave spectrum of methylenimine are critically reviewed for information applicable to radio astronomy. Molecular data such as rotational constants, centrifugal distortion parameters, hyperfine coupling constants, and dipole moments are tabulated. A detailed centrifugal distortion calculation has been carried out for the most abundant isotopic form of this molecule, $H_2{}^{12}C^{14}NH$. Transitions have been predicted and tabulated for the frequency range 100 MHz to 300 GHz. All predicted transitions include 95 percent confidence limits; error limits have been reported for all measured transitions.

Kirchhoff, W. H., Johnson, D. R., Powell, F. X., **Centrifugal distortion effects in SF_2: Calculation of the force field and infrared spectrum,** *J. Mol. Spectrosc.* **48,** No. 1, 157-164 (Oct. 1973).

Key words: Centrifugal distortion; force field; microwave spectrum; SF_2; structure; vibrational fundamental.

Measurements of the microwave spectrum of SF_2 have been extended up to $J=43$ in order to account for the effects of centrifugal distortion. Seventy-five transitions have been included in a weighted least squares fit of the measured spectrum with an rms deviation of 0.078 MHz. The force field for SF_2 has been determined from the centrifugal distortion constants. The vibrational spectrum, as yet unob-

served, has been predicted from the force field as have been the Coriolis coupling constants and the average structure.

Krupenie, P. H., **The spectrum of molecular oxygen,** *J. Phys. Chem. Ref. Data* **1,** No. 2, 423-534 (1972).

Key words: Molecular oxygen; molecular spectrum; review.

This is a critical review and compilation of the observed and predicted spectroscopic data on O_2 and its ions O_2^-, O_2^+, and O_2^{2+}. The literature survey upon which it is based was terminated in February 1971.

Leasure, W. A., Jr., **Automobile tire noise: A review of the open literature,** (Proc. 1973 National Noise Control Engineering Conf., Washington, D.C., Oct. 15-17, 1973), Paper in *Noise-Con 73 Proceedings,* D. R. Tree, Ed., pp. 187-195 (Institute of Noise Control Engineering, Noise/News, Poughkeepsie, N.Y., Oct. 1973).

Key words: Acoustics; automobile; noise (sound); tire noise; transportation noise.

Automobiles, the primary mode of transportation in the United States, contribute significantly to the noise environment due to the large number in operation. In this paper, one aspect of automobile noise is discussed, namely the contribution to overall vehicle noise made by the interaction of the tires with the road surface. For passenger cars, tire noise can be a significant contributor to overall levels at speeds as low as 35-40 mph and typically is the major contributor at higher speeds. Based on the limited data base available in the open literature, a discussion is given of the effects of various vehicle operational modes, tire mechanical properties, and road surface texture on the noise generated by passenger car tires. Both community noise and the noise heard by the occupants of the vehicle are considered. Possible noise generation mechanisms, although not well understood, are presented. Areas for future research and development are identified based on gaps in present knowledge.

Lees, R. M., Lovas, F. J., Kirchhoff, W. H., Johnson, D. R., **Microwave spectra of molecules of astrophysical interest. III. Methanol,** *J. Phys. Chem. Ref. Data* **2,** No. 2, 205-214 (1973).

Key words: Internal rotation; interstellar molecules; methanol; microwave spectra; molecular parameters; radio astronomy; rotational transitions; torsion.

The available data on the microwave spectrum of methanol is critically reviewed for information applicable to radio astronomy. Molecular data such as moments and product of inertia, torsional potential constants, centrifugal distortion and torsion-rotation-interaction constants, dipole moment, and structural parameters are tabulated. Observed rotational transitions are presented for the astronomically interesting isotopic forms of methanol when available. Detailed centrifugal distortion and torsion-rotation interaction calculations have been carried out for the most abundant isotopic form of methanol with transitions tabulated for the frequency range from 500 MHz to 200 GHz. Measured transition error limits have been reproduced from the original literature. References are given for all data included.

Leiss, J. E., **Future accelerators for photonuclear studies,** (Proc. Int. Conf. on Photonuclear Reactions and Applications, Pacific Grove, Calif., Mar. 26-30, 1973), Paper in *International Conference on Photonuclear Reactions and Applications,* B. L. Berman, Ed., pp. 1241-1248 (Ernest O. Lawrence Livermore Laboratory, University of California, Livermore, Calif., 1973). (Available as CONF-730301 from the National Technical Information Service, Springfield, Va. 22151).

Key words: Electron accelerators; linear accelerators; photonuclear physics; race track microtron; storage rings.

The status of electron accelerator developments and the need for new accelerators in photonuclear studies is discussed. The development of 100 percent duty cycle accelerators is identified as a major goal. Specific accelerators which would satisfy this goal are identified. The possibility of modifying existing facilities to enhance the application of photon activation analysis is given as an example of ways in which photonuclear applications can be encouraged.

Lide, D. R., Jr., Rossmassler, S. A., **Status report on critical compilation of physical chemical data,** *Annu. Rev. Phys. Chem.* **24,** 135-158 (1973).

Key words: Compilation; critical evaluation; data; NSRDS; physical chemistry; reference data; status report.

The significance of data evaluation and the importance of sources of reliable reference data are pointed out. A review is provided of major past and present data compilation activities of interest to physical chemists, including early efforts (before 1930); isolated programs in the period 1930-1960; the National Standard Reference Data System; other government and non-government programs; other national programs; and international programs. A rationale and discussion of methodology of data evaluation are presented with brief illustrations. Finally, three types of data sources are listed: systematic publication series, data centers, and recent compendia.

Liebman, J. F., **Regularities and relations among ionization potentials of nontransition elements,** *J. Chem. Educ.* **50,** No. 12, 831-834 (Dec. 1973).

Key words: Atoms; extrapolation; ionization potentials; nontransition elements; semiemphirical rules.

In this paper, we ask "How does the ionization potential vary with increasing atomic number?" and in addition inquire about higher ionization potentials. Five classes of semiempirical procedures are given, utilized and discussed. Two new procedures are introduced and found to be reliable.

Lovas, F. J., Johnson, D. R., **Reaction of BF_3 with NH_3: Microwave spectrum of BF_2NH_2,** *J. Chem. Phys.* **59,** No. 5, 2347-2353 (Sept. 1, 1973).

Key words: Aminodifluoroborane; dipole moment; gas-phase reaction; microwave spectrum; molecular structure; rotational transitions.

Microwave spectra assignable to gas phase aminodifluoroborane (BF_2NH_2) have been detected in the reaction of BF_3 with NH_3. A centrifugal distortion analysis has been carried out on the species $^{11}BF_2{}^{14}NH_2$ and $^{10}BF_2{}^{14}NH_2$. Distortion corrected rotational constants have also been obtained for $^{11}BF_2{}^{15}NH_2$, $^{10}BF_2{}^{15}NH_2$, $^{11}BF_2{}^{14}ND_2$, and $^{10}BF_2{}^{14}ND_2$. The molecule has been found to be planar with the following geometry: $r_{B-F} = 1.325(12)$Å, $r_{B-N} = 1.402(24)$Å, $r_{N-H} = 1.0029(18)$Å, $\angle FBF = 117.9(17)°$ and $\angle HNH = 116.94(30)°$. The observed dipole moment of BF_2NH_2 is $\mu = 2.595(30)$ D.

Lowke, J. J., Phelps, A. V., Irwin, B. W., **Predicted electron transport coefficients and operating characteristics of CO_2-N_2-He laser mixtures,** *J. Appl. Phys.* **44,** No. 10, 4664-4671 (Oct. 1973).

Key words: Attachment coefficient; CO_2 cross sections; CO_2 laser; electron distribution; electron transport; ionization coefficient.

Calculations have been made of transport coefficients of electrons in gas mixtures for ratios CO_2:N_2:He of 1:1:8, 1:2:3, 1:7:30, and 1:0.25:3. New cross sections for CO_2 derived from swarm experiments are used together with previously published cross sections for N_2 and He. Curves are presented of the predicted electron drift velocity, transverse and longitudinal diffusion coefficients, and ionization and attachment coefficients for E/N values ranging from 10^{-18} to 1×10^{-15} V cm^2; E is the electric field strength and N the gas number density. Examples are given of derived distribution functions and comparisons are made with a Maxwellian distribution function.

The percentage of the input electrical power which excites vibrational processes coupled to the 001 upper laser level of CO_2 is given as a function of E/N. The maximum efficiency from these calculations increases for increasing ratios of N_2:CO_2, because the proportion of energy used to excite the bending and stretching modes of CO_2 is then reduced. By assuming a recombination coefficient of 10^{-7} cm^3 sec^{-1}, the operating E/N for self-sustained glow discharges is predicted as a function of current density for various laser mixtures by equating the ionization rate to the attachment and recombination rate.

Martin, W. C., **Energy levels of neutral helium (^{4}He 1)**, *J. Phys. Chem. Ref. Data* **2**, No. 2, 257-265 (1973).

Key words: Atomic energy levels; atomic spectra; autoionization; electron scattering; fine structure; helium; photoionization resonances; photon absorption.

This compilation of all identified levels is based on the most accurate available observations. It includes 48 levels above the HE II $1\,^2S$ limit (two-electron excitation).

Mauer, F. A., Hubbard, C. R., Hahn, T. A., **Thermal expansion and low temperature phase transition of thallous azide**, *J. Chem. Phys.* **59**, No. 7, 3770-3776 (Oct. 1, 1973).

Key words: Bond method; phase transition; thallous azide; thermal expansion.

Thallous azide, TlN_3, is tetragonal at room temperature. It transforms at 248 ± 5 K to a phase that can be indexed on the basis of an orthorhombic cell. Lattice parameters of the tetragonal phase have been determined by the Bond single crystal method at intervals of approximately 25 K from 248 to 498 K. Single crystals do not survive the transition, so the parameters of the orthorhombic phase were measured by powder diffraction at intervals of 25 K down to 133 K. Representative parameters, after corrections for the effects of radiation damage, are $a = 6.2094$ Å, $c = 7.3583$ Å at 298.2 K for the tetragonal phase, and $a = 8.718$ Å, $b = 8.766$ Å, $c = 7.395$ Å at 238.2 K for the orthorhombic. Thermal expansion parameters show anomalies that are believed to be the result of changes in the orientation of azide ions. The linear expansion coefficients, α_a and α_c, for the tetragonal phase are both approximately 5.2×10^{-5} K^{-1} at the transition. By 486 K, α_c has increased to 21×10^{-5} K^{-1} and α_a has decreased to -1.2×10^{-5} K^{-1}. For the orthorhombic phase α_b remains constant at 5.2×10^{-5} K^{-1} while α_a increases from 10×10^{-5} K^{-1} to 22×10^{-5} K^{-1} and α_c decreases from -1.5×10^{-5} K^{-1} to -11×10^{-5} K^{-1} in the temperature range 150 to 225 K. There does not appear to be a discontinuity in the volume at the transition. The volume expansion coefficient is approximately 17×10^{-5} K^{-1} for the orthorhombic phase and 15×10^{-5} K^{-1} for the tetragonal.

McAlister, A. J., Dobbyn, R. C., Cuthill, J. R., Williams, M. L., **Soft x-ray emission spectra of metallic solids: Critical review of selected systems**, *J. Phys. Chem. Ref. Data* **2**, No. 2, 411-426 (1973).

Key words: Alloys; critical review; emission spectra; intermetallic compounds; metals; soft x-ray spectra.

Theory and experimental practice in the field of soft x-ray emission from metallic solids are briefly reviewed, and measurements on a number of systems are critically evaluated and compared with the results of other techniques and theory, with a view to establishing the pertinence of the soft x-ray measurements and indicating specific guidelines for enhancing their value.

McCulloh, K. E., **Photoionization of carbon dioxide**, *J. Chem. Phys.* **59**, No. 8, 4250-4259 (Oct. 15, 1973).

Key words: Carbon dioxide; CO^+; CO_2^+; dissociative ionization; O^+; photoionization.

The yields of photoions from CO_2 cooled to 150 K have been measured at a resolution of 0.22 Å for CO_2^+ and 0.4 Å for the O^+ and CO^+ fragments, in the photon energy region extending from onset for each species to approximately 20 eV. Most of the observed structure of the molecular ion yield curve recapitulates the well known features of the absorption spectrum, but a number of anomalies are reported. Autoionization peaks at photon energies just above the first molecular ionization limit of 13.773 ± 0.002 eV do not fit into a pattern characteristic of Rydberg series converging to excited vibrational levels of the ion. Although the Tanaka-Ogawa series and Henning's sharp series can be assigned as *ns* Rydberg series on the basis of quantum defects, the expected 3*s* members could not be observed in the present study. The most prominent feature of the O^+ yield curve is a step at 19.39 eV, suggesting that the principal mechanism for production of this fragment is predissociation of $CO_2^+(C\ ^2\Sigma_g^+)$ in its ground vibrational state. Completeness of this predissociation is inferred, although the proposed explanation involves doublet-quartet mixing at large bending angles. The structure of the O^+ yield curve between 19.07 and 19.39 eV suggests that Rydberg states converging to $CO_2^+(C)$ also undergo predissociation, with spontaneous ionization, to produce this fragment ion. Evidence pertaining to production of CO^+ fragments by predissociation of excited vibrational states of $CO_2^+(C)$ is also presented.

Mies, F. H., **Stimulated emission and population inversion in diatomic bound-continuum transitions**, *Mol. Phys.* **26**, No. 5, 1233-1246 (1973).

Key words: Continuum emission; lasers; line shapes; molecular spectroscopy; quantum chemistry; stimulated emission.

Exact expressions are derived for the rate of stimulated emission and the conditions for population inversion in a diatomic bound-continuum transition. The resultant formulae resemble those of a simple, homogeneously broadened, discrete transition with the Lorentzian lineshape replaced by a continuum lineshape, $g^C(h\nu = E_{v'} - \epsilon'')$, which is approximately equal to the square of the overlap between the initial, emitting, vibrational level v' and the final, energy-normalized continuum state ϵ'', i.e. $g^C \approx \langle v' | \epsilon'' \rangle^2$. Using the "reflection method," which is most applicable to a strongly repulsive final state, equations are obtained which allow simple, but accurate, estimation of the pertinent parameters which influence lasing action. Some general conclusions are extracted, and specific results are presented for the stimulated vacuum ultraviolet emission in high pressure Xe.

Moore, L. J., Moody, J. R., Barnes, I. L., Gramlich, J. W., Murphy, T. J., Paulsen, P. J., Shields, W. R., **Trace determination of rubidium and strontium in silicate glass standard reference materials**, *Anal. Chem.* **45**, No. 14, 2384-2387 (Dec. 1973).

Key words: Isotope dilution; mass spectrometry; rubidium; standards; strontium; trace analysis.

Procedures have been developed for the accurate trace analysis of Rb and Sr by mass spectrometric isotope dilution. A new Sr isotopic assay technique capable of measuring the three abundant Sr isotopes to < 0.05 percent (ts) was combined with recently available high purity reagents and absolute standards to produce accurate and reliable analytical techniques. Application of these techniques to the determination of Rb and Sr in silicate glass standard reference materials has resulted in accuracies within < 0.25 percent at the ppm (μg/g) level and within < 0.6 percent at the ppb (ng/g) level.

Mordfin, L., Robusto, R., Jr., **Plastic deformation characteristics of refractory metals above 3000 °F**, (Proc. 5th National Society for the Advancement of Material and Process Engineering Technical Conf., Kiamesha Lake, N.Y., Oct. 9-11, 1973), Paper in *Materials & Processes for the 70's* **5**, 378-393 (SAMPE, National Business Office, Azusa, Calif., Oct. 1973).

Key words: Evaluation; high temperature tests; molybdenum; plastic flow; Poisson ratio; refractory metals; strain hardening; strain rate; stress strain diagrams; tantalum; tensile properties.

Using a photographic strain-measuring technique, exploratory tensile tests were conducted to investigate the plastic behavior of unalloyed molybdenum and tantalum in the hot-working temperature range. Several unusual characteristics were observed, including serrated flow, a negative strain-rate sensitivity and, in one case, considerable strain hardening. These observations indicate a need for further research in this area, before hot-working processes for refractory metals can be made practical.

Morrissey, B. W., McCrackin, F. L., Stromberg, R. R., **Determination of distributions in inhomogeneous films,** *J. Colloid Interface Sci.* **42,** No. 1, 198-200 (Jan. 1973).

Key words: Attenuated total reflection; distributions; ellipsometry; inhomogeneous films.

The distribution of material in an inhomogeneous film is an important parameter in many problems. By representing the inhomogeneous film as a stack of thin homogeneous films, we have developed a method for utilizing concomitant ellipsometric and attenuated total reflection measurements to determine the distribution of films whose thickness can be modified stepwise. We have compared our method to that of Beckman and Harrick, using their data for SiH impurity within an SiO_2 film. For two distributions, an exponential and a Gaussian, our method produced good fits with an accuracy limited only by the incremental thickness used for the calculations. Application of the method of Beckmann and Harrick yielded less accurate results which can also show artificial minima in the distribution.

Nelson, C. A., Steele, D., **Symmetry relations among pionization cross sections,** *Phys. Rev. D* **8,** No. 9, 2908-2915 (Nov. 1, 1973).

Key words: Inclusive reactions; pionization region; quark model; Regge residue; SU(3); symmetry relations.

From Mueller's Regge analysis of the *pionization region*, symmetry relations to order $s^{-1/4}$ among invariant cross sections at $x=0$, in which a final pion is observed, are derived. SU(3) and quark universality are assumed to relate the Regge residues at the projectile-Reggeon vertex. There is good agreement with experiment to 10 — 15 percent indicating that the approximate symmetry pattern at nonasymptotic energies is that of total cross sections. The rising of the invariant cross sections to their asymptotic forms as $c - bs^{-1/4}$ can be understood in terms of *known* j-plane singularities if the f-Pomeron central vertex $g_{fp}{}^{\pi+}(q_\perp{}^2) < 0$. Symmetry relations valid for final kaons and nucleons and for both the pionization and the target-fragmentation regions are also given.

O'Connell, J. S., **Electromagnetic interactions of the few-nucleon systems,** *Proc. Seminar Electromagnetic Interactions of Nuclei at Low and Medium Energies, Moscow, U.S.S.R., Dec. 11-13, 1972*, pp. 299-309 (Dec. 1973).

Key words: Deuterium; electron scattering; helium-3; helium-4; photonuclear; weak interactions.

Recent progress on the photodisintegration electron scattering reactions on the hydrogen and helium isotopes is reviewed. The connection to weak interactions and the effect of meson dynamics on few-nucleon properties and reactions are discussed.

Plummer, E. W., **Electronic characterization of submonolayer films,** (Proc. Symp. on Monolayer and Submonolayer Helium Films, Stevens Institute, Hoboken, N.J., June 7-8, 1973), Paper in *Proceedings of Symposium on Monolayer and Submonolayer Helium Films*, J. G. Daunt and E. Lerner, Eds., pp. 157-160 (Plenum Press, New York, N.Y., 1973).

Key words: Electronic characterization; submonolayer films; surfaces; surface spectroscopy.

The complete characterization of a surface or a submonolayer film on a surface must specify the chemical identity of the atoms present, the geometrical or structural arrangement of these atoms, and the distribution in space and energy of electrons around these atoms. Various forms of electron emission spectroscopy are sensitive to the surface region, yet each technique has a different sensitvity and produces a different perturbation of the surface or adsorbed film. Several methods of probing the electronic properties of the surface and submonolayer films are described, and the advantages of each technique are discussed.

Post, M. A., **Liquid latex paint analysis,** *Paint Varnish Prod. Part 1,* **63,** No. 9, 21-25 (Sept. 1973); *Paint Varnish Prod. Part 2,* **63,** No. 10, 27-38 (Oct. 1973).

Key words: Acrylic; alkyd modified latex paints; deep-tone latex paints; infrared spectroscopy; polyvinyl acetate; styrene-acrylate; vinyl-acrylic; vinyl acetate-dibutyl maleate; vinyl acetate-ethylene; vinyl acetate-ethyl acrylate; vinyl acetate-2-ethyl-hexyl acrylate; vinyl chloride-acrylate.

The qualitative identification by infrared spectroscopy of latex resins, the quantitative determination of the latex resin and alkyd modifier in alkyd modified latex paints and of the latex resin in unmodified latex paints are discussed. Four procedures for latex resin identification and two methods for quantitative determination of the latex resin are presented. One of the quantitative methods can be used for any latex paint. The other, which is shorter is useful only for paints based on polyvinyl acetate, vinyl acetate-dibutyl maleate and vinyl-acrylic copolymers.

Rasberry, S. D., Heinrich, K. F. J., **Calibration for interelement effects in x-ray fluorescence analysis,** *Anal. Chem.* **46,** No. 1, 81-89 (Jan. 1974).

Key words: Calibration; empirical calibration; iron-nickel-chromium alloys; x-ray fluorescence; x-ray spectrochemical analysis.

A new empirical method for the calibration of x-ray fluorescence analysis in the presence of interelement effects is given. The effects of secondary fluorescence and of absorption are considered separately, with different expressions, in the calibration equation. The new approach is compared with empirical methods previously proposed by other authors, and is accurate and applicable over wide ranges of composition, even when the number of standards available is limited. An alloy system, in which the interelement effects are severe (Fe-Ni-Cr, over a range of composition from 0 to 100%), is studied experimentally; also evaluated are data, previously presented by other authors, for the calcium carbonate-silica system. With reference to 23 chemical determinations, in the two systems, the relative error is ± 1 percent or less in 13 instances and ± 4 percent or less in all but two determinations.

Reimer, G. M., Carpenter, B. S., **Thorium determination in glasses using fission track technique,** *Nature* **247,** 101-102 (Jan. 11, 1974).

Key words: Fast flux; fission track technique; thorium determination; Th/U ratio; track excess.

The fission track technique has been applied for the determination of thorium in glasses. Two irradiations are performed. The first is with a thermalized flux to determine the uranium content by fission of ^{235}U. The second irradiation is with a fast flux to induce fission of thorium in addition to uranium. By comparing track counts of both irradiations to a uranium standard, the "track excess" of the second irradiation is related to the thorium content. The accuracy is dependent on the Th/U ratio. The uncertainty for the Th/U ratio of 4 is approximately 20 percent and increases as the ratio decreases.

Romanoff, M., Gerhold, W. F., Schwerdtfeger, W. J., Iverson, W. P., Sanderson, B. T., Escalante, E., Watkins, L. L., Alumbaugh, R. L., **Protection of steel piles in a natural seawater environment—Part I,** (Proc. 3d Int. Congress on Marine Corrosion and

Fouling, Gaithersburg, Md., Oct. 2-6, 1972), Paper in *Proceedings: Third International Congress on Marine Corrosion and Fouling*, pp. 103-119 (Northwestern University Press, Evanston, Ill., Oct. 1973).

Key words: Cathodic protection; coating index; corrosion rates; marine environment; polarization techniques; protective coatings; steel piling.

In a joint research effort between the National Bureau of Standards, the U.S. Army Corps of Engineers, and the U.S. Naval Civil Engineering Laboratory, the corrosion behavior of protected carbon and low alloy steel piling in seawater is being investigated. Nine-three "H" and pipe pile specimens, 35 feet long, were jetted into the Atlantic Ocean floor off the coast of Dam Neck, Va. The results of this study, which will take about 15 years to complete, will demonstrate which of the systems tested are best for protecting steel piles in seawater. Many types of protective methods are included in the investigation consisting of coating systems (coal-tar epoxy, hot-dip zinc, flamesprayed aluminum and zinc, zinc-rich paints, epoxies, etc.), cathodic protection by zinc and aluminum sacrificial anodes, and combinations of coatings and cathodic protection. At one-year intervals, polarization measurements and visual observations are made on the piles to determine the effectiveness of the coating systems and to measure the rates of corrosion. Potentials of cathodically protected piles are also measured. These data will be correlated with physical determinations made on the piles when they are removed from exposure. The first removal of one set of piles (31 in number) is scheduled for October 1972, after exposure for approximately 5 years.

Schooley, J. F., **Superconductive transition in cadmium,** *J. Low. Temp. Phys.* **12,** Nos. 5/6, 421-437 (Mar. 14, 1973).

Key words: Cryogenics; pure cadmium; reproducibility; superconductivity; thermometric fixed point; transition temperature; transition widths.

Mutual inductance measurements of the superconductive transitions occurring in single-crystal and polycrystalline cadmium samples in magnetic fields of $0 - 10^{-4}$T ($0 - 1$ G) are presented. The temperature at which the zero-field superconductive transition midpoints occur appears to be constant within ± 0.2 mK for transitions narrower than 2 mK, but T_c increases for broader transitions. The transitions exhibited both narrowing and hysteresis, the latter perhaps due to supercooling, in fields of a few tenths of a gauss. T_c has been measured as $0.515 \pm 0.002_5$K on the T_{62} temperature scale.

Simmons, G. L., Eisenhauer, C., **Moments method calculations of neutron distributions in concrete,** *Nucl. Sci. Eng.* **53,** 197-219 (1974).

Key words: Concrete; function fitting; moments; neutron transport; reactor shields; shielding.

The moments method is applied to the problem of calculating neutron distributions in an infinite medium. Several comparisons are given of these results with similar data calculated by the discrete ordinates method. New calculations are presented on the distribution of doses from neutrons, originating in a plane-slant fission source and incident, at various angles, on concrete utilized in radiation measurements at the Tower Shielding Facility of the Oak Ridge National Laboratory (TSF concrete). For a given set of neutron cross sections, these results give reliable estimates of the dose distribution at deep penetrations, i.e., attenuation of six orders of magnitude or more. Functional representations of the distributions are included in order to facilitate the use of the data in shield design calculations.

Smith, E. W., Cooper, J., Chappell, W. R., Dillon, T., **An impact theory for Doppler and pressure broadening—I. General theory,** *J. Quant. Spectrosc. Radiat. Transfer* **11,** 1547-1565 (1971).

Key words: Molecular collisions; scattering theory; spectral line widths.

A quantum-mechanical impact theory for the combined effects of Doppler and pressure broadening is developed from quantum radiation theory. The results are compared with other semiclassical theories and certain simplifying approximations relevant to cases of experimental and theoretical interest are discussed.

Smith, E. W., Cooper, J., Chappell, W. R., Dillon, T., **An impact theory for Doppler and pressure broadening—II. Atomic and molecular systems,** *J. Quant. Spectrosc. Radiat. Transfer* **11,** 1567-1576 (1971).

Key words: Molecular collisions; scattering theory; spectral line widths.

A semiclassical theory for Doppler and pressure broadening in neutral gases is derived as a limiting case of a more general quantum mechanical theory. This theory is compared with other semiclassical theories and methods of calculation are discussed.

Smith, E. W., Cooper, J., Roszman, L. J., **An analysis of the unified and scalar additivity theories of spectral line broadening,** *J. Quant. Spectrosc. Radiat. Transfer* **13,** 1523-1538 (1973).

Key words: Relaxation theory; scalar additivity theory; spectral line broadening; unified theory.

A new derivation of both unified and scalar additivity theories is given. This derivation concentrates on their regions of validity and certain key differences are analyzed in detail.

Smith, E. W., Cooper, J., Vidal, C. R., **Comments on the validity of the unified classical path theory of Stark broadening,** *J. Phys. B* **5,** L33-L35 (1972).

Key words: Electron gas; Stark broadening; unified theory.

In a recent paper by Frisch and Brissaud certain aspects of the unified classical path theory for Stark broadening are criticized; since we feel that their results could be misleading, we offer some comments on their paper.

Smith, M. W., Wiese, W. L., **Atomic transition probabilities for forbidden lines of the iron group elements,** (A critical data compilation for selected lines), *J. Phys. Chem. Ref. Data* **2,** No. 1, 85-120 (1973).

Key words: Chromium; cobalt; forbidden transitions; iron; manganese; nickel; transition probabilities; vanadium.

Atomic transition probabilities for about 750 forbidden spectral lines for elements of the iron group, specifically V, Cr, Mn, Fe, Co, and Ni, have been critically evaluated and compiled using all available literature sources. The selection of the spectra and elements has been made primarily according to their astrophysical importance. The data are presented in separate tables for each element and stage of ionization and for each ion the data are arranged according to multiplets. For each line within a multiplet the transition probability for spontaneous emission is listed along with the standard spectroscopic designation, the wavelength, the statistical weights, and the energy levels of the upper and lower states. In addition, the estimated accuracy and the source are indicated. In short introductions which precede the tables for each ion the main justifications for the choice of the adopted data and for the accuracy rating are discussed. A general introduction contains a detailed discussion of the critical factors entering into the calculations. It also includes detailed comparisons of calculated data with astrophysical observations and a few laboratory results, which serve as a valuable indication for the validity of the estimated accuracies.

Soulen, R. J., Jr., Schooley, J. F., Evans, G. A., Jr., **Simple instrumentation for the inductive detection of superconductivity,** *Rev. Sci. Instrum.* **44,** No. 10, 1537-1538 (Oct. 1973).

Key words: ac susceptibility; superconductivity; temperature; thermometric fixed point.

A circuit is described which can be used to detect the superconductive transitions of several elements used as thermometric fixed points. The circuit is found to perform as well as much more elaborate mutual inductance bridges previously used for this research. Details for construction and operation for the circuit are given.

Stern, K. H., **The effect of anions on sodium-determined glass membrane potentials in molten salts,** *J. Phys. Chem.* **74,** No. 6, 1329-1337 (Mar. 19, 1970).

Key words: Glass electrode; glass membrane potential; molten salts.

The effect of changing anion composition on the sodium-determined glass membrane potential was studied using the molten salt concentration cell

$$\underset{\text{I}}{\text{Ag/AgCl, AgA, Na}^+\text{/fused silica/AgCl, AgA, Na}^+\text{/Ag or Pyrex}}\quad\underset{\text{II}}{}$$

for low concentrations of Na^+, and $A = NO_3^-$, SO_4^{2-}, CrO_4^{2-}, PO_4^{3-}. For all of these anions the ion-exchange selectivity constant increases in a regular manner with increasing oxyanion concentration. Since the cation mobility ratio in the glass is unaffected by changing melt composition, the ion-exchange equilibrium constant similarly increases. These results are accounted for in terms of Eisenman's selectivity theory and the double layer at the glass-melt interface.

Stern, K. H., **The effect of cations on the thermal decomposition of salts with oxyanions. A semi-empirical correlation,** *J. Chem. Educ.* **46, No. 10, 645-649 (Oct. 1969).**

Key words: Inorganic oxyanions; thermal decomposition; thermodynamics.

Decomposition reaction enthalpies of sulfates, carbonates, nitrates and phosphates to the respective oxides are linear functions of the cation radius/electronegativity (r/S) ratio. Alkali metal salts are more stable than predicted by this relation since their oxides have the antifluorite structure which is less stable than the NaCl structure in which most of the other oxides crystallize.

Swanson, N., Cooper, J. W., Kuyatt, C. E., **Resonant structure in near-threshold electron excitation of krypton,** *Phys. Rev. A* **8,** No. 4, 1825-1834 (Oct. 1973).

Key words: Electron excitation; high resolution; krypton; resonance.

By using a monochromator-analyzer combination, electron-excitation functions of the lowest-lying electronic states of krypton have been obtained at a scattering angle of 45° in the near-threshold region (9-14 eV). All excitation functions display a complex resonant structure. Additional data have been obtained on elastic scattering at 45° to provide further information on the resonances. In addition to the $4p^5 5s^2\ J = 3/2, 1/2$ resonance doublet, a number of narrow resonances appear below about 12 eV in both the excitation data and elastic scattering which correlate in energy with recent measurements on transmission by Sanche and Schulz. Broad resonant structure is found in a number of the excitation curves and the excitation process in the near-threshold region appears to be dominated by resonant effects. An analysis of the elastic-scattering data on the $4p^5 5s^2$ doublet is presented and resonance parameters obtained compared with theory. A comparison of the narrow resonant structure data with optical absorption data Rb I obtained by Beutler indicates that the narrow resonances in the 10.5 – 12-eV region are probably due to levels of the $4p^5 5s 4d$ configuration.

Taylor, P. O., Dunn, G. H., **Absolute cross sections and polarization for electron-impact excitation of the *K* and *H* resonance lines of the Ca^+ ion,** *Phys. Rev. A* **8,** No. 5, 2304-2321 (Nov. 1973).

Key words: Ca II; electron impact; excitation cross sections; polarization; resonance lines.

Crossed beams of electrons and Ca^+ ions have been used to measure absolute cross sections for electron-impact excitation of the resonance *K* and *H* lines of Ca II at 3934 and 3968 Å, respectively. Polarization fractions of the light were also measured. The cross sections presented are absolute in the sense that all measurables including photon flux, have been compared to relevant standards. The cross section for excitation of the *K* line is observed to have a value of about $(18 \pm 2)\pi a_0^2$ at the 3.15-eV threshold, and to decrease to a magnitude of $(1.5 \pm 13)\pi a_0^2$ at 700-eV electron energy. Experimental uncertainties have been presented at the 98 percent confidence level, typically three standard deviations of random fluctuations combined in quadrature with the systematic uncertainties. The experimental results for both the *K* and *H* emissions are in agreement at 350 eV with the Coulomb distorted-wave calculation of Burgess and Sheorey but lie about 35 percent below the low-energy three-state close-coupling calculations of Burke and Moores. The ratio of the cross sections for the *K* and *H* emission is found to be 2.0 at all energies. Detailed study of the cross section at low energies demonstrates the expected finite value at threshold (within the accuracy allowed by the electron energy spread of 0.3 eV), and does not indicate the presence of a large (greater than 5%) contribution from cascade. Structure in the *K* cross section about 2 eV above threshold suggests interactions with autoionizing levels of Ca I, presumably belonging to the $5snl$ or $4dnl$ series. The polarization fraction at low energy is about 25 percent higher than the calculation of Saraph which is based on the Burke and Moores close-coupling calculation.

Thomas, R. N., Gebbie, K. B., **Theory of stellar atmospheres,** *Trans. Int. Astron. Union* **15A,** 537-569 (1973).

Key words: Stellar atmospheres.

This report has been prepared by the President in collaboration with the Secretary of the Commission. It is based on (1) material supplied by those members and associates of the Commission who responded to requests made in our circulars, (2) a bibliographical search intended to supplement the above material, (3) discussions with other interested persons, and (4) our own knowledge and impressions of the activity within the province of the Commission over the last three years. The report is divided into three parts. Part A is a scientific review aimed not at a comprehensive summary of all work but at a selective review of that which has, in our opinion, introduced some significant change in our concept of a stellar atmosphere or in the likely direction of future developments. Part B is a bibliography. It is this part of the report that is intended to provide an exhaustive summary of work done in the field over the last three years. To authors of those papers we have inadvertently omitted, we offer our apologies: neither were they sent to us nor did we locate them ourselves. Finally, Part C is an outline of the aims and activities of the Commission.

The decision to write the entire report ourselves, rather than delegate specific sections to other people, was aimed at providing a more coherent approach to the subject as a whole. Clearly, this represents only one of many possible approaches, and the form of the report is highly individual. The choice of what to include without encroaching on the fields of other commissions has become increasingly difficult. No longer can Commission 36 confine itself to theoretical models of stellar atmospheres. Empirical analyses that reveal inconsistencies in our theoretical assumptions must also be included, as must some consideration of solar phenomena, which are now recognized as being relevant to a wide variety of stars. Reference must also be made to those results of physics that are immediately applicable to the theory of stellar atmospheres. Inevitably, the selection has to some extent been arbitrary.

Thomas, R. N., **Suggested interpretation of the correlations in intensity fluctuations in the lines Ca II H and K, magnesium b, and hydrogen Hβ,** *Solar Phys.* **27,** 303-304 (Dec. 1972).

Key words: Intensity fluctuations; solar spectral lines.

In the preceding note, Evans and Catalano have found interesting behavior in the correlation between intensity fluctuations in the continuum and in the lines H and K of Ca II, b1 and b2 of MgI, and hydrogen Hβ. In the first four lines, the correlation drops smoothly from ~ 0.9 near the continuum to negative values; followed by a rise to about zero at line center. For H, the correlation is never negative, reaching zero at about 0.25 Å.

We suggest that this behavior reflects a combination of effects. First the source-sink terms in the source-functions depend on different physical parameters in the two sets of lines. In addition, the line center regions are dominated by transfer effects at the top of the atmosphere.

Tilford, S. G., Simmons, J. D., **Atlas of the observed absorption spectrum of carbon monoxide between 1060 and 1900 Å,** *J. Phys. Chem. Ref. Data* **1,** No. 1, 147-187 (1972).

Key words: Absorption spectra; carbon monoxide; electronic transitions; identification atlas; potential energy curves; rotational constants; ultraviolet; vibrational constants.

This atlas summarizes the results of a recent investigation of the carbon monoxide absorption spectrum between 1060 and 1900 Å. Twelve electronic transitions are observed in this region; four electric dipole allowed electric transitions from the ground state $X^1\Sigma^+$ to the $A\,^1\Pi$, $B\,^1\Sigma^+$, $C\,^1\Sigma^+$, and $E\,^1\Pi$ states, and eight forbidden transitions to the $a'\,^3\Sigma^+$, $e\,^3\Sigma^-$, $a\,^3\Pi$, $D\,^1\Delta$, $d\,^3\Delta_i$, $I\,^1\Sigma^-$, $j\,^3\Sigma^+$, and $c\,^3\Pi$ states. The following items are presented in the atlas: (1) A photograph of the spectrum with band assignments; (2) a table of band head measurements and assignments arranged by wavelength; (3) a summary of the spectroscopic constants and potential curve for each electronic state; (4) a line list, arranged by wavelength, of the observed rotational lines of the allowed transitions.

Tschiegg, C. E., Greenspan, M., **Helmholtz resonators as sonic bubble chambers?,** *J. Acoust. Soc. Amer.* **54,** No. 4, 1112-1113 (oct. 1973).

Key words: Bubble chamber; Helmholtz resonators; rapid-cycling bubble chamber; sonic bubble chamber.

It has been found possible to develop alternating pressures of up to 10 atm in liquid-filled Helmholtz resonators. Some advantages and disadvantages of the construction of a rapid-cycling bubble chamber along such lines are discussed.

Vidal, C. R., Cooper, J., Smith, E. W., **Hydrogen Stark-broadening tables,** *Astrophys. J. Suppl. Ser.* **25,** No. 214, 37-135 (Jan. 1973).

Key words: Stark broadening of hydrogen.

Tables of Stark broadening of the first four Lyman lines and the first four Balmer lines of hydrogen are presented. They are based on a recently developed "unified theory" of line broadening which generates normalized profiles covering the entire profile from the impact limit in the line center to the quasi-static limit in the line wings. The tables are presented in a convenient form for accurate numerical interpolation.

Vidal, C. R., **Spectroscopic observations of subsonic and sonic vapor flow inside an open-ended heat pipe,** *J. Appl. Phys.* **44,** No. 5, 2225-2232 (May 1973).

Key words: Heat pipe oven; resonance fluorescence spectra; sonic flow.

Spectroscopic measurements of the vapor flow velocities inside a heat-pipe oven have been performed as a function of pressure, heater power, and radial position inside the pipe. For this purpose the relative intensity of the collision-induced satellite lines in laser-induced resonance fluorescence spectra of the $^7Li_2$ molecule has been employed. A one-dimensional flow model is presented which determines the vapor parameters as a function of position along the pipe. It predicts the onset of the sonic flow which has been verified experimentally. A criterion is derived from which the parameters of the vapor can be obtained from the ideal gas relation, neglecting velocity-dependent terms.

Weisman, I. D., Bennett, L. H., Maxwell, L. R., Sr., **In vivo NMR relaxation studies of tumors,** *IEEE Trans. Magn.* **MAG-9,** No. 3, 454-456 (Sept. 1973).

Key words: In vivo; melanoma; nuclear magnetic resonance; spin-lattice relaxation; spin-spin relaxation; tumor.

Pulsed nuclear magnetic resonance has been used to differentiate between normal mouse tail tissue and a malignant transplanted melanoma S91 located on the tail of a live mouse. Measurements of proton spin-lattice and spin-spin relaxation serve to detect and monitor the tumor growth. The mature tumor exhibits a spin-lattice relaxation time T_1 of ~ 0.7-0.8 s contrasting with the corresponding normal tail tissue T_1 of half this value. On the other hand spin-spin relaxation in normal tissue cannot be characterized by a single relaxation time T_2. The corresponding relaxation in a mature tumor is found to be closer to a single exponential but still requires at least two superimposed exponential decays.

Weisman, I. D., Swartzendruber, L. J., Bennett, L. H., **Nuclear resonances in metals: Nuclear magnetic resonance and Mössbauer effect,** Chapter 9 in *Techniques in Metals Research,* E. Passaglia and E. Bunshah, Eds., **6,** Part 2, 165-504 (John Wiley and Sons, Inc., New York, N.Y., 1973).

Key words: Experimental techniques; ferromagnetic nuclear resonance; metallurgy; Mössbauer effect; nuclear magnetic resonance; pure quadrupole resonance.

It is the purpose of this chapter to review nuclear magnetic resonance, nuclear quadrupole resonance, ferromagnetic nuclear resonance and the Mössbauer effect in metals, alloys and intermetallic compounds. The emphasis is on the technique of measurement, and includes only such theory as is deemed essential to understand the purpose of the measurement, its limitations, the sample preparation required, and when a particular kind of measurement is most appropriate.

Wiederhorn, S. M., Hockey, B. J., Roberts, D. E., **Effect of temperature on the fracture of sapphire,** *Phil. Mag.* **28,** No. 4, 783-796 (Oct. 1973).

Key words: Alumina; crack growth; critical stress intensity factor; fracture; plastic deformation; sapphire; strength; transmission electron microscopy.

At low temperatures, metastable crack growth dictates the environment free strength of sapphire. Plastic deformation by dislocation motion or twin formation and growth plays no role in the fracture process at temperatures below 400 °C. These conclusions are supported both by crack growth studies and critical stress intensity factor measurements on sapphire crystals, and by transmission electron microscopy studies of arrested cracks in sapphire and alumina.

Wiese, W. L., **Arc plasmas as radiation standards in the vacuum ultraviolet,** (Proc. VI Yugoslav Symp. and Summer School on the Physics of Ionized Gases, Miljevac by Split, Yugoslavia, July 16-21, 1972), Paper in *Physics of Ionized Gases,* M. V. Kurepa, Ed., pp. 597-625 (Institute of Physics, Beograd, Yugoslavia, 1972).

Key words: Hydrogen arc plasma; radiation standard; radiometric calibrations; vacuum ultraviolet.

The principle of using arc plasmas as radiation standards in the

vacuum ultraviolet is described, and it is shown that a hydrogen arc plasma has particularly suitable properties due to the fact that its atomic radiation constants are exactly known. The calibration work with a hydrogen arc plasma at NBS is discussed, and preliminary results with this recently established facility are presented.

Yates, J. T., Jr., Madey, T. E., Rook, H. L., **Wear of English monumental brasses caused by brass rubbing,** *Nature* **243,** No. 5407, 422-424 (June 15, 1973).

Key words: Monumental brasses; neutron activation; preservation of historical objects; wear.

Measurements of the wear of English monumental brasses during brass rubbing have been made using neutron activation analysis. The median rate of wear as determined from twenty-six measurements corresponds to an average thickness of 1.8×10^{-5} cm of brass removed per rubbing.

Young, K. F., Frederikse, H. P. R., **Compilation of the static dielectric constant of inorganic solids,** *J. Phys. Chem. Ref. Data* **2,** No. 2, 313-409 (1973).

Key words: Dielectric loss (tangent); permittivity; static dielectric constant, frequency dependence of, temperature dependence of, pressure dependence of.

This monograph contains values of the static dielectric constant of more than 300 inorganic solids. The temperature and frequency of the measurements are listed and the magnitude of the loss tangent is indicated if known. For ninety materials—including most ferroelectrics and antiferroelectrics and several oxides and halides—additional information is presented in the form of graphs depicting the temperature dependence of the dielectric constant. In a few cases the frequency and pressure dependences are also shown. The basic principles and formulas pertinent to the field of dielectrics are reviewed in a short introduction. This part also mentions several measuring techniques and indicates the criteria used for data selection.

U. S. GOVERNMENT PRINTING OFFICE : 1974 OL - 533-558

UNITED STATES
GOVERNMENT PRINTING OFFICE
PUBLIC DOCUMENTS DEPARTMENT
WASHINGTON, D.C. 20402

OFFICIAL BUSINESS
PENALTY FOR PRIVATE USE $300

U.S. DEPARTMENT OF COMMERCE
POSTAGE AND FEES PAID
COM-375

JOURNAL OF RESEARCH of the National Bureau of Standards
A. Physics and Chemistry

Vol. 78A, No. 3 May–June 1974

SJRA UNIVE300UA R 1
UNIVERSITY MICROFILMS INC
ATTN SERIALS SECTION
300 NORTH ZEEB RD
ANN ARBOR MI 48106

Page

Photoionization of CO_2-CO-O_2 mixtures. Formation and reactions of ion clusters. L. W. Sieck and R. Gorden, Jr. 315

Analysis of low temperature viscosity data for three NBS standard glasses. A. Napolitano, J. H. Simmons, D. H. Blackburn, and R. E. Chidester. 323

PVT relationships for liquid and glassy poly(vinyl acetate). John E. McKinney and Martin Goldstein. 331

Correction and extension of van der Poel's method for calculating the shear modulus of a particulate composite. Jack C. Smith. 355

The formation of curved polymer crystals: Polychlorotrifluoroethylene. J. D. Barnes and F. Khoury. 363

Enthalpy of formation of phosphorus pentachloride; derivarion of the enthalpy of formation of aqueous orthophosphoric acid. R. H. Schumm, E. J. Prosen, and D. D. Wagman. 375

Heat capacities of polyethylene from 2 to 360 K. II. Two high density linear polyethylene samples and thermodynamic properties of crystalline linear polyethylene. S. S. Chang. 387

The specific heats, C_σ, C_V, of compressed and liquefied methane. B. A. Younglove. 401

An improved procedure for synthesis of DL-4-hydroxy-3-methoxymandelic acid (DL-"vanillyl"-mandelic acid, VMA). Alexander J. Fatiadi and Robert Schaffer. 411

Single particle motions in liquids: qualitative features of memory functions. Raymond D. Mountain. 413

The infrared spectra of matrix isolated uranium oxide species. S. Abramowitz and N. Acquista. 421

Publications of the National Bureau of Standards. 425

Library of Congress Catalog Card Number: 62–37059

For sale by the Superintendent of Documents, U.S. Government Printing Office, Washington, D.C. 20402. (Order by SD Catalog No. C 13.22/sec.A:78/3). Single copy price varies. This issue $3. Subscription price $17.00 a year; $4.25 additional for foreign mailing.

UNITED STATES GOVERNMENT PRINTING OFFICE, WASHINGTON : 1974